The Partial Frequency Energy Converter: A Novel Device for Low-Frequency Offshore Wind Electricity Transmission

PhD Thesis

Edgar Lucas Macleod

Department of Electronic and Electrical Engineering

University of Strathclyde, Glasgow

May 18, 2022

This thesis is the result of the author's original research. It has been composed by the author and has not been previously submitted for examination which has led to the award of a degree.

The copyright of this thesis belongs to the author under the terms of the United Kingdom Copyright Acts as qualified by University of Strathclyde Regulation 3.50. Due acknowledgement must always be made of the use of any material contained in, or derived from, this thesis.

Dedicated to

Rachel Ann Lucas Macleod.

My wife and best friend.

Abstract

Low frequency AC transmission has been proposed for the integration of distant offshore wind farms to offer a compromise between HVAC and HVDC. The advantages in transmission distance due to the reduced power losses over HVAC and an improved fault-handling capability over HVDC suggests that there is room for this technology in the wind industry. However research and industrial trends have favoured the continued use of HVDC connections despite growing concerns over cost and reliability. HVDC connections are not without issues, and questions regarding to this technology's robustness, cost, size and synchronisation are still left unanswered. Additionally the limited supply chain and the bespoke nature of each HVDC connection introduces a further set of unknowns to project cost. Technical problems arising from recent HVDC developments have shaken the confidence of the industry and left large risk premiums on all future deployments of the technology. This thesis looks into developing novel technology to unlock the advantages of LFAC but without the downsides associated with large power-electronic converters. This technology is called the Partial Frequency Energy Converter (PFEC) which combines the controllability of DC converters with the robustness of large electrical machines. By using a combination of modern control techniques and the manipulation of electromagnetic fields in a novel arrangement of induction machines, the PFEC exists as a fusion between old and new technology. The PFEC not only allows the integration of LFAC systems to the AC grid but it is also capable of providing inertia and stabilisation to power systems. The PFEC therefore offers a solution that is not only technologically viable, but also timely and necessary to the industry.

Acronyms

Acronym	Description
PFEC	Partial frequency energy converter
RT	Rotary transformer
DFIM	Doubly-fed induction machine
DFIG	Doubly-fed induction generator
WRIM	Wound rotor induction machine
B2B-VSC	Back-to-back voltage sourced Converter
HVAC	High voltage alternating current
HVDC	High voltage direct current
LFAC	Low frequency alternating current
BDFIG	Brushless doubly-fed induction generator
BCDFIG	Brushless cascade doubly-fed induction generator
BDFM	Brushless doubly-fed machine
BPFEC	Brushless partial frequency energy converter
PLL	Phase locked loop
VFT	Variable frequency transformer
MG	Motor-generator
DSP	Digital signal processor
XLPE	Cross-linked polyethylene
LCC	Line commutated converter
IGBT	Insulated gate bipolar transistor
TSO	Transmission system operator
PRC	Partially rated converter
FRC	Fully rated converter
PWM	Pulse width modulation
PI	Proportional integral
RMS	Root mean squared
RSC	Rotor side converter
GSC	Grid side converter
SVC	Static VAR compensator
GIS	Gas insulated switchgear
FRT	Fault ride-through
HVRT	High voltage ride-through

Contents

List of Figures

List of Tables

Chapter 1

Introduction

The evolution of offshore wind over the past few years has been a major success story, particularly in the UK and has provided hope for a clean energy future that is no longer dependent on fossil fuels. There is currently a global shift to clean growth motivated by government emissions targets and the continually decreasing costs of energy which have resulted in an increased annual share of UK generation up to around 10% in 2020 and a predicted installed capacity of 30GW by 2030. Likewise, huge expansion of offshore wind is also forecast around the world, with some estimates predicting an increase in total installed capacity from 22GW to 154GW by the end of the decade [1].

The trend to move offshore has been driven by the lack of availability of land and public opposition to large onshore wind turbines concerning their visual impact. Other significant factors surrounding the geographical migration of wind energy are due to the improved wind resource at locations situated far from the shore. These stronger, more reliable and less turbulent winds result in higher capacity factors and reduced wind loads making offshore wind all the more appealing. This is particularly evident in the UK and most notably in Scotland, which claims to have some of the greatest wind resources in the world [2].

The technical difficulties in migrating further offshore require a re-evaluation of the available technology. The average distance to shore for a UK offshore wind farm in-

stalled in 2017 was 41km, but to capture the full potential of the available energy this distance will need to increase. Pushing further out into the UK exclusive economic zone and towards the perimeters of the continental shelf, the water depths continually deepen and bring challenges associated with the foundations, the access to the site, and the method of power transmission back to the shore. The latter of these points provides the main motivation for this work.

There are currently only two commercially available methods of power transmission for offshore wind, with no universally agreed consensus on which technology is superior from an economic standpoint. HVAC is the more mature technology and has the advantage of relatively low terminal costs owing to its simplicity. However, at long cable lengths the existence of charging currents greatly inhibit the maximum transmissible range without compensation. HVDC on the other hand boasts an almost unlimited range but suffers from massively increased terminal costs due largely to the presence of the offshore converter station. The relatively new and innovative application of HVDC technology to offshore wind has also resulted in costly delays to recent installations.

A proposed solution to the dilemma of HVAC vs HVDC comes in the form of low frequency alternating current (LFAC), in which power is transmitted at a reduced frequency, typically 16.7Hz, and is stepped-up to 50Hz for use in the utility grid by a single converter. This technology is well established in electric locomotives throughout Europe yet it is seemingly neglected in the application to wind energy, with no proposed installations planned for the near future. The charging currents experienced in HVAC exhibit a linear dependence on frequency, so by reducing the frequency, the distance of the conductors can be increased by the same ratio. LFAC has been described as being the best of both worlds [3] in the offshore environment, offering longer cable lengths and requiring only a single converter station. Given its advantages it is envisioned that this method of transmission could provide an alternative option for medium-range wind farms, serving as a cost-effective intermediary step between HVAC and HVDC.

It has been suggested in the literature that any future LFAC project is likely to utilise a power-electronic based frequency converter, probably a VSC due to their popularity in HVDC. However, the lack of any clear plans opens up the potential for a novel solution, namely the partial frequency energy converter (PFEC) which is at the core of this thesis. The PFEC is in essence a pair of controllable asynchronous machines that exploit the principles of electromagnetic induction to perform a frequency conversion that is analogue in nature. The benefits of this are a smooth transition between operating points because of the lack of switching devices, and an increased inertia owing to the large mass of the rotors. Control of the PFEC is achieved by exploiting the dependence of frequency on slip in a similar way to how a DFIG operates inside a wind turbine via a partially rated converter. The PFEC therefore provides the interconnection between the low-frequency wind farm and the grid in a manner that is both flexible and robust, combining well established machine theory with modern power electronics.

1.1 Research Scope and Objectives

The general objective is to develop and validate a technology to enable an alternative for bulk offshore power integration to power networks. The major research questions are therefore:

1. Does the technology work?
2. Does the PFEC make sense as a solution for offshore wind, both from a practical and economic standpoint?

The first of these questions is covered in chapters 3 and 4 which focus on the modelling and validation through simulation of the PFEC respectively. The validation of the PFEC power transfer is covered specifically in section 4.3. The second question is the focus of the remainder of the thesis, with chapters 4 and 5 exploring the functionality of the PFEC and chapter 6 introducing a cost model. Beyond these most favourable questions are some minor research questions which are also considered:

a) How robust is the PFEC?

b) Is the PFEC stable in the absence of power electronics?

c) What ancillary services can the PFEC provide to the grid?

Parts a) and b) are dealt with in chapter 4 which looks at the PFEC under a range of operating scenarios and faults. Part c) is the focus of chapter 5 which looks at synthetic inertia provisions.

This thesis focuses on the development of novel technology to incorporate LFAC power into power networks. The scope of this work includes the following:

- electrical modelling, deployment and analysis of the PFEC
- the control system
- self-sustaining and equilibrium capabilities of the PFEC
- services to the grid
- development of a cost model

Although the workings of a PFEC are discussed in detail, the specific electromagnetic design of such a machine is not included in this work, for example the physical geometries of the stator, rotor and airgap, winding topology, slit design etc. It is understood that careful consideration of these factors could dramatically improve efficiency but the scope of this subject is too large. Similarly, although reactive power is introduced, a detailed study on the flows of reactive power is not provided. The mechanisms of slip ring fatigue are not mentioned directly but appendix A does discuss the concept of a brushless PFEC.

1.2 Main Contributions

This dissertation offers a methodological approach to the modelling of the PFEC which is concise and well documented with the intention of enabling an ease of understanding

for any future developments that build upon this work. The framework that is laid down in the opening chapters aims to provide a solid foundation and understanding of the simulation process such that every detail and component of the PFEC power transmission system is explained in full. The control structure of the PFEC is similarly well documented and offers insight into how the control principles of the DFIG can be modified for use in this novel power transmission solution. Beyond this, some important mathematical fundamentals of the PFEC are derived, such as the relationship between pole ratio and operating frequency, the concept of using frequency as a controllable variable, the combined torque-speed curve of the RT and the DFIM, and how this results in a self-sustaining equilibrium allowing the PFEC to remain connected in a stable configuration in the absence of power-electronics.

Other contributions focus on the ancillary services that the PFEC can offer to the grid, namely the release of stored inertia in response to a grid fault and how this impacts the stability of the wider electrical network. Custom synthetic inertia controllers have been developed for the PFEC based on those found in the literature, and by changing the gains of these controllers, it is possible to control how much the PFEC participates to the fast frequency response. Following this, an investigation into the small-signal stability of a PFEC outfitted with a synthetic inertia controller is presented.

Additionally, a cost model has been developed allowing a direct comparison into the CAPEX of the PFEC as an offshore wind electricity transmission solution. Data compiled from various sources on HVDC and HVAC transmission topologies are supplied along with cost estimations for the PFEC based on the most similar technology currently in existence.

Finally, work in the appendix introduces the concept of a brushless-PFEC as a way of removing the slip-rings from the device. Comprehensive models designed from first-principles are thoroughly explained, as are the innovative control systems used to manipulated the currents in this double-stator version of the PFEC. The models

are then validated through simulation. Also in the appendix is the current state of developing a working PFEC prototype. This was unfortunately interrupted by the outbreak of the Covid-19 pandemic such that all lab activity had to cease, and what is presented here is only the development of the converter board and control system interface.

1.3 Structure of Thesis

The thesis is structured as follows:

- In **Chapter 2**, the theory and main components required for an LFAC transmission system are introduced, as are the various methods of frequency conversion which collectively come together to form the PFEC
- In **Chapter 3**, a power system model is developed that is suitable for electromagnetic simulations. The modelling process and design of the controllers are derived for each the various PFEC components
- In **Chapter 4**, simulations of the newly developed models are run to investigate some key operating characteristics of the PFEC
- In **Chapter 5**, we explore how the PFEC can be augmented with a synthetic inertia controller to aid the grid during a frequency event. However, the downsides of this increased participation come in the form of a reduced small-signal stability, exhibited by a decrease in damping of inter-area modes which are discussed for a range of network scenarios
- In **Chapter 6**, a cost model is developed to assess how the CAPEX of the PFEC compares with that of a standard HVAC and HVDC transmission system. Cost figures published by industry on the most similar technology to the PFEC, along with some assumptions on scaling are used to provide an estimated upper and lower bound of PFEC cost
- In **Appendix A**, the constraints imposed by the slip rings on the maximum power rating of a single PFEC unit are discussed which leads to the development

of a brushless-PFEC model that may be used to avoid the technological limitation of the brushgear

- In **Appendix B**, the current progress towards a PFEC prototype is presented. The theory, design and testing of a custom converter board built in-house is provided and serves as a starting point for any future hardware development
- In **Appendix C**, the parameters used throughout the thesis are listed for reference

1.4 Research Outputs

- E. Lucas Macleod, D. Campos-Gaona, O. Anaya-Lara, "**Assessing the Impact of DFIG Synthetic Inertia Provision on Power System Small-Signal Stability**". Published in Energies: Control Schemes for Wind Electricity Systems, Special Issue, 2019
- Patent Application: currently at STAGE 2, "**TECH2029: Process to deliver offshore wind power to the onshore grid using low-frequency alternating current**". D. Campos-Gaona, E. Lucas Macleod, O. Anaya-Lara, W. Leithead.

Chapter 2

Technical Review and State of Knowledge on LFAC

This chapter presents the background and motivation for LFAC transmission for offshore wind and introduces some fundamental components which must be understood for their application to the Partial Frequency Energy Converter (PFEC). In particular, special focus is placed on the design of the frequency converter. A variety of converter topologies, both digital and analogue, are introduced to develop a firm basis of understanding about the many ways in which the frequency conversion is possible. In the final part of this chapter modern power electronic converters are combined with electrical machines to form the PFEC, which performs the AC/AC frequency conversion and thus offering a novel solution to LFAC connections for offshore wind.

2.1 LFAC Introduction

The history of LFAC began in World War I when a shortage of coal necessitated the introduction of electric motors to the railway industry. The trains required controllable speed operation but the existing DC motor drives which were favoured for speed control were not suitable due to the difficulty in voltage transformations. Long distance DC transmission was therefore impossible without incurring unacceptable losses so an AC

solution was sought. At the time, three-phase induction motor technology was available but the 50Hz frequency of the AC grid placed too much stress on the collector systems of series wound motors. The compromise was to use 1/3 of the nominal frequency, or 16 2/3 Hz, which was later altered slightly to 16.7 Hz to improve stability [4]. This trend has continued into the present day, with several European countries still deploying LFAC to some degree in their railway electrification systems.

Some studies have suggested that LFAC could be used a method for interconnecting grids that operate at different frequencies and voltage levels using conventional AC cables [5]. Cross-linked polyethylene (XLPE) is the most widely used and suitable insulation material for a long transmission cable, however it struggles to operate with an HVDC system because of the space charge accumulation phenomenon which leads to non-uniformities of the electric field in the dielectric, ultimately resulting in insulation breakdown. Instead of improving the dielectric material, the authors proposed the use of LFAC to make the most of the XLPE material and to improve cable utilisation.

LFAC transmission has since been proposed as an alternative to HVDC and HVAC for offshore wind due to the extension of power transmission distance over AC solutions and the reduction in the number of converter stations over DC solutions. While an HVDC offshore wind system requires a pair of converters, one to rectify and one to invert, an LFAC system requires only a single converter to increase the frequency to that of the utility. This single converter station can be located onshore to offer significant cost reductions and improvements to reliability and down-times in the case of a fault.

2.2 LFAC Power Transmission Fundamentals

There are essentially three factors that limit the power transmission capability of an AC cable: the thermal limit; the stability limit; and the voltage limit. Of these three the thermal limit is of least importance and is not a significant factor in the design of long distance AC transmission. Maximum loadability mainly depends on the stability and

voltage limits [6]. The stability limit of an AC transmission system can be approximated by (2.1), and the voltage drop along a cable is given in (2.2).

$$P_{max} = \frac{V^2}{X} \tag{2.1}$$

$$\Delta V\% = \frac{QX}{V^2} \times 100 \tag{2.2}$$

where V is the voltage, X is the reactance of the transmission line, Q is reactive power and P_{max} is the maximum transmissible active power. According to these relationships, the transmission capability of an AC cable can be improved either by increasing the voltage or decreasing the reactance. The latter of these can be exploited by LFAC due to the relationship between reactance and frequency.

The increased current carrying capability of a low frequency cable can be further understood by considering the charging currents associated with the capacitance of the cable. The expression in (2.3) shows the linear relationship between charging current I_c and frequency f, length l, capacitance C and voltage V such that by decreasing the frequency, the charging currents decrease in the same proportion. This has the effect of reducing the reactive power generated by the cable in (2.4), thereby increasing the maximum active power capability according to (2.5), where S is apparent power.

$$I_c = 2\pi f l C V \tag{2.3}$$

$$Q = I_c V \tag{2.4}$$

$$P = \sqrt{S^2 - Q^2} \tag{2.5}$$

A schematic of a low frequency AC system is shown in figure 2.1 which demonstrates the interconnection of two 50Hz networks via an LFAC link with a frequency converter located at each end.

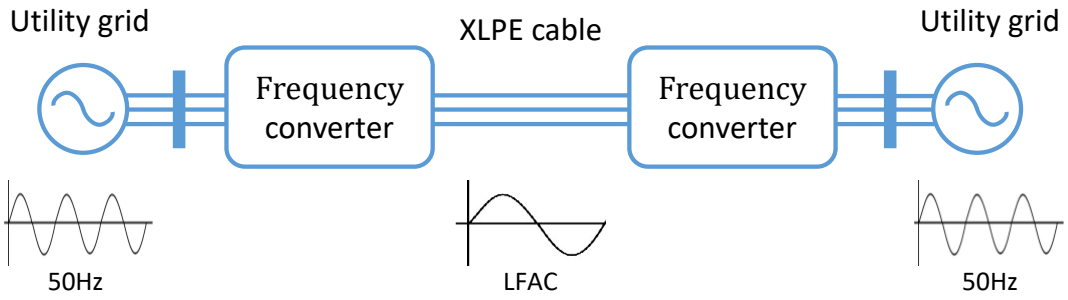

Figure 2.1: Low frequency AC system

2.3 LFAC for Offshore Wind

LFAC drew revised interest with the growing popularity of offshore wind when it was discovered that this transmission method could offer potential benefits to the maximum transmissible distance of power. The integration of offshore wind with the main utility grid is a subject of ongoing research. Presently, the only two commercially available transmission systems consist of HVAC or HVDC connections which are both well-established technologies [7]. The main advantages of HVAC transmission are in its simplicity in transforming voltage levels and the ease of designing the protection systems. A major drawback is the high capacitance of the submarine cables caused by the close proximity of the three phases within the cable housing which leads to considerable charging current and a reduced active power transmission capacity. This imposes a limit on the maximum transmission distance such that HVAC is only adopted for relatively short cable lengths of up to around 50 - 75km [8].

The main advantage of HVDC technology, whether it is line-commutated using thyristors (LCC-HVDC) or self-commutated using IGBTs (VSC-HVDC), is that there is essentially no limit to transmission distance due to the absence of reactive current in the transmission line [9]. LCC-HVDC systems can handle very large power levels of up to 1 GW with a high reliability [10] but also introduce low-order harmonics and consume large amounts of reactive power, thus necessitating the addition of auxiliary equipment such as AC filters and static VAR compensators. VSC-HVDC systems suf-

fer from a reduced reliability and a decreased power level capacity when compared to LCC-HVDC [10], typically rated at around 300 - 400MW, however they do allow independent control over the active and reactive power. HVDC is applied for distances greater than 100km for offshore wind transmission due to the complexity of the power electronics converters at each end of the line and the associated high costs of the system [11].

2.3.1 Practical Difficulties Encountered with HVDC

An ongoing question for many developers is the decision of whether to use AC or DC for transmission for offshore wind. A number of developers have noted significant challenges associated with DC solutions, relating to long lead times, cost overruns, technological immaturity and a poor track record in using VSCs for bulk power transmission. The initial experiences from the German HVDC sector have negatively impacted the uptake of this technology and in a 2014 study by the Crown Estate on offshore transmission [12], some of the most cited problems refer to HVDC installations, as shown in figure 2.2.

The second and third largest points in figure 2.2 which refer to a lack of competition and long lead times are especially true of HVDC systems. Almost all HVDC substations built to date have required a bespoke design which inevitably leads to higher costs due to the limited compatibility between projects.

Other problems associated with HVDC contained are given below:

- Installation delays
- Technological immaturity of VSC technology for offshore wind
- Large size of HVDC converter platforms in the range of 10,000 - 17,000 tonnes
- Addition of risk premium to future HVDC projects

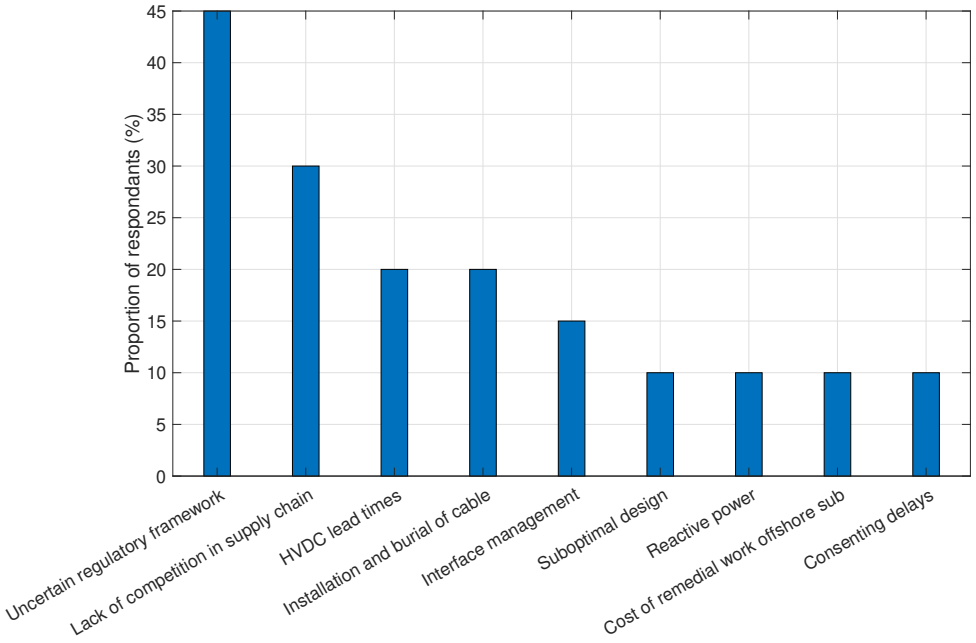

Figure 2.2: Problems cited most often by interviewees

The significance of converter platform size can be explained by the difficulty in installing such a large mass. There are very few vessels in the world capable of lifting greater than 10,000 tonnes, which leads to restricted installation windows, increased risk and increased cost. Delays associated with the supply chain, bespoke technology and installation of recent HVDC projects have led to multi-million euro compensation claims such that all future projects must pay for the mistakes of the past via an inflated risk premium.

The problems faced with HVDC have led some to consider using LFAC at 16.7Hz as a potential alternative for offshore wind [5], [6] [13]. Replacing the offshore HVDC converter stations with a single LFAC onshore substation could lead to significant cost reductions, especially if the wind turbines themselves produce power directly at the reduced frequency. It should also be pointed out that in the above analysis, there were very few concerns raised over the onshore assets which is considered to be representative of the industry [12]. The layouts of a typical HVAC, HVDC and LFAC offshore wind

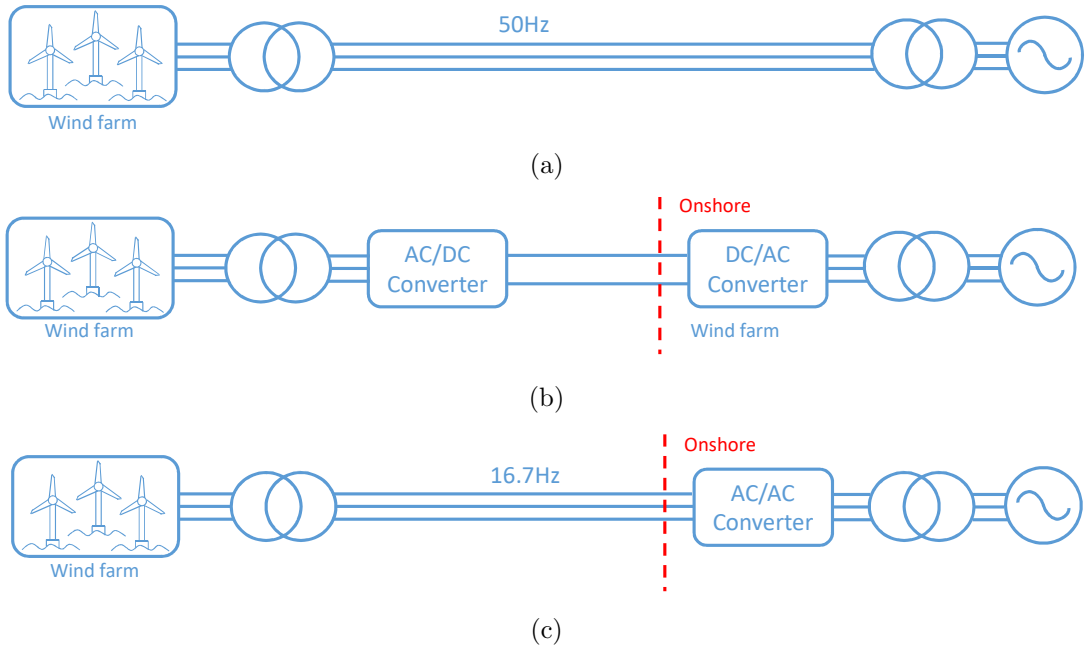

Figure 2.3: Single-line diagrams for typical offshore wind transmission systems: a) HVAC, b) HVDC, c) LFAC

power plant are shown in figure 2.3.

One of the main advantages of LFAC is the reduced charging current in the submarine cables leading to an increased transmission distance and power capacity when compared to an equivalent 50Hz HVAC system. This also allows the use of standard AC circuit breakers for protection. Low frequency AC transmission is therefore proposed for the purpose of decreasing the cost of transmission and making the wind farm a more reliable power source [14]. Another advantage of the low frequency offshore grid is the possibility of a meshed 16.7 Hz network using largely existing equipment. Offshore wind projects designed with different voltage levels could be interconnected in much the same way as they are onshore with relative ease when compared to the proposed DC meshed grid [15].

For a 16.7Hz LFAC system, only one frequency converter is required which will be located onshore for ease of access for maintenance. The only change to the operation of

a B2B-VSC is in adapting the converter to the 16.7Hz frequency. Transformers, reactors and indeed any device that operates via a magnetic flux must be larger due to the inverse relationship between core area and electrical frequency. A DFIG-based wind turbine is therefore an unattractive configuration for an offshore LFAC wind farm due to the increased size and weight of the generator. However, by extending the reduced frequency condition throughout the entire offshore network, FRC wind turbines can be used by adapting the converters to operate at 16.7 Hz and increasing the size of the transformers [15].

Standard B2B-VSC stations are already in operation for connecting 50 Hz with 60 Hz networks, such as the Garabi converter station that links the utility networks of Brazil and Argentina [16], and could be modified for 16.7/50 Hz operation. Fully developed 50/16.7 Hz converters are already available from the European railway industry which allow conversion from three phase 50Hz AC to single phase 16.7 Hz AC [17]. These could easily be extended to three phase operation without any fundamental changes to the device.

2.4 LFAC Components

This section introduces the main components present in LFAC transmission systems and covers cables, transformers, switchgear and the converter station so as to fully describe the design and operation of an LFAC offshore wind power plant. The method of frequency conversion is of particular importance as it underpins the subject of this thesis, therefore various converter topologies from the literature are discussed before ultimately introducing the PFEC.

2.4.1 Cables

Practically, there is no difference in design between AC cables operated at 50 Hz or 16.7 Hz, meaning that the commercially available AC submarine cables that have been used for decades to interconnect different networks across large underwater distances can be readily applied to an LFAC transmission system. In fact, a 50 Hz cable operated at the reduced frequency performs better due to the decreased sheath and dielectric losses as well as the decreased resistance due to the lower skin effect. The problem associated with space charge accumulation encountered in HVDC cables are not applicable to LFAC since this effect is neutralised in frequencies higher than 0.1Hz [18]. It is also reported that the breakdown voltage for a low frequency cable is higher than its 50Hz AC counterpart.

Parameters for a 155kV and a 245kV AC submarine cable are provided in tables 2.1 and 2.2 respectively, which show the increase in current-carrying capability and associated maximum power rating when a cable is operated at the reduced frequency of 16.7 Hz. The decreased resistance and lower reactance are also visible [15].

The equivalent circuit for a lossless AC cable is shown in figure 2.4a, which represents a transmission line as an impedance Z and a shunt admittance Y. A more detailed representation of a transmission line is shown in figure 2.4b which takes into account resistance R, inductance L, conductance G and capacitance C.

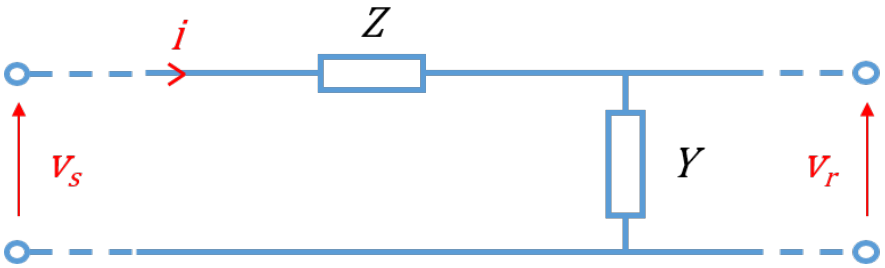

(a) Simplified electrical cable

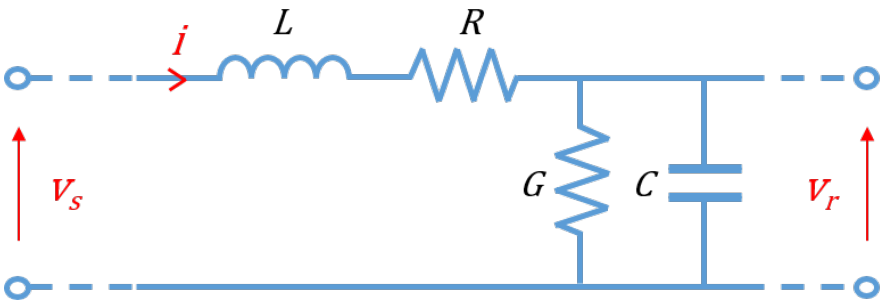

(b) Electrical cable showing resistive and reactive components

Figure 2.4: Three-phase electrical cable schematic

Reducing the frequency results in both a decrease in inductive reactance and an increase in capacitive reactance as shown by (2.6) and (2.7) respectively, both of which are beneficial from an active power transmission standpoint. At the extreme when frequency equals zero, the capacitive reactance becomes infinite, resembling an open circuit, whereas the inductive reactance becomes zero and resembles a short circuit. If the frequency is reduced to 1/3 of conventional AC then the voltage drop across the line decreases owing to a lower inductive reactance and an increased shunt capacitance. This increases the maximum transmission distance before an unacceptable voltage drop occurs.

$$X_L = 2\pi f L \tag{2.6}$$

$$X_C = \frac{1}{2\pi f C} \tag{2.7}$$

The difference between sending and receiving end voltage is given in (2.8) and the total voltage drop is given as a percentage in (2.9), where it can be seen that the voltage

Table 2.1: Parameters of 155kV, 1200mm^2 Cu submarine cable

Parameter	**50Hz**	**16.7Hz**
I_{max}	1012 A	1230 A
S_n	271.7 MVA	330.3 MVA
R	25 mΩ/km	16.6 mΩ/km
L	0.426 mH/km	0.426 mH/km
X	133.8 mΩ/km	44.6 mΩ/km
C	236 nF/km	236 nF/km

drop depends on the inductance and resistance of the cable.

$$V_r = V_s - iZ \tag{2.8}$$

$$\Delta V(\%) = \frac{|V_s| - |V_r|}{|V_r|} \times 100 \tag{2.9}$$

The effect of a reduced inductive reactance owing to a lower electrical frequency also impacts the amount of active power that can be transferred between two sources, as shown 2.10.

$$P = \frac{V_s V_r}{X_L} \sin(\delta) \tag{2.10}$$

Table 2.2: Parameters of 245kV, 1200mm^2 Cu submarine cable

Parameter	**50Hz**	**16.7Hz**
I_{max}	1262 A	1534 A
S_n	480.9 MVA	584.7 MVA
R	25 mΩ/km	16.6 mΩ/km
L	0.366 mH/km	0.366 mH/km
X	115 mΩ/km	38.3 mΩ/km
C	183 nF/km	183 nF/km

2.4.1.1 Resistance

For AC currents the skin effect and the proximity effect must be taken into account, both of which contribute to the resistance of a cable. The skin effect is the name given to the non-uniform distribution of current through a conductor which results in a greater concentration of current density near the surface. The skin effect causes electric current to flow mainly through the surface of the conductor thus reducing the effective

cross-sectional area and increasing resistance. This is due to opposing eddy currents induced by the changing magnetic field. The proximity effect arises when two or more AC conductors are arranged in close proximity to one-another such that the AC current in one conductor induces eddy currents in the other conductor (and vice versa) opposing the original currents and increasing the resistance. Both of these effects are dependent on frequency. [19]

For three core submarine cables commonly used in electrical power transmission, the AC resistance can be expressed by (2.12)

$$R = R_{DC}(1 + y_s + y_p) \tag{2.11}$$

$$\begin{aligned} \text{where} \quad y_s &= \frac{x_s^4}{192 + 0.8x_s^4} \\ y_p &= \frac{x_p^4}{192 + 0.8x_p^4}\left(\frac{d}{s}\right)^2\left[0.312\left(\frac{d}{s}\right)^2 + \frac{1.18}{\frac{x_p^4}{192+0.8x_p^4} + 0.27}\right] \\ \text{and} \quad x_s^2 &= \frac{8\pi f}{R_{DC}}10^{-7}k_s \\ x_p^2 &= \frac{8\pi f}{R_{DC}}10^{-7}k_p \end{aligned} \tag{2.12}$$

where R_{DC} is the DC resistance of the conductor, d is the diameter of the conductor, s is the distance between the conductor axis, k_s and k_p are constants that depend on the shape and material of the conductor. For a round, stranded copper conductor k_s and k_p are both equal to 1. The effect of frequency on the skin effect parameter y_s and the proximity effect parameter y_p is shown in figure 2.5, where the cable parameters are taken from [20].

The reduction in resistance when using a reduced frequency is evident from figure 2.5, where it can be seen that when moving from 50 to 16.7Hz, the skin effect and proximity effect reduce by approximately 96% and 88% respectively. This feature has been considered an advantage of LFAC systems over nominal AC frequency systems.

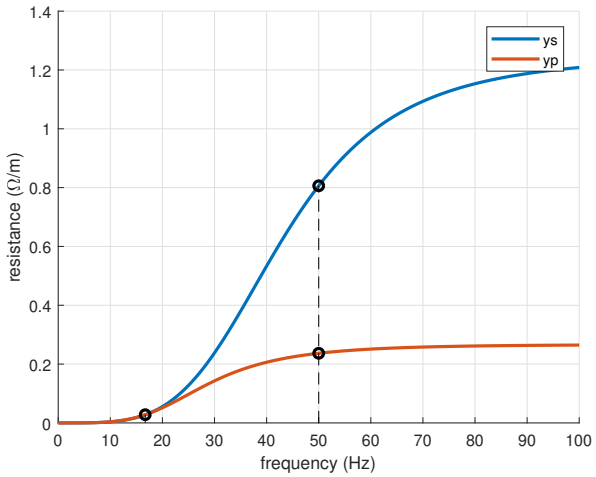

Figure 2.5: Skin and proximity effect of a 245kV 1000mm^2 conductor [19]

2.4.1.2 Inductance

Inductance is a property caused by the magnetic field generated by the flow of charge in a conductor, where the magnetic field induces a current in the opposite direction to the current flow that produced. Inductance is a frequency dependent term as shown by (2.14).

$$L = \frac{\mu}{2\pi} \ln\left(\frac{D_e}{GMR}\right) \tag{2.13}$$

$$\text{where} \quad D_e = 659\sqrt{\frac{\rho_e}{f}} \tag{2.14}$$

where μ and GMR are the permeability and geometric mean radius of the conductor respectively, ρ_e is the resistivity of the earth and f is the frequency. The relationship in (2.14) is plotted in figure 2.6a and shows that an increased frequency actually leads to a lower inductance. However, since $X_L = 2\pi f L$, the frequency term dominates over the inductance term and results in an increasing inductive reactance as frequency increases. This effect is shown in figure 2.6b.

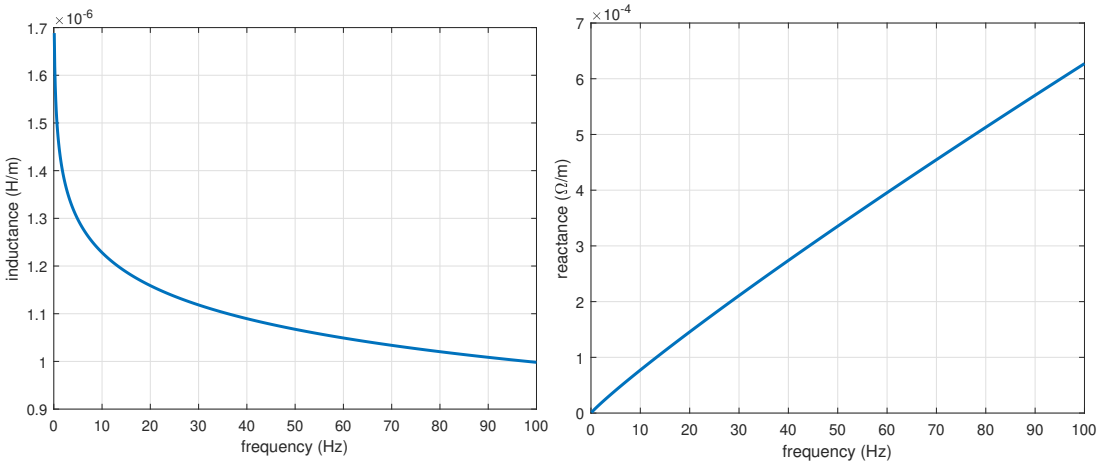

(a) Inductance L

(b) Inductive reactance $X_L = 2\pi fL$

Figure 2.6: Relationship between frequency, inductance and inductive reactance

2.4.1.3 Capacitance and Conductance

Unlike resistance and inductance, the capacitance and conductance of a cable are not influenced by the frequency. The capacitance of a conductor is given by:

$$C = \frac{2\pi\epsilon}{\ln\left(\frac{r_2}{r_1}\right)} \tag{2.15}$$

where r_1 and r_2 are the radii of the conductor and insulation respectively and ϵ is the permittivity of the insulation.

The conductance of a cable is defined as the leakage current between the conductor and the ground, which is non-zero in the absence of an infinite impedance insulator. This is similarly defined by:

$$G = \frac{2\pi\sigma}{\ln\left(\frac{r_2}{r_1}\right)} \tag{2.16}$$

where σ is the conductivity of the insulation. The absence of a frequency term in both of (2.15) and (2.16) is evident, however frequency does have an effect on capacitive reactance since $X_C = \frac{1}{2\pi fC}$.

2.4.1.4 Sheath, Armour and Dielectric Losses

The heat generated by losses within any sheath or armour also need to be evaluated because if they are significant they become a factor in the sizing of cables. Sheath losses have a circulating current component and an eddy current component as given by the expression:

$$\lambda_1 = \lambda_{1c} + \lambda_{1e} \tag{2.17}$$

λ_{1c} losses only occur in single core cables. In a 3-core cable the sheath surrounds all cores so the possibility of circulating current does not exist and the λ_{1c} can be ignored. λ_{1e} are small eddy currents setup in the sheath due to changing magnetic fields. Eddy current losses in screen and sheaths of three phase pipe-type cables can be expressed as:

$$\lambda_{1e} = \frac{R_s}{R_{DC}} \frac{1.5}{(1 + (\frac{R_s}{X_s})^2)} \tag{2.18}$$

$$\text{where} \quad X_s = 4\pi f \ln\left(\frac{2s}{d_s}\right) 10e^{-7} \tag{2.19}$$

where R_s is the resistance of the sheath, R_{DC} is the DC resistance of the conductor, s is the separation between the conductors and d_s is the diameter of the sheath.

The armour loss coefficient for a three core cable with steel wire armour are given by the expression:

$$\lambda_2 = 1.23 \frac{R_a}{R_{DC}} \left(\frac{2c}{d_a}\right)^2 \frac{1}{\left(\frac{2.77 R_a 10e^6}{2\pi f}\right)^2 + 1} \tag{2.20}$$

where R_a is the DC resistance of the armour and d_a is the diameter of the armour. The effect of increasing frequency on sheath and armour losses for an XLPE cable is shown in figure 2.7.

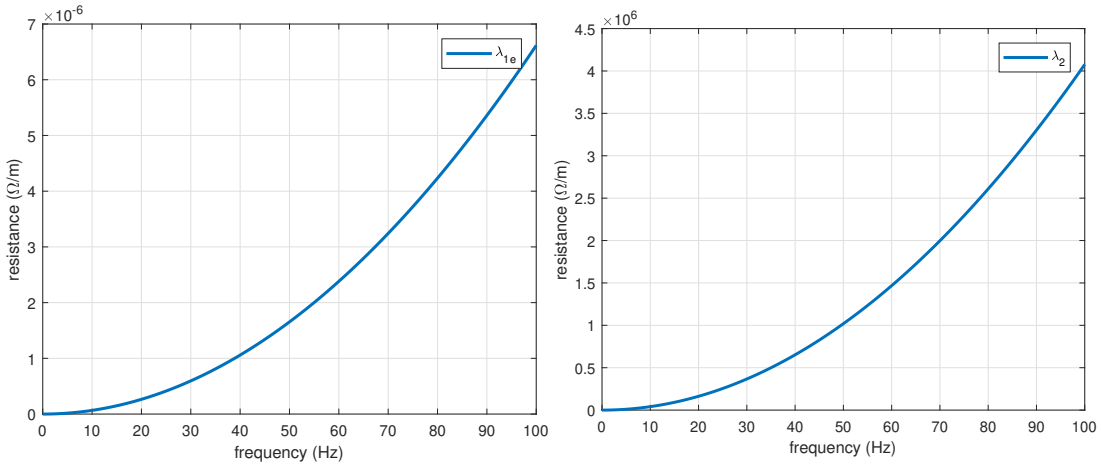

(a) Sheath losses

(b) Armour losses

Figure 2.7: Cable loss characteristics

The dielectric loss is associated with the insulation of the cable and is expressed by:

$$W_d = 2\pi f C V^2 \tan\delta \tag{2.21}$$

where $\tan\delta$ is the insulation loss factor.

A study in [3] gives the losses of two Aluminium cables of different voltage levels as a function of frequency, which shows the decreasing conductance, sheath armour and dielectric losses with decreasing frequency. The results are shown in figure 2.8.

2.4.2 Transformers

The effect of lowering the frequency from its nominal value of 50 Hz (or 60 Hz) on the size of the transformers, reactors and wind turbine generators is also of critical importance to the feasibility of LFAC. The transformer must be redesigned for the low frequency by either increasing the core area or increasing the number of turns as per the induced voltage equation of a transformer in (2.22):

$$E = 4.44 f B N A_c \tag{2.22}$$

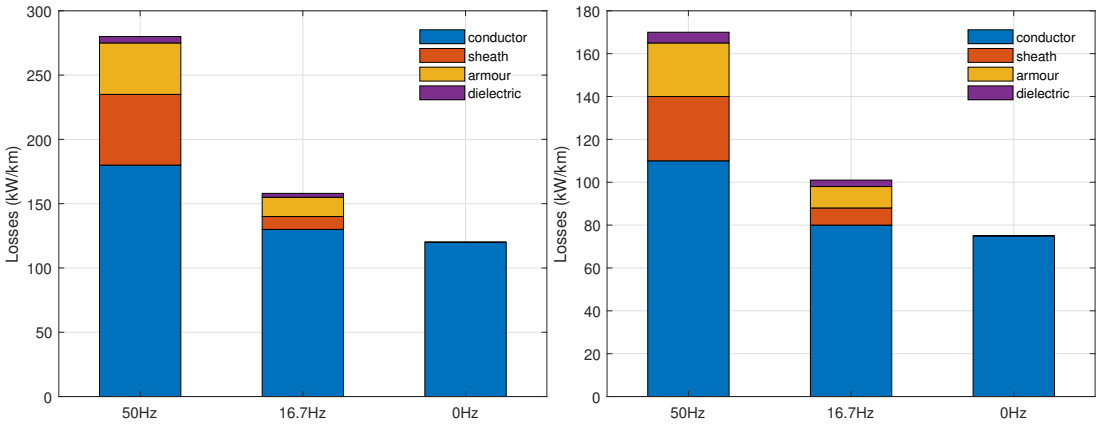

(a) 230kV 1900mm^2 (b) 345kV 1400mm^2

Figure 2.8: Cable loss components as a function of frequency [3]

where B = magnetic flux density, N = number of turns, A_c = core area. The hysteresis component of core losses for a 16.7Hz transformer reduce from those in a 50Hz system according to the expression:

$$P_{loss} = v_t k f^{\alpha} B_{pk}^{\beta} \tag{2.23}$$

where v_t is the transformer volume, k is a constant, B_{pk}^{β} is the peak flux density and α and β are material constants. Transformer core losses due to hysteresis for a 16.7Hz system are quoted as being 1/6th of the losses for a 50Hz transformer [21].

One of the greatest advantages of LFAC over HVDC for offshore wind is the reduction in size of the offshore platform. For an HVDC system this must included the B2B-VSC converter as well as filters to eliminate switching harmonics. For LFAC this platform only contains the AC transformer and switchgear. Rearranging equation (2.22) for core area shows the inverse proportionality of area with frequency. Similarly the reduced frequency will have an effect on the size of the switchgear which must also be larger.

Although it is possible to use standard 50Hz transformers if the V/f ratio is kept constant, a study in [22] investigates the effect of fractional frequencies on the various

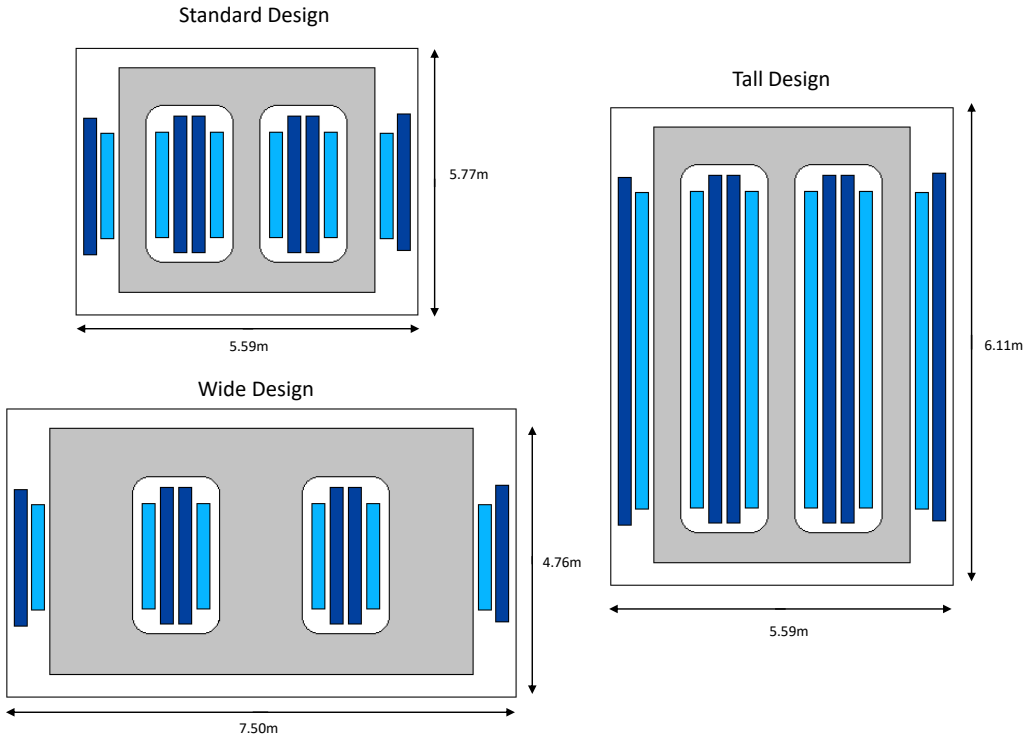

Figure 2.9: Low frequency transformer designs (not to scale) [23]. Wide design increases core thickness while leaving windings unchanged. Tall design keeps core diameter constant and increases number of windings

components of an offshore wind farm and concludes that a new transformer should be designed for low frequency applications. Two new designs for a low frequency transformer were presented in [23], with the wide design and tall design shown in figure 2.9 with parameters in table 2.3.

The study concludes that keeping the core diameter constant and increasing the number of turns gives a lighter design because of the fact that the core is more dense than the windings. It is therefore possible to limit the increase in size of the transformer to an additional 77% over the standard design. The optimal design may lie somewhere in-between the tall and the wide design, but it is clear that the low frequency will incur a significant increasing in weight and therefore cost of the transformers and offshore platform.

Table 2.3: Transformer design parameters [23]

freq. (Hz)	weight (t)	W_{core}	W_{coil}	W_{oil}	[l, w, h] (m)
50	143.42	77.87	34.65	30.89	[5.19, 1.75, 3.48]
16.7 (wide)	413.84	321.41	36.10	56.33	[7.10, 2.39, 4.76]
16.7 (tall)	253.93	130.40	73.80	49.73	[5.19, 1.75, 6.11]

2.4.3 Switchgear

AC circuit breakers operate on the zero crossing of the current waveform which naturally extinguishes any arc twice per cycle. The zero crossing points occur less often for a reduced system frequency so a fault will take longer to clear. Gas insulated switchgear (GIS) with sulphur hexafluoride (SF6) circuit breakers for 16.7 Hz AC networks are already in commercial operation in European railway systems [24].

When compared with the operational conditions in single phase railway networks, the short circuit level within offshore grids are much lower, making the interruptions in a 16.7 Hz offshore grid easier. The downside is that the lower short circuit levels make it more difficult to detect faults. Additionally, the voltage ratings of switchgear installed in the railway industry are typically small when compared to a proposed offshore grid and they would therefore need to be scaled up to higher voltage. This shows that further research into the components of LFAC is necessary for this to become a viable method of power transmission [19].

2.4.4 Reactive Power Compensation

The power transmission capabilities of an AC subsea cable are impacted heavily by the charging currents that arise due to the high cable capacitance, which is about 15 to 25 times larger than for an overhead line due to the much closer proximity of the conductors. The increase of reactive power associated with the charging current decreases the active power that can be transmitted by the cable.

The expression of charging current is shown in (2.3). For long cables such as those required for offshore wind farms, the charging current must be compensated for by

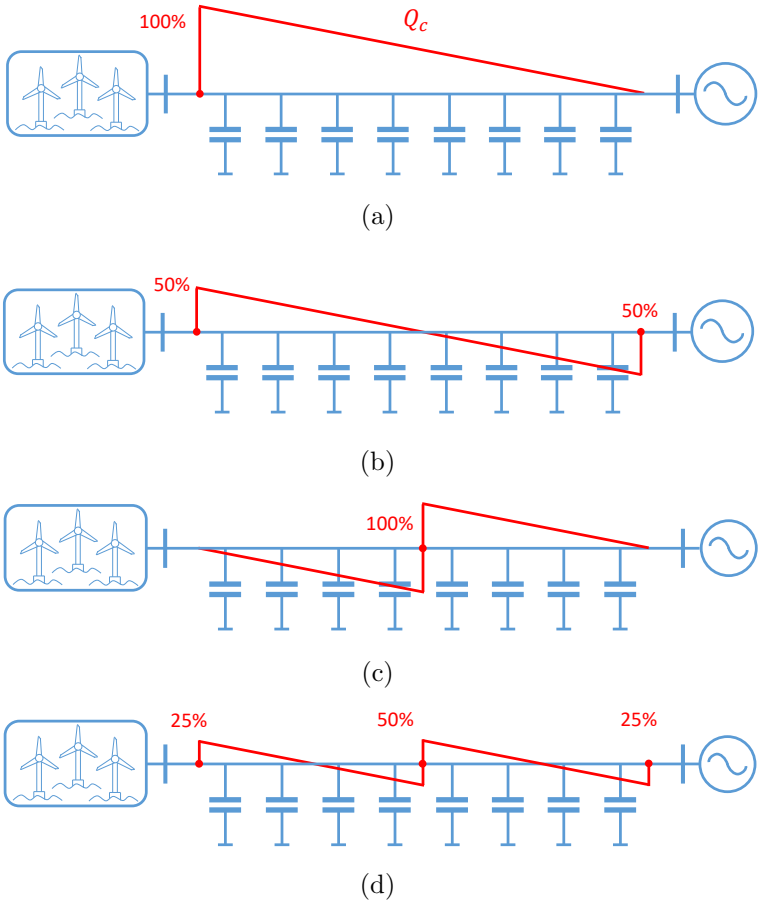

Figure 2.10: Configurations for shunt reactor placement. a) 100% compensation with a single reactor at wind farm end of cable; b) 50% compensation with two reactors, one at each end c) 100% mid-way offshore platform; d) 25% at each end and 50% mid-way offshore platform [25]

connecting shunt reactors which can be positioned in several configurations. The most typical configuration is to install two shunt reactors each rated at 50% of the total required compensation at either end of the cable, however other layouts exist such as installing a single reactor rated at 100% at only one end; or by connected a shunt reactor mid-way along the cable on an additional offshore platform as shown in figure 2.10.

The size of the reactors is calculated using the expression in (2.4). The maximum distance between reactors is a trade-off between cable utilisation and the additional

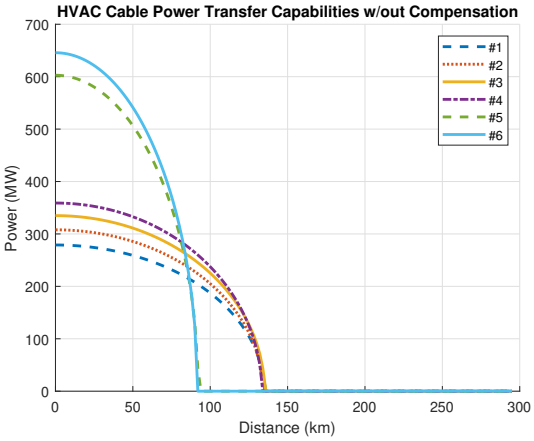

Figure 2.11: Power transfer capability without compensation

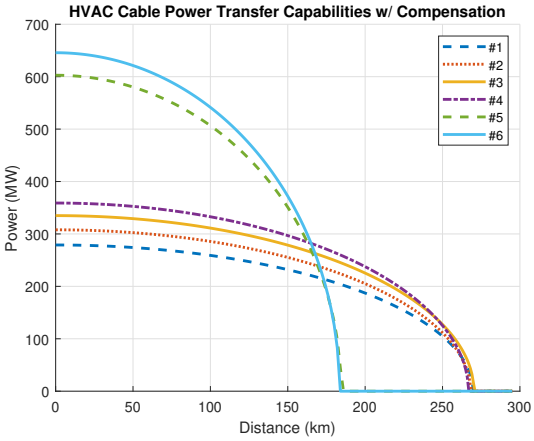

Figure 2.12: Power transfer capability with compensation (scenario from fig.2.10a) showing increased range

cost of reactors which can be considerable if an additional offshore platform is required.

HVAC cables have an effective range beyond which it is either not economical or not technically possible to transfer active power due to the presence of reactive power. Longer cables generate more reactive power and have a reduced maximum power carrying capability. Beyond a certain length for a particular cable, the economic limit is reached and it becomes necessary to either upgrade to a larger diameter cable; increase the number of sets; or increase reactive power compensation. The maximum power carrying capabilities of some common cables are shown with and without compensation in figure 2.12 where it can be seen that the limit is reached at much shorter distances without compensation [15].

If the cable is operated at at a frequency of 16.7 Hz then the charging current and amount of reactive compensation is reduced, however the need for compensation still exists. The increased range of an AC cable (no.6 from previous figure) operated at 16.7Hz is shown with and without compensation in figure 2.13 with parameters taken from table C.7.

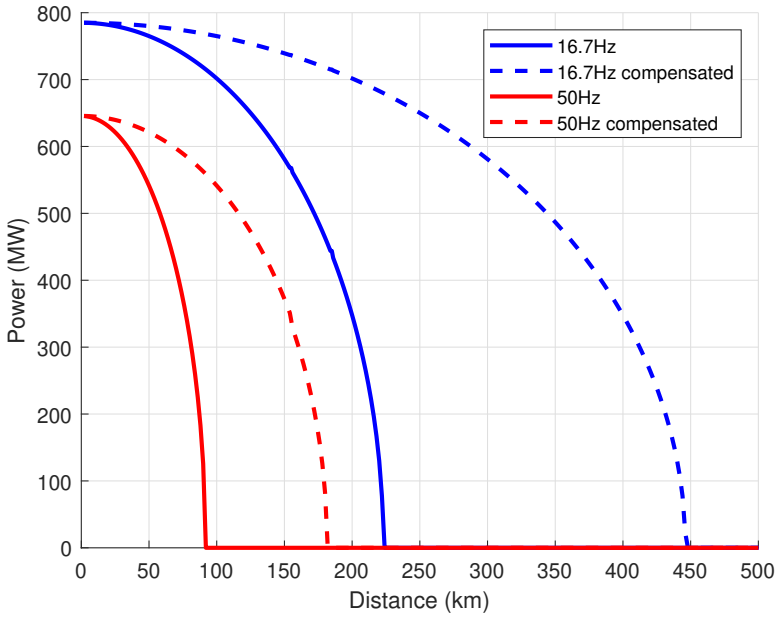

Figure 2.13: Power transfer capacity of an AC cable operated at 50Hz and 16.7Hz with and without compensation

2.4.5 Wind Turbine Design

Wind turbines are classified based on the type of power control, i.e. stall or pitch regulated, and the type of speed control, i.e. fixed speed or variable speed. Fixed speed turbines fall into the type-1 category; limited variable speed turbines are classed as type-2; variable speed with a partially rated converter are type-3; and variable speed with a fully rated converter are type-4. There also exists a less common type-5 category in which a mechanical torque converter sits between the low-speed shaft of the rotor and the high-speed shaft of the generator to control the generator speed [26]. Modern wind turbines all operate with variable speed generators due to advantages in increased power capture and load reduction and are usually either type-3 or type-4, therefore the type-1, -2, and -5 configurations are not discussed here.

Assuming that the wind turbine is redesigned to generate power directly at the reduced frequency to negate the requirement of an additional offshore collector network, LFAC transmission affects the design of the turbine in two significant ways. The first is that the transformer in the nacelle requires an increase in core area (or an increase in

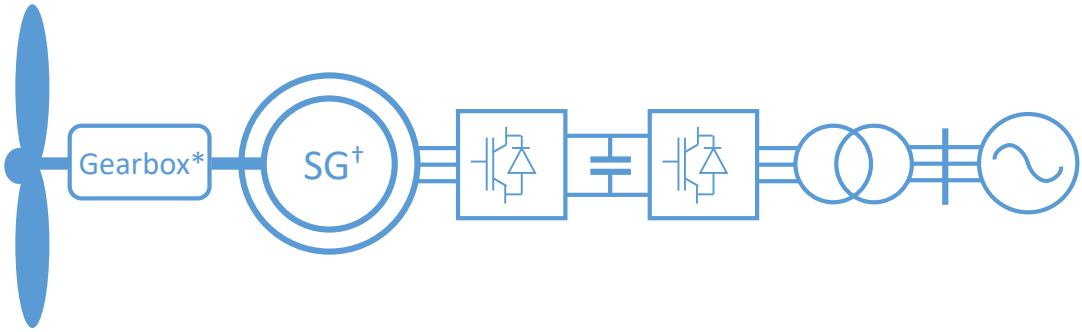

Figure 2.14: Type-4 featuring a synchronous generator and a fully-rated converter, *can be gearless. †can be permanent magnet synchronous generator

the number of turns) to maintain the appropriate magnetic flux. The second depending on the turbine type is that the generator may need to be scaled up in size according to the same principles governing transformers. This section covers the modifications that would need to applied to a wind turbine to enable the use of LFAC transmission technology and the PFEC.

2.4.5.1 Type-4

A typical type-4 wind turbine is shown in figure 2.14 and consists of a fully rated converter (FRC) and a synchronous generator (SG), however this can theoretically be any generator type since the electrical system is completely decoupled from the grid. The presence of the FRC offers a great deal of flexibility in design and operation of the generator which is allowed to rotate at the aerodynamic speed since the generator output is converted by the FRC. It is therefore possible to remove the gearbox altogether to produce a direct drive (DD) machine. Direct drive permanent magnet synchronous generator (PMSG) based turbines are currently the preferred design for offshore wind [27].

Type-4 PMSG turbines have been proposed in the literature for use in low frequency offshore wind farms [28], since the only change from their standard applications would be to adapt the converter to the 16.7Hz frequency [15], [29]. The transformers would

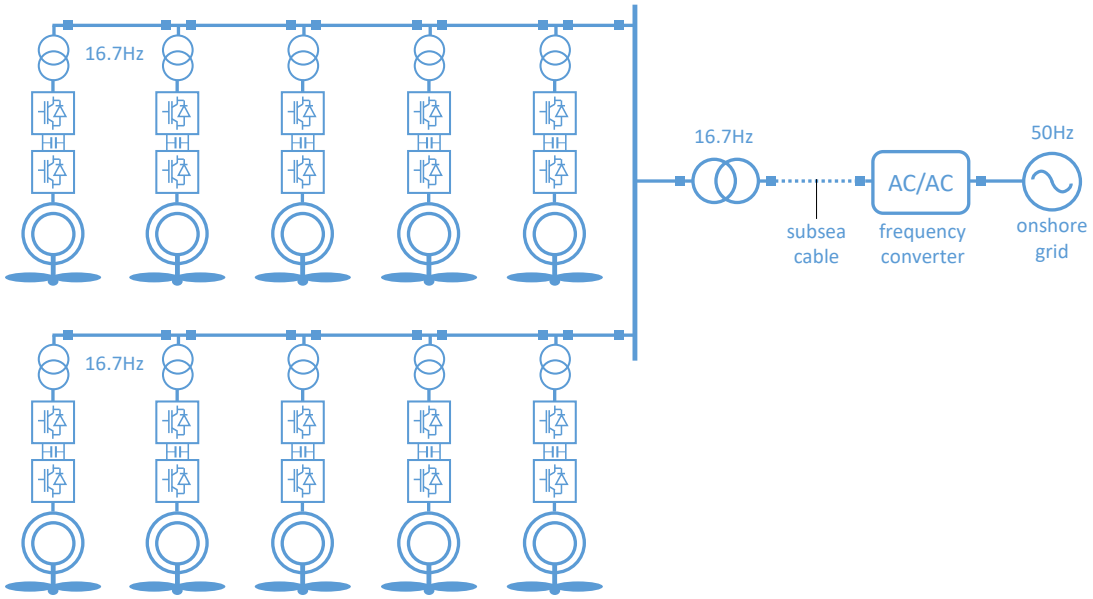

Figure 2.15: Offshore collector network of low-frequency type-4 turbines connected to onshore AC/AC converter

still need to be redesigned in the same way as for the type-3 turbines but the ease of reprogramming the FRC for LFAC transmission has lead to this turbine topology being the favourite for any future LFAC connections. A representative offshore wind farm is displayed in figure 2.15 showing a collector network consisting of PMSG type-4 turbines adapted for the low frequency.

2.5 Frequency Converter Technologies

An LFAC transmission system requires a method of converting the low frequency up to the 50Hz (or 60Hz) of the utility grid. A variety of different converter types have been specified in the literature, including power-electronic based options such as the cycloconverter, matrix converter and back-to-back voltage sourced converter (B2B-VSC), but there also exist some analogue solutions which exploit the principles of electromagnetic induction to perform the frequency conversion. These include the magnetic frequency changer which utilises an arrangement of three-phase transformers to step-up the frequency, and also several applications of induction machines which operate via a difference in pole ratio to achieve the desired effect. The components required to make up the LFAC transmission system require careful consideration and each of these options is covered in this section.

2.5.1 Power-Electronic Frequency Converters

2.5.1.1 Cycloconverter

A cycloconverter consists of several phase-controlled, line-commutated thyristors connected to an AC supply. The individual circuits are controlled so that a low frequency output voltage waveform is fabricated from segments of the polyphase input voltages [30].

Since the cycloconverter output is derived from the AC power system, the maximum output frequency is limited to a fraction (typically one-third) of the power system frequency to maintain an acceptable output voltage waveform with low harmonic content. The efficiency of the cycloconverter is high due to the use of static components such as thyristors.

The problem with using a cycloconverter is the presence of significant low-order harmonics which require large, costly filters to remove. Depending on the ratio of

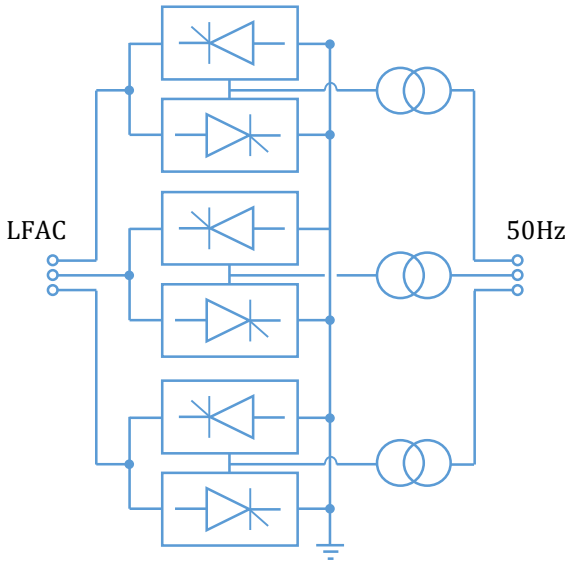

Figure 2.16: Single-line diagram of a 36-pulse cycloconverter

output to input frequency there may also be inter-harmonics and sub-harmonics. This can be explained with the equation:

$$f_H = |6f_i - (2n+1)f_o| \tag{2.24}$$

where f_H is the frequency of the $(2n+1)^{th}$ harmonic, f_i is the input frequency and f_o is the output frequency.

Figure 2.17 shows (2.24) plotted for a 16.7Hz and a 20Hz system, where the harmonics have been circled for an output frequency of 50Hz. In figure 2.17a, the harmonics of the 16.7Hz system can be seen to be multiples of the output frequency, such that there are no sub- or inter- harmonics. However, the presence of these harmonics at low orders produce a poor power quality and introduce the requirement of additional AC filters. In figure 2.17b, an input frequency of 20Hz gives rise to harmonics that are non-integer multiples of the fundamental. Additionally the 1st harmonic appears at a frequency below the fundamental. Sub- and inter- harmonics are therefore present, highlighting that different frequency conversion ratios introduce different filtering requirements.

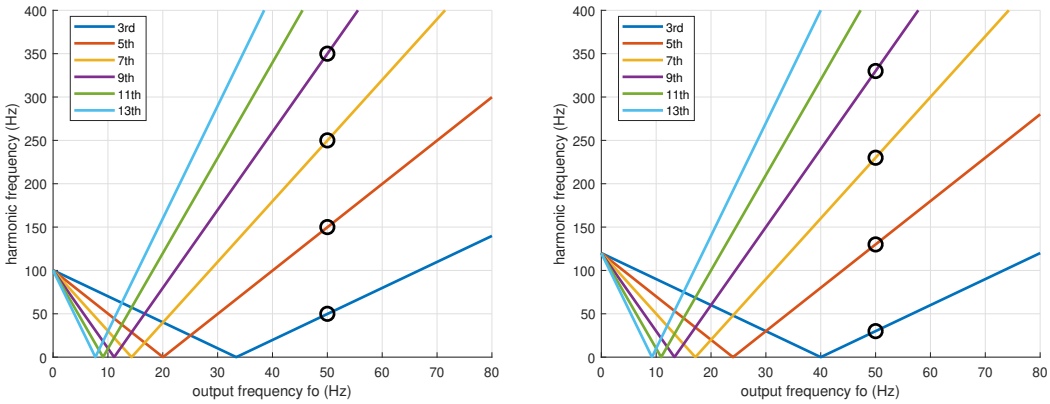

(a) $f_i = 16.7$Hz (b) $f_i = 20$Hz

Figure 2.17: Harmonic frequency plotted against output frequency for 16.7Hz and 20Hz cycloconverter connections

A converter-connected wind turbine system can be classified as a variable harmonic source because of the random nature of the wind field and the varying operating point of the converters [31]. The presence of these harmonics produces a large amount of harmonic distortion leading to a poor power quality which results in the requirement for auxiliary equipment such as AC filters, capacitor banks and static VAR compensators [8].

Studies in [32] and [13] assess the harmonic content of a cycloconverter-based LFAC offshore wind system. In this example, the wind farm output is rectified to DC and is then converted to the reduced frequency AC before transmitting the power to the onshore cycloconverter. The voltage and current on the low frequency side are found to contain only odd harmonics according to (2.24). In the absence of any AC filters, the total harmonics of the current flowing into the 50Hz system are listed in table 2.4, which shows a fairly poor total harmonic distortion of 0.2243, or $\approx 22\%$.

2.5.1.2 Matrix Converters

The matrix converter has been suggested as an alternative to the cycloconverter to address the problems of high harmonic content in the output waveforms. The matrix

Table 2.4: Typical harmonic distortions of cycloconverter-based LFAC

Harmonic #	3	5	7	9	11	13	15
Amplitude	0.129	0.127	0.085	0.057	0.029	0.024	0.041
Harmonic #	17	19	21	23	25	27	29
Amplitude	0.023	0.012	0.035	0.016	0.033	0	0.027

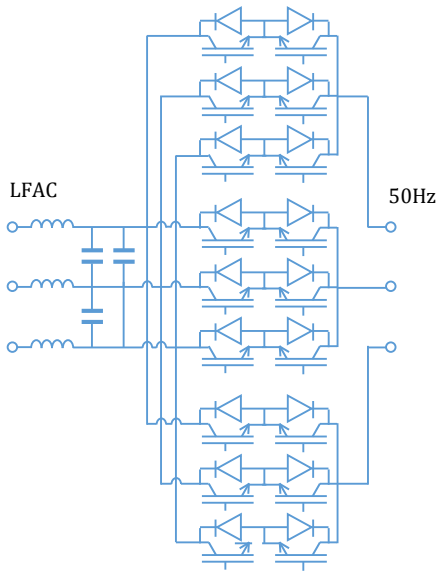

Figure 2.18: Single-line diagram of a matrix converter

converter is a forced-commutated converter which utilises controllable bidirectional switches such as IGBTs to create a variable output voltage of a different frequency to the input. Upgrading to a forced-commutated converter from a line-commutated improves the harmonic content and also removes the presence of sub- and inter-harmonics. Figure 2.18 shows a schematic of the matrix converter.

There is no DC-link circuit present in the matrix converter which brings advantages in the form of a size and weight reduction due to the reduced footprint, but also brings disadvantages caused by the lack of decoupling between input and output. Any harmonics present on the input voltage or current will be reflected in the output waveforms. Filters must be used to reduce the switching frequency harmonics present in the input current. For wind energy applications, filters will be needed on both the input and the output sides of the converter [33].

Similarly, any overvoltages in the input circuit will be transferred to the output, and vice-versa. For these reason there are additional protection requirements that must be installed to protect the switching devices. The possibility of faults in the grid necessitate an additional clamp circuit to protect the matrix converter. Fault ride-through capability is also a direct requirement for any modern generating unit, but since the matrix converters do not have a DC-link capacitor for short-term energy storage, additional equipment must be installed [34].

The matrix converter requires a bidirectional switch capable of blocking voltage and conducting current in both directions. Up to this day there are no such devices currently available, so discrete devices need to be used to construct suitable switch cells. Despite the fact that matrix converter is a technology that has been studied for decades, its complexity and requirement of bidirectional switches have contributed to reduce its interest by conventional industry.

2.5.1.3 Voltage Sourced Converters

Perhaps the most common converter topology found in the global power system is the VSC which has been utilised to a large extent in the field of HVDC transmission. Advantages such as fully controllable active and reactive power (even when P = 0 due to the energy stored in the DC-link) and the full control over voltage that this implies have given B2B-VSC the edge over rival technology.

As shown in figure 2.19, The B2B-VSC system consists of two VSCs connected together via the DC link. One converter maintains the DC link voltage while the other controls the power flow via specific switching of the IGBTs. A detailed review of VSC based transmission is given in [9], and the inner workings of the B2B-VSC, including its control, will be covered in a chapter 3 due to this device's application to the PFEC.

The B2B-VSC has been singled out in literature as being the most suitable choice

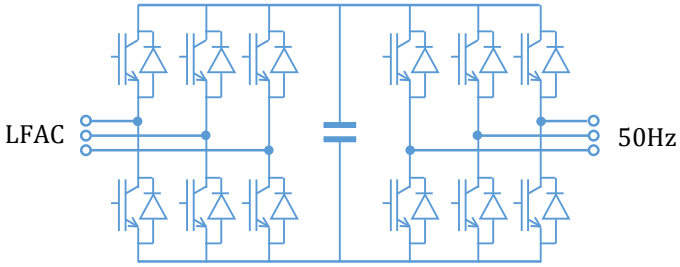

Figure 2.19: Single-line diagram of a B2B-VSC

Table 2.5: Comparison of frequency converter options [36]

	Cycloconverter	**Matrix Converter**	**B2B-VSC**
Conversions	AC-AC	AC-AC	AC-DC-AC
Decoupled	No	No	Yes
Power Control	P only	Q provided P > 0	P and Q
AC Filters	Yes (large)	Yes	Yes
Black Start	No	No	Yes
FRT	No	No	Yes
Power Factor	0.78 lagging	Controllable	Controllable
Voltage Control	No	Limited	Yes

for an LFAC system [3], however there is an issue surrounding the harmonic content because of a large third harmonic due to the cable's natural resonant frequency. Unlike in the HVDC applications of the B2B-VSC where the DC link acts as the submarine cable to shore, in LFAC applications there exist resonances between the cable and the 50Hz grid [35] which require costly filters to remove.

A comparison of the three power-electronic based frequency converter designs is shown in table 2.5.

2.5.2 Analogue Frequency Converters

The concepts and designs found in this section are a prerequisite to understanding the technology and fundamentals of the PFEC. In section 2.5.1 the frequency conversion was handled entirely by power-electronic converters which maintain the low frequency interconnection by synchronising their firing angles with the conditions imposed by the

utility grid. Power-electronic converters must therefore closely follow the grid conditions set by large synchronous machines or become desynchronised.

The following section provides alternative designs for frequency converters which do not fully rely on power-electronics. They introduce the idea of using the principles of electromagnetic induction via transformers and electrical machines rather than switching devices for the interface between two asynchronous networks which will ultimately lead to the PFEC.

2.5.2.1 Magnetic Frequency Changer

It is possible to build a frequency converter using a set of three phase transformers which are purposefully driven into saturation. When a star-connected three phase transformer becomes saturated, the flux becomes very distorted and contains the fundamental and all odd harmonics of the supply. If the secondary windings are connected in an open-delta configuration as in figure 2.20 then only the triple harmonics appear across the output terminals [37]. It is therefore possible to create a magnetic frequency tripler using three phase transformers to produce a frequency ratio from input to output of 1:3 (or 3:1 if the connections are reversed). The first magnetic frequency changers were designed to supply 150/180Hz from a standard 50/60Hz source to induction heating and melting loads. Large frequency changers have been designed to deliver output currents as high as 5000A [38].

A magnetic frequency changer, sometimes referred to as a frequency tripler, is shown in figure 2.21. Each transformer unit is connected in star-open delta formation with a highly saturated core. When there is a large enough voltage angle difference, the direction of active power flow reverses, meaning that bidirectional power flow is possible with this design. Analysis into the efficiency of such a device is given in [39], which concludes that efficiencies of up to 96% are possible with proper core area optimisation.

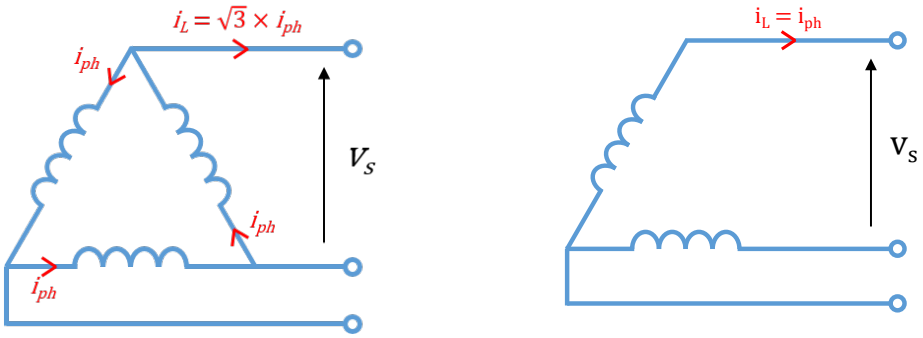

(a) Delta configuration

(b) Open delta configuration

Figure 2.20: Delta and open-delta connection schematics

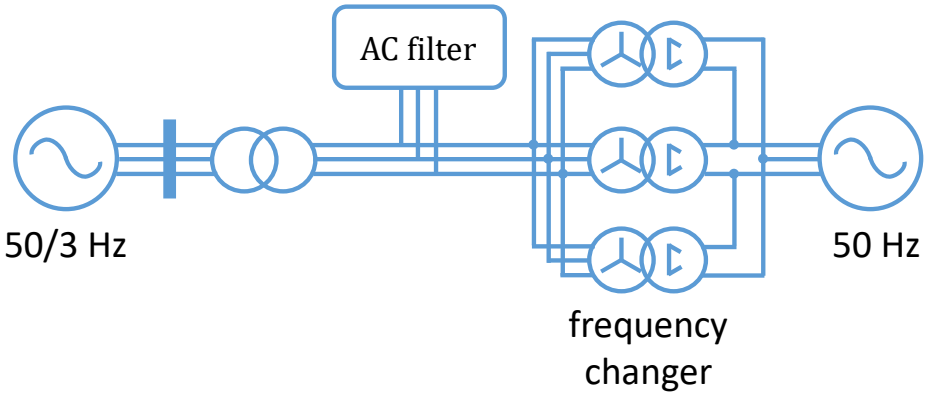

Figure 2.21: Single-line diagram of a magnetic frequency changer

The main features of the magnetic frequency changer are:

1. An increase in transmission capacity when compared to a 50Hz line...
2. ... or an increased transmission distance for the same capacity
3. Efficiencies of 95% and above
4. Bidirectional power flow allowing the interconnection of two different frequency systems
5. Excessive reactive power requirements
6. Need for bulky inductors

2.5.3 Motor-Generators

The concept of using machines to perform a frequency conversion via the principles of induction is an idea that dates back to the late nineteenth century. The first instances of induction machines can be attributed to Galileo Ferraris (1885) and Nikola Tesla (1886), with a subsequent patent filed in 1888 [40]. The 'Dynamo-Electric Machine' is now referred to as a motor-generator set (MG-set) and it can be arranged several configurations to allow the conversion of power from one form to another, i.e. AC to DC (and vice versa); fixed voltage to variable voltage [41]; AC at one frequency to AC at another frequency etc. A schematic demonstrating the latter of these examples is given in figure 2.22. By varying the ratio of poles between the two machines it is possible to electrically connect two asynchronous networks.

The relationship between the speed of rotation of the electrical wave and the mechanical shaft is defined by (2.25), where ω_e, ω_m are the electrical and mechanical rotational speeds respectively, p is the number of pole pairs and the subscripts 1,2 refer to each machine according to figure 2.22.

$$\omega_{m1} = \frac{\omega_{e1}}{p_1} \quad \text{and} \quad \omega_{m2} = \frac{\omega_{e2}}{p_2} \tag{2.25}$$

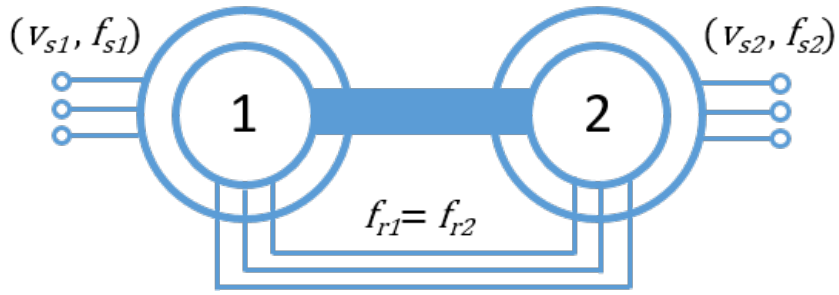

Figure 2.22: MG set allowing AC at one frequency to be connected to AC at another frequency

Since the two machines share a common shaft, $\omega_{m1} = \omega_{m2}$ and the equation can be simplified to give (2.26)

$$\begin{aligned} \frac{\omega_{e1}}{p_1} &= \frac{\omega_{e2}}{p_2} \\ \Rightarrow \quad \omega_{e1} &= \frac{p_1}{p_2}\omega_{e2} \\ \text{therefore} \quad f_1 &= \frac{p_1}{p_2} f_2 \end{aligned} \tag{2.26}$$

To connect a $f_1 = 50$Hz grid to a $f_2 = 25$Hz grid for example, one would need a pole ratio $p_1/p_2 = 2$. Similarly for a 50:16.7 Hz interconnection, the pole ratio would need to be 3.

Some examples of where MG-sets have been deployed in industry are in the railway networks across several European countries. Germany, Switzerland, Austria, Norway and Sweden all deploy LFAC to some degree in their 15kV AC railway electrification systems. Some of these systems have a dedicated fractional frequency supply (i.e. hydro power stations which can provide power directly at 16.7Hz), but much of the rail network of Germany typically relies on a conversion using rotary converters. In Norway nearly all railway substations use motor-generators which convert three phase AC from public grid into single phase AC [42].

2.5.3.1 Brushless DFIG MG-set configuration

While many applications of MG sets have gradually been phased out by semiconductor based devices, there are still some examples to be found. As well as the MG-sets used by the rail industry in some European countries, another example is the brushless doubly-fed induction generator (BDFIG). The slip-rings found within a DFIG are a major contributor to maintenance costs because the graphite brushes get gradually worn away by the motion of the electrical contacts within the commutator. The powdered, highly conductive graphite has a tendency to settle on the insulation surrounding high voltage cables which can then undergo partial discharge, ultimately leading to a breakdown of the insulation [43]. The high voltages within the commutator can also cause sparking between the electrical contacts and the slip ring rendering them hazardous in certain environments. An induction machine of this design would not be suitable in certain applications, for example in the petrochemicals industry. The BDFIG poses a solution to these problems.

The design of a BDFIG is shown in figure 2.23. A DFIG is mechanically coupled to a rotary transformer (RT) such that they share a common shaft (grey). The stator circuit of the DFIG is shown in blue; the stator of the RT is shown in green and the red circuit represents the shared rotor connection. This arrangement has the effect of decoupling the stator from the rotor for both the DFIG and the RT respectively, such that the two stator connections are electrically isolated from each other. There is no requirement for brushgear since there is no direct electrical connection and power can be transferred from blue-to-red-to-green via the principles of induction.

The rotor windings of the DFIG and the rotor windings of the RT are electrically connected and hence have the same frequency. This is determined from the resultant of the frequency of the DFIG stator and the mechanical frequency of the rotor, which must be corrected for the number of poles in the machine. This relationship is demonstrated in (2.27).

$$f_r = f_{s1} - p_1 f_m \tag{2.27}$$

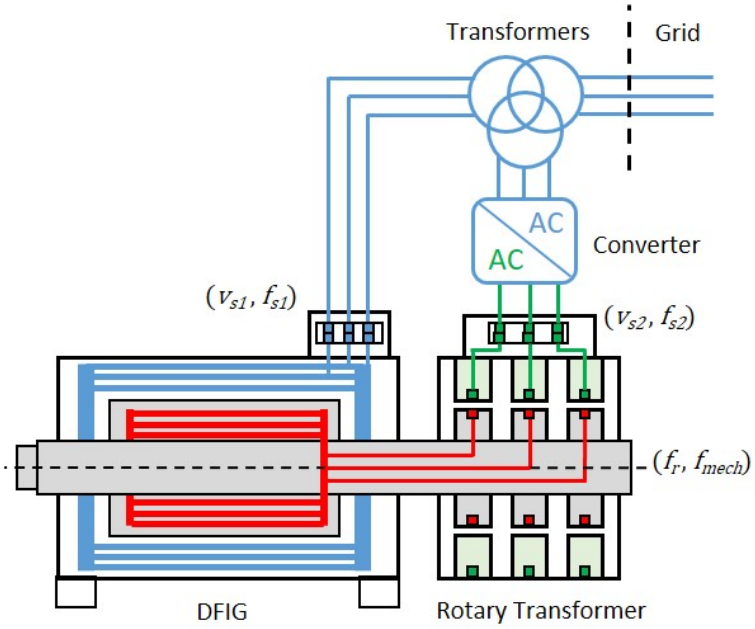

Figure 2.23: Layout of a BDFIG

where f_{s1} is frequency of the DFIG stator, f_r is the electrical frequency of the rotor, p_1 is the number of pole pairs and f_m is the mechanical frequency of the rotor. This can be rearranged to give the mechanical frequency of the machine as evidenced in (2.28). It is therefore possible to control the speed of the shaft by changing the rotor frequency f_r with a converter connected to the RT as in figure 2.23.

$$f_m = \frac{f_{s1} - f_r}{p} \tag{2.28}$$

An important consideration for a BDFIG particularly in wind turbine applications is the size implication. The relationship between transformer area and frequency is given in (2.29) which shows that the area of a transformer is inversely proportional to the operating frequency. The rotor currents of the BDFIG appear at slip frequency which is typically around ±30% of the stator, hence the rotary transformer will need to have a larger core area to establish the magnetic flux.

$$A_{core} = \frac{E}{4.44 f N B_{sat}} \tag{2.29}$$

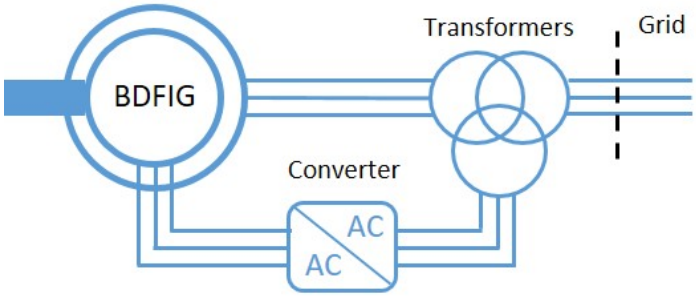

(a) DFIG grid-tied configuration

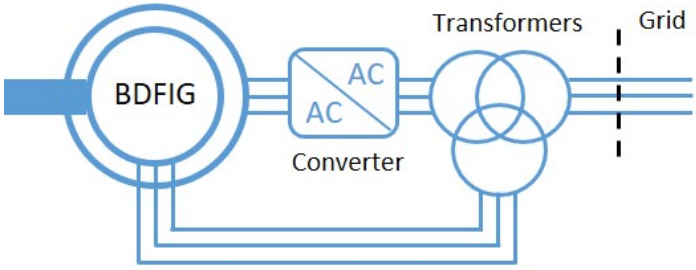

(b) RT grid-tied configuration

Figure 2.24: Brushless-DFIG converter configurations

A solution to this is to increase the operating frequency of the RT by having a grid-tied RT instead of a grid-tied DFIG, such that the stator of the BDFIG is then connected through a converter [44]. This will have a negative cost implication on the converter because of the increased rating but it may be more economical to have a large converter rather than a large transformer depending on the power rating of the machine. The two configurations are shown in figures 2.24a and 2.24b.

Another drawback is the presence of the airgap on the RT side. An airgap has a much higher reluctance than an iron core and will experience more flux leakage. Also as the airgap increases the magnetising inductance decreases resulting in a greater magnetising current and greater losses [45]. This relationship is shown in figure 2.25. Like other devices for contactless energy transmission, the rotary transformer has a high leakage-to-magnetising reactance ratio.

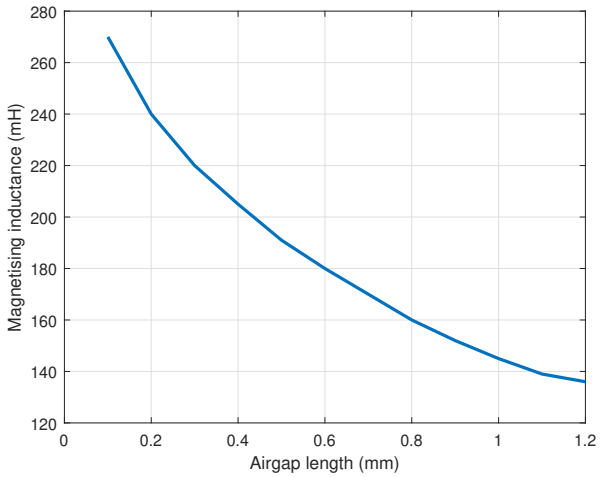

Figure 2.25: Relationship between magnetising inductance and airgap length [45]

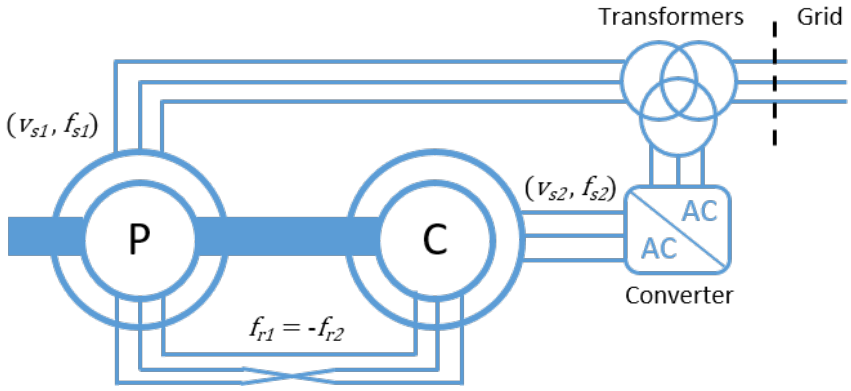

Figure 2.26: Layout of a BC-DFIG

2.5.3.2 Brushless Cascade DFIG

Another method to achieve brushless operation is to use two induction machines in an arrangement termed the brushless cascade doubly-fed induction machine (BC-DFIG) [46] [47] [48]. One induction machine is termed the power machine and is connected directly to the grid, the other is called the control machine and is decoupled from the grid through a back-to-back converter. These are labelled P and C respectively in figure 2.26. The rotor circuits are directly connected and since they share a common shaft the requirement of slip rings and brushgear is avoided.

A downside of the BC-DFIG is that it absorbs a lot of reactive power and it is dif-

ficult to achieve the same level of power flow control because of the strongly non-linear behaviour. However, the advantages related to the absence of slip rings and brushes can outweigh these factors, particularly in remote locations such as wind farms.

When the shaft of the machine is driven by a prime mover, the mechanical power is converter to electrical power and is delivered to the grid through both stators. The main power machine handles the greater fraction of this power, while the control machine's power handling capacity is determined by the frequency ratio. It is therefore possible to use a partially rated converter for the control machine in much the same way as in a standard DFIG arrangement [49][50].

It is a necessary requirement for the two machines to have different pole numbers. This can be seen in the following derivation [51]. The airgap fields set up by the two stator windings are expressed as

$$b_{g1}(\theta, t) = \hat{B}_{g1} \cos(\omega_1 t - p_1 \theta + \alpha_1) \tag{2.30}$$

$$b_{g2}(\theta, t) = \hat{B}_{g2} \cos(\omega_2 t - p_2 \theta + \alpha_2) \tag{2.31}$$

where $\hat{B}_g$ is the magnetic flux density, p_1, p_2 are the pole pairs of the two machines, ω_1, ω_2 are the excitation frequencies, α_1, α_2 are the phase angles. Since the rotor rotates at speed ω_r, these fields can be expressed in the rotor frame as

$$b_1(\theta', t) = \hat{B}_1 \cos((\omega_1 - p_1\omega_r)t - p_1\theta' + \alpha_1) \tag{2.32}$$

$$b_2(\theta', t) = \hat{B}_2 \cos((\omega_2 - p_2\omega_r)t - p_2\theta' + \alpha_2) \tag{2.33}$$

The main requirement for a BC-DFIG is that the frequency of the two airgap fluxes are the same, allowing the two stator windings to be coupled via the rotor regardless of pole number. This can be seen by equating the frequency terms in (2.32) and (2.33)

to give

$$\begin{aligned} & \omega_1 - p_1\omega_r = \omega_2 - p_2\omega_r \\ \Rightarrow \quad & \omega_r = \frac{\omega_1 - \omega_2}{p_1 - p_2} \end{aligned} \tag{2.34}$$

For a non-zero rotor speed we therefore have the condition that $p_1 \neq p_2$.

2.5.4 Variable Frequency Transformers

The VFT is a type of continuous phase shifting transformer which consists of a wound rotor induction machine (WRIM) re-purposed for the transmission of power between networks while also allowing the interconnection of two asynchronous grids. It is similar to a hydro-generator in design except with the added condition that the rotor windings must be designed to handle the rated current. With the growing capabilities of control engineering it is thought that this modified transformer could serve as a reliable and robust alternative to power-electronic converter stations to connect between asynchronous networks. Note the maximum difference in frequency between networks is around around ± 1 Hz and beyond this point the stator and rotor magnetic fields can lose synchronism. While this tolerance may seem low, it is an ideal range to deal with fluctuations between neighbouring grids. There are currently only a small number of these machines in operation around the world, with 100MW examples installed at Hydro-Quebec, Canada; Laredo, Texas and a 300MW machine located in Linden, New Jersey [52] [53] [54].

The main unit of the VFT is similar to that of a rotary transformer, with three-phase windings on both the stator and the rotor. Grid 1 is connected to the stator while grid 2 is connected to the rotor via a collector system similar to that in a DFIG. A DC drive motor is connected to the rotor to adjust the difference in phase angle between rotor and stator. Power flow through the VFT is given by equation (2.35) and is proportional to the angle of the rotary transformer.

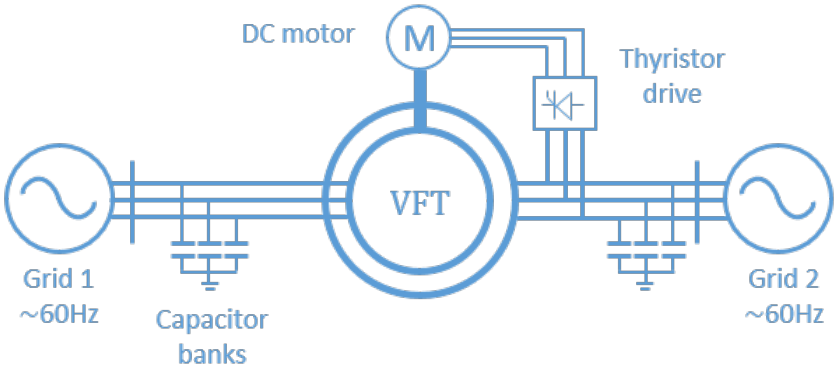

Figure 2.27: Layout of the VFT

$$P_{VFT} = \frac{v_s v_r}{X_{sr}} \sin(\theta_{net}) \tag{2.35}$$

$$\text{where} \quad \theta_{net} = \theta_s - (\theta_r + \theta_{rs}) \tag{2.36}$$

where v_s, v_r are the stator and rotor terminal voltage respectively, X_{sr} is the total reactance, θ_s, θ_r are phase angles of the stator and rotor voltage respectively, and θ_{rs} is the phase angle of the transformer.

Harmonic effects on the connected electrical system due to torque, voltage, and current are negligible therefore the VFT produces no harmonics and cannot cause undesirable interactions with neighbouring generators or other equipment on the grid. The VFT aids in system stability via its large inertia and also by providing an alternative short circuit path in the event of a fault [52]. While a power electronic converter may fail at a fault a little over 1 PU, the VFT is capable of withstanding many more multiples of this [55]. A schematic layout of the VFT is shown in figure 2.27.

A vector diagram of (2.36) is shown in figure 2.28 to illustrate the voltage angles involved. If torque is applied to the shaft, power will flow between the stator and rotor circuits, with a direction dependent on the direction of applied torque.

If the two systems are not in synchronism, the rotor will rotate constantly at a

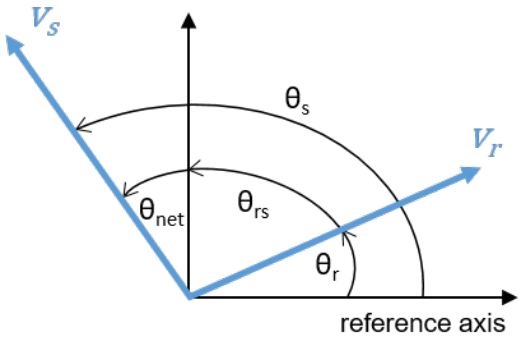

Figure 2.28: Phasor diagram of the VFT

speed proportional to the difference in frequencies as described by (2.37). Load flow is maintained during this operation despite the drifting frequencies since the rotor electrical and mechanical frequencies will always add up to the stator frequency, meaning that from the stator point of view, there is always a synchronous rotating field in the airgap [56].

$$\omega_r = \frac{120}{p}(f_s - f_r) \tag{2.37}$$

where f_s and f_r are the frequencies of the stator and rotor respectively and p is the number of poles.

The VFT can be modelled as a 5th order asynchronous machine with grid 1 connected to the stator windings and grid 2 connected to the rotor windings. A more detailed description of the modelling process will be covered in a chapter 3. In a simulation, torque was applied to the machine to simulate a power transfer of -0.5 PU followed by an order +0.5 PU to demonstrate the capability of bi-directional power flow between synchronous networks. Figure 2.29a shows the results where it can be seen that torque applied in one direction causes a smooth flow of power from grid 1 to grid 2, while a change in sign reverses the direction of power flow.

When two networks of different frequencies are connected through the VFT, the natural response of the machine is to rotate at a speed proportional to the phase dif-

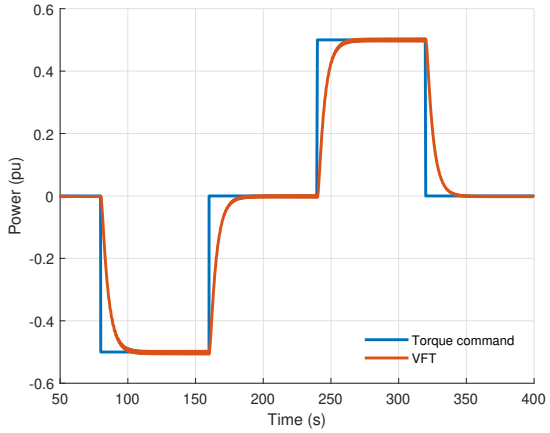

(a) Power seen from the VFT stator side as a function of applied mechanical torque

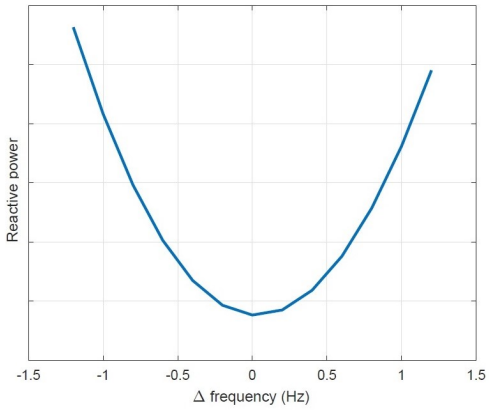

(b) Reactive power seen at the rotor terminals of the VFT as a function of Δ frequency

Figure 2.29: VFT Power Characteristics

ference. As shown in figure 2.29b, this acceleration comes at the expense of reactive power consumption which rises sharply as the difference in frequency increases.

As mentioned previously, a downside of the VFT is the substantial reactive power requirement due to the large leakage reactance. To alleviate this, shunt capacitor banks are used for compensation which are turned on and off to compensate the device. Reactive power flow through the VFT is a natural response which depends on the difference in voltage between the two networks and the series impedance and is not the effect of a control system.

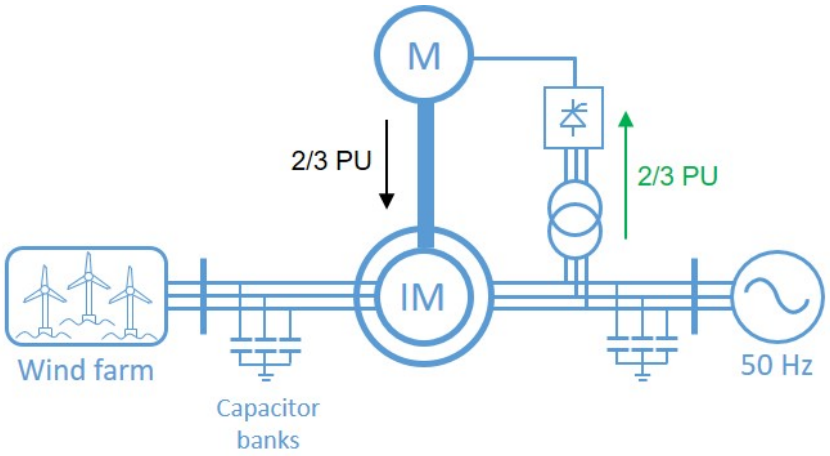

Figure 2.30: VFT for offshore wind

2.5.4.1 VFT for Low Frequency Offshore Wind Power

The VFT could theoretically be used as an interconnection for LFAC offshore wind by increasing the rotational speed of the shaft [23]. To connect a 50/3 Hz wind farm with a 50Hz grid for example, the shaft would need to rotate at a speed of 2/3 PU according to (2.38).

$$f_r = s f_s \tag{2.38}$$

where f_r is the frequency of the rotor, f_s is the frequency of the stator and s is the slip.

To maintain the correct slip required for synchronisation between the 16.7Hz and the 50Hz networks, the DC motor would require 2/3 PU power to prevent deceleration of the rotor. Even by neglecting losses, a VFT of this design would achieve a maximum power transfer efficiency of 33%. Poor efficiency aside, the VFT in its original configuration would require oversized components to handle the balance of power. The DC motor needs to be sized based on the required rotational speed of the machine, which for a standard VFT is very low. In the application to LFAC offshore wind the DC motor would need to rated for 2/3 PU power, as would the thyristor-controlled drive and the rectifier, all of which would incur significant costs.

Despite the downsides associated with efficiency and component costs, the VFT offers some very desirable features. Only a single converter station is required which would be located onshore for ease of access and maintenance. Power quality would be smooth due to the absence of switching harmonics. Operation under faulted conditions and grid disturbances would be partially improved [57] [58], however the power electronics would still be prone to faults in much the same way as with HVDC and would therefore need to disconnect to protect the delicate circuitry. Without power electronics the VFT would lose control over the applied torque in the shaft and would therefore lose the capability to enable power flow between stator and rotor circuits. Without control, the VFT would naturally fix to a rotation that would align the stator and rotor magnetic fields but no power would flow. In the case of a VFT dictating the AC voltage of the offshore wind farm, the AC voltage in the offshore side will increase in frequency as the rotor slows down.

The concept of using a VFT for LFAC offshore wind is an impractical idea in economic terms, however certain positive attributes cannot be overlooked. The large rotating mass of the VFT provides inertia to the power system and improves stability, and the stored kinetic energy in the rotor could even be extracted in the event of a frequency drop to provide a fast frequency response. However, the VFT as a solution to offshore wind is inelegant, inefficient, unidirectional, uneconomical and requires power electronics with large ratings.

2.6 Summary and Conclusions

This chapter has presented some of the main fundamentals of an LFAC transmission system. The motivation for LFAC has been discussed based on the technical limitations of HVAC transmission at long distances combined with the complications of HVDC and the associated cost overruns that have been recently encountered by industry. The main pieces of electrical equipment that make up an LFAC transmission system have been introduced as well as a discussion on how the design and operation of such equipment

differs from those found in conventional HVAC and HVDC systems based on the literature.

The effect of a reduced frequency has been shown to have positive consequences on the utilisation of AC cables characterised by a reduction in charging current and decreased losses, showing that a standard HVAC cable operated at a reduced frequency could see a considerable benefit in transmission range. The trade-off for this increased distance comes at the expense of the transformers and switchgear which must be considerably larger to account for the reduced frequency. The design and size of the transformers have also been discussed, as well as the implications this may have on the design of the wind turbine and any offshore platforms.

Of particular importance is the method of frequency conversion which sits at the heart of any LFAC system which transforms the power at the reduced frequency up to that of the utility. A history of frequency converters has been provided with an added distinction made between the digitally based power-electronic devices and the analogue class of devices which use the principles of electromagnetic induction to perform the conversion. Out of those devices introduced, VSC-HVDC offers the greatest controllabilty but suffers problems with robustness and confidence, and on the other side of the spectrum with the MG-set we have have great robustness but poor controllability and losses. The ideal device would be able to combine the controllability offered by power-electronics with the reliable, highly mature field of electrical machines. The following chapter introduces the PFEC as a novel device to sit in this category, as well as answering some of the previously posed limitations of the VFT, such as an increased power transmission efficiency, and a reduction of both the ratings and the dependence of the power-electronics.

Chapter 3

Introduction and Modelling of the Partial Frequency Energy Converter

This section introduces the PFEC as a solution to the problems raised by the VFT when applied to LFAC offshore wind. The PFEC is a combination of the technology found within a VFT, a B2B-VSC, and the working principles of an MG-set. The work in this thesis shall assume a low-frequency of 16.7Hz and a grid frequency of 50Hz, although it will be shown that other configurations are possible.

Later in this chapter a detailed description of the modelling process is presented with the goal of developing a full PFEC model that is suitable for electromagnetic simulations. The modelling is performed in the Matlab Simulink environment and unless stated otherwise uses the default simulation parameters which are given in table C.1.

Because the PFEC is an amalgam of different technologies, the modelling of each component will be introduced one-by-one in the following order:

1. Operation and control of single-phase and three-phase VSC 3.2
2. B2B-VSC for induction machine applications 3.2.7

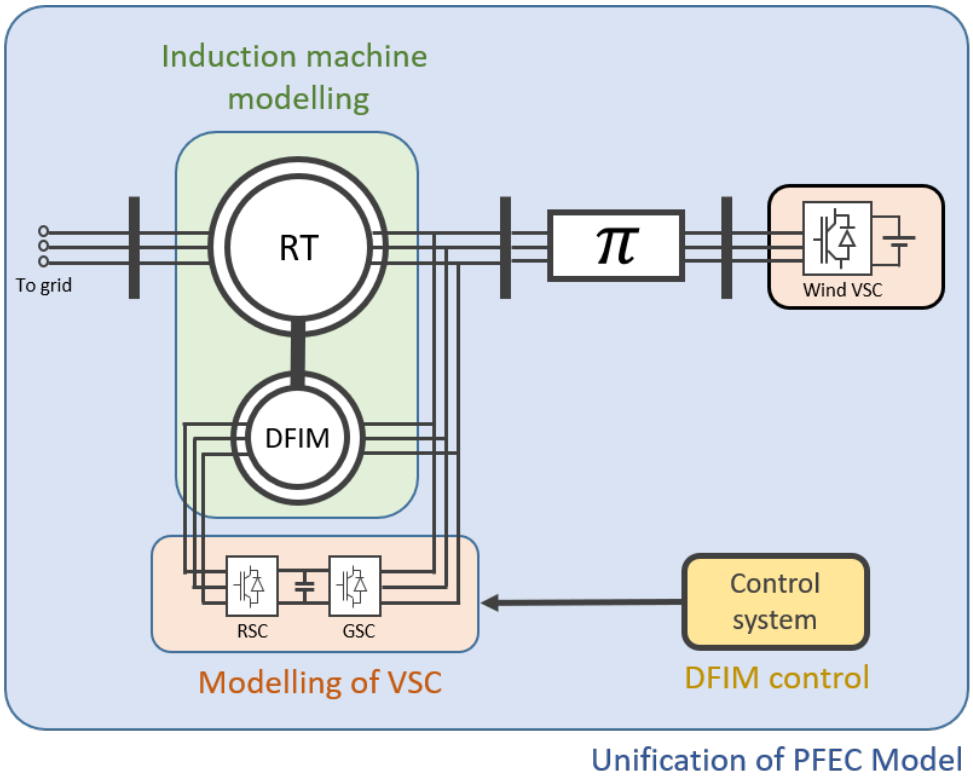

Figure 3.1: System level overview of PFEC showing the different sections that will be considered in this chapter as distinct colours

3. Fifth-order induction machine model 3.3

4. Modelling and control of DFIM 3.4

5. Grand unification of PFEC model 3.6

A system-level overview of the PFEC is shown in figure 3.1 which shows the different sections that will be considered in this chapter as distinct colours. The final part of this chapter is dedicated to unifying each individual component to produce the complete model of the PFEC. The models derived in this section are implemented mathematically in the Simulink software package. Later work on the PFEC involving larger power systems also incorporate the SimPower Systems block-set.

3.1 Partial Frequency Energy Converter

The technology of the PFEC is reliant on the following disciplines in electrical machine theory:

- Induction machine operating principles
- DFIM Control
- VFT for asynchronous grid connection
- Electromagnetic frequency conversion using an MG-set

By specifying suitable equipment such as type-4 wind turbines that produce power directly at the reduced frequency, and low frequency transformers both on the offshore platform and those in the turbines themselves, it is postulated that an LFAC onshore wind farm connected through a PFEC located on the shore may provide an alternative approach to low frequency power transmission.

The core technology of the PFEC is similar to a VFT, i.e. a wound rotor induction machine that spins at a speed proportional to the difference in stator and rotor electrical frequencies to connect the two asynchronous networks. Power transfer between the two networks is proportional to the torque applied to the rotor and is provided by a motor. For a commercial VFT the speed of rotation of the shaft is very low, and since the mechanical power required from the DC motor to exert 1 PU of torque in the VFT shaft (and thus force a 1 PU power flow between the stator and rotor circuit) is proportional to the speed of rotation of the VFT shaft and thus very small (a 100MW VFT uses a 2MW DC motor to control the power flow of between stator and rotor circuits, resulting in an efficiency of approximately 98% at full load [59]).

For the case of a VFT interconnecting a 50 Hz network with a 16.7Hz network, the speed of rotation of the shaft would be 2/3 PU, meaning the DC motor would require two thirds of the power coming out of the stator of the VFT to provide enough torque to the shaft. It is possible to feed the DC motor from the rotor circuit as shown in

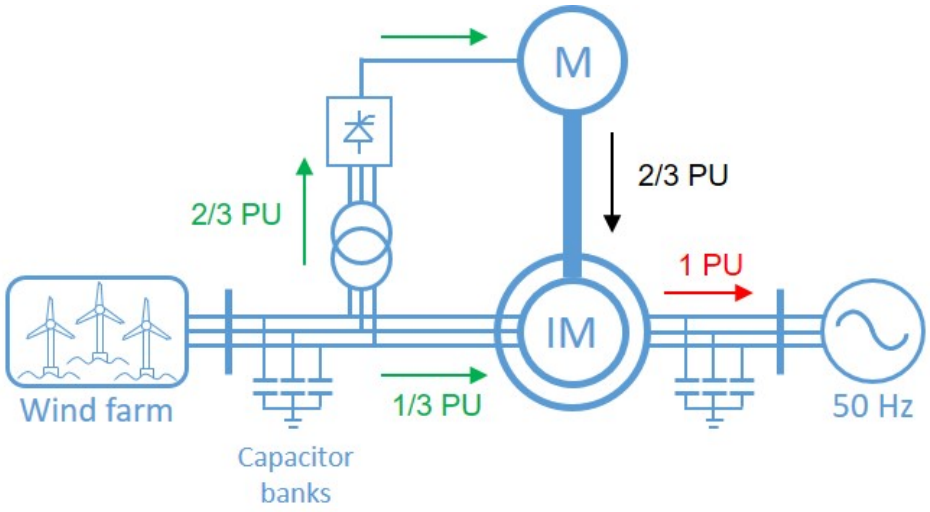

Figure 3.2: VFT for offshore wind with motor powered by rotor circuit

figure 3.2, where one-third of the power arrives at the rotor circuit according to the slip-power relationship in 3.1 and the other two-thirds of the power travels towards the motor circuit where it converted into shaft mechanical power. These power fractions combine in the stator circuit to transmit the full 1 PU power to the grid.

$$P_r = -sP_s \tag{3.1}$$

The layout described in figure 3.2 is still plagued by the requirement of high-power electronics which must be rated for 2/3 PU power, an issue which is likely to increase the cost of this design to uneconomic levels. For example, a VFT of this design rated for 100MW would require a DC motor, a thyristor-controlled drive and a rectifier all rated for 66.7MW. Additionally, the unidirectionality of the VFT power-electronics would further harm the viability of this method.

The presence of the DC rectifier also introduces another conversion stage with an associated efficiency term η_{dc}. If the two fractions of transmitted power are treated as separate entities, namely the one-third and the two-thirds in figure 3.2 then the

conversion steps are as follows:

$$\frac{1}{3}\text{ PU (elec.)} \xrightarrow{\eta_g} \frac{1}{3}\text{ PU (elec.)} \tag{3.2}$$

$$\frac{2}{3}\text{ PU (elec.)} \xrightarrow{\eta_{dc}} \frac{2}{3}\text{ PU (d.c.)} \xrightarrow{\eta_m} \frac{2}{3}\text{ PU (mech.)} \xrightarrow{\eta_g} \frac{2}{3}\text{ PU (elec.)} \tag{3.3}$$

The one-third PU power fraction only encounters the large induction machine with efficiency η_g. The two-thirds (ignoring the efficiency of the transformer) is first converted to DC via the rectifier; then into mechanical power by the motor; before finally entering the large induction machine. If the efficiencies of each of these devices are given by η_{dc}, η_m and η_g respectively, then the efficiency of the collective VFT for offshore wind is given by (3.4).

$$\begin{aligned}\eta_{vft} &= \frac{\eta_g}{3} + \frac{2\eta_{dc}\eta_g\eta_m}{3} \\ &= \frac{\eta_g}{3}\left(1 + 2\eta_{dc}\eta_m\right)\end{aligned} \tag{3.4}$$

The PFEC provides an alternative approach by replacing the DC motor with a WRIM which avoids the DC conversion stage altogether. Instead of a DC motor, the rotor torque of the VFT is now provided by a DFIG (or DFIM, since the device is acting as a motor) in a configuration shown in figure 3.3. At first, one might assume that this replaces the issue of the expensive thyristor-controlled drive with an equally expensive power-electronic converter, however the size of the B2B-VSC is directly proportional to the desired range in speed, i.e. a desired speed range of 30% implies a converter rated at 30% power. The DFIM can therefore be designed such that its synchronous speed sits at precisely 2/3 PU_{RT}, where the subscript RT indicates it is the base of the transformer. The need for this distinction will be made more clear in section 3.6.1.1 . The desired speed range will vary based on application and functionality but even with a generous allowance of $\pm$ 10% deviation from the steady state speed, the B2B-VSC would have a rating of $2/3 \times 10\% = 0.0667$ PU_{RT}.

The final question posed by the application of the VFT to offshore wind is whether

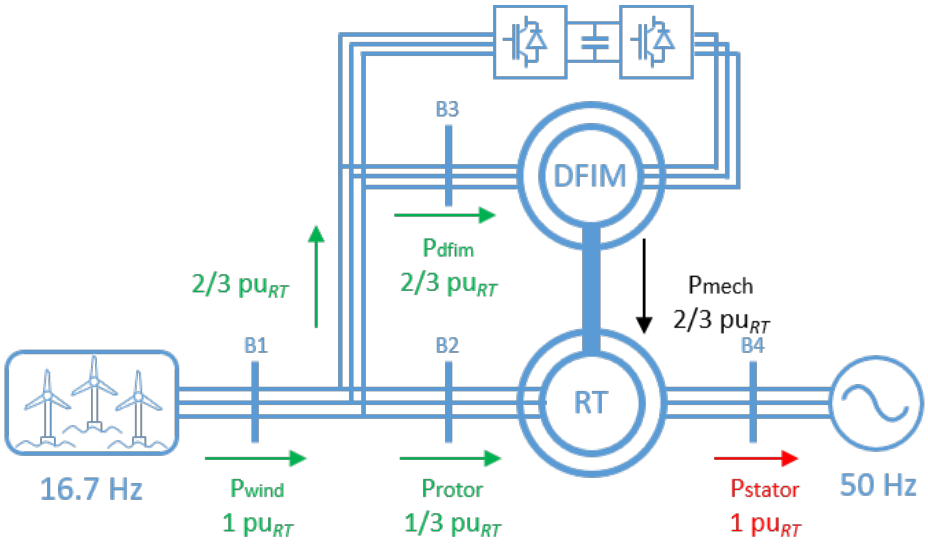

Figure 3.3: Partial frequency energy converter for LFAC offshore wind

it is possible to eliminate the dependence on power-electronics such that the device remains connected during grid faults. The simple answer is yes. Although the B2B-VSC would still need to disconnect in the event of a fault to protect the power-electronics, this no-longer causes the rotor to rapidly lose synchronism or stability.

The DFIM can be designed such that the output-input feedback loop of the rotary transformer with the DFIM is stable, with an equilibrium point where the frequency of the voltages and currents in the rotor circuit are 1/3 PU_{RT} (i.e. the nominal LFAC frequency) of the stator frequency. With this configuration, in steady-state the DFIM will remain at 2/3 PU_{RT} speed even in the absence of power-electronics just by the natural principles that govern its operation, and similar to the principles that were applicable to MG-sets. This inherent stability in steady-state means that even if the power-electronics were disconnected, the machine would return to its equilibrium point of 2/3 PU_{RT}, which just so happens to be the exact speed required for synchronisation between the 16.7Hz wind farm and the 50Hz grid. The power electronics provide the controllability and are able to modify the rotor speed to correctly match the network conditions, but without them the machines act as an uncontrolled MG-set that is still able to maintain the interconnection and power flow between frequencies.

3.2 Voltage-Sourced Converters

The modelling and control of the VSC contains some fundamental mathematical principles and techniques which are common to every subsequent component of the PFEC model. The VSC is therefore introduced first as it incorporates dq-transformations; PI controllers; and methods of controller design that will recur later in the modelling process.

3.2.1 Single Phase, Half-bridge Converter

The first building block in the lead-up to the B2B-VSC is the half-bridge converter. Shown in figure 3.4, it consists of two uni-directional, self-commutated IGBTs connected in anti-parallel with a diode to provide a return path for the current. Control signals are fed to the gate inputs of the IGBTs to control the conducting and blocking phases. The purpose of the DC/AC half bridge converter is to supply a controlled, bi-directional current from an ideal DC source by generating a specific voltage based on the switching patterns. Depending on the voltage, a current of any type can be made to flow through the circuit.

A downside of the half bridge converter is the need for a neutral point within the DC circuit which splits the DC voltage into two, therefore requiring two identical capacitors. In practice, it is often necessary to impose an additional control structure to ensure that the two capacitors charge and discharge evenly, as defects in the manufacturing may cause one to age faster than the other [60].

The half-bridge converter operates based on the alternate switching patterns of S_1 and S_4. The commands to turn on or off can be issued in a variety of methods but most commonly this is achieved using pulse-width modulation (PWM) techniques [61], where a high frequency carrier signal is compared to the desired waveform, termed the modulator. When the two signals intersect this corresponds to an on or off command as

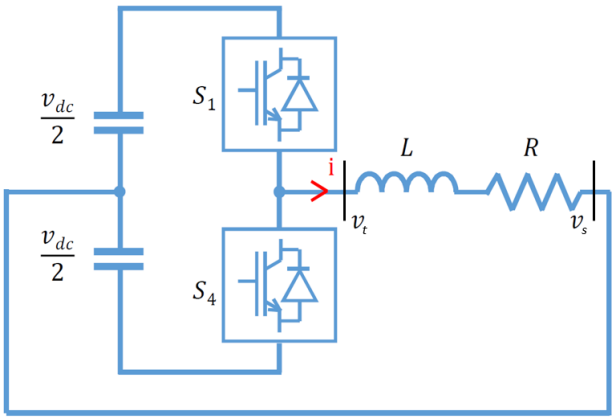

Figure 3.4: Half-bridge DC/AC converter

depicted in figure 3.5. A very high frequency carrier signal produces more intersections leading to an output PWM pattern which more closely emulates the modulator. From the figure it is shown that the two switches are in anti-phase with each other and can never both be on or off at the same time, as this would case a short-circuit.

The switching logic is based on the rule in (3.5). If the modulating signal intersects the carrier signal as the carrier is rising, then S_1 turns off and S_2 turns on. When the modulator crosses the falling carrier signal then this pattern is reversed. These binary pulses are then fed into the gate inputs of the IGBTs.

$$S(t) = \begin{cases} 1 & \text{if modulator} \geq \text{carrier} \\ 0 & \text{if modulator} < \text{carrier} \end{cases} \tag{3.5}$$

The AC-side voltage V_t in figure 3.4 is given by the equation (3.6):

$$v_t = \frac{v_{dc}}{2}[S_1(t) + S_4(t)] \tag{3.6}$$

3.2.2 Averaged Model of Half Bridge Converter

Figure 3.5 and equation (3.5) describe what is termed the switched model of the converter which captures both the steady state and the dynamic behaviour of the VSC. However, it is often not necessary to capture the high frequency components that

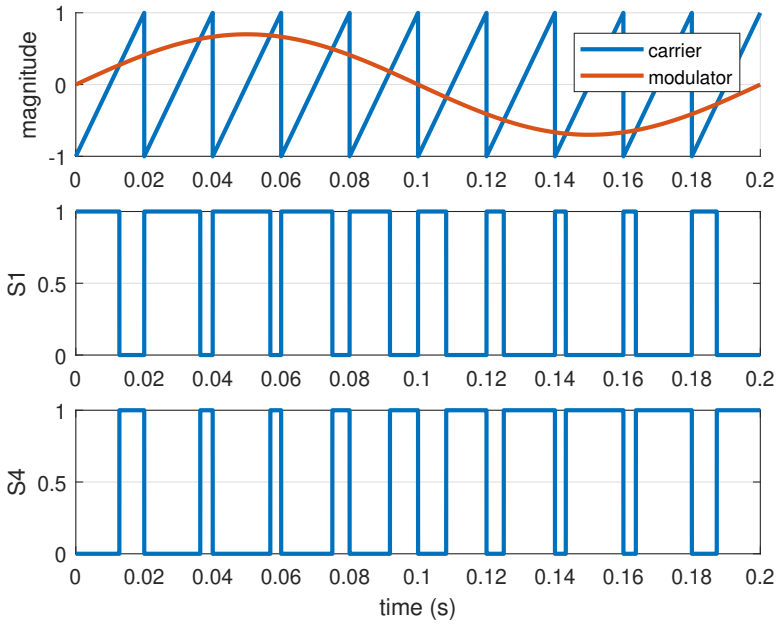

Figure 3.5: PWM technique and switching patterns of the IGBTs [62]. Top: carrier and modulator signals, mid: gate pulses of S_1, bottom: gate pulses of S_4

arise because of the switching of the IGBTs. Moreover, the relationship between the modulating index M (which is the main control variable) and the current and voltage variables are not easily understood from the switched models [62]. To simplify the control problem, an averaged model of the VSC can be used.

Equation 3.7 defines the averaging operator:

$$\bar{x}(t) = \frac{1}{T_s} \int_{t-Ts}^{t} x(\tau)\, d\tau \tag{3.7}$$

Applying (3.7) to S_1 and S_2 gives the switching functions in terms of the duty cycle d, which can assume any value between 0 and 1:

$$\begin{aligned} S_1(t) &= d \\ S_4(t) &= 1 - d \end{aligned} \tag{3.8}$$

Furthermore, if the switching logic is based on a PWM strategy, then:

$$M = 2d - 1 \tag{3.9}$$

where M is the average representation of the switching in one cycle of the fundamental which can be regarded as linear. Applying (3.8) and (3.9) to the equation describing the switched VSC model (3.6) now gives an expression in which v_t changes linearly from $-\frac{v_{dc}}{2}$ to $\frac{v_{dc}}{2}$:

$$\begin{aligned} v_t &= \frac{v_{dc}}{2}[S_1(t) + S_4(t)] \\ &= \frac{v_{dc}}{2}M \end{aligned} \tag{3.10}$$

3.2.3 Control of Averaged Half Bridge Converter

Controlling the current of the half-bridge converter is achieved through the use of proportional-integral (PI) controllers which act on the error of the measured current compared to that of a reference signal. The block layout for the half-bridge converter control problem is shown in figure 3.6.

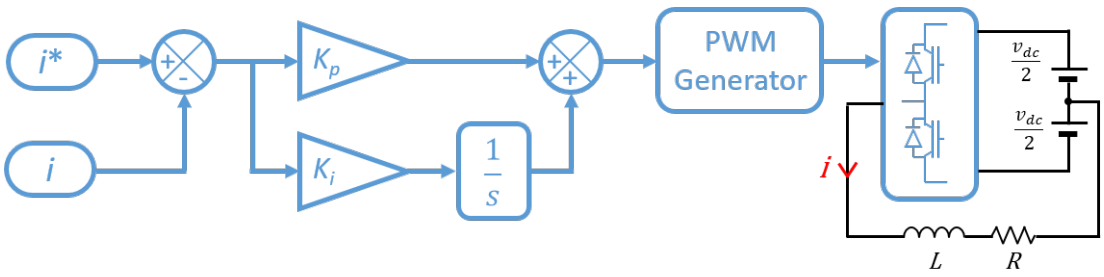

Figure 3.6: Half bridge converter model layout

From the block diagram and the circuit in figure 3.4, the terminal voltage of the converter is described by (3.11)

$$v_t = Ri + L\frac{di}{dt} \tag{3.11}$$

Where R and L are the resistance and inductance of the AC branch. The relation-

ship between the DC-side voltage and the AC-side terminal voltage is a function of the modulating function M and was given in (3.10). Substituting v_t from (3.10) into (3.11) gives the relationship between the DC-side and the AC-side of the circuit:

$$M\frac{v_{dc}}{2} = Ri + L\frac{di}{dt} \tag{3.12}$$

In this form it is now possible to control the current in the circuit through the use of the modulation index M, which is fed into the gate inputs of the half-bridge converter block for conversion into the respective gate signals for each switch. To enable the use of standard control techniques, the plant transfer function from i to the modulation index M is presented in the s-plane (3.13)

$$P(s) = \frac{i(s)}{M(s)} = \frac{v_{dc}}{2\big(R + Ls\big)} \tag{3.13}$$

where $P(s)$ denotes the dynamics of the plant which can be seen to contain a stable pole located at $s = -R/L$. A PI controller can be used to cancel out the dynamics of the system, giving a one-to-one relationship from current to the modulation index and hence the terminal voltage. The tuning of the PI controller is achieved using the modulus optimum technique [63]. First, a PI controller is defined by $C(s)$ and then rearranged into the form in (3.14):

$$\begin{aligned} C(s) &= K_p + \frac{K_i}{s} \\ &= \frac{K_p}{s}\left(s + \frac{K_i}{K_p}\right) \end{aligned} \tag{3.14}$$

The product of the PI controller $C(s)$ and the plant $P(s)$ gives the open loop gain of the system (3.15)

$$\ell(s) = C(s)P(s)$$

such that,

$$\ell(s) = \frac{K_p}{s}\left(s + \frac{K_i}{K_p}\right)\frac{v_{dc}}{2\big(R + Ls\big)} \tag{3.15}$$

The objective of this derivation is to obtain a stable, closed-loop system. This

can be achieved by using the Nyquist stability criterion which states that the closed loop frequency response can be determined from its open-loop characteristics. Shown in (3.16) is the gain of a typical open-loop system with the corresponding closed-loop system in (3.17), which is a first order function with unity gain. By rearranging an open-loop transfer function to the form in (3.16), the stable closed loop system in (3.17) is obtained with a speed of response determined by the selection of the bandwidth α:

$$\ell(s) = \frac{\alpha}{s} \tag{3.16}$$

$$F(s) = \frac{\alpha}{s+\alpha} \tag{3.17}$$

where $\ell(s)$ and $F(s)$ are the open and closed loop gains respectively. To improve the open-loop frequency response of the half bridge controller, the pole at $s = -R/L$ can be cancelled by the zero of the PI controller by letting $\dfrac{K_i}{K_p} = \dfrac{R}{L}$

$$\ell(s) = \frac{K_p}{s}\left(\frac{R+Ls}{L}\right)\frac{v_{dc}}{2\big(R+Ls\big)} \tag{3.18}$$

such that

$$\ell(s) = \frac{K_p v_{dc}}{2Ls} \tag{3.19}$$

By denoting the bandwidth of the system by α, the relationship between the rise time required to reach 90% of the reference value and the bandwidth is detailed in [64] and can be approximated by (3.20), where T_R is the rise time. T_R is a design variable that can be set arbitrarily, however the designed should take into consideration the range of control action of the actuator and the time constants of the plant.

$$\alpha \approx \frac{2.2}{T_R}(rads^{-1}) \tag{3.20}$$

Finally, by defining K_p as in (3.21), K_i can be derived to give the two gains required for the tuning of the PI control. The system now has the open-loop and closed-loop

Table 3.1: Half-bridge Simulation Parameters

Parameter	**Value**	**Parameter**	**Value**
Sampling time, T_s	1e-6 s	v_{dc}	1000 V
Rise time, T_R	0.01 s	R	2 Ω
Switching frequency	5e3 Hz	L	0.02 H

characteristics as in (3.22), as required.

$$K_p = \frac{2L\alpha}{v_{dc}} \qquad K_i = \frac{2R\alpha}{v_{dc}} \tag{3.21}$$

$$\ell(s) = \frac{\alpha}{s} \qquad F(s) = \frac{\alpha}{s+\alpha} \tag{3.22}$$

3.2.3.1 Half-Bridge Controller Performance

The measured current i is compared to the reference current i^* and the error between the two is sent to the PI controller. The control signal is then fed into a PWM generator which outputs the modulation index M for use in the half-bridge converter. The simulation parameters are given in table 3.1.

To test the dynamic response of the model, a step change in reference current was applied,increasing from 0 to 100A at 0.002 seconds. Figure 3.7 shows how the current responds to the step change, gradually rising to meet the new reference. The middle plot shows the output from the PI labelled as control action which feeds into the the PWM generator. The actual current displays a smooth, first-order response with a rise time equal to that specified in table 3.1.

The effect of increasing and decreasing the time constant can be seen in figure 3.8 where a step signal of 1 PU is applied to the reference current. A very fast rise time of 0.1ms results in saturation of the actuator (in this case the power converter) evidenced by the red curve with constant gradient, whereas a slow rise time of 10ms produces a system that is sluggish and slow to react as evidenced by the purple curve. The ideal speed of response sits between the linear region of the controller (i.e. an unsaturated output) such that it can fully capture the linear dynamics of the system.

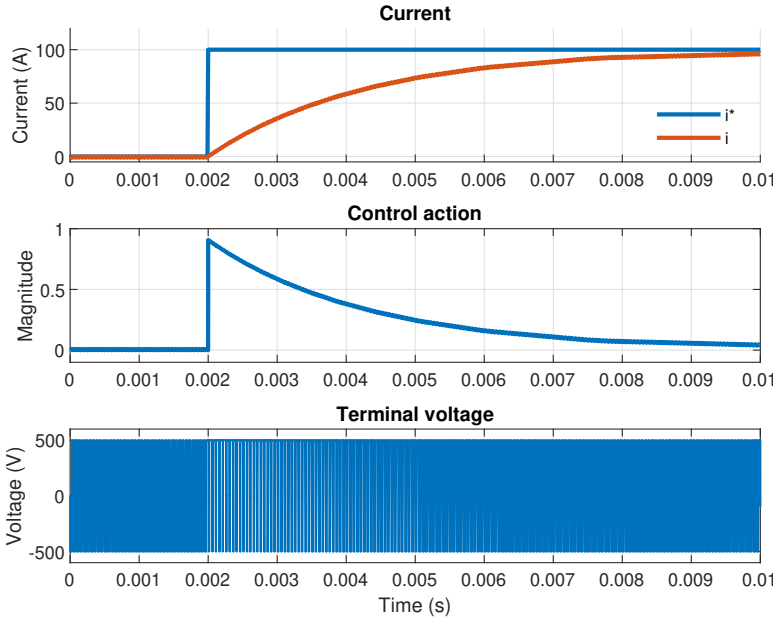

Figure 3.7: Dynamic response of half-bridge model to a step change in reference current. Top: Measured current and reference current. Middle: Output from PI controller. Bottom: Terminal voltage

3.2.4 dq0 Transformation

The PFEC is a three phase AC machine and will therefore require a three-phase VSC based on a PI controllers. To avoid the issues associated with PI controllers tracking sinusoids, a three phase system needs to be transformed into a fictitious two-phase system in which the variables appear as DC quantities which are then easily tracked and acted upon by the controller. This is achieved by a compound transformation; first by the Clarke transform and then the Park transform. The dq0 reference frame has found extensive use both in converter and machine modelling because of its transformation from sinusoidally changing variables to constant DC values so the derivation is not covered here.

Combining the Clarke and Park transformation gives the abc to dq0 transformation

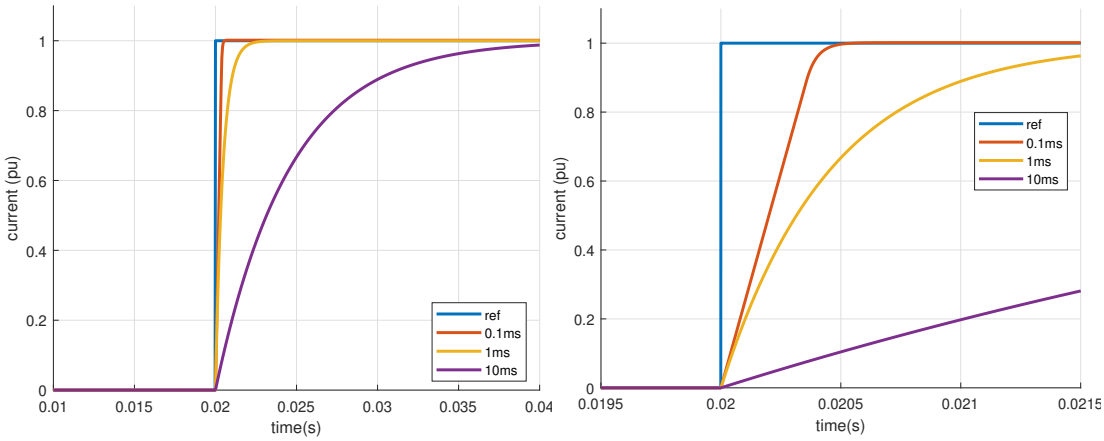

(a) Controller response to step change

(b) Zoom to show saturation

Figure 3.8: First-order Butterworth plots showing the effects of varying T_R

and its inverse in (3.23) and (3.24) respectively.

$$\begin{bmatrix} v_d \\ v_q \\ v_0 \end{bmatrix} = \frac{2}{3} \begin{bmatrix} \cos(\theta) & \cos\left(\theta - \frac{2\pi}{3}\right) & \cos\left(\theta + \frac{2\pi}{3}\right) \\ \sin(\theta) & \sin\left(\theta - \frac{2\pi}{3}\right) & \sin\left(\theta + \frac{2\pi}{3}\right) \\ \frac{1}{2} & \frac{1}{2} & \frac{1}{2} \end{bmatrix} \begin{bmatrix} v_a \\ v_b \\ v_c \end{bmatrix} \tag{3.23}$$

$$\begin{bmatrix} v_a \\ v_b \\ v_c \end{bmatrix} = \sqrt{\frac{2}{3}} \begin{bmatrix} \cos(\theta) & \sin(\theta) & \sqrt{\frac{1}{2}} \\ \cos\left(\theta - \frac{2\pi}{3}\right) & \sin\left(\theta - \frac{2\pi}{3}\right) & \sqrt{\frac{1}{2}} \\ \cos\left(\theta + \frac{2\pi}{3}\right) & \sin\left(\theta + \frac{2\pi}{3}\right) & \sqrt{\frac{1}{2}} \end{bmatrix} \begin{bmatrix} v_d \\ v_q \\ v_0 \end{bmatrix} \tag{3.24}$$

It is now possible to move between a balanced three-phase time-varying AC signal to an equivalent DC system with constant variables, and then back to AC again by using the inverse transformation. This allows the PI controller to act on the DC quantities in the central step of this process before being converted back into AC.

3.2.5 Three-phase, Full-bridge Converters

The introduction of the dq0 transformation allows the use of PI controllers on three-phase AC systems such that the control of the three-phase converter can now be derived. From this it is a short step towards the back-to-back VSC and its application on the PFEC. A schematic representation of the three-phase full bridge converter is shown in figure 3.9.

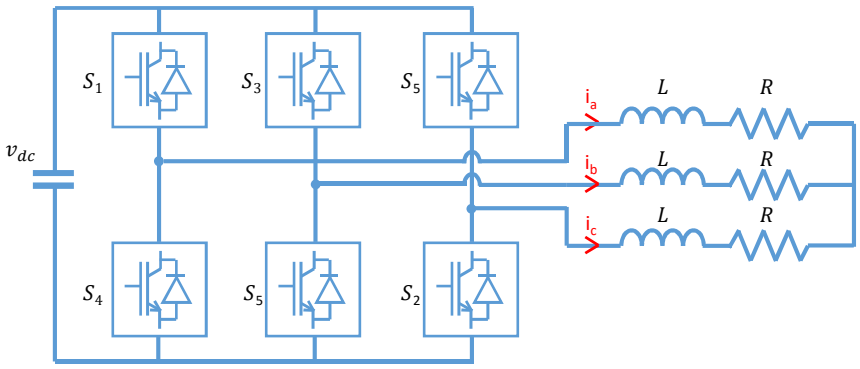

Figure 3.9: Three-phase, full bridge schematic

If in figure 3.9 a voltage source representing the utility grid were to be placed at the AC-side, an additional voltage component would be added to the dynamics of the system and there would be an associated frequency imposed by the grid. This situation is shown in figure 3.10.

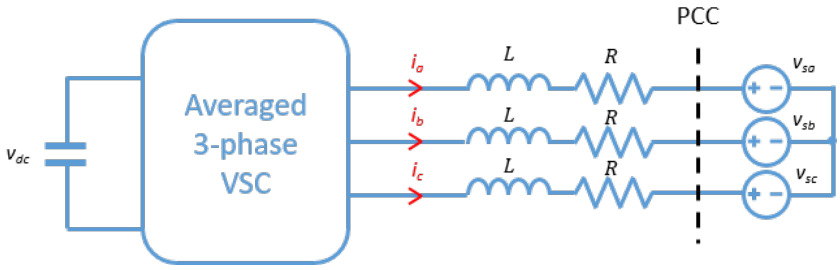

Figure 3.10: Grid connected, full-bridge converter where PCC indicates the point of common coupling

For a three phase system, the AC voltage components v_{sabc} can be described by the

sinusoids in (3.25), where $\hat{v_s}$ = peak phase voltage, ω = system frequency and θ_0 = initial phase angle.

$$\begin{aligned} v_{sa}(t) &= \hat{v_s}\cos(\omega t + \theta_0) \\ v_{sb}(t) &= \hat{v_s}\cos(\omega t + \theta_0 - \frac{2\pi}{3}) \\ v_{sc}(t) &= \hat{v_s}\cos(\omega t + \theta_0 - \frac{4\pi}{3}) \end{aligned} \tag{3.25}$$

The terminal voltage equations of the converter are given in state-space representation in (3.26)

$$\vec{v_t} = R\vec{i} + L\frac{d\vec{i}}{dt} + \vec{v_s} \tag{3.26}$$

Applying the dq transformation to this equation and using the substitution for the DC-side voltage as in (3.10), the d and q axis components are given by (3.27).

$$\begin{aligned} \frac{v_{dc}}{2}M_d &= Ri_d + L\frac{di_d}{dt} - L\omega i_q + v_{sd} \\ \frac{v_{dc}}{2}M_q &= Ri_q + L\frac{di_q}{dt} + L\omega i_d + v_{sq} \end{aligned} \tag{3.27}$$

It can be seen that these two expressions are coupled due to the $L\omega$ terms. To decouple these for use in simulation, the substitution in (3.28) is introduced.

$$\begin{aligned} M_d &= \frac{2}{v_{dc}}\Big(u_d - L\omega i_q + v_{sd}\Big) \\ M_q &= \frac{2}{v_{dc}}\Big(u_q + L\omega i_d + v_{sq}\Big) \end{aligned} \tag{3.28}$$

such that the system is now described by the new control inputs u_d and u_q.

$$\begin{aligned} u_d &= Ri_d + L\frac{di_d}{dt} \\ u_q &= Ri_q + L\frac{di_q}{dt} \end{aligned} \tag{3.29}$$

Applying the Laplace transform and rearranging gives the transfer functions from

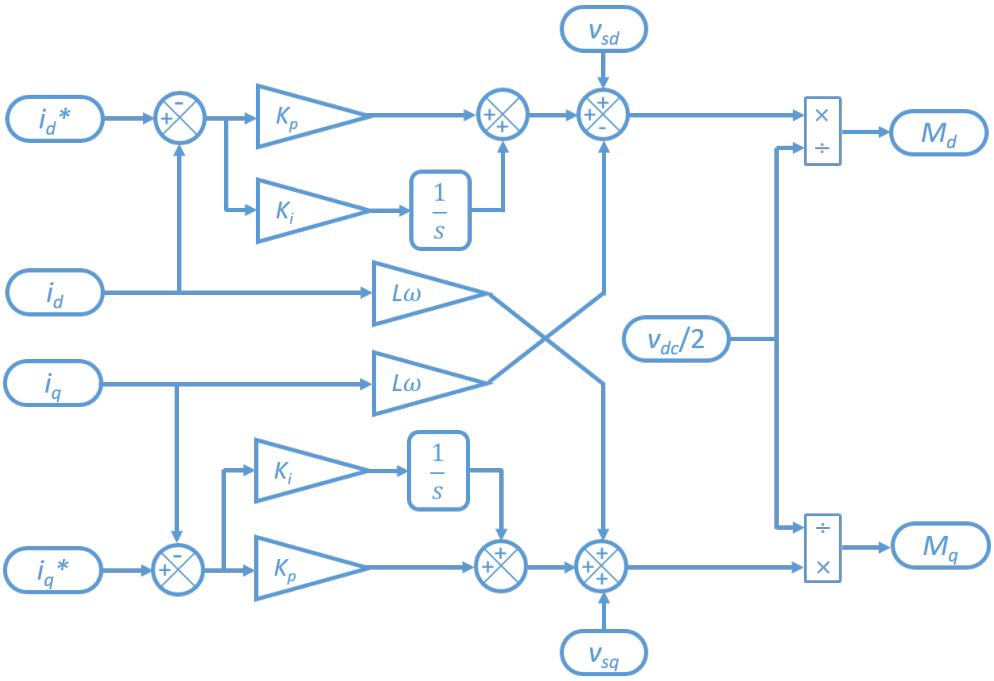

Figure 3.11: Control layout of dq-current loops showing cross-coupled terms

i_{dq} to u_{dq} as:

$$\frac{i_d(s)}{u_d(s)} = \frac{1}{R+Ls} \qquad \frac{i_q(s)}{u_q(s)} = \frac{1}{R+Ls} \tag{3.30}$$

The system can be now be designed based on the control inputs u_{dq}. The cross-coupling terms are then introduced giving the dq components of the modulator index which is then converted back into the abc reference frame for use in PWM.

3.2.5.1 Three-phase VSC Controller Performance

The performance of the grid-connected VSC is now tested based on the control structure shown in 3.11 and the simulation parameters in table 3.2.

To test the dynamic response of the model, a step change in reference d-axis current was applied, stepping from 0 to 0.5 PU at time t = 3s. Figure 3.12 shows the linear, first-order response to the step change and also shows the effect of the cross-coupling. Despite the fact that the two axes are called orthogonal, a change in d-current has an effect on the q-current because of the cross coupling term.

Table 3.2: Half-bridge Simulation Parameters

Parameter	Value	Parameter	Value
Sampling time, T_s	10e-6 s	Rated power S_b	1 kW
Rise time, T_R	5e-3 s	v_{dc}	2000 V
Voltage, v_s	480 V	R	0.346 Ω
Frequency, f	50 Hz	L	0.110 H

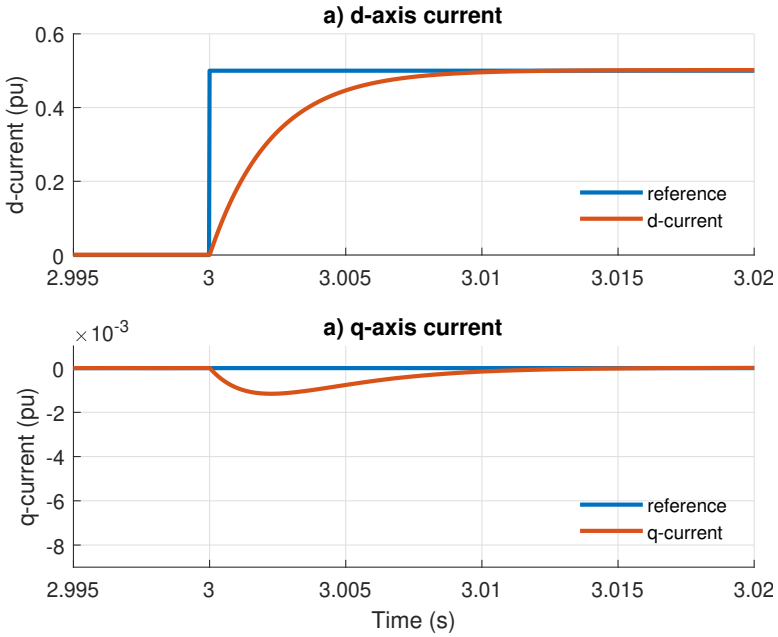

Figure 3.12: Controller response to a step-change in d-current. Top: d-axis. Bottom: q-axis showing the effect of the cross-coupling terms

3.2.6 DC Voltage Control

Up until now the voltage source has been treated as ideal, meaning that it can supply any voltage required no matter the feasibility to a real-world application. In back-to-back converters, the DC-side voltage is usually provided by a capacitor sufficiently sized to meet demand and charged using the active d-current through the use of a VSC. This situation is presented in figure 3.13 showing the different flows of power through the circuit. An additional control loop must be added to control the DC voltage by measuring any error in v_{dc} with respect to a reference value.

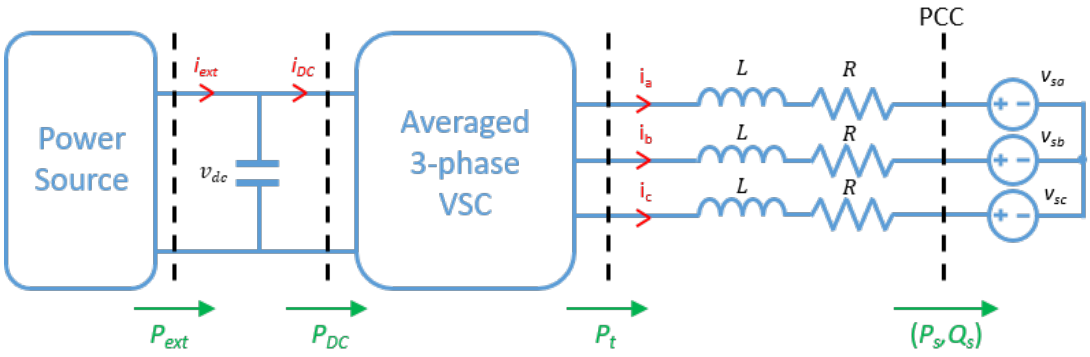

Figure 3.13: Schematic of VSC with an external power source supplying the DC-link capacitor

Assuming zero losses, the power balance equation for the VSC system is given by (3.31)

$$P_t = P_{ext} - \frac{d}{dt}\left(\frac{1}{2}Cv_{dc}^2\right) \tag{3.31}$$

Together, (3.31) represents a dynamic system with P_{dc} as the control input, v_{dc}^2 as the state variable and P_{ext} as a disturbance which is not present in the design of the controller and can therefore only be compensated for. By removing P_{ext} from the equation and neglecting the losses and the instantaneous energy stored in the RL impedance between the VSC and the grid, then $P_t = P_s$ and is given by (3.32)

$$P_t = \frac{3}{2}v_d i_d \tag{3.32}$$

Because of the quadratic term in (3.31) is it not possible to perform the Laplace transform directly. Instead, a change of variables must be introduced such that the energy of the DC capacitor is being controlled instead of the square of the voltage directly. The energy of the DC capacitor is given by $(1/2)Cv_{dc}^2$, such that by introducing the substitution $W = v_{dc}^2$ into (3.31) and applying Laplace, the transfer function from d-current to the capacitor energy is obtained. The controller block diagram is shown in figure 3.14.

$$\frac{W(s)}{i_d(s)} = -\frac{3v_d}{Cs} \tag{3.33}$$

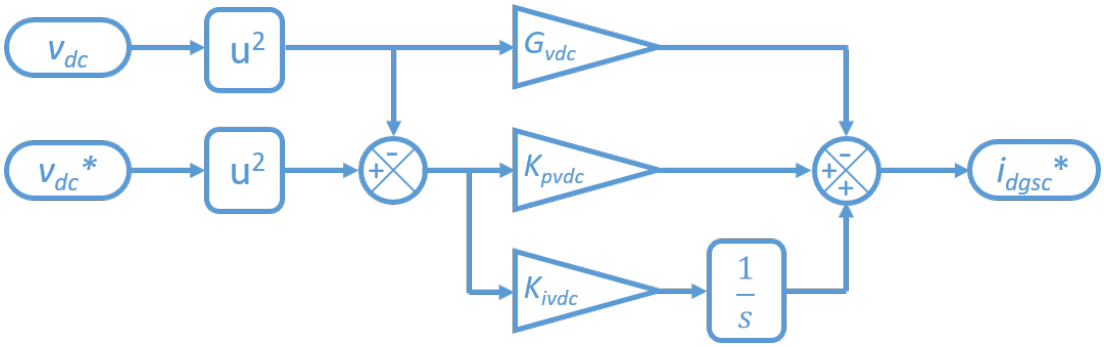

Figure 3.14: Control design of DC voltage controller

(3.33) has a pole located at the origin meaning that there is no damping to this system and disturbance rejection is very poor. If we apply the same modulus optimum tuning techniques then we obtain an integral gain of zero leading to large steady-state errors. This effect is shown with the open loop transfer function ℓ in (3.34):

$$\ell(s) = \left[\frac{K_{pvdc}}{s}\left(s + \frac{K_{ivdc}}{K_{pvdc}}\right)\right]\left[\frac{-3v_d}{Cs}\right] \tag{3.34}$$

Setting $K_{ivdc}/K_{pvdc} = 0$ gives the open-loop gain:

$$\ell(s) = -\frac{3v_d K_{pvdc}}{Cs} \tag{3.35}$$

Now, by letting $K_{pvdc} = \dfrac{\alpha C}{3v_d}$ a transfer function is obtained with the desired open-loop gain of $\ell(s) = \dfrac{\alpha}{s}$ and closed loop gain $F(s) = \dfrac{\alpha}{s+\alpha}$. However, the substitution $\dfrac{K_{ivdc}}{K_{pvdc}} = 0$ implies an integral term of zero and results in steady state errors as well as very poor disturbance rejection which would result in unsatisfactory controller performance.

To counter this, a second loop must be introduced to artificially move the pole away from the origin. The theory behind this is to add a feedback loop within the plant dynamics themselves. The transfer function of the new system is then given as:

$$\frac{W(s)}{i_d(s)} = -\frac{3v_d}{Cs + 3v_d G_{vdc}} \tag{3.36}$$

However, since it is impossible to alter the plant everything must be handled by the PI controller. To virtually alter the plant, the substitution $i_{d_ref} = i'_{d_ref} - G_{vdc}v_{dc}^2$ is made, giving the system shown in figure 3.15. The transfer function of this new system is now given in (3.37).

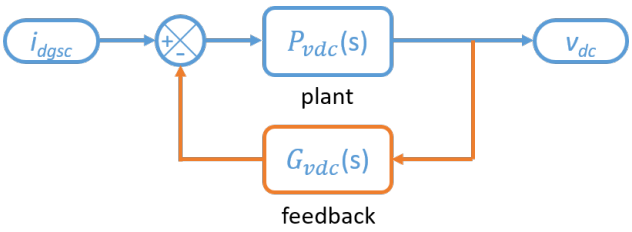

Figure 3.15: Internal feedback loop to artificially move the pole away from the origin

$$G(s) = -\frac{3v_d}{Cs + 3v_d G_{vdc}} \tag{3.37}$$

The PI controller can now be tuned using the familiar modulus optimum technique. The open-loop transfer function of the PI controller and the plant are given in (3.38).

$$\ell(s) = \left[\frac{K_p}{s}\left(s + \frac{K_{ivdc}}{K_{pvdc}}\right)\right]\left[-\frac{3v_d}{Cs + 3v_d G_{vdc}}\right] \tag{3.38}$$

Making the substitutions in (3.39):

$$\frac{K_{ivdc}}{K_{pvdc}} = \frac{3v_d G_{vdc}}{C}; \qquad K_{pvdc} = \frac{\alpha C}{3v_d} \tag{3.39}$$

the open-loop and corresponding closed-loop gains are found, as required:

$$\ell(s) = \frac{\alpha}{s}; \qquad F(s) = \frac{\alpha}{s + \alpha} \tag{3.40}$$

There are no specific rules for determining the value of G_{vdc}. A large value of will exhibit more damping [65], however to stick within realistic margins the same bandwidth is assigned to G_{vdc} as found in the rest of the system. The closed loop gain of the modified system is:

$$\frac{G(s)G_{vdc}}{1 + G(s)G_{vdc}} \tag{3.41}$$

Setting this equal to $\frac{\alpha}{\alpha + s}$ we obtain (3.42)

$$G_{vdc} = \frac{\alpha C}{3v_d} \tag{3.42}$$

3.2.6.1 Controller Performance

The controller from figure 3.14 is tested with difference values for the term G_{vdc}. The purpose of the G_{vdc} term is to improve the damping of the system after a disturbance. To test this, a disturbance can be introduced to the DC circuit by means of a switched load.

The experimental set up is shown in figure 3.16. At $t = 10$ seconds the switch is closed to connect the additional load on the DC circuit and the controller immediately acts to regulate v_{dc} back to the nominal value.

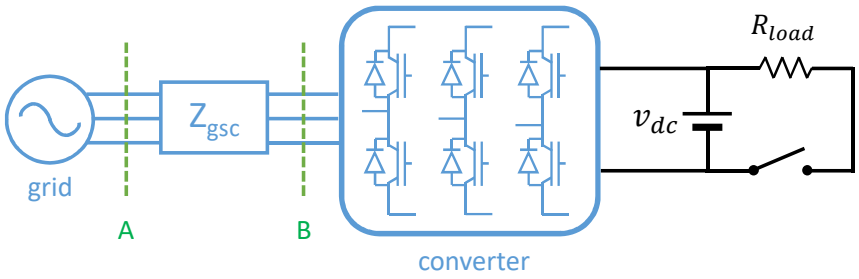

Figure 3.16: Experimental set-up to test disturbance rejection

The effect of the additional load on DC voltage is seen in figure 3.17 for a range of values of G_{vdc}. When $G_{vdc} = 0$ the disturbance produces a large oscillation which characterises a poor disturbance rejection due to insufficient damping. When the G_{vdc} term is added this oscillation appears much smaller, however when the gain is made too large the controller saturates and produces a much longer rise time. The correct tuning of G_{vdc} operates on the same principles as for the time constant, where a trade-off between disturbance rejection and speed-of-response is encountered.

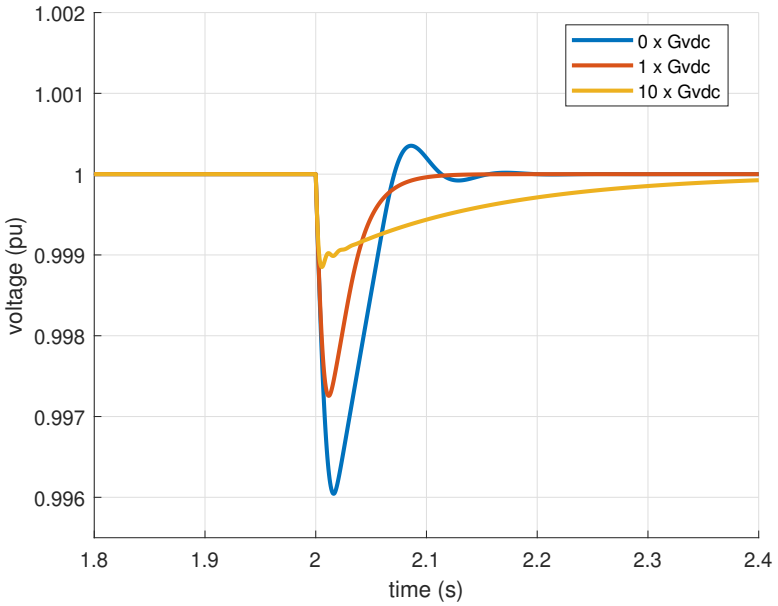

Figure 3.17: Disturbance rejection showing increased damping when G_{vdc} is introduced

3.2.6.2 Non-minimum phase behaviour

Expanding equation (3.31) for the rate of change of DC voltage shows that the voltage variation is defined by the difference between the power supplied by the external source P_{ext} and the power at the VSC terminals P_t.

$$\frac{dv_{dc}^2}{dt} = \frac{2(P_{ext} - P_t)}{C} \tag{3.43}$$

This is a simplified assumption for linear control purposes which does not take into account the dynamics of the inductor voltage. The expression for the power at the VSC terminals actually consists of two parts, i.e. the AC active power P_t and the energy stored in the inductor P_L as shown below:

$$\begin{aligned} P_{dc} &= P_t + P_L \\ &= \frac{3}{2} v_d i_d + \left(\frac{3L}{4}\right) \frac{di_d^2}{dt} \end{aligned} \tag{3.44}$$

The full dynamics of the DC voltage, if resistive losses are neglected, can therefore

be described as

$$\frac{C}{2}\frac{dv_{dc}^2}{dt} = P_{ext} - \frac{3}{2}v_d i_d - \left(\frac{3L}{4}\right)\frac{di_d^2}{dt} \tag{3.45}$$

The quadratic term i_d^2 in (3.45) introduces non-minimum phase behaviour in the DC plant. Regardless of the polarity of i_d, the squared term forces all values to be positive meaning that there is no difference in sign regardless of whether the VSC is acting as an inverter or a rectifier. In inverting mode this isn't a problem since the sign of $-P_L$ is equal to the polarity of the VSC power, but in rectifying mode the polarities are opposite. This difference in sign polarity causes the non-minimum behaviour. During a transient, the inductor will release a lot of energy creating a differential between points A and B in figure 3.14. Current remains the same as it is a series connection, but voltage exhibits a drop due to the inductance. This effect can be ignored in small systems with a large capacitance and small interface inductance, but it becomes a problem in large HVDC systems.

Figure 3.18 shows the characteristic non-minimum phase behaviour when the DC voltage is stepped up from 3000V to 3300V. The non-minimum phase behaviour of the system manifests itself as an initial inversion in the output variable which in turn produces a delay at $t = 10$ seconds and has the effect of limiting the maximum speed of response of the controller. This phenomenon is studied in more detail in [66].

3.2.7 Back-to-Back Converter

As the name suggests, the back-to-back voltage-sourced converter (B2B-VSC) consists of two voltage-sourced converters connected back-to-back via the DC-link. The orientations of the devices are inverted with respect to each other and it allows the decoupling of two AC networks. This is advantageous because it allows the connection of two AC systems that are at different frequencies. Applications of the B2B-VSC are numerous and it has seen increased penetration into the wind industry in recent years. At the individual turbine level within the type-3 and type-4 turbines, a B2B-VSC is housed within the nacelle to enable the independent operation of the rotor and stator-side networks. At transmission level, a pair of VSCs connected together via the DC circuit

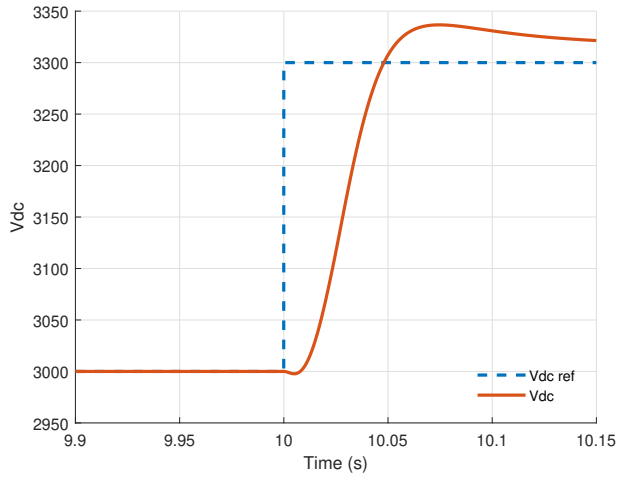

Figure 3.18: Nonminimum-phase behaviour of DC voltage controller, showing the initial inversion of the control variable at t = 10s

are commonly used for the bulk transferral of power in HVDC transmission.

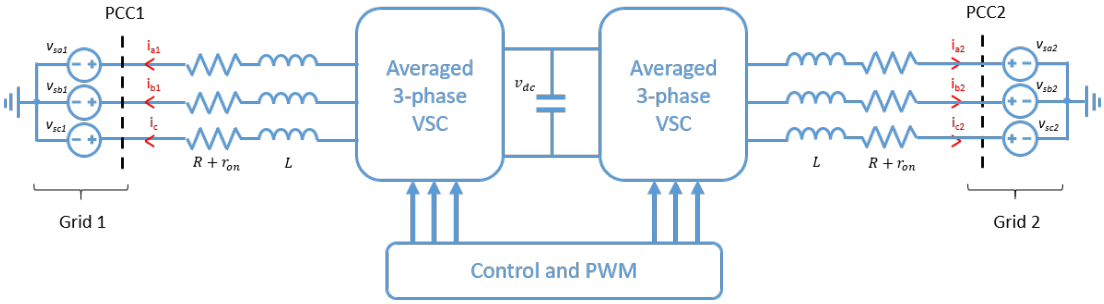

Figure 3.19: Schematic of a B2B-VSC

The control strategies of the B2B-VSC are the same as those covered in the three phase full-bridge converter. In this arrangement, one VSC is used to regulate the voltage of the DC link by supplying active current from the AC-side. The second VSC draws energy from the DC-link and uses it to supply either d or q current to the network. Provided that each individual control loop is functioning correctly in isolation, the only task that remains is to ensure that the time constants are in agreement.

To test the experimental arrangement of the B2B-VSC, the model in figure 3.19 was set up, with parameters defined in table 3.3. For simplicity, the two networks

Table 3.3: Simulation parameters for B2B-VSC

Parameter	**Value**	**Parameter**	**Value**	Parameter	Value
T_s	50e-6 s	v_{dc}	3000 V	$T_{R_{is}}$	5e-3 s
v_s, v_r	480 V	C	1000 μF	$T_{R_{ir}}$	5e-3 s
f_s, f_r	50 Hz	R	0.0015 PU	$T_{R_{vdc}}$	30e-3 s
P_{rated}	1 kW	L	0.15 PU	G_{vdc}	-6.24 e-6

were designed to have the same voltages and frequencies, defined as v_s,v_r and f_s,f_r respectively, where the subscripts s and r denote the sending and receiving end of the network, defined to be moving from left to right. Similarly, the resistance R and inductance L are identical for each side.

At time t = 10s and t = 10.05s a demand of 0.5 PU reactive current and 0.3 PU active current are sent respectively, then at t = 10.15s a step change of 0.01 PU is applied to the DC voltage. The results are shown in figure 3.20 which demonstrates the smooth 1st order controller responses to the various step changes. The effects of the cross-coupling terms can be also be seen, first by the influence of the reactive current on the active current at t = 10s, and then again on the reactive current by the active current at t = 10.05s. The reactive current also has an effect on the DC-link voltage, however this effect is too small to be seen on the plots. The step change in active current introduces a small perturbation to the DC voltage however the step change to the DC-link voltage has little to no effect on the current. This is due to the relative speed of response of the two loops which differ by an order of magnitude. Current control occurs in the inner loop which performs operations at least 10 times faster than the outer DC loop, which provides enough separation of closed loop dynamics between the inner and outer control loops, which in turn allows independent tuning for each controller.

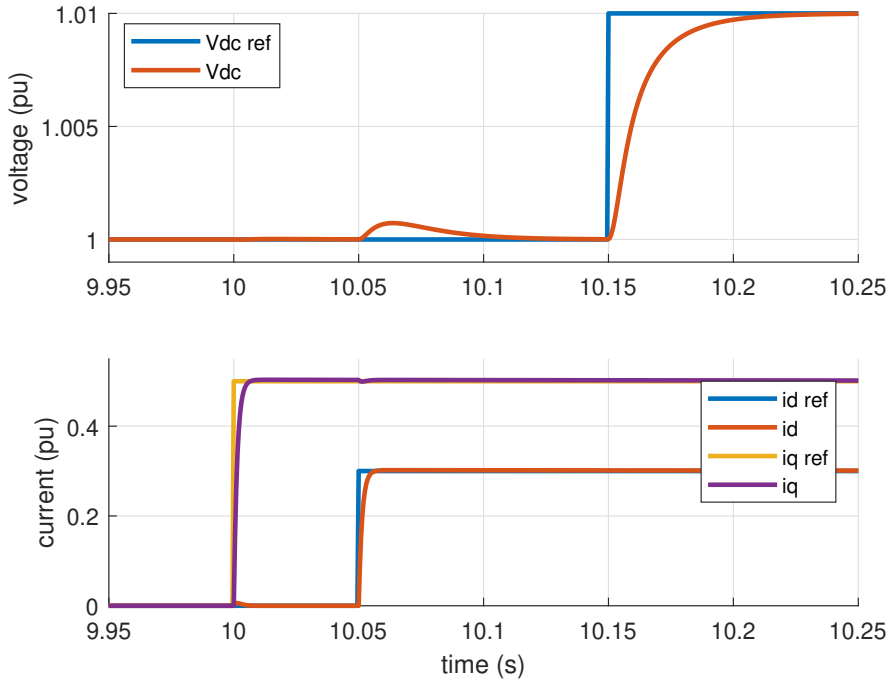

Figure 3.20: B2B converter waveforms showing that the model performs well under a range of reference step changes. Top: DC voltage. Bottom: active and reactive current

3.3 Induction Machine Modelling

Before moving on to controlling the PFEC it is first important to understand the modelling process of an induction machine since this is the fundamental technology within the PFEC.

The voltage equations of the stator and rotor windings of a three phase induction machine can each be represented by a resistance and an inductance, which total to a sixth order system of equations as in (3.46),

$$\begin{aligned} v_{as} &= i_{as}R_{as} + \frac{d\lambda_{as}}{dt} & \qquad v_{ar} &= i_{ar}R_{ar} + \frac{d\lambda_{ar}}{dt} \\ v_{bs} &= i_{bs}R_{bs} + \frac{d\lambda_{bs}}{dt} & \qquad v_{br} &= i_{br}R_{br} + \frac{d\lambda_{br}}{dt} \\ v_{cs} &= i_{cs}R_{cs} + \frac{d\lambda_{cs}}{dt} & \qquad v_{cr} &= i_{cr}R_{cr} + \frac{d\lambda_{cr}}{dt} \end{aligned} \tag{3.46}$$

where the subscripts a, b, c represent each of the three-phases , the subscripts s, r represent either the stator or the rotor, v is the voltage, i is current, R is resistance and λ is the flux linkage and all quantities are referred to the stator. This system is represented by the equivalent circuit in figure 3.21. These equations combined with the dynamics of the mechanical systems together make up the seventh order model.

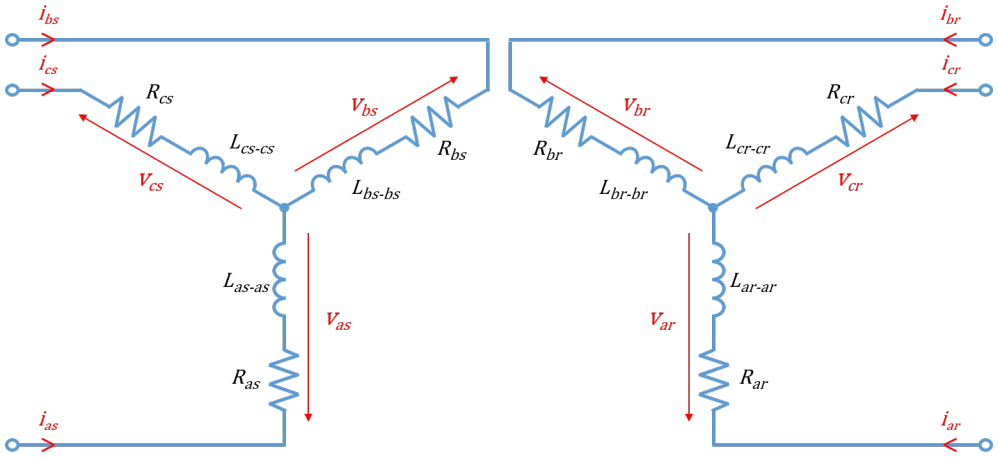

Figure 3.21: Equivalent circuit of the stator and rotor windings of an induction machine

The flux linkage λ is defined by an inductance matrix which takes into account both the self and mutual inductances which arise due to the proximity of the coils. This is shown in (3.47).

$$[\lambda] = [\lambda_{as}, \lambda_{bs}, \lambda_{cs}, \lambda_{ar}, \lambda_{br}, \lambda_{cr}]^T = \mathbf{L}[i_{as}, i_{bs}, i_{cs}, i_{ar}, i_{br}, i_{cr}]^T$$

$$\text{where} \qquad \mathbf{L} = \begin{bmatrix} L_{as-as} & L_{as-bs} & L_{as-cs} & L_{as-ar} & L_{as-br} & L_{as-cr} \\ L_{as-bs} & L_{bs-bs} & L_{bs-cs} & L_{bs-ar} & L_{bs-br} & L_{bs-cr} \\ L_{as-cs} & L_{bs-cs} & L_{cs-cs} & L_{cs-ar} & L_{cs-br} & L_{cs-cr} \\ L_{as-ar} & L_{bs-ar} & L_{cs-ar} & L_{ar-ar} & L_{ar-br} & L_{ar-cr} \\ L_{as-br} & L_{bs-br} & L_{cs-br} & L_{ar-br} & L_{br-br} & L_{br-cr} \\ L_{as-cr} & L_{bs-cr} & L_{cs-cr} & L_{ar-cr} & L_{br-cr} & L_{cr-cr} \end{bmatrix} \tag{3.47}$$

A full derivation of the seventh order model is presented in [67]. The difficulty of solving the seventh order system of equations has prompted the development of simplified models to reduce the complexity and speed up the computation times. The inductance matrix in (3.47) is time varying and therefore must be solved at every iteration, however if a change of reference frame is introduced, entries within this matrix become DC values. This is accomplished via the dq0 transformation.

Applying the transformation to the system of equations in (3.46) gives the dq-voltage equations in (3.48). By setting the angular frequency equal to the frequency of the electrical system, the time-varying quantities rotate at the same speed and thus appear to be DC values from the perspective of the machine:

$$\begin{aligned} v_{ds} &= i_{ds}R_s + \frac{d\lambda_{ds}}{dt} - \omega_s\lambda_{qs} & v_{dr} &= i_{dr}R_r + \frac{d\lambda_{dr}}{dt} - (\omega_s - \omega_r)\lambda_{qr} \\ v_{qs} &= i_{qs}R_s + \frac{d\lambda_{qs}}{dt} + \omega_s\lambda_{ds} & v_{qr} &= i_{qr}R_r + \frac{d\lambda_{qr}}{dt} + (\omega_s - \omega_r)\lambda_{dr} \\ v_{0s} &= i_{0s}R_s + \frac{d\lambda_{0s}}{dt} & v_{0r} &= i_{0r}R_r + \frac{d\lambda_r}{dt} \end{aligned} \tag{3.48}$$

The zero sequence components $v_{0s,r}$ can be removed from the system because the connection of the windings employed on an induction machine can be such that they

do not include a neutral. Applying the dq transformation (noting the removal of the zero sequence entries) to the inductance matrix **L** gives the dq equivalent inductance matrix (3.49)

$$\begin{bmatrix} \lambda_{ds} \\ \lambda_{qs} \\ \lambda_{dr} \\ \lambda_{qr} \end{bmatrix} = \begin{bmatrix} L_{ls}+L_m & 0 & L_m & 0 \\ 0 & L_{ls}+L_m & 0 & L_m \\ L_m & 0 & L_{lr}+L_m & 0 \\ 0 & L_m & 0 & L_{lr}+L_m \end{bmatrix} \begin{bmatrix} i_{ds} \\ i_{qs} \\ i_{dr} \\ i_{qr} \end{bmatrix} \tag{3.49}$$

where L_m is the magnetising inductance and L_{ls} and L_{lr} are the leakage inductances of the stator and rotor respectively. To put these into a form for use in simulation the substitution in (3.50) is made.

$$\begin{aligned} \lambda_{dm} &= L_m(i_{ds}+i_{dr}) \\ \lambda_{qm} &= L_m(i_{qs}+i_{qr}) \end{aligned} \tag{3.50}$$

Such that the equations in (3.49) become:

$$\begin{aligned} \lambda_{ds} &= L_{ls}i_{ds}+\lambda_{dm} & \lambda_{dr} &= L_{ls}i_{dr}+\lambda_{dm} \\ \lambda_{qs} &= L_{ls}i_{qs}+\lambda_{qm} & \lambda_{qr} &= L_{ls}i_{qr}+\lambda_{qm} \end{aligned} \tag{3.51}$$

Rearranging in terms of the currents (3.52), and making the substitution (3.53):

$$\begin{aligned} i_{ds} &= \frac{\lambda_{ds}-\lambda_{dm}}{L_{ls}} & i_{dr} &= \frac{\lambda_{dr}-\lambda_{dm}}{L_{lr}} \\ i_{qs} &= \frac{\lambda_{qs}-\lambda_{qm}}{L_{ls}} & i_{qr} &= \frac{\lambda_{qr}-\lambda_{qm}}{L_{lr}} \end{aligned} \tag{3.52}$$

$$L_M = \frac{1}{\frac{1}{L_{ls}}+\frac{1}{L_{lr}}+\frac{1}{L_m}} \tag{3.53}$$

The equations from (3.51)become:

$$\begin{aligned}\lambda_{dm} &= L_M\left(\frac{\lambda_{ds}}{L_{ls}} + \frac{\lambda_{dr}}{L_{lr}}\right)\\ \lambda_{qm} &= L_M\left(\frac{\lambda_{qs}}{L_{ls}} + \frac{\lambda_{qr}}{L_{lr}}\right)\end{aligned} \tag{3.54}$$

Finally for use in simulation, the original system of voltage equations must be put into integral form. This is because the Laplace transform of a pure differentiator is s, while for a pure integrator it is 1/s, therefore the gain of a differentiator is directly proportional to frequency and the gain of an integrator is inversely proportional to frequency. In other words, a differentiator is much more susceptible to high frequency noise than an integrator. Therefore integration is the preferred method of simulation [68]. Making the substitution $s = j\omega$, then:

$$\mathcal{L}\left[\frac{d}{dt}\right] = j\omega \tag{3.55}$$

$$\mathcal{L}\left[\int dt\right] = \frac{1}{j\omega} \tag{3.56}$$

Rearranging the original dq voltage equations into integral form with the fluxes forming the state variables and making the substitutions in (3.54), the four orders for the dq model are shown in (3.57).

$$\begin{aligned}\lambda_{ds} &= \int \left(v_{ds} - \frac{r_s}{L_{ls}}\left(\lambda_{ds} - \lambda_{dm}\right) + \omega_s\lambda_{qs}\right)\mathrm{d}t\\ \lambda_{qs} &= \int \left(v_{qs} - \frac{r_s}{L_{ls}}\left(\lambda_{qs} - \lambda_{qm}\right) - \omega_s\lambda_{ds}\right)\mathrm{d}t\\ \lambda_{dr} &= \int \left(v_{dr} - \frac{r_r}{L_{lr}}\left(\lambda_{dr} - \lambda_{dm}\right) + (\omega_s - \omega_r)\lambda_{qr}\right)\mathrm{d}t\\ \lambda_{qr} &= \int \left(v_{qr} - \frac{r_r}{L_{lr}}\left(\lambda_{qr} - \lambda_{qm}\right) - (\omega_s - \omega_r)\lambda_{dr}\right)\mathrm{d}t\end{aligned} \tag{3.57}$$

The system in (3.57) makes up four of the five orders with the fifth coming from

the mechanical dynamics of the system (3.58):

$$\frac{d\omega_r}{dt} = \frac{1}{J}(T_e - T_{mech} - T_{damp}) \tag{3.58}$$

Where ω_r is the angular frequency of the rotor, J is the inertia of the machine, T_e is the electromagnetic torque, T_{mech} is the mechanical input torque and T_{damp} is the damping torque. To link the dynamics of the electrical and mechanical parts of the system, the electromagnetic torque is derived. This begins by defining the instantaneous three-phase power (3.59).

$$P_{inst} = v_{as}i_{as} + v_{bs}i_{bs} + v_{cs}i_{cs} + v_{ar}i_{ar} + v_{br}i_{br} + v_{cr}i_{cr} \tag{3.59}$$

Converting this from the abc frame to the dq0 frame gives (3.60)

$$P_{in} = \frac{3}{2}\big(v_{ds}i_{ds} + v_{qs}i_{qs} + 2v_{0s}i_{0s} + v_{dr}i_{dr} + v_{qr}i_{qr} + 2v_{0r}i_{0r}\big) \tag{3.60}$$

Using equation (3.48) to substitute for the voltages in (3.60), the following equation for power is obtained:

$$\begin{aligned} P_{in} = \frac{3}{2}\Bigg[&\big(i_{ds}^2 + i_{qs}^2 + 2i_{0s}^2\big)r_s + \big(i_{dr}^2 + i_{qr}^2 + 2i_{0r}^2\big)r_r \\ &+ i_{ds}\frac{d\lambda_{ds}}{dt} + i_{qs}\frac{d\lambda_{qs}}{dt} + 2i_{0s}\frac{d\lambda_{0s}}{dt} + i_{dr}\frac{d\lambda_{dr}}{dt} + i_{qr}\frac{d\lambda_{qr}}{dt} + 2i_{0r}\frac{d\lambda_{0r}}{dt} \\ &+ \big(i_{qs}\lambda_{ds} + i_{qr}\lambda_{dr} - i_{ds}\lambda_{qs} - i_{dr}\lambda_{qr}\big)\omega_s + \big(i_{dr}\lambda_{qr} - i_{qr}\lambda_{dr}\big)\omega_r\Bigg] \end{aligned} \tag{3.61}$$

There are three distinct types of terms within (3.61) which are grouped more visibly in (3.62) - (3.64)

$$P_{loss} = \frac{3}{2}\Big[\big(i_{ds}^2 + i_{qs}^2 + 2i_{0s}^2\big)r_s + \big(i_{dr}^2 + i_{qr}^2 + 2i_{0r}^2\big)r_r\Big] \tag{3.62}$$

$$P_{inductor} = \frac{3}{2}\Big[i_{ds}\frac{d\lambda_{ds}}{dt} + i_{qs}\frac{d\lambda_{qs}}{dt} + 2i_{0s}\frac{d\lambda_{0s}}{dt} + i_{dr}\frac{d\lambda_{dr}}{dt} + i_{qr}\frac{d\lambda_{qr}}{dt} + 2i_{0r}\frac{d\lambda_{0r}}{dt}\Big] \tag{3.63}$$

$$P_{em} = \frac{3}{2}\Big[\big(i_{qs}\lambda_{ds} - i_{ds}\lambda_{qs} - i_{dr}\lambda_{qr} + i_{qr}\lambda_{dr}\big)\omega_s + \big(i_{dr}\lambda_{qr} - i_{qr}\lambda_{dr}\big)\omega_r\Big] \tag{3.64}$$

Here, P_{loss} refers to the copper losses within the windings. $P_{inductor}$ is descriptive of the energy stored within the inductance of the coils and finally P_{em} is the power associated with the electromechanical power upon which the electromagnetic torque is developed. Furthermore, by noticing that (3.65) from the relationship in (3.49):

$$i_{qs}\lambda_{ds} - i_{ds}\lambda_{qs} = i_{dr}\lambda_{qr} - i_{qr}\lambda_{dr} \tag{3.65}$$

we get,

$$P_{em} = \frac{3}{2}\big(i_{dr}\lambda_{qr} - i_{qr}\lambda_{dr}\big)\omega_r \tag{3.66}$$

Therefore, T_e is found by dividing (3.66) by the mechanical speed of the induction machine ω_m:

$$T_e = \frac{P_{em}}{w_m} = \frac{P}{2}\frac{P_{em}}{w_r} \tag{3.67}$$

since,

$$\omega_m = \frac{2}{P}\omega_r \tag{3.68}$$

where P is the number of poles. A variety of substitutions for torque can be made based on the relationship between the flux linkages, some of which are presented in (3.69) such that it is possible to calculate electromagnetic torque in a number of ways based on what variables are easily available within the simulation.

$$\begin{aligned} T_e &= \left(\frac{P}{2}\right)\left(\frac{3}{2}\right)\big(i_{dr}\lambda_{qr} - i_{qr}\lambda_{dr}\big) \\ &= \left(\frac{P}{2}\right)\left(\frac{3}{2}\right)\big(i_{qs}\lambda_{ds} - i_{ds}\lambda_{qs}\big) \\ &= \left(\frac{P}{2}\right)\left(\frac{3}{2}\right)\big(i_{qs}\lambda_{dm} - i_{ds}\lambda_{qm}\big) \\ &= \left(\frac{P}{2}\right)\left(\frac{3}{2}\right)\big(i_{qr}\lambda_{dm} - i_{dr}\lambda_{qm}\big) \\ &= \left(\frac{P}{2}\right)\left(\frac{3}{2}\right)L_m\big(i_{qs}i_{dr} - i_{ds}i_{qr}\big) \end{aligned} \tag{3.69}$$

3.3.1 Equivalent Steady-State Circuit

The power flows within the stator, rotor and mechanical subsystem of the DFIM can be assessed by using an equivalent circuit approach. Applying Kirchhoff's law to figure

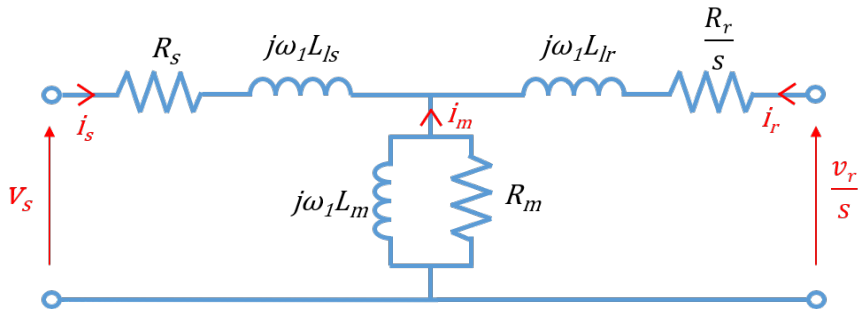

Figure 3.22: DFIG equivalent circuit

3.22 gives the voltage equations as in (3.72).

$$v_s = R_s i_s + j\omega_1 L_{ls} i_s + j\omega_1 L_m (i_s + i_r + i_m) \tag{3.70}$$

$$\frac{v_r}{s} = \frac{R_r}{s} i_r + j\omega_1 L_{lr} i_r + j\omega_1 L_m (i_s + i_r + i_m) \tag{3.71}$$

$$0 = R_m i_m + j\omega_1 L_m (i_s + i_r + i_m) \tag{3.72}$$

Substitutions can be made for the airgap flux λ_m, stator flux λ_s and rotor flux λ_r to give:

$$\lambda_m = L_m (i_s + i_r + i_m) \tag{3.73}$$

$$\lambda_s = L_{ls} i_s + L_m (i_s + i_r + i_m) = L_{ls} i_s + \lambda_m \tag{3.74}$$

$$\lambda_r = L_{lr} i_r + L_m (i_s + i_r + i_m) = L_{lr} i_r + \lambda_m \tag{3.75}$$

The voltage equations describing the equivalent circuit now become:

$$v_s = R_s i_s + j\omega_1 \lambda_s \tag{3.76}$$

$$\frac{v_r}{s} = \frac{R_r}{s} i_r + j\omega_1 \lambda_r \tag{3.77}$$

$$0 = R_m i_m + j\omega_1 \lambda_m \tag{3.78}$$

The apparent power of the stator and rotor, S_s and S_r respectively, are defined in

(3.79):

$$\begin{aligned} S_s &= 3v_s i_s^* \\ S_r &= 3v_r i_r^* \end{aligned} \tag{3.79}$$

Substituting v_s into (3.79) yields:

$$S_s = 3R_s|i_s|^2 + 3j\omega_1 L_{ls}|i_s|^2 + 3j\omega_1 \lambda_m i_s^* \tag{3.80}$$

Introducing the expression for i_s^*:

$$i_s^* = \frac{\lambda_m^*}{L_m} - i_r^* - i_m^* \tag{3.81}$$

We get the stator apparent power as:

$$S_s = 3R_s|i_s|^2 + 3j\omega_1 L_{ls}|i_s|^2 + 3j\omega_1 \frac{|\lambda_m|^2}{L_m} - 3j\omega_1 \lambda_m i_r^* + 3R_m|i_m|^2 \tag{3.82}$$

Similarly for S_r:

$$S_r = 3R_r|i_r|^2 + 3sj\omega_1 L_{lr}|i_r|^2 + 3sj\omega_1 \lambda_m i_r^* \tag{3.83}$$

Stator and rotor power can now be expressed by (3.84) and (3.84) respectively:

$$\begin{aligned} P_s &= \mathrm{Re}[S_s] \\ &= 3R_s|i_s|^2 + 3\omega_1 \mathrm{Im}[\lambda_m i_r^*] + 3R_m|i_m|^2 \end{aligned} \tag{3.84}$$

$$\begin{aligned} P_r &= \mathrm{Re}[S_r] \\ &= 3R_r|i_r|^2 - 3s\omega_1 \mathrm{Im}[\lambda_m i_r^*] \end{aligned} \tag{3.85}$$

Assuming the resistive and magnetising losses to be small, the above equations

simplify to:

$$P_s \approx 3\omega_1 \mathrm{Im}[\lambda_m i_r^*] \tag{3.86}$$

$$P_r \approx -3s\omega_1 \mathrm{Im}[\lambda_m i_r^*] \tag{3.87}$$

The mechanical power is given by the sum of stator and rotor power:

$$\begin{aligned} P_m &= P_s + P_r \\ &= 3\omega_1 \mathrm{Im}[\lambda_m i_r^*] - 3s\omega_1 \mathrm{Im}[\lambda_m i_r^*] \\ &= 3\omega_1(1-s)\mathrm{Im}[\lambda_m i_r^*] \\ &= 3\omega_r \mathrm{Im}[\lambda_m i_r^*] \end{aligned} \tag{3.88}$$

From this, the electromagnetic torque can be found by dividing mechanical power with rotor speed:

$$\begin{aligned} T_e &= \frac{P_m}{\omega_m} \\ &= \frac{p}{\omega_r} 3\omega_r \mathrm{Im}[\lambda_m i_r^*] \\ &= 3p\mathrm{Im}[\lambda_m i_r^*] \end{aligned} \tag{3.89}$$

Ignoring resistive losses, the stator, rotor and mechanical power can be related as:

$$P_s = \frac{\omega_1}{\omega_r} P_m = \frac{P_m}{(1-s)} \tag{3.90}$$

$$P_r = -\frac{s\omega_1}{\omega_r} P_m = -\frac{sP_m}{(1-s)} \tag{3.91}$$

Therefore:

$$P_r \approx -sP_s \tag{3.92}$$

The factor $1/(1-s)$ in (3.90) causes the mechanical power to be higher for positive slips than for negative slips. This effect is shown by plotting the graphs of $y = 1/(1-s)$ and $y = -s/(1-s)$ in figure 3.23 which demonstrates the slip-dependent factors that

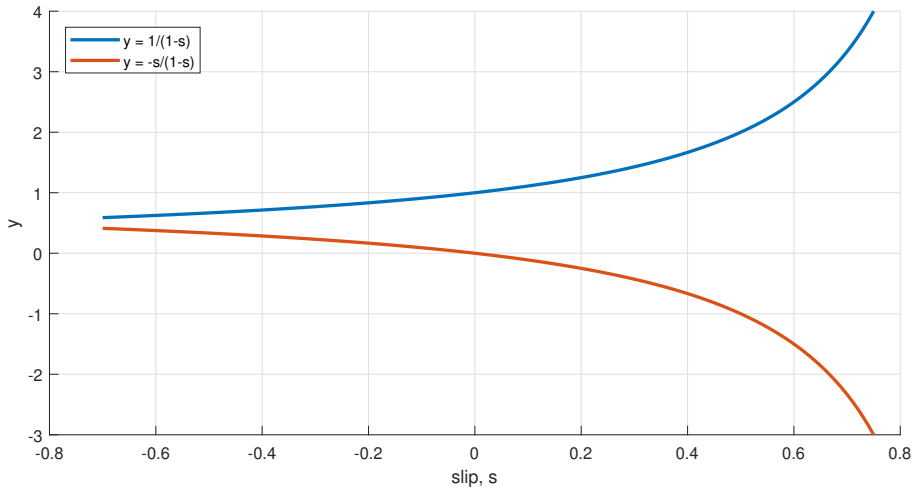

Figure 3.23: Slip factor showing the increased values for positive slips

affect stator and rotor power.

3.3.2 5th Order Model Summary

The fifth order model is presented in (3.93).

$$\begin{aligned}
\lambda_{ds} &= \int \left(v_{ds} - \frac{r_s}{L_{ls}}\left(\lambda_{ds} - \lambda_{dm}\right) + \omega_s \lambda_{qs}\right)\mathrm{d}t \\
\lambda_{qs} &= \int \left(v_{qs} - \frac{r_s}{L_{ls}}\left(\lambda_{qs} - \lambda_{qm}\right) - \omega_s \lambda_{ds}\right)\mathrm{d}t \\
\lambda_{dr} &= \int \left(v_{dr} - \frac{r_r}{L_{lr}}\left(\lambda_{dr} - \lambda_{dm}\right) + (\omega_s - \omega_r)\lambda_{qr}\right)\mathrm{d}t \\
\lambda_{qr} &= \int \left(v_{qr} - \frac{r_r}{L_{lr}}\left(\lambda_{qr} - \lambda_{qm}\right) - (\omega_s - \omega_r)\lambda_{dr}\right)\mathrm{d}t \\
\omega_r &= \frac{1}{J}\int \left(T_e - T_{mech} - T_{damp}\right)\mathrm{d}t
\end{aligned} \tag{3.93}$$

3.3.3 Model Performance

A short analysis of the fifth order model of an induction machine is presented in this section using the per-unit parameters provided in table 3.4, where S_b is the rated power of the machine, v_s is the RMS phase-to-phase voltage and H is the per-unit inertia of the machine. For simplicity, the rotor of the machine is short-circuit by connected the three phases together.

Table 3.4: Induction machine parameters

Parameter	Value	Parameter	Value
S_b	2 MW	L_{ls}	0.09241 PU
v_s	690 V	L_{lr}	0.09955 PU
R_s	0.00488 PU	L_m	3.935 PU
R_r	0.00549 PU	H	3.5 s

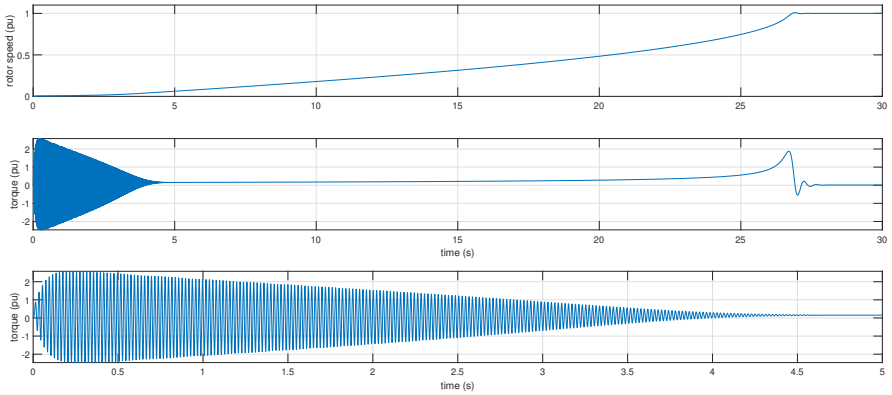

Figure 3.24: Initialisation of induction machine model. Note that the bottom plot is a zoom of the starting transient

Upon initiation of the simulation, the rotor of the machine accelerates up to the synchronous speed of 1 PU where the electromagnetic torque becomes zero. It remains at this steady state until a torque is applied. The start-up characteristics of the 5th order induction machine are shown in figure 3.24. The large starting transient which occurs due to the large inductive properties of the induction machine windings is also visible in the electromagnetic torque plot.

A positive torque represents a load and makes the machine act as a motor whereas a negative torque does the opposite and simulates generator action. This effect is shown in figure 3.25. At t = 40s a negative load torque of 0.3 PU which causes the machine to accelerate. Since the machine is being forced to speed up, the electromagnetic torque decreases to settle at the new equilibrium point. At t = 45s a positive torque representing a load is applied which causes the machine to slow down. The oscillations

present are the transients associated with a sudden change in operating conditions. In reality a machine of this size would be adjusted slowly with a predefined maximum ramp rate.

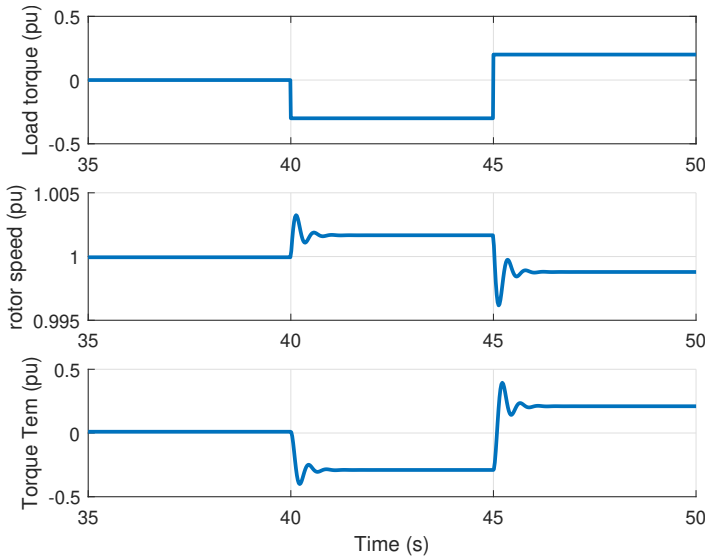

Figure 3.25: Response of induction machine model to a step change in load

3.4 DFIM Control

The doubly-fed induction machine is a common wind turbine generator configuration which allows variable speed operation by manipulating the currents in the rotor. It is also an integral part of the PFEC and acts as the motor which drives the shaft of the rotary transformer. This section introduces the control of the DFIM which is also applicable to the control of the PFEC with a few changes to the controller parameters.

The DFIM consists of a wound rotor induction machine and a partially rated converter (PRC) in the form of a B2B-VSC. By interfacing the B2B-VSC with the DFIM, independent control over the direct and quadrature components of the current is achieved, allowing simultaneous commands relating to active and reactive current to be sent. The rotor side converter (RSC) is responsible for supplying current to the rotor with the key control variables being rotor speed ω_r, electromagnetic torque T_e, active power P_s and reactive power Q_s, depending on the type of control strategy in

operation. The grid side converter (GSC) is designed to maintain the DC link voltage v_{dc} by supplying active current from the AC network but can also provide reactive power support Q_{gsc} via the independent q-axis. In this section, each of those control variables is presented and derived for dynamic simulation.

To allow the independent control of active and reactive currents, a dq-reference frame is required to generate the orthogonal components. The dq-axis is aligned such that:

$$v_{ds} = \hat{v_s} \qquad\qquad v_{qs} = 0 \tag{3.94}$$

where $\hat{v_s}$ is the stator peak phase voltage which is also taken as the base. Since the current lags the voltage by 90° and flux is proportional to current, then (3.95) is also true, with $\hat{\lambda_s}$ as the stator peak phase flux linkage.

$$\lambda_{ds} = 0 \qquad\qquad \lambda_{qs} = -\hat{\lambda_s} \tag{3.95}$$

3.4.1 Rotor Current Control

Switching pulses from the IGBTs within the converter rely on a pulse-width modulator which takes voltage as an input and modulation index as an output. The relationship between this voltage and the rotor currents is then used in the control of the current. The rotor voltage equations were presented in (3.48) but are defined again here with v_{dr} isolated as in (3.96).

$$\begin{aligned} v_{dr} &= R_r i_{dr} + \frac{d\lambda_{dr}}{dt} - (\omega_s - \omega_r)\lambda_{qr} \\ v_{qr} &= R_r i_{qr} + \frac{d\lambda_{qr}}{dt} + (\omega_s - \omega_r)\lambda_{dr} \end{aligned} \tag{3.96}$$

By treating the $(\omega_s - \omega_r)\lambda_{qr}$ term as a disturbance it can be removed from the equation, meaning that it is not present in the design of the PI controller and can only

be compensated for. Making the substitution for λ_{dr} from (3.49) gives:

$$v_{dr} = R_r i_{dr} + \frac{d}{dt}\left[L_m i_{ds} + (L_{lr} + L_m) i_{dr}\right] \tag{3.97}$$

The relationship between i_{ds} and i_{dr} is found by substituting (3.95) into the expression for λ_{ds} from (3.49):

$$\lambda_{ds} = (L_{ls} + L_m) i_{ds} + L_m i_{dr}$$

using (3.95): $$0 = (L_{ls} + L_m) i_{ds} + L_m i_{dr}$$

such that, $$i_{ds} = \frac{-L_m i_{dr}}{L_{ls} + L_m} \tag{3.98}$$

Using the substitution $L_{ss} = L_{ls} + L_m$ (and similarly $L_{rr} = L_{lr} + L_m$ for the rotor circuit), the relationship between i_{ds} and i_{dr} becomes:

$$i_{ds} = \frac{-L_m i_{dr}}{L_{ss}} \tag{3.99}$$

Similarly for i_{qr}, we have:

$$\lambda_{qs} = L_{ss} i_{qs} + L_m i_{qr}$$

such that $$i_{qs} = \frac{\lambda_{qs} - L_m i_{qr}}{L_{ss}} \tag{3.100}$$

Substituting L_{ss}, L_{rr} and i_{ds} into (3.97) gives the d-axis rotor voltage equation (3.101)

$$v_{dr} = R_r i_{dr} + \frac{d}{dt}\left[\frac{L_{ss} L_{rr} i_{dr} - L_m^2 i_{dr}}{L_{ss}}\right] \tag{3.101}$$

This process is repeated for the q-axis voltage v_{qr} to give a relationship between

the q-components of rotor voltage and current:

$$\begin{aligned} v_{qr} &= R_r i_{qr} + \frac{d\lambda_{qr}}{dt} \\ &= R_r i_{qr} + \frac{d}{dt}\left[L_m i_{qs} + L_{rr} i_{qr}\right] \\ &= R_r i_{qr} + \frac{d}{dt}\left[\left(\frac{L_m \lambda_{qs} - L_m^2 i_{qr}}{L_{ss}}\right) + L_{rr} i_{qr}\right] \\ &= R_r i_{qr} + \frac{d}{dt}\left[\frac{L_m \lambda_{qs}}{L_{ss}}\right] + \frac{d}{dt}\left[\frac{L_{ss} L_{rr} i_{qr} - L_m^2 i_{qr}}{L_{ss}}\right] \end{aligned} \tag{3.102}$$

From (3.95) it is seen that λ_{qs} is a constant such that $\frac{d\lambda_{qs}}{dt} = 0$, giving:

$$v_{qr} = R_r i_{qr} + \frac{d}{dt}\left[\frac{L_{ss} L_{rr} i_{qr} - L_m^2 i_{qr}}{L_{ss}}\right] \tag{3.103}$$

Equations (3.101) and (3.103) share the same form hence the transfer function from i_{dr} to v_{dr} is similar to that from i_{qr} to v_{qr} (3.104):

$$P_{ir}(s) = \frac{i_{dr}(s)}{v_{dr}(s)} = \frac{i_{qr}(s)}{v_{qr}(s)} = \frac{L_{ss}}{s(L_{ss} L_{rr} - L_m^2) + R_r L_{ss}} \tag{3.104}$$

(3.104) contains a stable pole at $s = \frac{-R_r L_{ss}}{(L_{ss} L_{rr} - L_m^2)}$ which can be cancelled by the zero of the PI controller. Introducing a PI controller gives the open-loop gain $\ell_{ir}(s)$ as in (3.105)

$$\begin{aligned} \ell_{ir}(s) &= C_{ir}(s) P_{ir}(s) \\ &= \frac{K_{pirsc}}{s}\left(s + \frac{K_{iirsc}}{K_{pirsc}}\right)\left[\frac{L_{ss}}{s(L_{ss} L_{rr} - L_m^2) + R_r L_{ss}}\right] \end{aligned} \tag{3.105}$$

where C_{ir} is the transfer function of the PI controller. Making the substitution

$K_{iirsc}/K_{pirsc} = \dfrac{R_r L_{ss}}{(L_{ss}L_{rr} - L_m^2)}$ gives:

$$\begin{aligned}\ell_{ir}(s) &= \frac{K_{pirsc}}{s}\left(\frac{s(L_{ss}L_{rr} - L_m^2) + R_r L_{ss}}{L_{ss}L_{rr} - L_m^2}\right)\left[\frac{L_{ss}}{s(L_{ss}L_{rr} - L_m^2) + R_r L_{ss}}\right] \\ &= \frac{K_{pirsc}}{s}\left(\frac{L_{ss}}{L_{ss}L_{rr} - L_m^2}\right) \\ &= \frac{\alpha_{irsc}}{s} \end{aligned} \tag{3.106}$$

with the tuning parameters K_{pirsc}, K_{iirsc} defined as:

$$K_{pirsc} = \left(\frac{L_{ss}L_{rr} - L_m^2}{L_{ss}}\right)\alpha_{irsc}; \qquad K_{iirsc} = R_r\alpha_{irsc} \tag{3.107}$$

To improve disturbance rejection, an internal feedback loop can be added in much the same way as for the back-to-back DC voltage controller. The derivation follows the same process as outlined in section 3.2.6, such that the new proportional and integral gains together with the internal feedback loop gain are given in (3.108).

$$\begin{aligned} &K_{pirsc} = \left(\frac{L_{ss}L_{rr} - L_m^2}{L_{ss}}\right)\alpha_{irsc}; \qquad K_{iirsc} = \alpha_{irsc}\big(R_r + G_{irsc}\big) \\ \text{where} \qquad &G_{irsc} = \frac{-R_r L_{ss} + \big(L_{rr}L_{ss} - L_m^2\big)\alpha_{irsc}}{L_{ss}} \end{aligned} \tag{3.108}$$

The system now has a closed-loop gain of $\dfrac{\alpha_{irsc}}{s + \alpha_{irsc}}$. The selection of α_{irsc} defines the speed of response of the system based on (3.20) and should be set as fast as the controller will allow, which is typically around 2ms [67]. A layout of the controller is presented in figure 3.26.

Note that to improve model performance, particularly during start-up, an anti-windup scheme is fitted just before the integrator If the controller saturates then the feedback loop breaks causing an accumulation of the error in the integrator. To prevent this an anti-wind-up scheme is implemented using the back-calculation method which supplies a supplementary feedback path around the integrator. This loop activates only during saturation and has the effect of resetting the integrator such that no more error

accumulates. This method is shown by the K_{sat} term in figure 3.26.

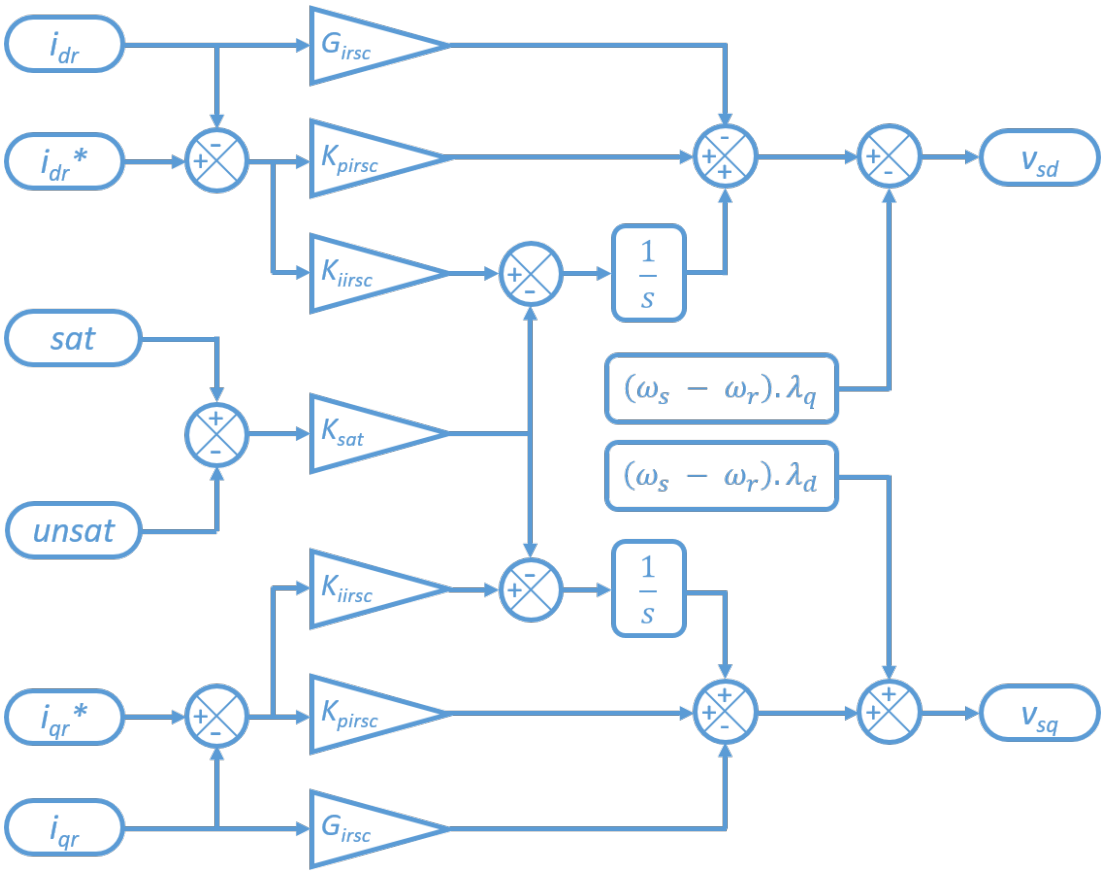

Figure 3.26: RSC dq-current controller showing additional internal feedback terms and anti-windup

3.4.2 Torque Control

The reference currents processed by the RSC can be defined from a number of ways, one of which is from a reference torque. When the machine is held at a constant speed, a torque demand can be used to transfer torque through the machine. The requirement is then to find a transfer function linking electromagnetic torque with rotor current. Equation (3.69) shows that that electromagnetic torque T_e is proportional to the stator

d-current i_{ds}:

$$\begin{aligned} T_e &= \frac{3}{2}p\big(i_{qs}\lambda_{ds} - i_{ds}\lambda_{qs}\big) && (3.109)\\ &= -\frac{3p}{2}i_{ds}\lambda_{qs} && (\text{since } \lambda_{ds} = 0 \text{ from } (3.95)) \end{aligned}$$

Using the relationship linking i_{ds} with i_{dr} in (3.99), electromagnetic torque can be related to the rotor currents allowing the RSC to control this parameter,

$$T_e = \frac{3p}{2}\left(\frac{L_m\lambda_{qs}}{L_{ss}}i_{dr}\right) \tag{3.110}$$

therefore,

$$i_{dr} = T_e\frac{2}{3p}\left(\frac{L_{ss}}{L_m\lambda_{qs}}\right) \tag{3.111}$$

This algebraic relationship between electromagnetic torque and rotor currents can be implemented directly, however an integral controller can be introduced to eliminate the errors associated with measuring λ_{qs}. Let P_T be the plant represented by the transfer function from T_e to i_{dr} and let C_T be the integral controller, then the open loop gain of the system $\ell_T(s)$ becomes:

$$\begin{aligned} \ell_T(s) &= C_T P_T \\ &= \left[\frac{K_{iT}}{s}\right]\left(\frac{3p}{2}\frac{L_m\lambda_{qs}}{L_{ss}}\right) \\ &= \frac{\alpha_T}{s} \end{aligned} \tag{3.112}$$

where the integral gain the controller is given as $K_{iT} = \dfrac{2L_{ss}}{3pL_m}\alpha_T$ with α_T the bandwidth of the system. The corresponding block layout for this controller is shown in figure 3.27.

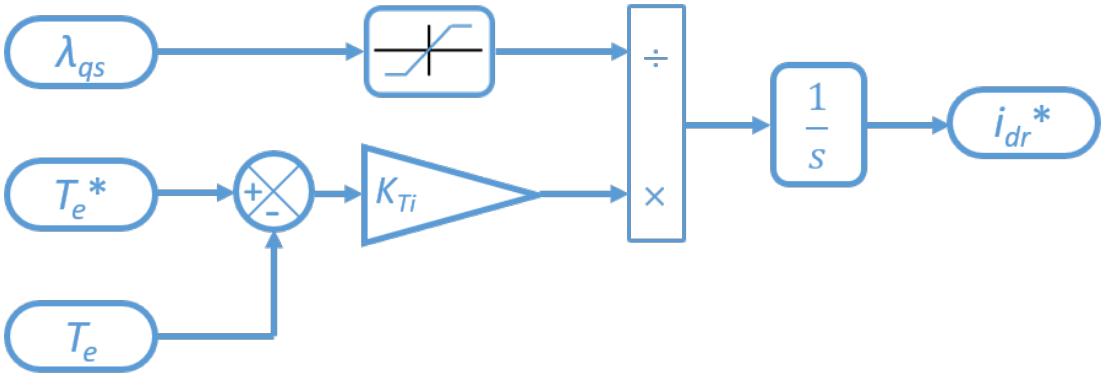

Figure 3.27: Control design of torque loop

3.4.3 Rotor Speed Control

Instead of controlling the torque of the machine, an additional step can be made to control the rotor speed via the rotor d-currents. This is the dominant control technique within the PFEC as the the DFIM must maintain the rotor speed of the RT at the correct slip to allow the interconnection of the two networks.

The mechanical system linking rotor speed to electromagnetic torque and hence rotor current is defined by (3.58). By treating T_{mech} as a disturbance it can be removed from the tuning process giving the rotor speed as in (3.113)

$$\begin{aligned} \frac{d\omega_r}{dt} &= \frac{1}{J}(T_e - T_{damp}) \\ &= \frac{1}{J}(T_e - B\omega_r) \end{aligned} \tag{3.113}$$

where B is the damping constant of the system. The transfer function from ω_r to T_e representing the plant dynamics is defined as $P_\omega(s)$ and given in (3.114),

$$P_\omega(s) = \frac{\omega_r(s)}{T_e(s)} = \frac{1}{Js + B} \tag{3.114}$$

which has a pole at $s = -B/J$. This can be cancelled with a PI controller, C_ω,

using the modulus optimum technique:

$$\begin{aligned}\ell_\omega(s) &= C_\omega P_\omega \\ &= \left(\frac{1}{Js+B}\right)\frac{K_{p\omega}}{s}\left(s+\frac{K_{i\omega}}{K_{p\omega}}\right) \\ &= \frac{K_{p\omega}}{Js} \\ &= \frac{\alpha_\omega}{s}\end{aligned} \tag{3.115}$$

with tuning parameters as in (3.116):

$$K_{p\omega} = J\alpha_\omega; \qquad\qquad K_{i\omega} = B\alpha_\omega \tag{3.116}$$

Note that since the damping constant B is typically small, the integral gain $K_{i\omega}$ is also small which could lead to steady-state errors. To avoid this, an additional internal feedback term is required which follows the same process as before.

The open-loop transfer function of the new plant dynamics is given in (3.117) and contains a pole at $s = -(B + G_\omega)/J$ which can be cancelled by a PI controller.

$$P'_\omega(s) = \frac{1}{Js + B + G_\omega} \tag{3.117}$$

where G_ω is the gain of the internal feedback term. Adding a PI controller gives the open-loop transfer function which can be tuned using the same methods as before.

$$\begin{aligned}\ell'_\omega(s) &= \left(\frac{1}{Js+B+G_\omega}\right)\frac{K_{p\omega}}{s}\left(s+\frac{K_{i\omega}}{K_{p\omega}}\right) \\ &= \frac{K_{p\omega}}{Js} \\ &= \frac{\alpha_\omega}{s}\end{aligned} \tag{3.118}$$

$$\implies \qquad L'_\omega(s) = \frac{\alpha_\omega}{s+\alpha_\omega} \tag{3.119}$$

where $\ell'_\omega(s)$ and $L_\omega(s)$ are the open loop and closed loop gains respectively, with

tuning parameters defined in (3.120):

$$K_{p\omega} = J\alpha_\omega \qquad\qquad K_{i\omega} = \alpha_\omega(B + G_\omega) \tag{3.120}$$

The value of G_ω is determined by setting the bandwidth of the closed loop transfer function equal to the same as the rest of the system. That is:

$$L'_\omega(s) = \frac{P_\omega(s)G_\omega}{1 + P_\omega(s)G_\omega} = \frac{\alpha_\omega}{s + \alpha_\omega} \tag{3.121}$$

which gives $G_\omega = J\alpha_\omega - B$. The output of the PI controller is now equal to the electromagnetic torque which can be converted into rotor current using (3.111). The relationship between rotor speed and rotor current is shown in block form in figure 3.28.

Also present in figure 3.28 is an anti-windup scheme designed to avoid the negative effects associated with controller saturation.

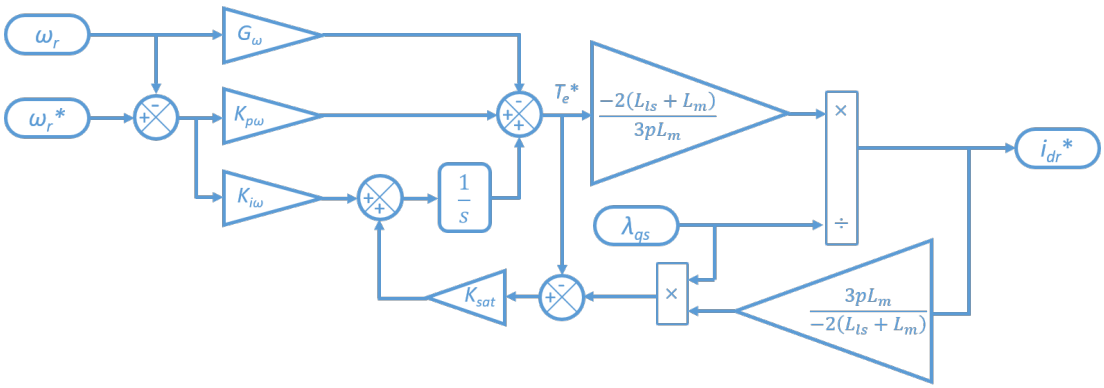

Figure 3.28: Rotor speed loop

The response of the rotor speed controller to a series of step changes in reference signal is demonstrated in figure 3.29. The plot exhibits a smooth, first-order transition between the set-points in both the positive and negative direction showing that proper tuning of the controller has been achieved.

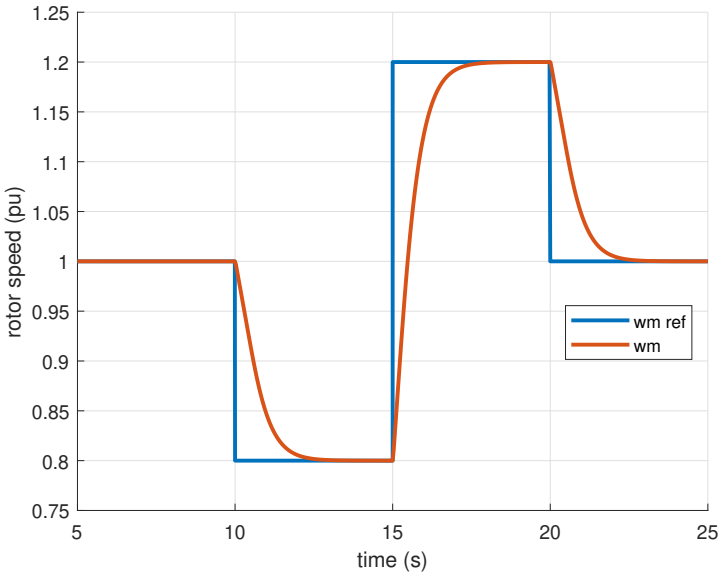

Figure 3.29: Rotor speed controller performance

3.4.4 RSC Reactive Power Control

Everything so far has focused on the manipulation of the rotor d-currents but the rotor q-currents are just as easily controllable and can be used for reactive power control in the rotor circuit. This additional functionality allows the DFIM and hence the PFEC to fulfil grid codes associated with voltage levels which are specified in any connection agreements by the TSO. Reactive power control also enables the DFIM to contribute to the total reactive power compensation requirements to either offset the large capacitance of the transmission line or the large inductance associated with the windings.

Although a detailed study into reactive power flows throughout the PFEC is not included in this work, the control scheme for q-current control is still derived here in full.

Reactive power must first be written in terms of the q-component of the rotor

current:

$$Q_s = \frac{3}{2}(v_{ds}i_{qs} - v_{qs}i_{dr}) \tag{3.122}$$
$$= \frac{3}{2}v_{ds}i_{qs} \tag{3.123}$$
$$= \frac{3}{2}v_{ds}\left(\frac{\lambda_{qs} - L_m i_{qr}}{L_{ss}}\right) \tag{3.124}$$

Rearranging in terms of i_{qr}:

$$i_{qr} = \left(\frac{3v_{ds}\lambda_{qs} - 2Q_s L_{ss}}{2L_{ss}}\right)\left(\frac{2}{3v_{ds}}\right) \tag{3.125}$$

The equation relating Q_s and i_{qr} in (3.125) can be implemented directly or it can be combined with an integral component to eliminate the errors associated with measuring λ_{qs}. The transfer function from Q_s to i_{qr} is given as:

$$\frac{i_{qr}}{Q_s} = \frac{2}{3}\left(\frac{L_{ss}}{v_{ds}\lambda_{qs} - L_m v_{ds}}\right) \tag{3.126}$$

An integral controller C_{Qs} can be introduced, giving the open-loop gain of the system:

$$\begin{aligned}\ell_{Qs}(s) &= C_{Qs}(s)P_{Qs} \\ &= \frac{K_{iQs}}{s}\frac{2}{3}\left(\frac{L_{ss}}{v_{ds}\lambda_{qs} - L_m v_{ds}}\right) \\ &= \frac{\alpha_{Qs}}{s}\end{aligned} \tag{3.127}$$

with tuning parameter K_{iQs} given in (3.128).

$$K_{iQs} = \frac{2}{3}\left(\frac{v_{ds}\big(\lambda_{qs} - L_m\big)}{L_{ss}}\right)\alpha_{Qs} \tag{3.128}$$

This relationship is shown in block form within Simulink in figure 3.30.

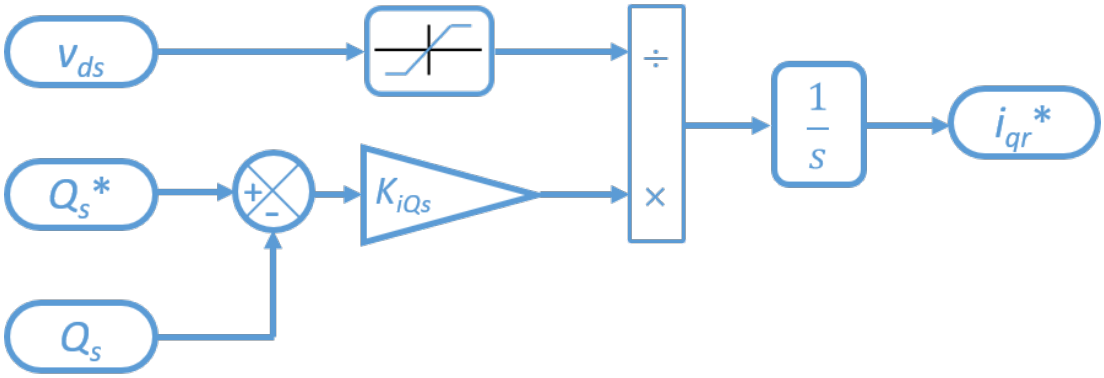

Figure 3.30: Reactive power loop

3.4.5 GSC Current Control

The block diagram as displayed in Simulink is shown in figure 3.31 which is identical to the VSC model described in section 3.2.6.1 except for the change of nomenclature of the PI controller variables and the addition of the internal feedback loop and saturation terms to improve model performance.

3.4.6 GSC DC Voltage Control

Likewise, the current reference required for maintaining the DC link is found via the same method described in section 3.2.6 and is shown in figure 3.32 with saturation.

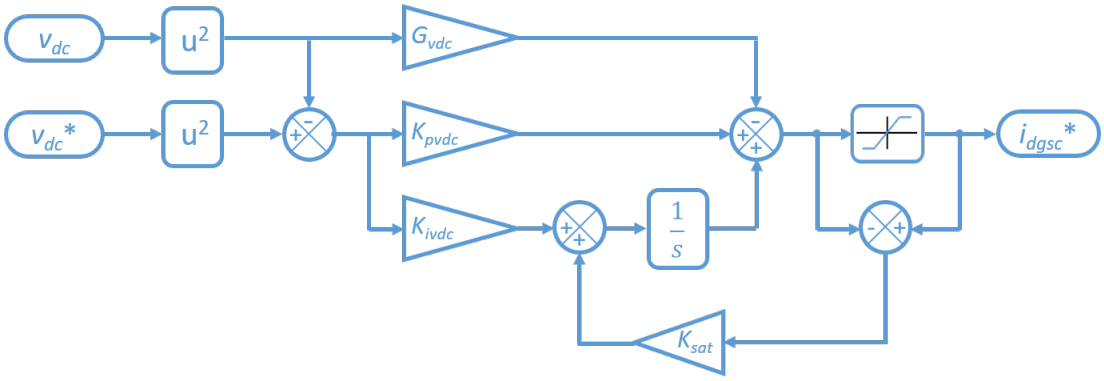

Figure 3.32: GSC DC voltage controller

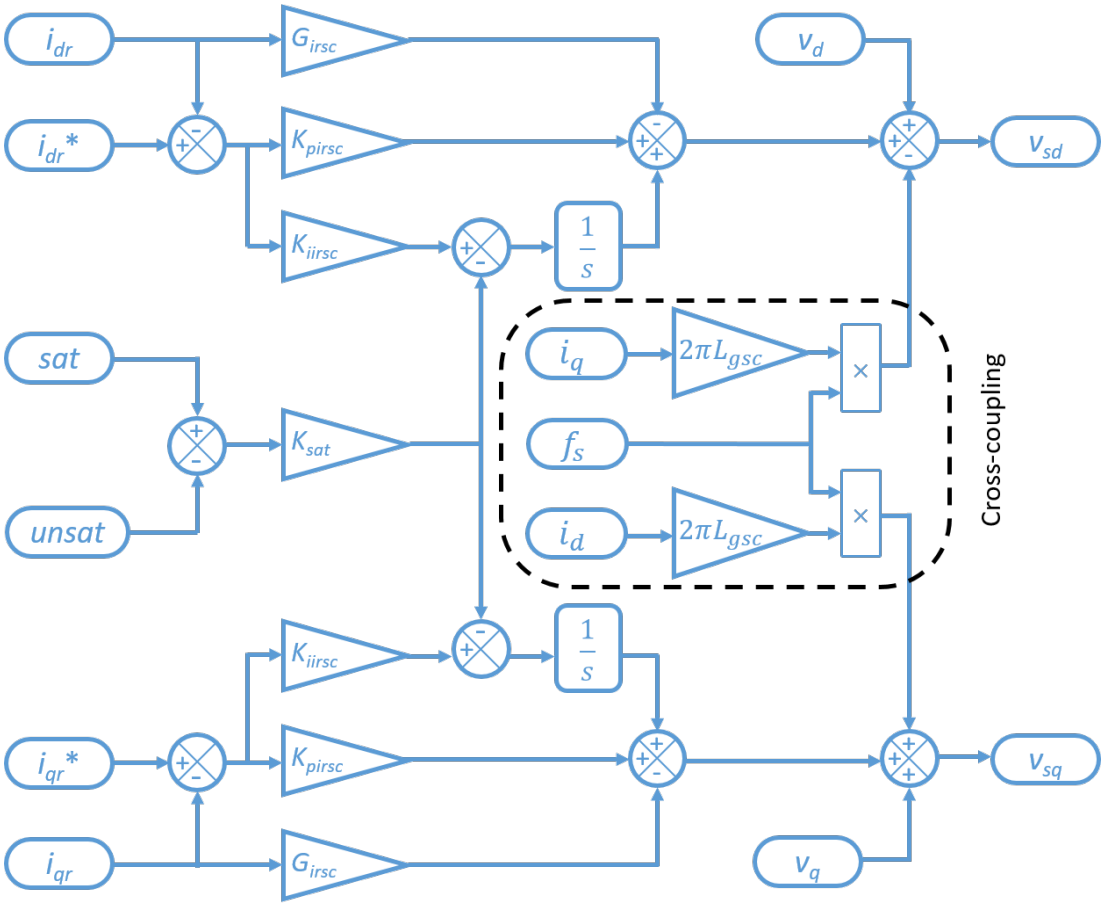

Figure 3.31: GSC current controller

3.4.7 GSC Reactive Power Control

Reactive power can be supplied or absorbed on demand to help improve the power quality of the network. By supplying or absorbing q-current, the GSC is able to have a small effect on maintaining the grid voltage which enables the compliance of certain grid codes. Reactive power is given by:

$$\begin{aligned} Q_{gsc} &= \frac{3}{2}(v_{ds}i_{qs} - v_{qs}i_{ds}) \\ &= \frac{3v_{ds}i_{qs}}{2} \end{aligned} \tag{3.129}$$

such that

$$i_{qs} = Q_{gsc}\frac{2v_{ds}}{3} \tag{3.130}$$

This equation shows that reactive power is directly proportional to q-current. Equation (3.130) can be implemented directly or it can be combined with an integral term to compensate for errors when measuring v_{ds}. The transfer function from Q_{gsc} to i_{qs} is:

$$P_{Qgsc} = \frac{i_{qs}}{Q_{gsc}} = \frac{2v_{ds}}{3} \tag{3.131}$$

Introducing an integral term gives the open loop function:

$$\begin{aligned} \ell_{Qgsc}(s) &= C_{Qgsc} P_{Qgsc} \\ &= \frac{K_{Qgsc}}{s} \frac{2v_{ds}}{3} \\ &= \frac{\alpha_{Qgsc}}{s} \end{aligned}$$

where $$K_{Qgsc} = \frac{3\alpha_{Qgsc}}{2v_{ds}} \tag{3.132}$$

This configuration is shown in block diagram form in figure 3.33.

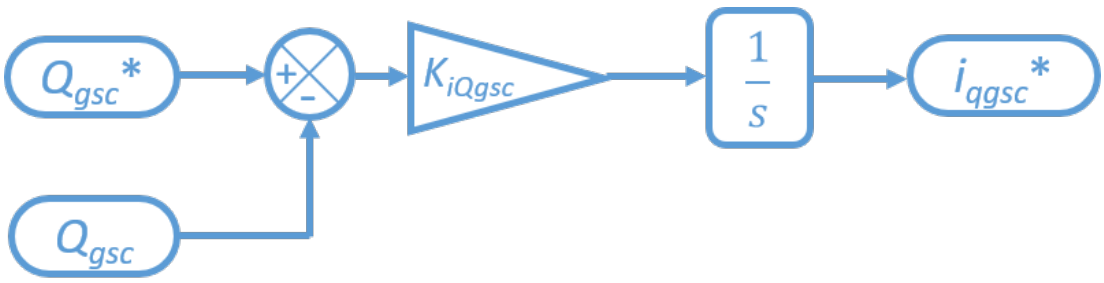

Figure 3.33: GSC reactive power control

The reactive power controller is now tested to verify that it can handle switching between operating conditions. The response of the controller is demonstrated in figure 3.34 in which a step change of 0.4 PU is applied in increments before being abruptly stepped back down to zero. The plot exhibits smooth transitions between the reference signals which are characteristic of a first order system and indicative that the controller has been tuned correctly.

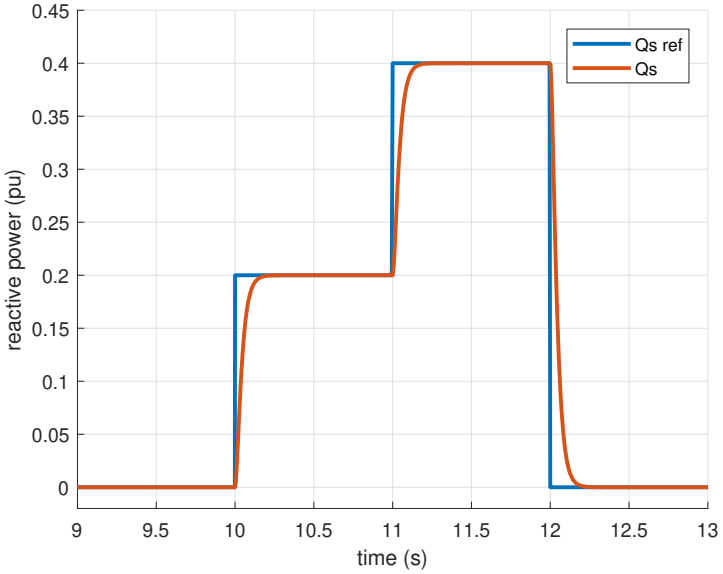

Figure 3.34: Response of GSC reactive power controller to a change in reference signal

3.5 Phase-Locked Loop

Synchronisation with the grid has has so far been a trivial exercise since the network has been represented by an ideal source and is free from frequency and voltage fluctuations. In future applications this will not be the case so a method of calculating the correct phase is required.

The phase locked loop (PLL) is one such method of synchronisation which consists of a phase detection step, a loop filter and a voltage controlled oscillator. In the synchronous frame, the phase detection is accomplished by the abc to dq transformation as the outputs are DC variables. Under the prescribed axis alignment, v_q is defined to be zero in steady state. The loop filter can then be modelled as a PI controller which works to fix the q-axis voltage at zero. The output of this regulator is the grid frequency. Finally, the voltage controlled oscillator (which in this instance is just an integrator) outputs the voltage angle of the system. This is then fed back as an input into the abc to dq transformation.

The implementation of a PLL begins by measuring the grid voltages v_a, v_b, and v_c

which are assumed to be balanced,

$$\begin{aligned} v_a &= \hat{v}\cos(\theta) \\ v_b &= \hat{v}\cos(\theta - \frac{2\pi}{3}) \\ v_c &= \hat{v}\cos(\theta + \frac{2\pi}{3}) \end{aligned} \tag{3.133}$$

where $\hat{v}$ is the amplitude of the voltage and θ is the phase angle. These voltages are first transformed to the $\alpha\beta$-reference frame to obtain v_α and v_β:

$$\begin{bmatrix} v_\alpha \\ v_\beta \end{bmatrix} = \frac{2}{3}\begin{bmatrix} 1 & -\frac{1}{2} & -\frac{1}{2} \\ 0 & \frac{\sqrt{3}}{2} & -\frac{\sqrt{3}}{2} \end{bmatrix}\begin{bmatrix} v_a \\ v_b \\ v_c \end{bmatrix} \tag{3.134}$$

which gives v_α and v_β as:

$$\begin{aligned} v_\alpha &= \frac{2}{3}\left(\hat{v}\cos\theta - \frac{1}{2}\left[\hat{v}\cos\left(\theta - \frac{2\pi}{3}\right) + \hat{v}\cos\left(\theta + \frac{2\pi}{3}\right)\right]\right) \\ &= \frac{2}{3}\left(\hat{v}\cos\theta + \frac{1}{2}\hat{v}\cos\theta\right) \\ &= \frac{2}{3}\left(\frac{3}{2}\hat{v}\cos\theta\right) \\ &= \hat{v}\cos\theta \end{aligned} \tag{3.135}$$

$$\begin{aligned} v_\beta &= \frac{2}{3}\left(\frac{\sqrt{3}}{2}\left[\hat{v}\cos\left(\theta - \frac{2\pi}{3}\right) - \hat{v}\cos\left(\theta + \frac{2\pi}{3}\right)\right]\right) \\ &= \frac{2}{3}\left(\frac{\sqrt{3}}{2}\left(\sqrt{3}\hat{v}\sin\theta\right)\right) \\ &= \hat{v}\sin\theta \end{aligned} \tag{3.136}$$

The $\alpha\beta$ voltages are then transformed to the dq-reference frame using an estimate

of the phase angle $\hat{\theta}$ from the PLL output to obtain v_d and v_q:

$$\begin{bmatrix} v_d \\ v_q \end{bmatrix} \begin{bmatrix} \cos\hat{\theta} & \sin\hat{\theta} \\ -\sin\hat{\theta} & \cos\hat{\theta} \end{bmatrix} \begin{bmatrix} v_\alpha \\ v_\beta \end{bmatrix} \tag{3.137}$$

This gives the dq voltages as:

$$\begin{aligned} v_d &= \hat{v}\big(\cos\hat{\theta}\cos\theta + \sin\hat{\theta}\sin\theta\big) \\ &= \hat{v}\cos(\hat{\theta}-\theta) \\ v_q &= \hat{v}\big(\cos\hat{\theta}\sin\theta - \sin\hat{\theta}\cos\theta\big) \\ &= -\hat{v}\sin(\hat{\theta}-\theta) \end{aligned} \tag{3.138}$$

When the PLL is locked to the grid frequency, the estimated phase angle $\hat{\theta}$ is equal to the actual phase angle θ and v_q becomes zero. A PI controller can therefore be used to regulate the value of v_q at zero such that the two frequencies are synchronised. The transfer function of the closed loop PLL is a second order function and can be written in general form as (3.139) and used to derive the controller gains [69].

$$\begin{aligned} P_{PLL}(s) &= \frac{K_{ppll}s + K_{ipll}}{s^2 + K_{ppll}s + K_{ipll}} \\ &= \frac{2\xi\omega_n s + \omega_n^2}{s^2 + 2\xi\omega_n s + \omega_n^2} \end{aligned} \tag{3.139}$$

where ξ is the damping factor, ω_n is natural frequency of the system and K_{ppll},K_{ipll} are the gains of the PI controller. The values of ξ and ω_n determine the characteristics of the system, where a trade-off is established between stability and synchronisation times. A method detailed in [70] states that K_{ppll} and K_{ipll} should be selected as follows for good performance:

$$K_{ppll} = \frac{9.2}{T_s} \qquad K_{ipll} = \frac{K_{ppll}}{T_i}$$

where, $$T_i = \frac{T_s\xi^2}{2.3} \tag{3.140}$$

where T_s is the settling time of the system. A damping factor of $\frac{\sqrt{2}}{2} \approx 0.707$ is chosen to give an overshoot of 5%. Advantages of this method are that it works on most types of grids. Disadvantages are the slow dynamic response.

3.5.1 DFIM Modes of Operation

Whether an induction machine is acting as a motor or a generator is determined by the direction of power flow in the rotor, stator and shaft respectively. Shown in figure 3.35 are the directions of power flow which govern the four-quadrant operation of a wound rotor induction machine. The four possible orientations are defined by the rotor speed (sub- or supersynchronous) and the mode of operation (motoring or generating). A motor is defined by the direction of mechanical power, deemed positive if it is pointing out of the rotor. A generator is defined by a negative mechanical power which is directed into the rotor. This naming convention of positive and negative is reversed for the direction of stator and rotor currents, where positive is always into the windings, and negative is always out of the windings. This nomenclature is demonstrated with the correct polarities in table 3.5, where for ease of reference it can be seen that a supersynchronous motor has all of its quantities greater than zero, and a supersynchronous generator has the opposite with all of its quantities less than zero.

Table 3.5: Sign convention for sub- and super- synchronous operation of motor and generator [71]

slip:	$0 < s < 1$		$s < 0$	
operation mode:	motor	generator	motor	generator
P_m	>0	<0	>0	<0
P_s	>0	<0	>0	<0
P_r	<0	>0	>0	<0

The sign convention often differs between sources with some authors preferring to use the version in (3.141), [72] [73] while others opt for the version in (3.142) [74] [71]. Depending on which swing equation is used, a negative T_e arising from a positive i_{dr} (into the rotor) would either accelerate or decelerate the machine. The swing convention adopted in this work is that in (3.141), where a negative T_e causes a deceleration of

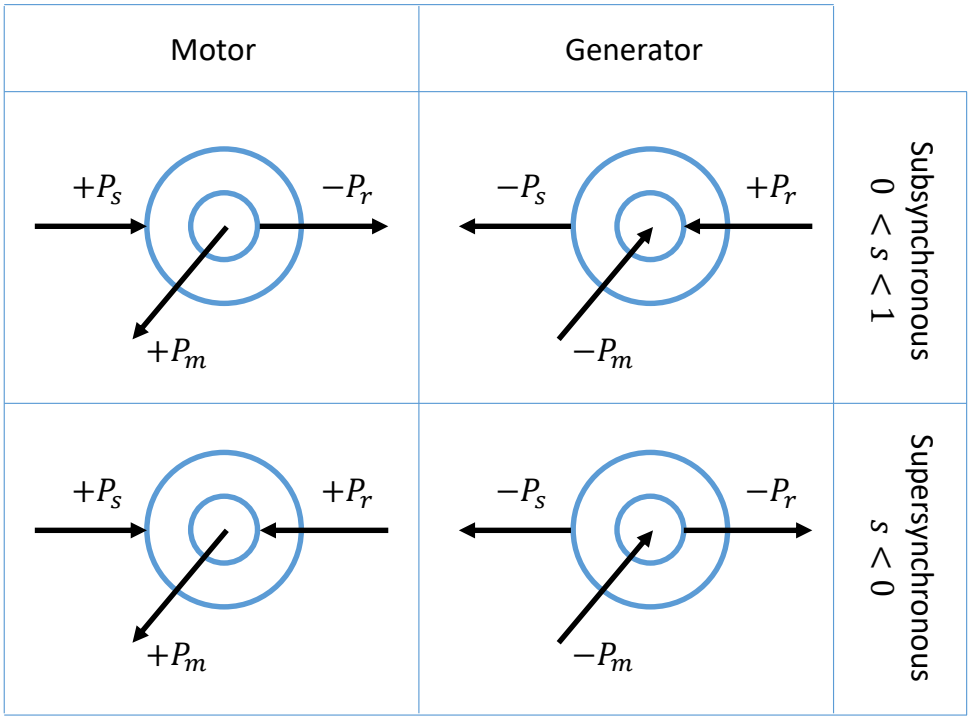

Figure 3.35: Direction of power flow for the four quadrants of an induction machine. Supersynchronous motor shows the positive sign convention for P_s, P_r and P_m

rotor speed.

$$\frac{d\omega_m}{dt} = \frac{1}{H}(T_e - T_m) \tag{3.141}$$

$$\frac{d\omega_m}{dt} = \frac{1}{H}(T_m - T_e) \tag{3.142}$$

To validate the modes of operation of a DFIM, a simple simulation of a DFIM with a back-to-back converter with standard control over the d- and q-currents of the rotor and the DC voltage is presented to evidence the modes of operation presented in figure 3.35. A schematic diagram of the simulation is presented in figure 3.36.

The results of the subsynchronous simulation is shown in figure 3.37. The machine is set to operate in subsynchronous mode by setting the initial rotor speed to provide a slip of 1/3. During the simulation the DFIM is not supplied with any mechanical torque implying that any artificial change of rotor currents produced by the RSC will

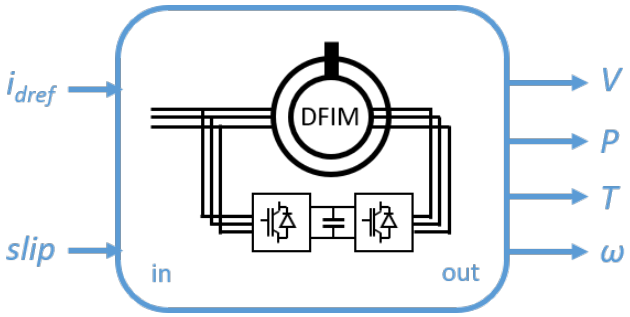

Figure 3.36: Schematic of simulation to validate DFIM modes of operation. Inputs are d-current and slip; outputs are DC voltage, stator power, electromagnetic torque and rotor speed respectively.

be reflected as a production of electromagnetic torque that modifies the rotor speed. At the start of the simulation the rotor currents are set to zero, then at t = 15 seconds the d-axis reference current of the RSC $i_{dr_{ref}}$ is stepped up to +0.1 PU_{DFIM} and at t = 20 seconds $i_{dr_{ref}}$ it is reduced to -0.1 PU_{DFIM}.

To avoid confusion with sign conventions the voltage of the DC link has been provided along with the direction of rotor currents. This is because v_{dc} provides an unambiguous description of the power flow in the rotor circuit. If v_{dc} decreases, energy is being taken from the DC link implying that currents are flowing away from the RSC and towards the rotor. If v_{dc} increases, currents are flowing into the DC link and away from the rotor.

When a positive $i_{dr_{ref}}$ command is sent, v_{dc} drops implying that energy is being taken from the RSC and sent to the rotor. Stator power becomes negative according to (3.92) and flows out of the DFIM and into the grid. The negative electromagnetic torque causes a reduction in rotor speed giving the characteristics of a subsynchronous generator as described in table 3.5. When the direction of rotor current is reversed at t = 20 seconds, power flows into the machine and T_e is positive, resulting in an increase in rotor speed. These effects give the characteristics of a subsynchronous motor.

The results for the supersynchronous simulation are shown in figure 3.38. The rotor

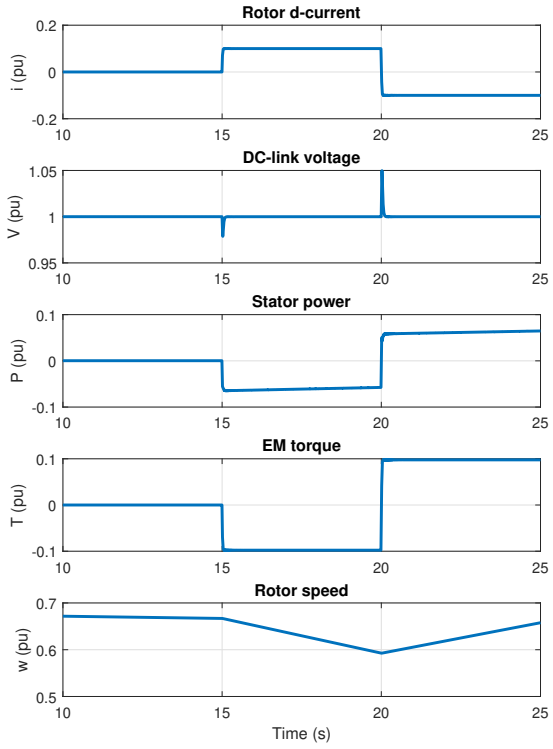

Figure 3.37: Subsynchronous operation of DFIM. The DFIM acts as a generator and then as a motor at 15s and 20s respectively.

speed is set to provide a slip of -1/3 (i.e. the rotor speed is 1.33 times the stator angular frequency) with no mechanical torque input such that $T_m = 0$. This time a positive $i_{dr_{ref}}$ causes an increase in v_{dc} showing that power is flowing away from the rotor and into the RSC. A negative electromagnetic torque causes a reduction in rotor speed and stator power is seen to flow in the negative direction, from the machine into the grid, thus characterising a supersynchronous generator. The situation is reversed when rotor current flows from RSC to rotor, resulting in a supersynchronous motor. The results from figures 3.37 and 3.38 validate all four modes of operation of the DFIM.

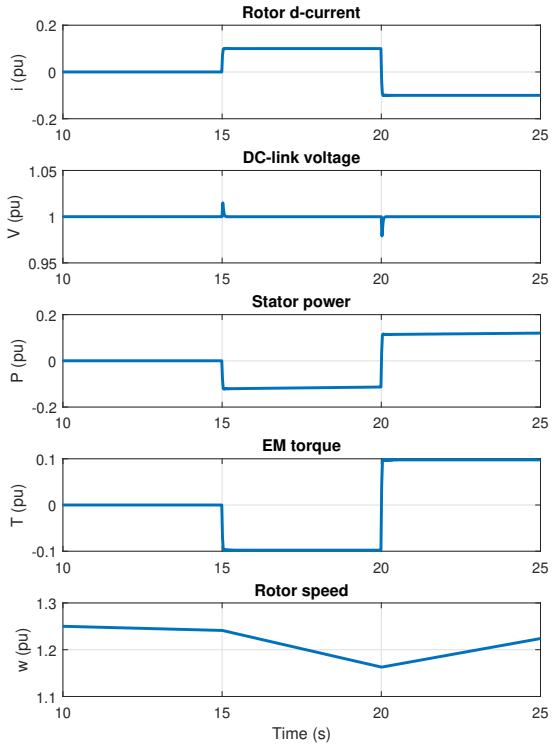

Figure 3.38: Supersynchronous operation of DFIM. At t = 15s, despite the positive sign on the rotor current power actually flows from the rotor into the RSC as shown by the increase in DC voltage. At t = 20s this situation is reversed. The DFIM acts as a generator and then as a motor at 15s and 20s respectively

3.6 PFEC Modelling

The previous sections have introduced all of the constituent parts required to assemble the PFEC, which consists of two WRIMs labelled the rotary transformer and DFIM respectively, and a B2B-VSC connected in the configuration shown in figure 3.39. Since the PFEC is a device for enabling the connection of low-frequency offshore wind, the wind farm and transmission line have also been included, modelled as a pi-section and an ideal voltage source connected through a VSC respectively.

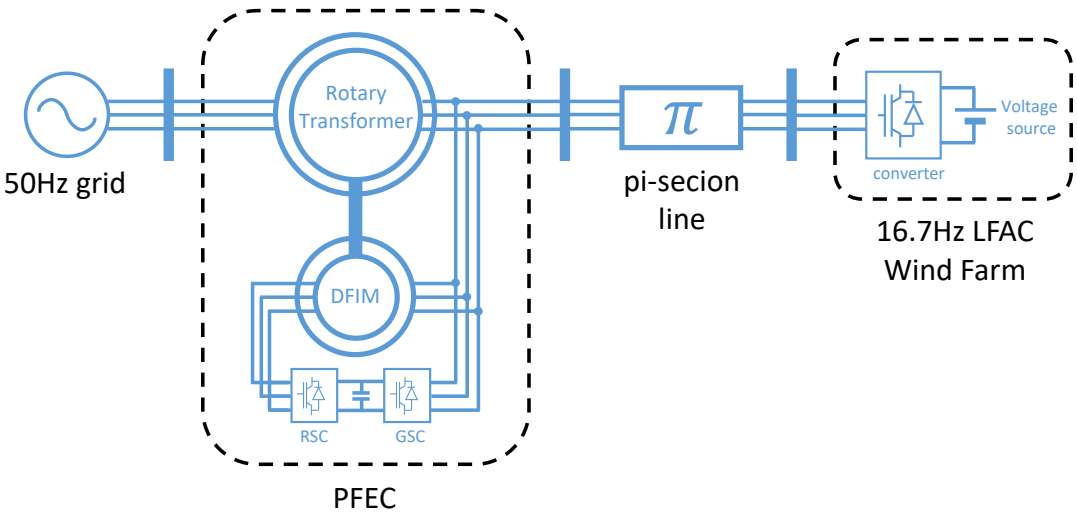

Figure 3.39: Schematic representation of PFEC wind energy system

The rotary transformer of the PFEC acts as the interface between the 50Hz grid and the low frequency wind farm which will be designed to operate at a frequency of 16.7Hz, although other frequencies are possible. Just as with a power transformer, the PFEC is intended to provide an AC voltage output at its terminals and dictate the voltage in the LFAC network. To maintain the connection it must possess a slip of 1/3 based on (2.38). It is the role of the DFIM and the B2B-VSC to maintain the slip at this value via the rotor speed controller.

Some adjustments need to be made to the models before the technology of the PFEC can be fully integrated, namely the coupling of the joint shaft, setting up the required rotating reference frames, setting the pole ratio between the two machines and configuring the controller to act on LFAC-side frequency rather than rotor speed.

3.6.1 PFEC Reference Frames

The concept of synchronously rotating reference frames was introduced in section 3.2.4, and in order to synchronise the electrical and mechanical dynamics of the machine with the network the model relies on an electrical angle that is output from a PLL.

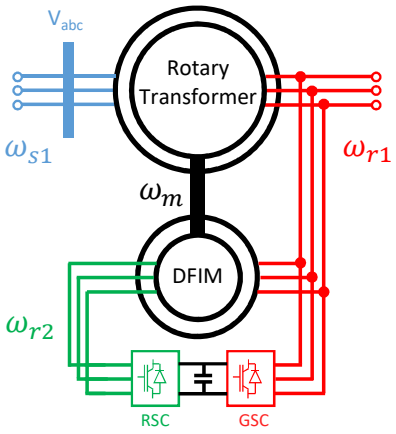

Figure 3.40: PFEC map showing colour-coded areas of distinct reference frames

In the application of the PFEC, there are three distinct reference frames corresponding to three distinct areas that arise due to the configuration of the two machines as shown in figure 3.40. The first is the grid reference frame defined by ω_{s1}, to which the stator of the RT is connected. The second is the rotor frame of the RT which is dependent on ω_{s1} and the rotor angle $\theta_1(t)$ as defined by (3.143). This defines the synchronous reference frame of the RT rotor circuit with respect to the stator.

$$\omega_{r1}t = \omega_{s1}t - \theta_1(t)p_1 \tag{3.143}$$

where p is the number of pole pairs and the subscripts 1 and 2 refer to the RT and the DFIM respectively. The stator of the DFIM shares the same circuit as the rotor of the RT, meaning that they also share the same frame of reference. This is also true for the transmission line and the wind farm.

The third distinct area is the rotor of the DFIM, which is a superposition of the other two reference frames. The rotor frame of the DFIM is determined from the stator of the DFIM, which is in-turn determined from the stator of the RT. This cascade of synchronous reference frames is shown in figure 3.41, where v_{abc} is the 3-phase voltage at the grid bus; ω_{s1}, ω_{r1}, ω_{r2} are the frequencies associated with the reference frames for the grid, the RT rotor (and DFIM stator) and the DFIM rotor respectively; θ is the

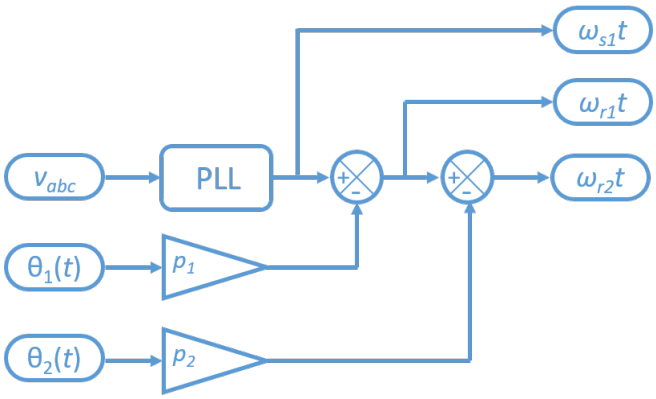

Figure 3.41: Calculation of reference frame frequencies

rotor angle and p is the number of pole pairs.

3.6.1.1 A Note on the PFEC Per-Unit System

The presence of two machines with two different rated electrical frequencies causes a dual per-unit system to arise. Depending on which machine is taken as the reference, the rated quantities of one machine with respect to other vary. For example, to maintain synchronism between 50Hz (1PU) and 16/7Hz (1/3PU) the RT must rotate at a speed 2/3PU. However, viewed from the reference frame of the DFIM this same speed is equal to 1PU because of how the machine is designed (note: the proper selection of pole pairs for RT and DFIM to achieve this equilibrium is described in detail in section 4.1).

Because of this, the PU quantities will be given subscripts to identify the different base systems, where PU_{RT} and PU_{DFIM} represent the per-unit quantities for the RT and DFIM respectively, and $2/3\text{PU}_{RT} = 1\text{PU}_{DFIM}$.

3.6.2 Frequency to Rotor Speed Transformation

So far we have two machines, the DFIM and the RT, each with a stator and rotor circuit that are linked both physically and electromagnetically. We now need a suit-

able transformation to relate the electrical frequency of the RT rotor-side network f_{r1} (the LFAC side) to the rotational speed of the coupled shaft. The LFAC-side frequency would then become an indirect control variable. Under this scheme the frequency could be controlled at a reference value of 16.7Hz regardless of what happens in the wider network. For example, in the event of a loss of generation normally the grid frequency would begin to fall, but with the frequency controller enabled the low frequency side of the PFEC would be regulated at 16.7Hz by making appropriate adjustments to the rotor speed.

Starting with the slip equation that describes the frequency either side of the RT, the derivation in 3.144 presents a mathematical relationship between LFAC-side frequency f_{r1} and DFIM rotor speed ω_{r2}

$$
\begin{aligned}
& s_1.f_{s1} = f_{r1} \\
& \left(\frac{\omega_{s1} - \omega_{r1}}{\omega_{s1}}\right) f_{s1} = f_{r1} \\
& \left(1 - \frac{\omega_{r1}}{\omega_{s1}}\right) f_{s1} = f_{r1} \\
& \frac{\omega_{r1}}{\omega_{s1}} = \left(1 - \frac{f_{r1}}{f_{s1}}\right) \\
& \omega_{r1} = \omega_{s1}\left(1 - \frac{f_{r1}}{f_{s1}}\right) \\
& \omega_{r2} = \frac{p_2}{p_1}\omega_{s1}\left(1 - \frac{f_{r1}}{f_{s1}}\right)
\end{aligned} \tag{3.144}
$$

therefore,

$$
\omega_{r2}^{*} = \frac{p_2}{p_1}\omega_{s1}\left(1 - \frac{16.7}{f_{s1}}\right) \tag{3.145}
$$

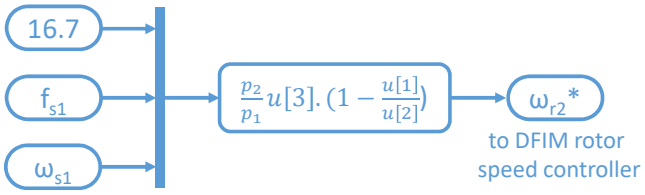

Figure 3.42: Transformation relating LFAC-side frequency to DFIM rotor speed reference ω_{r2}^*

3.7 Shaft Coupling

The RT and the DFIM are coupled via the common shaft such that the DFIM operates in the motoring mode to drive the RT which behaves as a subsynchronous generator. To model this coupling in the simulation software, the rotor speed output of the DFIM is connected to the rotor speed input of the RT. Likewise, the electromagnetic torque output of the RT is connected to the mechanical torque input of the DFIM as shown in figure 3.43. This arrangement is termed cascaded control and is further expanded on in the brushless-PFEC section in appendix A. Note that when rotor speed is set as an input to a machine then the inertia of that machine is ignored. The DFIM must therefore be modelled with the combined inertia of both machines.

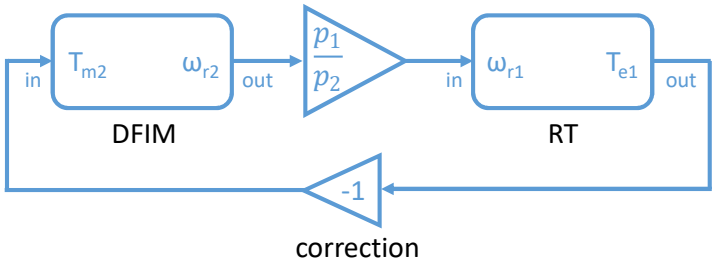

Figure 3.43: Coupling of the motor-generator set through a common shaft

3.7.1 Commercial Software Limitations of Asynchronous Machine Numerical Models

The coupling in figure 3.43 highlights a limitation within the simulation software in that there is no option to define which orientation the shafts are connected. The shafts of two physical machines can be connected either head-to-head or head-to-tail but the option of connecting two machines in tandem is unavailable within the software. Instead, the work around is to either reverse the phase sequence of the DFIM by interchanging phases b and c for example (although any two phases will do), or by adopting the method shown in figure 3.43 where a gain of minus 1 is applied to the electromagnetic torque output of the RT. Functionally these methods achieve the same result, but it was found during simulation that the switched phases approach resulted in a more complex design of the PLL, so the more simple negative unity gain method was adopted.

3.8 9th Order Model

The RT and the DFIM within the PFEC can each be represented by a 5th order model induction machine as introduced in section 3.3.2. Because of the coupling of the shafts the mechanical dynamics of the RT can be fully described by the DFIM which must now include the inertia of both machines. The RT receives its value of rotor speed directly from the output of the DFIM and in return it provides an electromagnetic torque T_{e1} to be substituted for load torque in the DFIM swing equation. Together this relationship only contributes one order to the system, resulting in a 9th order PFEC model:

$$\begin{aligned}
\lambda_{ds1} &= \int \big(v_{ds1} - \frac{R_{s1}}{L_{ls1}}\big(\lambda_{ds1} - \lambda_{dm1}\big) + \omega_{s1}\lambda_{qs1}\big)\mathrm{d}t \\
\lambda_{qs1} &= \int \big(v_{qs1} - \frac{R_{s1}}{L_{ls1}}\big(\lambda_{qs1} - \lambda_{qm1}\big) - \omega_{s1}\lambda_{ds1}\big)\mathrm{d}t \\
\lambda_{dr1} &= \int \big(v_{dr1} - \frac{R_{r1}}{L_{lr1}}\big(\lambda_{dr1} - \lambda_{dm1}\big) + (\omega_{s1} - \omega_{r1})\lambda_{qr1}\big)\mathrm{d}t \\
\lambda_{qr1} &= \int \big(v_{qr1} - \frac{R_{r1}}{L_{lr1}}\big(\lambda_{qr1} - \lambda_{qm1}\big) - (\omega_{s1} - \omega_{r1})\lambda_{dr1}\big)\mathrm{d}t \\
\omega_{r1} &= \frac{p_1}{p_2}\omega_{r2} \\
\lambda_{ds2} &= \int \big(v_{ds2} - \frac{R_{s2}}{L_{ls2}}\big(\lambda_{ds2} - \lambda_{dm2}\big) + \omega_{s2}\lambda_{qs2}\big)\mathrm{d}t \\
\lambda_{qs2} &= \int \big(v_{qs2} - \frac{R_{s2}}{L_{ls2}}\big(\lambda_{qs2} - \lambda_{qm2}\big) - \omega_{s2}\lambda_{ds2}\big)\mathrm{d}t \\
\lambda_{dr2} &= \int \big(v_{dr2} - \frac{R_{r2}}{L_{lr2}}\big(\lambda_{dr2} - \lambda_{dm2}\big) + (\omega_{s2} - \omega_{r2})\lambda_{qr2}\big)\mathrm{d}t \\
\lambda_{qr2} &= \int \big(v_{qr2} - \frac{R_{r2}}{L_{lr2}}\big(\lambda_{qr2} - \lambda_{qm2}\big) - (\omega_{s2} - \omega_{r2})\lambda_{dr2}\big)\mathrm{d}t \\
\omega_{r2} &= \frac{1}{(J_1 + J_2)}\int (T_{e1} + T_{e2} - T_{damp})\mathrm{d}t
\end{aligned} \tag{3.146}$$

where the subscripts 1 and 2 refer to the RT and DFIM respectively, and the symbols have their usual definitions as described in section 3.3.2.

3.9 Summary and Conclusions

This chapter presents the modelling process and controller design of the PFEC and concludes with a complete time-domain model that can be used for simulations in section

4. Mathematical derivations of the core components have been provided, including the converter, the two machines that make up the PFEC, the PLL used for synchronisation and the controllers.

A sequential approach has been taken by introducing each component separately, with the final part of this chapter dedicated to the unification of the PFEC. Controller design for the PFEC is similar to the DFIM but with added functionality relating to the now-controllable frequency on the LFAC-side.

A limitation of how to connect the shafts of the two machines was also identified and corrected within the software. The coupling of the DFIM and the RT must be done in a tandem orientation, so it was necessary to apply a negative unity gain to the electromagnetic torque output of the RT. This is equivalent to reversing the phase sequence of one of the machines but resulted in a more simple implementation in the model.

Chapter 4

PFEC Operating Principles and Simulations

Now that a functional model of the PFEC has been created, work can begin on investigating some of the properties of the PFEC to analyse the effectiveness of this new approach to LFAC transmission for offshore wind. The objectives of this section are to first verify the model by checking the fundamental principles which govern the PFEC at steady-state and then to take a more exploratory approach with the intention of discovering some of the many different properties of the device through appropriate simulations.

4.1 Determining the Pole Ratio

The assumption so far has been to connect a 50Hz network to a 16.7Hz wind farm through an appropriately sized PFEC, however by varying the ratio of poles between the two machines, an interconnection between any two frequencies is theoretically possible meaning that the PFEC can be customised to fit specific network requirements. For example, for shorter length transmission routes, an interconnection between 50Hz and 25Hz may have some merit over a 16.7Hz case, or similarly for longer cable lengths, a link between 50Hz and 10Hz may be viable. By correctly sizing the number of poles

within the DFIM and RT respectively, the natural equilibrium point can be scaled to correctly match any network conditions, providing that the number of poles required in the two machines are integer values.

To connect two asynchronous networks through an induction machine, the DFIM rotor must spin at a speed proportional to the frequency difference as defined in electrical radians in (4.1),

$$\omega_{r2} = \left(1 - \frac{f_{r1}}{f_{s1}}\right) \tag{4.1}$$

where ω_{r2} is the speed of the DFIM shaft (elec. rad/s) and f_{s1} and f_{r1} are the electrical frequencies of the grid (stator) and the low frequency side (rotor) of the RT respectively.

Upon arriving at the junction of the two machines, the power is split into two parts, one of which travels electrically through the rotary transformer while the other must be handled mechanically by the DFIM. The fraction which travels directly through the rotary transformer is proportional to the slip of the RT, s_1, and is given by (4.2). The remaining fraction travels through the DFIM which must therefore be sized appropriately according to (4.3).

$$s_1 = \frac{\omega_{s1} - \omega_{r1}}{\omega_{s1}} \tag{4.2}$$

$$P_{DFIM} = (1 - s_1)P_{RT} \tag{4.3}$$

where P_{RT} is the rated power of the rotary transformer. Problems associated with conflicting base quantities are encountered beyond this point. To demonstrate consider the example of a typical interconnection between a 50Hz grid and a 16.7Hz network. Following (4.1) and (4.3) with $f_{s1} = 50$ Hz and $f_{r1} = 16.7$ Hz we find that the shaft must be maintained at a constant speed $\omega_{r2} = 2/3$ PU$_{RT}$. In a per-unit system with $f_{base} = 50$Hz the slip is equal to 1/3 which determines that the rated power of the DFIM needs to be 2/3 PU$_{RT}$.

The stator and the rotor sides of the rotary transformer have different base values. To avoid confusion when referring to each set of bases, the stator of the rotary transformer (otherwise known as the grid) will be defined as the RT reference frame, while the rotor side (otherwise known as the low frequency side) shall be defined as the DFIM reference frame since the stator of the DFIM is connected to the low frequency side of the rotary transformer.

The base quantities of the DFIM will be smaller than those of the rotary transformer because of the reduced frequency. The main concern here is on the base electrical speeds which are given by (4.4) and (4.5). From (4.5) it is shown that a speed of 1 PU_{DFIM} in the DFIM reference frame is equal to 1/3 PU_{RT} in the RT reference frame.

$$w_{b1} = 2\pi f_{s1} \tag{4.4}$$

$$\begin{aligned} w_{b2} &= 2\pi f_{r1} \\ &= 2\pi s_1 f_{s1} \\ &= \frac{1}{3} w_{b1} \end{aligned} \tag{4.5}$$

where ω_{b1} and ω_{b2} are the base frequencies in electrical radians of the RT and DFIM respectively, f_{s1} is the frequency of the RT stator (Hz), f_{r1} is the frequency of the RT rotor (Hz) and s is the slip.

In the example, to connect a 50Hz grid to a 16.7Hz network the shaft must be maintained at a constant speed of ω_{r2}= 2/3 PU_{RT} in the RT reference frame, which corresponds to a speed of 2 PU_{DFIM} in the DFIM reference frame. To accomplish this the DFIM would need to run at twice its rated speed thus requiring twice the rated power.

Instead of doubling the rated power of the DFIM, the pole arrangement can be adjusted to account for the required increase in speed. The base mechanical speed is related to the base electrical speed as in (4.7) and is inversely proportional to the

number of pole pairs.

$$w_{bm1} = \frac{w_{b1}}{p_1}$$
$$w_{bm2} = \frac{w_{b2}}{p_2} \tag{4.6}$$
$$\tag{4.7}$$

where ω_{bm1} and ω_{bm2} are the RT and DFIM base mechanical speeds in mechanical radians, ω_{b1} and ω_{b2} are the RT and DFIM base electrical speeds in electrical radians and p_1 and p_2 are the number of RT and DFIM pole pairs respectively.

According to (4.7), by doubling the number of pole pairs on the RT p_1, the required mechanical speed of the shaft is halved. A pole ratio of 2:1 corresponding to RT:DFIM will therefore allow for the 50/16.7Hz interconnection.

This 2:1 pole ratio is specific to the 16.7 Hz example, however different arrangements of poles can be applied to allow a wide range of possible frequency interconnections. In general, assuming the number of pole pairs on the DFIM in normalised to 1, (that is $p_2 = 1$, then the pole pairs on the RT p_1 must be scaled by the rated power of the DFIM P_{DFIM} and the slip s_1 as in (4.8).

$$p_1 = \frac{P_{DFIM}}{s_1} \tag{4.8}$$

It can also be also be shown that, given $p_2 = 1$, then the number of pole pairs on the RT p_1 required for the interconnection between any two frequencies f_{s1} and f_{r1} is given by:

$$p_1 = \frac{(f_{s1} - f_{r1})}{f_{r1}} \tag{4.9}$$

The values for some possible frequency connections are given in table 4.1, while figure 4.1 shows a smooth curve representing the pole configurations for all frequencies

between 50Hz and 10Hz with the circles representing pole numbers that scale to integer values. As the curve passes through 1 the ratio switches indicating that the DFIM then requires a higher number of poles than the rotary transformer. At 50Hz the two frequencies are equal and the pole number becomes zero, implying that there is no need to use machines for the connection as the two networks would already be in synchronism. Theoretically, all frequency connections with rational pole ratios are possible however some of the more unusual ratios would need to have machines with non-standard numbers of poles. For example, to connect a 50Hz network with a 17.24 Hz network, the pole ratio would need to be 29:10, with 29 pole pairs on the RT and 10 pole pairs on the DFIM.

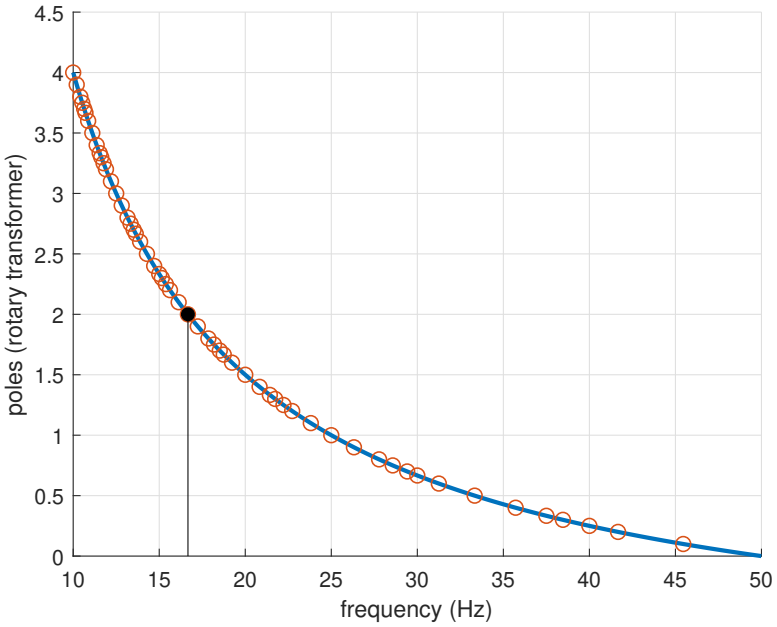

Figure 4.1: Curve showing the required RT pole ratio for specific frequency connections, normalised such $p_2 = 1$. Circles denote arrangements with integer values of poles

4.1.1 Self-Sustaining Equilibrium

An advantageous consequence of correct pole sizing is an inherent stability of the whole system. When sized correctly, the motor-generator action of the DFIM and the rotary transformer is strong enough to keep the entire system in equilibrium. In the 16.7Hz

Table 4.1: Pole ratios for some possible low-frequency configurations

f_{s1} (Hz)	f_{r1} (Hz)	p_2	p_1	Pole Ratio (RT:DFIM)
50	40	1	0.25	1:4
	33.3		0.5	1:2
	30		0.67	2:3
	25		1	1:1
	20		1.5	3:2
	16.7		2	2:1
	10		4	4:1

example above, the motoring action of the DFIM accelerates the shaft up to the rated speed of 2/3 PU_{RT} where it remains at steady-state. The decelerating torque exerted by the rotary transformer balances out with the accelerating torque of the DFIM such that they reach an equilibrium point. If the pole ratios were different, an equilibrium point would still be reached but at a different rotor speed value.

The benefits of this equilibrium point existing at 2/3 PU_{RT} rotor speed (50Hz base) is that it alleviates the use of power-electronics in the steady-state. The speed is being maintained at the correct value to allow a 16.7Hz interconnection as a natural property of the system. From a control perspective this is very desirable as it shows that the starting point upon which to apply control algorithms is inherently stable. That is, we are applying control to a stable system. In the steady-state the power-electronics therefore do not need to work as hard as they would have to in an unstable system. This result is henceforth referred to as the self-sustaining equilibrium.

A simulation to demonstrate this self-sustaining property is given below. In this set-up, the speed of the machine is artificially reduced using the power electronics in the rotor side converter. Once the machine reaches this speed the power electronics are disconnected leaving a short-circuited rotor and a redundant rotor-side controller. It is hypothesised that the system will return to the stable equilibrium at ω_{r1} =2/3 PU_{RT}.

The simulation layout is shown in figure 4.2. The original has been modified to add two breakers on the rotor circuit, one to disconnect the rotor-side converter and

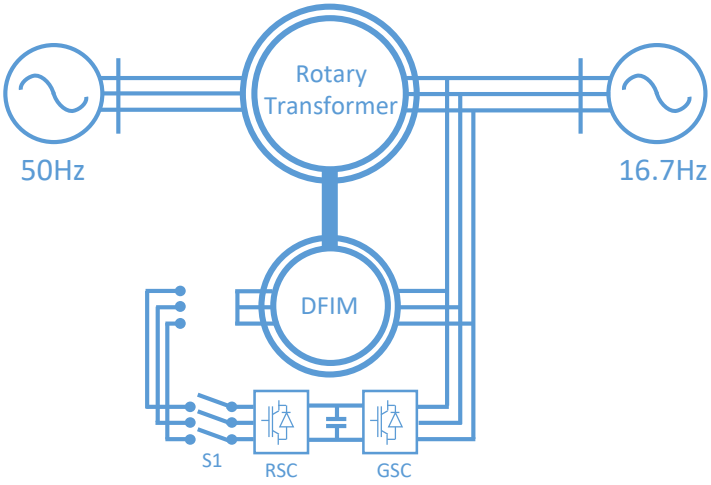

Figure 4.2: Simulation layout showing breaker S1. The breakers are tripped to disconnect RSC and activate the short circuited rotor

the other to connect the rotor windings to a small valued resistor representing a short circuit (not shown).

The simulation is initialised with steady-state values of rotor speed. At time t = 50s the speed setpoint is reduced from 2/3 PU_{RT} to (2/3 - 0.1) PU_{RT} using the rotor side controller and at time t = 100s a command is sent to the breakers to disconnect the power electronics and connect the phases of the DFIM rotor together in a short circuit. The results of this simulation are shown in figure 4.3.

The plots show that when the power electronics are disconnected after a forced reduction in rotor speed, the machine returns to the steady state value of $\approx$ 2/3 PU_{RT}, thus demonstrating the existence of the self-sustaining equilibrium.

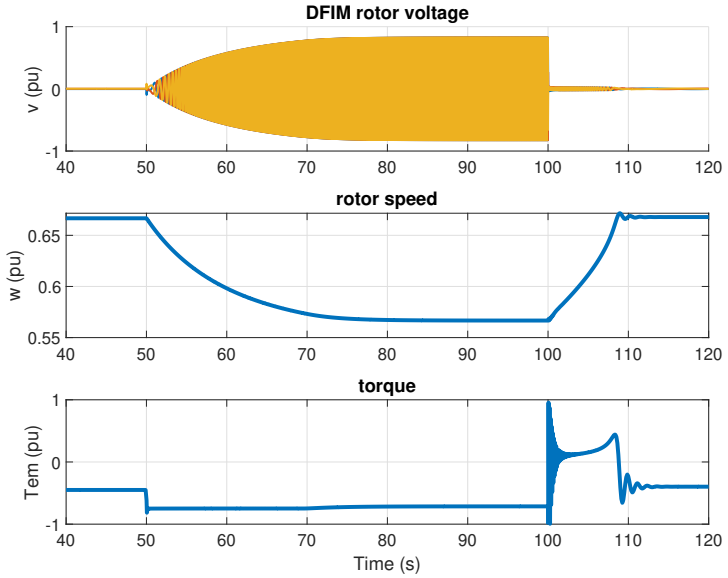

Figure 4.3: After disconnection of power electronics, the PFEC returns to steady-state values of 2/3 PU_{RT}

4.2 Torque-Speed Curve of the PFEC

Derivation of the torque-speed characteristics of the PFEC begins with the Thevenin model of an induction machine. Due to the differing number of poles between the RT and the DFIM, the PFEC has two equilibrium points; one at the synchronous speed of each machine. In the RT base these are found at rotor speeds of 0.67 PU_{RT} and 1 PU_{RT} respectively.

To distinguish between variables, the machines are labelled according to figure 4.4 where machine 1 refers to the RT and machine 2 is the DFIM. Figure 4.5a) shows a single-line diagram for one phase of the PFEC where the rotary transformer and the DFIM are electrically connected in series from rotor to stator. Note that for the purposes of developing a torque-speed curve, the wind farm is disconnected from the circuit and the rotor of the DFIM is connected in short-circuit.

The first step is to calculate the Thevenin equivalent circuit of the DFIM as a separate entity and to use this to determine the torque contribution from this machine

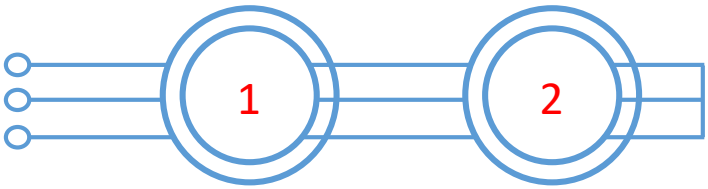

Figure 4.4: Nomenclature of machines, where machine 1 = RT, machine 2 = DFIM

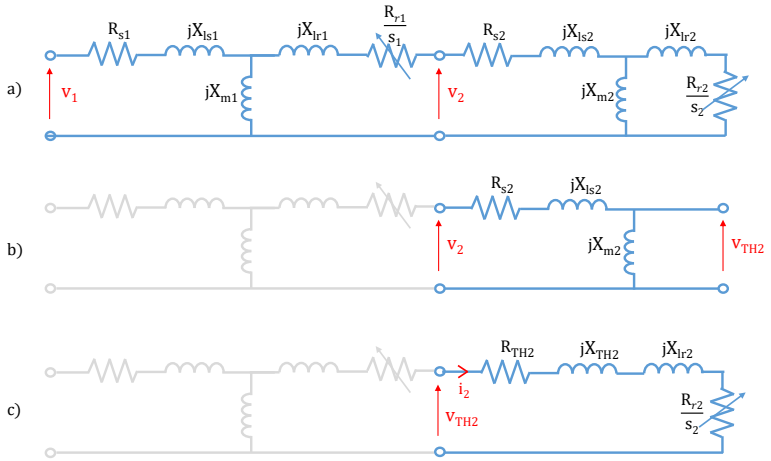

Figure 4.5: Single line diagrams showing derivation process. a) unsimplified single-phase equivalent circuit of PFEC, b) Thevenin process applied to DFIM, with the RT greyed-out for clarity, c) Thevenin equivalent circuit of DFIM

alone. This is shown in figure 4.5b) where the RT has been greyed out for clarity. Note that $v_2 = s_1 v_1$ since the turns ratio is set equal to 1 [75].

$$v_{tH2} = v_2 \left[\frac{jX_{m2}}{R_{s2} + j(X_{ls2} + X_{m2})} \right] \tag{4.10}$$

$$Z_{TH2} = \frac{jX_{m2}(R_{s2} + jX_{ls2})}{R_{s2} + j(X_{m2} + X_{ls2})} \tag{4.11}$$

The circuit can then be redrawn as in figure 4.5c), where it is now possible to determine the current i_2 and hence the torque contribution T_2 arising from the DFIM.

$$i_2 = \left| \frac{v_{tH2}}{\left(R_{TH2} + \frac{R_{r2}}{s_2} + j(X_{TH2} + X_{lr2}\right)} \right| \tag{4.12}$$

$$T_2 = \frac{3i_2^2 P_2 R_{r2}}{2 s_2 \omega_{s2}} \tag{4.13}$$

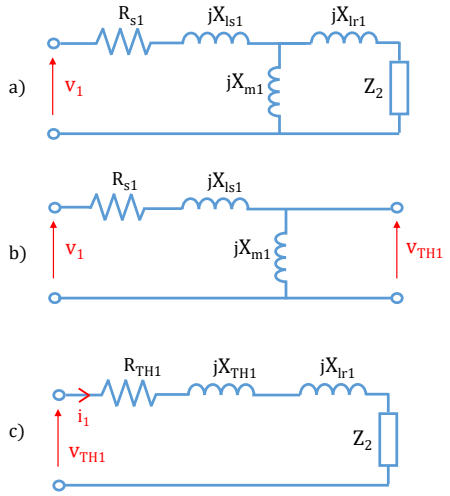

Figure 4.6: Single line diagrams showing derivation process. a) machine 1 with machine 2 represented by a load Z_2, b) rotor circuit removed in Thevenin process, c) Thevenin equivalent circuit of the PFEC

To calculate the torque contribution of the RT, the DFIM is represented as an equivalent load Z_2 on the RT rotor circuit, as demonstrated in figure 4.6a). The Thevenin approach is then repeated to find the equivalent current and torque contribution from the RT. The load Z_2 is given by:

$$Z_2 = \frac{R_{r1}}{s_1} + R_{TH2} + \frac{R_{r2}}{s_2} + X_{TH2} + X_{lr2} \tag{4.14}$$

The Thevenin equivalent circuit is then calculated as shown in figure 4.6b) and in (4.15) and (4.16):

$$v_{tH1} = v_1 \left[\frac{jX_{m1}}{R_{s1} + j(X_{ls1} + X_{m1})} \right] \tag{4.15}$$

$$Z_{TH1} = \frac{jX_{m1}(R_{s1} + jX_{ls1})}{R_{s1} + j(X_{m1} + X_{ls1})} \tag{4.16}$$

The resulting equivalent circuit is shown in figure 4.6c) which can then be used to

calculate the current and torque contributions of the RT:

$$i_1 = \left| \frac{v_{tH1}}{\left(R_{TH1} + Z_2 + j(X_{TH1} + X_{lr1}\right)} \right| \tag{4.17}$$

$$T_1 = \frac{3i_1^2 P_1 R_{r1}}{2s_1 \omega_{s1}} \tag{4.18}$$

The torque contributions from each machine are summed together as in (4.19) and plotted against rotor speed to give the torque-speed characteristics of the PFEC. This is shown in figure 4.7, where the two equilibrium points can be seen: eq1 at 0.67 PU_{RT} and eq2 at 1 PU_{RT}. The first of these points is the intended operating range for a 16.7Hz PFEC, but this will shift for different frequencies. For example, a 25Hz PFEC would have the first equilibrium at 0.5pu, while a 10Hz PFEC would be at 0.9pu. The second equilibrium point is always found at 1 PU_{RT} and would spell instability for the system. This is because the gradient of the torque speed curve is positive and would result in a positive feedback loop and unbounded oscillations. A PFEC operated at a lower frequency would have its two equilibrium points closer together, so the risk of jumping from the stable operating region to the unstable region is increased for decreasing PFEC frequencies.

$$T_{tot} = T_1 + T_2 \tag{4.19}$$

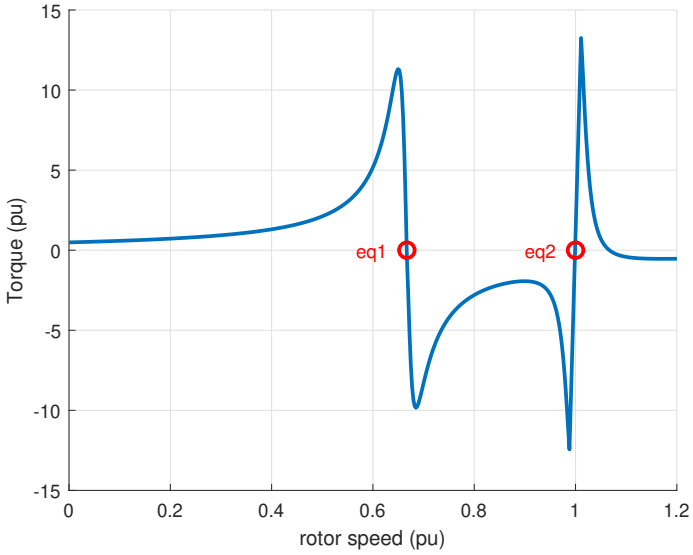

Figure 4.7: Torque-speed curve of the PFEC showing the existence of two equilibrium points

4.3 Validation of Power Flow Fractions

Figure 3.3 shows the hypothesised transit of active power of the PFEC (neglecting losses) and how the power is expected to split based on the calculations in section 3.1. In the figure, power traverses from left to right travelling from the 16.7Hz wind farm, through the PFEC, and into the 50Hz grid. Based on the value of the slip in (3.92) required for a 16.7Hz interconnection, the 1 PU_{RT} bulk of power is expected to split simultaneously into two streams of 1/3 PU_{RT} and 2/3 PU_{RT}. The former share of 1/3 PU_{RT} arrives at the rotor terminals of the RT and is measured by bus 2 while the latter share of 2/3 PU_{RT} is forced to travel down into the DFIM circuit where it is converted into mechanical power and transmitted through the shaft. The two portions of power then recombine to produce the full 1 PU_{RT} power which is then injected into the grid. The single-line diagram from figure 3.3 is repeated here in figure 4.8 again for ease of reference.

In this simulation, an aggregated 100MW wind farm represented by a VSC is programmed to generate power at 16.7Hz. This is connected to a 100MW PFEC which consists of a 100MW RT and a 66.7MW DFIM with a combined inertia constant of 4

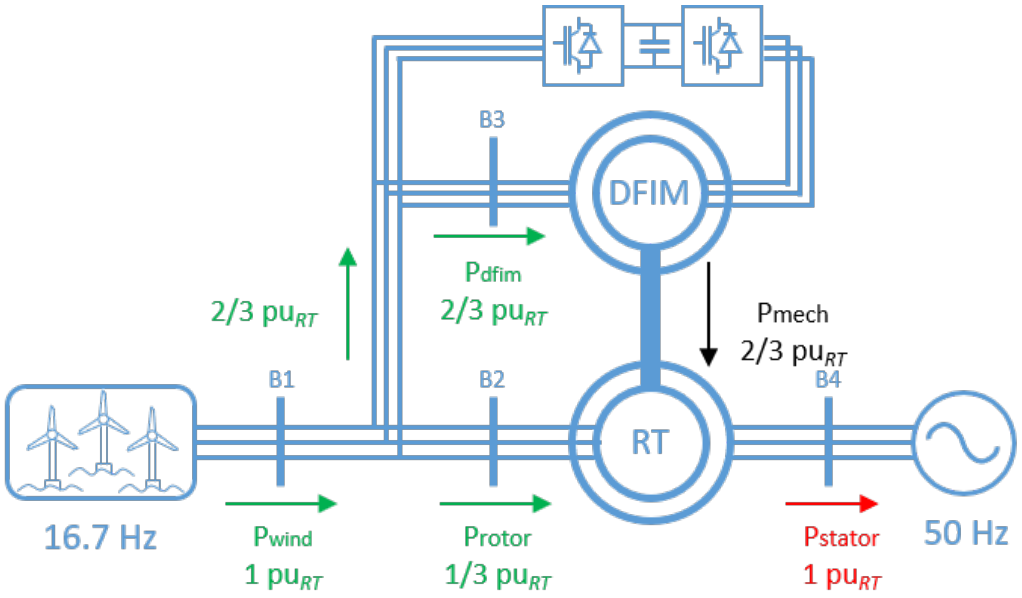

Figure 4.8: Partial frequency energy converter for LFAC offshore wind

seconds. The wind farm and the PFEC are connected via a 100km transmission line which is modelled as a pi-section. To account for the high capacitance of the subsea transmission line, 135MVar inductive reactive power compensation is provided at one end of the cable along with an additional 0.2 PU_{RT} reactive power provided by the q-axis of the DFIM RSC controller to give approximately a unity power factor of the PFEC system when measured at the 50Hz grid bus, B4 in figure 3.3.

The simulation results showing the transit of power are shown in figure 4.9 where the electrical and mechanical components can be traced throughout the system. At t = 40s, 1 PU_{RT} of active power is sent from the wind farm and through the transmission lines where it suffers some losses. The power then splits up into two components, one of which travels into the rotor circuit of the rotary transformer, traversing the airgap and entering the grid while the other component forks down into the DFIM stator circuit. The B2B-VSC maintains the rotor at a constant speed such any additional electrical energy reaching DFIM cannot influence the speed of rotation and is therefore converted into mechanical energy where it travels through the shaft and into the rotary transformer. It is then converted back into electrical energy where it sums with the

first component to transmit the full power to the grid.

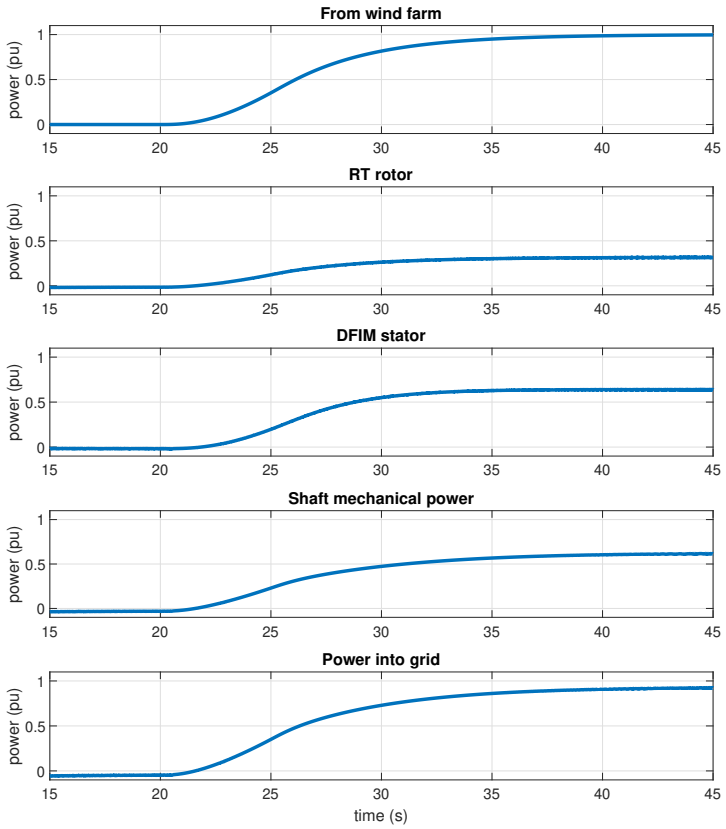

Figure 4.9: Active power flow through system. From top to bottom: 1) Power sent from wind farm, 2) power arriving at RT rotor terminals, 3) power arriving at DFIM stator terminals, 4) shaft mechanical power, 5) power exported to grid

From figure 4.9 the total power sent from the wind farm can be seen to be comprised of two components. Approximately 1/3 PU_{RT} power is transferred through the airgap of the rotary transformer as per the power-slip relationship. When rotating at a constant speed of $\omega_{r1} = 2/3$ PU_{RT} the slip is equal to 1/3, therefore 1/3 PU_{RT} power appears on the rotor-side of the machine. The remaining 2/3 PU_{RT} travels down into the DFIM circuit where it is entirely converted (neglecting losses) to mechanical power and transmitted through the shaft. The 2/3 PU_{RT} mechanical power sums together

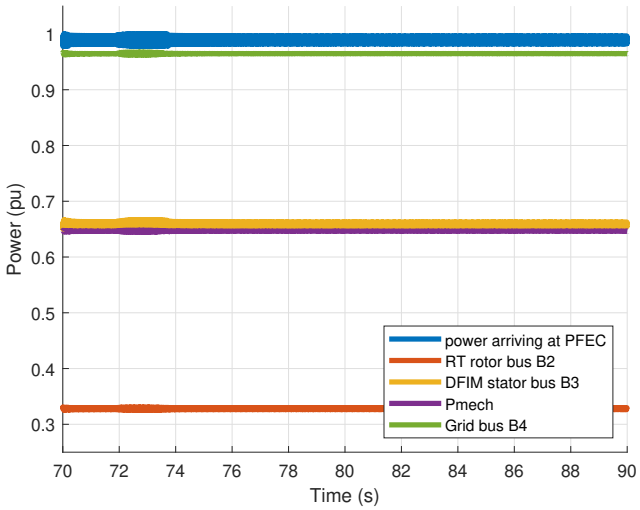

Figure 4.10: Simulation results of power flows within the PFEC. Bus labels refer to those in figure3.3

with the 1/3 PU_{RT} electrical power to produce the total 1 PU_{RT} power, minus losses, for export into the grid.

Figure 4.10 shows the steady-state simulation results of the scenario described above and it can be seen that the power sent from the wind farm exits the cable and arrives at the PFEC and splits into two parts. 1/3 PU_{RT} power is measured at bus 2 on the rotor-side of the rotary transformer and the remaining 2/3 PU_{RT} is measured at bus 3 at the DFIM stator terminals. There is a loss here associated with the conversion from electrical to mechanical power as shown by the difference between power at bus 3 and the mechanical power labelled in the figure. Finally, the power recombines at the RT stator terminals and is injected into the grid at bus 4 to complete the transmission of the full 1 PU_{RT} power, taking into account losses.

4.3.1 Effect of Power Transfer on Rotor Speed

The effect of power transfer on the rotational speed of the PFEC is shown in figure 4.11. When power is sent from the wind farm, the currents in the rotor of the RT increase, as do the currents in the stator of the DFIM circuit. The natural response to the increased magnetic fields is for the machines to slow down, however the RSC regulates the speed according to the set-point and the power-electronics work to keep the rotor of the DFIM in this perturbed state. It is also worth nothing that in case no power-electronics are present the power flow will not stop and the accelerating torque of the DFIM and decelerating torque of the RT will reach an equilibrium for any load condition to keep the frequency constant.

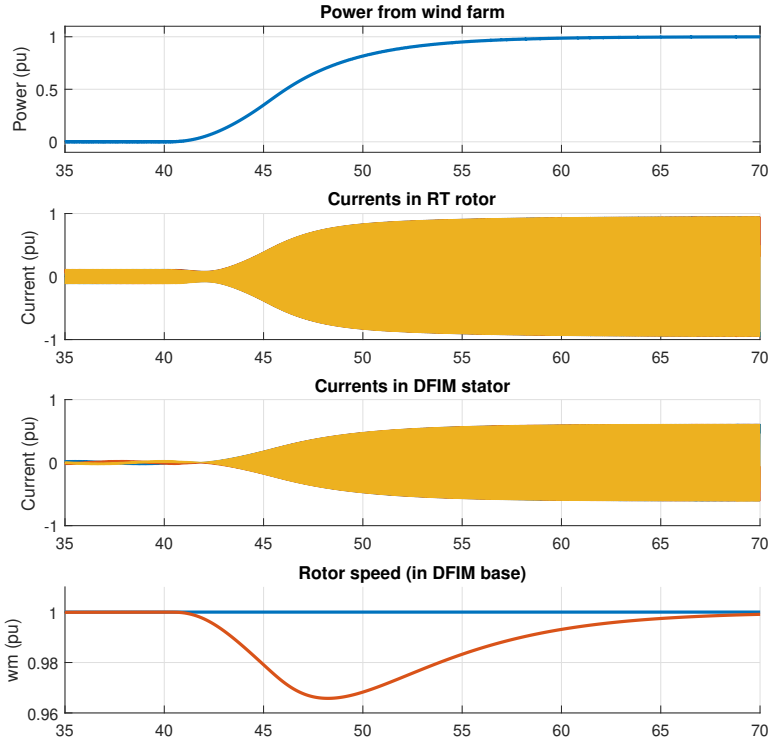

Figure 4.11: Effect of power flow on rotor speed. From top to bottom: 1) power sent from wind farm, 2) DFIM stator currents measured at bus 3, 3) RT rotor currents measured at bus 2, d) rotor speed in DFIM base

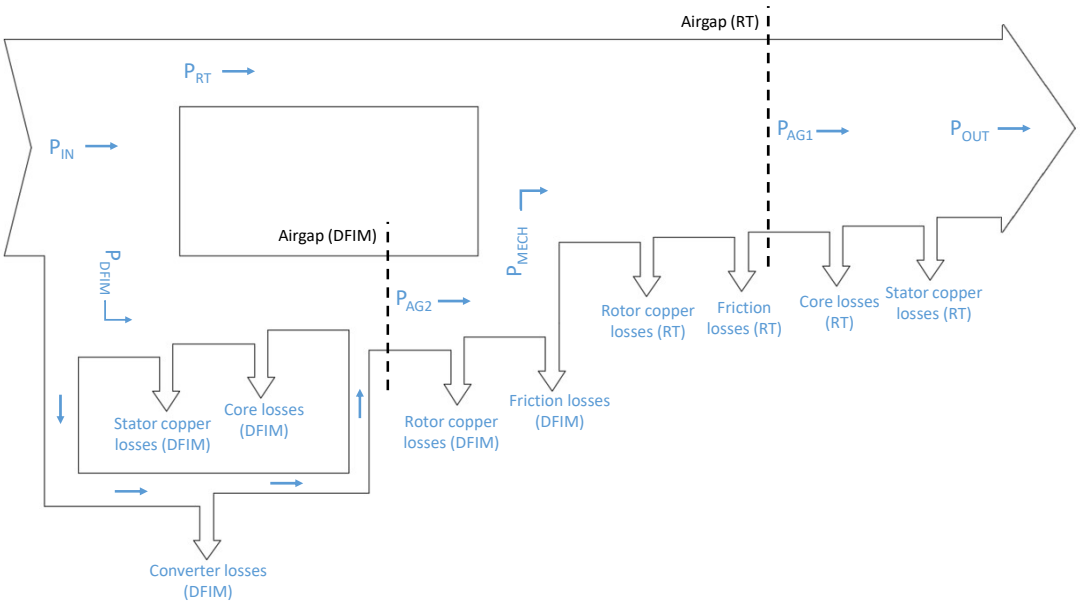

Figure 4.12: Graph showing losses throughout the PFEC

4.4 Losses throughout the PFEC System

The relationship between the input power and the output power of the PFEC is shown as a loss diagram in figure 4.12 which combines the loss diagrams of two machines, namely the RT and the DFIM, to provide a visual representation of the losses in the PFEC system.

The input power from the wind farm P_{in} is seen simultaneously to split into two streams P_{RT} and P_{DFIM} with proportions that are determined by the slip, in this case in a 3:1 ratio with the larger portion of the power travelling down into the DFIM. The first losses encountered in the DFIM branch are the I^2R losses in the stator windings. Some amount of power is then lost as hysteresis and eddy currents in the DFIM stator, referred in figure 4.12 as the core losses. The position of the core losses in the diagram is somewhat arbitrary because they come partially from the rotor and the stator of the DFIM, however the larger fraction of the losses come from the DFIM stator current so all of the core losses are lumped together on the stator-side of the DFIM. Some of the DFIM stator power is siphoned off by the power-electronic converter where it

encounters converter losses along the way before being injected back into the DFIM rotor circuit.

The power remaining after the copper losses and core losses reaches the DFIM airgap and is transferred to the DFIM rotor. This power is referred to as the DFIM airgap power P_{AG2}. After the power is transferred to the DFIM rotor circuit it again encounters I^2R losses, this time from the DFIM rotor windings. The rest is converted from electrical to mechanical and suffers losses due to friction. Finally, the remaining mechanical power P_{mech} recombines with the rotary transformer circuit.

The losses in the rotary transformer branch are similar to the DFIM but in reverse order and without the power-electronic converter arm. One-third of the total input power enters the RT rotor circuit P_{RT} and recombines with the mechanical power from the DFIM branch P_{mech} and encounters the same type of losses as found throughout the DFIM. The recombined power is then transferred across the airgap of the rotary transformer labelled as P_{AG1}. This total power encounters RT stator winding losses and core losses until finally the remaining power P_{out} is injected into the wider network.

A summary of the losses and their defining equations based on the equivalent circuit of an induction machine is given in table 4.2, where R is the winding resistance, I is the current, E is the internal voltage of the magnetising branch and G is the conductance of the magnetising branch. The subscripts s,r refer to stator and rotor quantities respectively and the subscripts 1,2 refer to the RT and the DFIM respectively.

4.4.1 Slip-Dependent Losses

It is well known that some of the losses in an induction machine are dependent on slip. This is an important factor in the design and operation of the PFEC because although a standard DFIM is operated at close to synchronous speed, the RT is maintained at a steady-state value of 1/3 PU_{RT} slip. This relatively high slip value is not unheard

Table 4.2: Summary of PFEC losses [76]

Machine	Loss	Equation
Rotary Transformer	stator copper loss	$P_{SCL1} = 3I_{s1}^2 R_{s1}$
	core loss	$P_{core1} = 3E_1^2 G_{c1}$
	rotor copper loss	$P_{RCL1} = 3I_{r1}^2 R_{r1}$
DFIM	stator copper loss	$P_{SCL2} = 3I_{s2}^2 R_{s2}$
	core loss	$P_{core2} = 3E_2^2 G_{c2}$
	rotor copper loss	$P_{RCL2} = 3I_{r2}^2 R_{r2}$

of especially in the applications to wind energy generation where a DFIG is commonly sized with a slip range of ±30% of the synchronous speed, however it is high enough to incur some additional losses which require attention.

The airgap power of the RT can be expressed by (4.20) where the different quantities are taken from the PFEC equivalent circuit in figure 4.5a):

$$P_{AG1} = 3I_{r1}^2 \frac{R_{r1}}{s_1} \tag{4.20}$$

Notice from (4.20) and table 4.2 that the rotor copper losses are equal to the air-gap power times the slip, $P_{RCL1} = s_1 P_{AG1}$. Therefore, the higher the slip of the rotary transformer, the higher the rotor losses [76]. This is not a problem for the DFIM since it is kept close to its own synchronous speed because it is being fed from the LFAC network, but for the rotary transformer the high slip used in PFEC operation is likely to negatively affect performance. A study into improving the efficiency of the DFIG is presented in [77], which states that the total electrical power loss of a DFIG is given by (4.21).

$$\begin{aligned} P_{loss} =& 3R_s(i_{ds}^2 + i_{qs}^2) + 3R_r(i_{dr}^2 + i_{qr}^2) + C_{Fe_s}\omega_s^2\lambda_m^2 \\ &+ C_{Fe_r}(\omega_s - \omega_r)^2\lambda_m^2 + C_{str}\omega_s^2(i_{dr}^2 + i_{qr}^2) \end{aligned} \tag{4.21}$$

where R_s and R_r are the resistances of the stator and rotor windings respectively, ω_e is the frequency of the stator-side network, ω_r is the rotor frequency, λ_m is the magnetising inductance, C_{Fe_s} and C_{Fe_r} are the stator and rotor iron loss coefficients

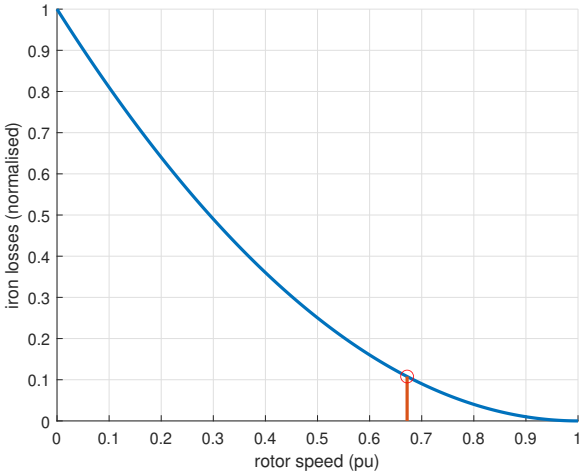

Figure 4.13: Effect of rotor speed on rotor iron loss showing the increased losses at 2/3 PU_{RT} speed

respectively, and C_{str} is the stray loss coefficient. It can be seen that the speed of the rotor has an effect on the rotor iron losses due to the ω_r term present in (4.21) and the greater the excursion of the rotor from synchronous speed, the greater the iron losses. In the application to the PFEC, the rotor speed of the rotary transformer is maintained at a speed of 2/3 PU_{RT} such that the $(\omega_s - \omega_r)^2$ term in (4.21) is non-zero. Plotting this relationship and normalising with respect to the losses at synchronous speed gives the relationship in 4.13 showing the increased rotor iron losses when operated at 2/3 PU_{RT} speed.

The increased rotor iron losses in the rotary transformer of the PFEC are offset slightly by the reduction to both the stator iron losses and the stray losses of the DFIM which are dependent on the stator-side grid frequency ω_e. The stator of the DFIM has a frequency which is one-third that of the RT which implies a reduction to the C_{Fe_s} and C_{str} terms in (4.21). These effects are shown in figure 4.14 which have been normalised with respect to the losses at 50Hz, demonstrating that the stray and stator core losses of the DFIM when operated at the reduced frequency of 16.7Hz are approximately 11% of the 50Hz case.

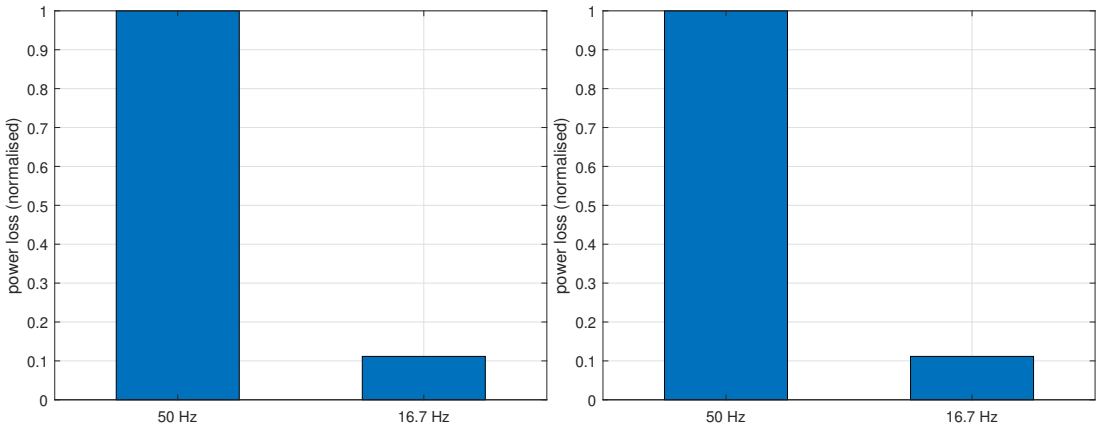

(a) Stator iron loss (b) Stray loss

Figure 4.14: Effect of reduced electrical frequency on DFIM stator iron losses and stray losses

4.4.1.1 Efficiency of the PFEC

Referring back to figure 4.12 it can be seen that some fraction of the power encounters the same kind of losses twice, once for the rotary transformer and once for the DFIM. Power entering the DFIM circuit must first pass through the stator and rotor windings of the DFIM before recombining in the rotary transformer and experiencing the copper losses of both sets of winding there also. Similarly, the core losses are duplicated due to there being two cores. The effect on the round-trip efficiency of such an arrangement remains to be seen experimentally, however an estimate can be reached by using the total efficiency of an existing wound rotor induction machine.

The most closely related relative of the PFEC is the VFT which is cited as being up to 99% efficient [78], however the rotational speeds of the VFT are considerably lower and this assumption is therefore not valid for the PFEC. Instead, one can look to the hydro-power industry where variable speed pumped-hydro is rapidly gain popularity. Upgrades to existing pumped hydro facilities are seeing replacement of conventional hydro-generators with large asynchronous doubly-fed machines which are stated at being up to 98% - 98.5% efficient [79],[80].

The majority of the losses encountered in both machines are in the core and the windings [81]. Any power entering the DFIM will experience duplicate core losses and winding losses such that the total efficiency of the PFEC can be given by (4.22), where η_g and η_m are the efficiencies of the rotary transformer in generating mode and the DFIM in motoring mode respectively.

$$\eta_{pfec} = \frac{\eta_g}{3} + \frac{2\eta_g\eta_m}{3} \tag{4.22}$$

The rationale behind (4.22) comes from the number of conversion steps that the power encounters. Upon entering the PFEC the power is split into two portions of uneven size, with one-third travelling to the rotary transformer and the other two-thirds travelling to the DFIM. The one-third fraction of power is transmitted electrically from RT rotor to RT stator. The two-thirds fraction arrives at the DFIM and is converted into mechanical power where it travels down the shaft before being converted back into electrical power. The two fractions of power then recombine to form the 1 PU_{RT} (minus losses) of power that is sent to the grid.

Conversion steps at the rotary transformer and DFIM are shown in (4.23) and (4.24) respectively, where each arrow represents a conversion stage. It can be seen that two-thirds of the power experiences two conversion steps and hence must include two efficiency terms to account for each machine of the PFEC.

$$\frac{1}{3}\ \text{PU}_{RT}\ \text{(elec.)} \xrightarrow{\eta_g} \frac{1}{3}\ \text{PU}_{RT}\ \text{(elec.)} \tag{4.23}$$

$$\frac{2}{3}\ \text{PU}_{RT}\ \text{(elec.)} \xrightarrow{\eta_m} \frac{2}{3}\ \text{PU}_{RT}\ \text{(mech.)} \xrightarrow{\eta_g} \frac{2}{3}\ \text{PU}_{RT}\ \text{(elec.)} \tag{4.24}$$

Assuming that the efficiencies of the rotary transformer and the DFIM are roughly equal such that $\eta_m = \eta_g$, then the total efficiency of the PFEC for a 16.7Hz system can be approximated by (4.25). This is an improvement over the efficiency of the VFT for offshore wind which was shown in section 3.1 to include an η term of order three due to the additional power-electronic conversion stages. To summarise, the PFEC may not

have the best efficiency of all the energy conversion devices available but it does have the best among its electromagnetic peers.

$$\eta_{pfec} \approx \frac{2\eta_g^2 + \eta_g}{3} \tag{4.25}$$

$$\eta_{vft} \approx \frac{\eta_g}{3} + \frac{2\eta_{dc}\eta_g\eta_m}{3} \tag{4.26}$$

4.5 Start-Up Procedure

Simulations up until this point have been initiated in the steady-state with the shaft already rotating at the requried 2/3 PU_{RT}. In reality it will be necessary to start the machine from a standstill during installation and planned outages for maintenance so a procedure for such an event is required.

The PFEC is a pair of cascaded induction machines which if treated individually would spin up to speed when connected to a source. By short-circuiting the rotor of the DFIM using a variable AC resistance it is possible to achieve a controlled acceleration up to rated speed without large transients arising from the inductive elements. When the induction machines are connected together in the PFEC arrangement the standard start-up approach for an induction motor should still be possible. Figure 4.15a) shows the layout of the PFEC in a single-line diagram where the rotor of the DFIM is connected to a small resistance R_{sc} to simulate a short-circuit. This has the effect of closing the circuit on the DFIM rotor but also closing the circuit on the rotary transformer rotor. When viewed from the rotary transformer's frame of reference, the rotor is simply connected to an equivalent impedance Z_{sc}. This process is seen in figure 4.15b) and c). The dynamics of how the rotary transformer responds to Z_{sc} is more complicated than how the DFIM responds to R_{sc}, however the effect is still the same in that a short circuit results.

In normal operation the rotary transformer takes speed as its input and electromagnetic torque as its output. The DFIM on the other hand takes mechanical torque

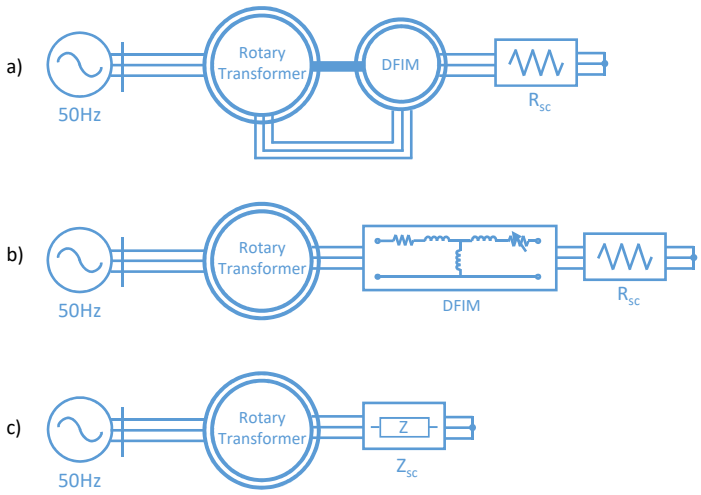

Figure 4.15: Equivalent machine layout for PFEC start-up procedure showing the DFIM acting as a short-circuited, rotor connected impedance

as its input and speed as its output. In this configuration the DFIM machine is able to regulate the rotor speed by means of the rotor-side converter. These roles must be swapped for the start-up procedure since the DFIM is merely acting as a load and cannot be used for control. It is therefore a requirement that the torque and speed inputs be exchanged so that the rotary transformer is able to accelerate naturally without having its rotor speed dictated. However, this exchange will happen naturally if the DFIM power electronics are disabled and the rotor of the DFIM is short-circuited via an impedance.

The plots of the start-up simulation for the rotary transformer are shown in figure 4.16. As the two machines accelerate, current is drawn from each of their stators, and since all current derives from the stator of the rotary transformer, this is seen to be considerably more current than would be drawn in the case of a single machine. The combined inductive reactance of the two machines is large and is seen to consume a great deal of reactive power for use in setting up the magnetic fields. Active power is consumed to provide the electromagnetic torque and some is lost due to the resistance of the windings. When the PFEC reaches the steady state value of 2/3 PU_{RT} in the RT reference frame (equivalent to 1 PU_{DFIM} in the DFIM reference frame) the PFEC

is fully magnetised and remains in equilibrium at the rated speed. Electromagnetic torque thus drops off as this is only required during acceleration/deceleration, and the active and reactive powers fall to their steady-state values. This is reflected by the sharp decline in the stator current.

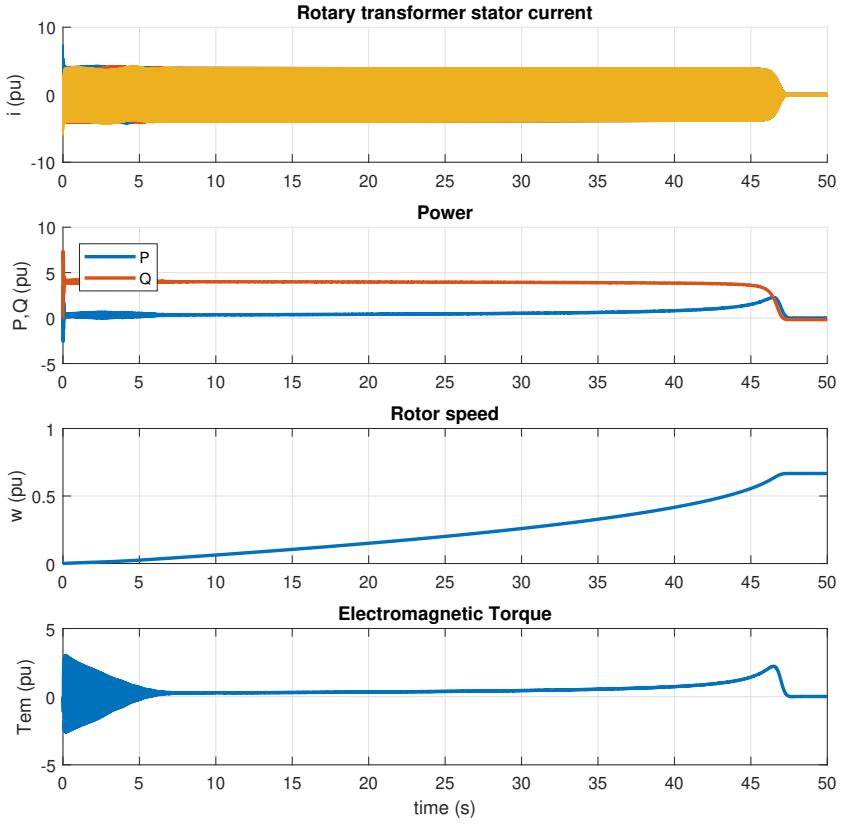

Figure 4.16: Plots of rotary transformer during startup

The DFIM exhibits similar behaviour with plots shown in 4.17. At synchronous speed, the stator and rotor fields align and thus no torque is produced. The DFIM then remains in equilibrium, drawing only enough current to remain at steady-state. Here, the speed is seen to be at 1 PU_{DFIM} and since the DFIM is rated 2/3 that of the rotary transformer, this corresponds to a speed of 2/3 PU_{RT} in the base of the rotary transformer.

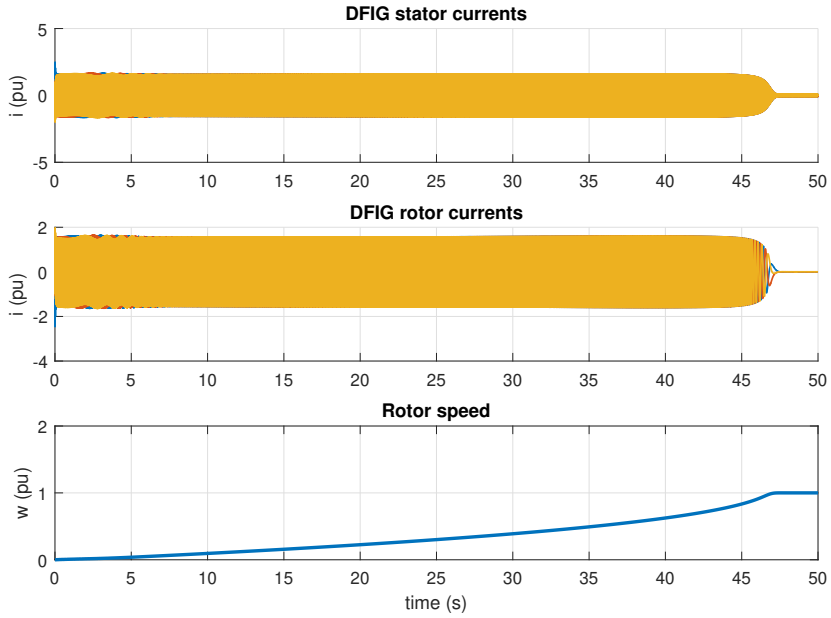

Figure 4.17: Plots of DFIM during startup

This section shows that the PFEC is able to start-up without the requirement of an auxiliary motor. The natural behaviour of the induction machines within the PFEC cause the system as a whole to accelerate up to synchronous speed where it remains at the self-sustaining equilibrium. At this point, the shaft of the rotary transformer remains at 2/3 PU_{RT} resulting in a slip of 1/3 PU_{RT} as required for the interconnection of a low frequency network to the rotor circuit. The steps for enabling this in simulation are shown below:

1. Shaft coupling I/Os are defined such that the RT takes DFIM electromagnetic torque as an input and outputs rotor speed. Conversely, the DFIM receives RT rotor speed as an input and outputs electromagnetic torque

2. Wind farm is disconnected from the circuit

3. RSC is disconnected from DFIM and replaced with a variable resistance R_{sc} during start-up. When $R_{sc} = 0$, the DFIM and hence the entire PFEC is in open-circuit and the rotor remains stationary

4. R_{sc} is increased gradually to complete the circuit and to avoid large inductive transients thereby acting as a soft-starter

5. PFEC accelerates up to the first natural equilibrium point of 2/3 PU_{RT} in the RT base (equivalent to 1 PU_{DFIM} in the DFIM base) where it remains in steady-state

6. The machine I/Os for the simulated shaft coupling are exchanged such that the RT now has DFIM rotor speed as input and electromagnetic torque as an output. Similarly, the DFIM now takes the RT electromagnetic torque as an input and outputs rotor speed

7. Variable rotor resistance is disconnected and replaced with RSC to enable full control over DFIM rotor current

8. Wind farm circuit is connected and power flows from wind farm through the PFEC and into the grid

In the real-world application of the PFEC the shaft coupling between the RT and the DFIM is a physical connection and the simulation requirement of exchanging the I/Os is not applicable. In this case the real world start-up procedure is described below:

1. Wind farm is disconnected from the circuit

2. RSC is replaced with a variable resistance in the DFIM rotor circuit

3. Variable resistance is gradually increased to avoid large inductive transients and to provide the short-circuited rotor of the DFIM required to complete the circuit. The DFIM now appears as an equivalent impedance connected to the RT rotor as shown in figure 4.15 and the machines begin to accelerate

4. PFEC reaches first natural equilibrium speed of 2/3 PU_{RT} rotor speed as defined by the pole ratio

5. Variable resistance on DFIM rotor is replaced with RSC to enable control over DFIM rotor currents

6. Wind farm circuit is connected and power flows from wind farm through the PFEC and into the grid

4.6 Frequency Control

The combined inertia of the motor-generator pair is large enough that it can be used to provide frequency support to the wider network. Modern B2B power-electronic converters store energy in the DC capacitor and can be called upon to release this energy when required, however the time constants are of the order of milliseconds. The PFEC is analogous to the B2B-VSC in that it provides a decoupling between two asynchronous networks with an energy store as a buffer between them. Instead of a capacitor, the energy buffer is characterised by the inertia and is stored as kinetic energy in the rotating masses of the rotary transformer and DFIM respectively, with time constants of several seconds which can be incorporated into modern control techniques for frequency support.

The PFEC can be made to release this energy simply by reducing the speed of the rotor, thus liberating some of the stored kinetic energy. This effect is shown in 4.18 where a reduction in rotor speed causes a dramatic, almost instantaneous spike of power. In the figure, a small rotor speed reduction of 0.05 PU_{RT} is enough to produce an additional $\approx$ 0.7 PU_{RT} of power to the grid for a short time. The effect on the electrical frequency of the low frequency side can be seen in the bottom plot of figure 4.18. A reduction in rotor speed causes an increase in slip as per (4.2) which in turn increases the frequency according to relationship in (4.27).

$$f_{r1} = s_1 f_{s1} \tag{4.27}$$

This increase in frequency will have repercussions throughout the low-frequency side of the system.

The relationship between active power and frequency is well documented in the literature but is derived here for reference. The equivalent circuit and the phasor diagram of a simple line element are shown in figure 4.19. The voltages V and E are

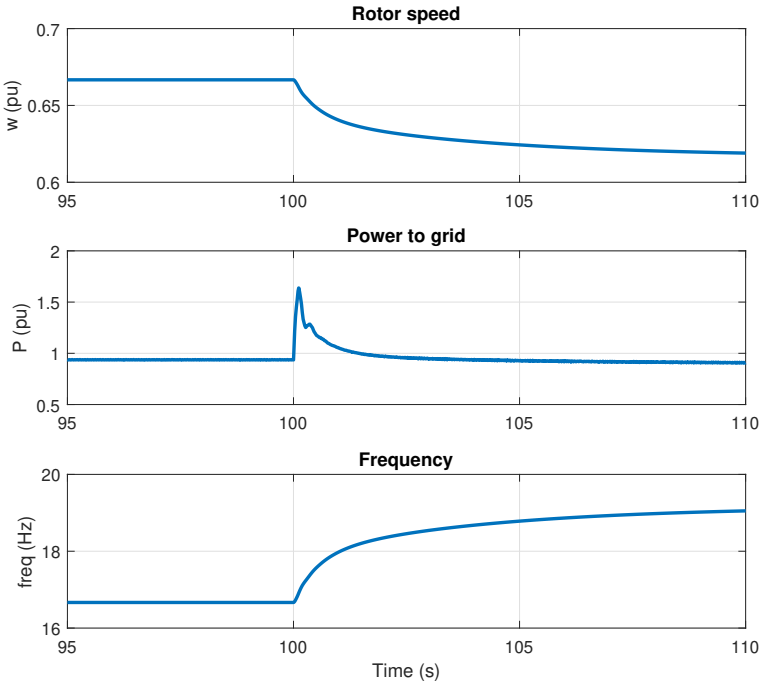

Figure 4.18: Reduction in rotor speed releases kinetic energy from rotor. From top: 1) rotor speed in RT reference frame; 2) power exported to grid; 3) electrical frequency on low-frequency side

phase voltages and the phasor $\underline{E}$ has been obtained by adding the voltage drop jXi to the voltage V. The triangles OAD and BAC are similar, and analysing triangles BAC and OBC gives:

$$|BC| = Xi\cos\phi = E\sin\delta \tag{4.28}$$

$$|AC| = Xi\sin\phi = E\sin\delta - V \tag{4.29}$$

Rearranging gives:

$$\begin{aligned} i\cos\phi &= \frac{E}{X}\sin\delta \\ i\sin\phi &= \frac{E\sin\delta - V}{X} \end{aligned} \tag{4.30}$$

The equations for active and reactive power are given in (4.31) which when com-

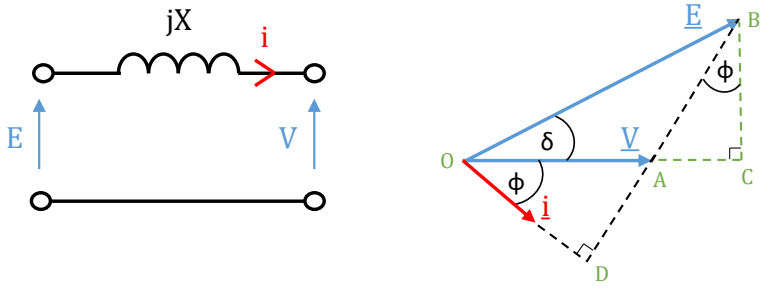

Figure 4.19: Circuit and phasor diagram of an inductive line element

bined with (4.30) give the relationships in (4.32).

$$\begin{aligned} P &= VI\cos\delta \\ Q &= VI\sin\delta \end{aligned} \tag{4.31}$$

$$\begin{aligned} P &= \frac{EV}{X}\sin\delta \\ Q &= \sqrt{\left(\frac{EV}{X}^2 - P^2\right)} - \frac{V_2}{X} \end{aligned} \tag{4.32}$$

The above analysis shows that (Q, V) and (P, δ) form two pairs of strongly connected variables. Voltage control strongly influences reactive power and vice versa. Similarly real power P is connected with angle δ. This angle is also strongly connected with system frequency f hence the pair (P, f) is also strongly connected [82]. It is therefore possible to increase the system frequency by increasing the amount of active power in the system, such as by releasing kinetic energy from the rotor as in figure 4.18.

4.6.1 Control of Rotor Kinetic Energy

In order to release the kinetic energy stored in the rotor some adjustments need to be made to the rotor speed controller. Synthetic inertia provision is the subject of chapter 5 so this section only introduces a simply control algorithm to highlight some key effects

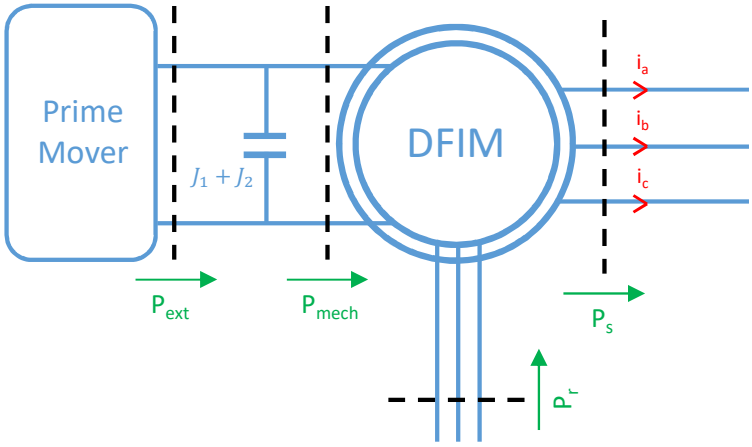

Figure 4.20: Power flows through DFIM showing the analogy between capacitor stored energy and rotational stored energy in the form of inertia $J_1 + J_2$

principles.

The kinetic energy stored in the rotor is given by eq. (4.33).

$$E_K = \frac{1}{2} J \omega_{r2}^2 \tag{4.33}$$

where $J = J_1 + J_2$ (kg/m^2) and ω_{r2} = DFIM rotor speed (rad/s). This is analogous to the electrical energy stored in a capacitor where instead of the energy being stored electrically via a capacitance C, the rotating machine stores mechanical energy via its inertia J. This analogy is shown in figure 4.20 (which is presented in the same form as figure 3.13) where the capacitor J represents the machine's inertia. Due to the similarity of the two equations, the methodology of designing the controller follows the same process.

The power balance equation is given by (4.34).

$$\begin{aligned} P_s &= P_{ext} + P_r - \frac{d}{dt}\left[\frac{1}{2}J\omega_{r2}^2\right] \\ &= P_{ext} + P_r - \frac{d}{dt}E_K \end{aligned} \tag{4.34}$$

Where P_s is the power at the stator terminals, P_{ext} is the power supplied from the prime mover and P_r is the power supplied from the rotor circuit. By treating P_{ext} and P_r as disturbances they can be removed from the equation. Substituting (4.35) into the power balance equation and neglecting the disturbance terms the power balance equation becomes that in (4.36).

$$P_s = \frac{3}{2}v_d i_d \tag{4.35}$$

$$\frac{3}{2}v_d i_d = -\frac{d}{dt}E_K \tag{4.36}$$

Applying the Laplace transformation and rearranging gives the transfer function from E_K to i_d:

$$P_J(s) = \frac{E_K(s)}{i_d(s)} = -\frac{3v_d}{2s} \tag{4.37}$$

The process of designing the controller is similar to the DC voltage controller methodology. To avoid an integral term of zero, an internal feedback loop is added to artificially move the pole away from the origin thus increasing stability. The new transfer function is given by (4.38).

$$P_J^{'}(s) = -\frac{3v_d}{2s + 3v_d G_J} \tag{4.38}$$

The PI controller can now be tuned. The open-loop transfer function of the PI controller and the plant are given in (4.39).

$$\ell(s) = \left[\frac{K_{pJ}}{s}\left(s + \frac{K_{iJ}}{K_{pJ}}\right)\right]\left[\frac{-3v_d}{2s + 3v_d G_J}\right] \tag{4.39}$$

Making the substitutions in (4.40):

$$\frac{K_{iJ}}{K_{pJ}} = \frac{3v_d G_J}{2}; \qquad K_{pJ} = \frac{\alpha_J 2}{3v_d} \tag{4.40}$$

the open-loop and corresponding closed-loop gains are found, as required:

$$\ell(s) = \frac{\alpha_J}{s}; \qquad F(s) = \frac{\alpha_J}{s + \alpha_J} \tag{4.41}$$

There are no specific rules for determining the value of G_J. A large value of will exhibit more damping, however to stick within realistic margins the same bandwidth is assigned to G_J as is found in the rest of the system. The closed loop gain of the modified system is:

$$\frac{G(s)G_J}{1 + G(s)G_J} \tag{4.42}$$

where

$$G(s) = \frac{3v_d}{2} \tag{4.43}$$

Setting this equal to $\frac{\alpha_J}{\alpha_J + s}$ we obtain the full set of tuning parameters in (4.44)

$$G_J = \frac{2\alpha_J}{3v_d}; \qquad K_{pJ} = \frac{2\alpha_J}{3v_d}; \qquad K_{iJ} = \alpha_J G_J \tag{4.44}$$

The kinetic energy of the PFEC rotor may now be related to the frequency of the electrical network via the inertia controller such that when there is a frequency excursion at the stator of the PFEC, the kinetic energy of the rotor may be released to provide frequency support.

To evidence the performance of the rotor speed controller a scenario is simulated where the nominal grid frequency drops in a step-like fashion. Although this is not realistic, it is helpful to assess the performance of the controller presented in section. The simulation introduces a step-change to the nominal frequency of the PFEC stator at t = 100s. As is the case for any PFEC, the reference rotor speed is derived from the grid and is used as an input to the controller. The response of the model is shown

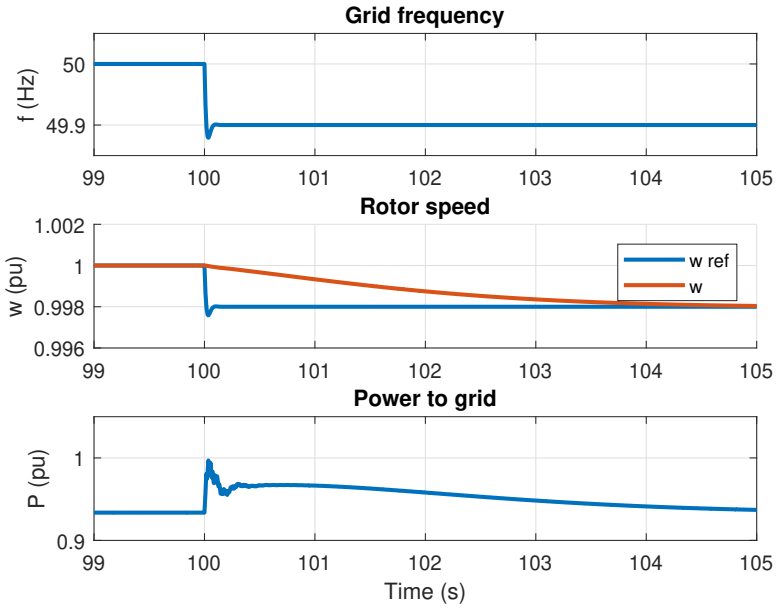

Figure 4.21: Controller response to a step change in grid frequency. 1) grid frequency as measured by the PLL, 2) rotor speed tracking the reference, 3) power exported to the grid

in figure 4.21 which shows that when the controller detects the frequency change, it slows the rotor reference speed down and releases kinetic energy in doing so. A spike in power is seen in the bottom plot of figure 4.21, which would benefit from an additional active power controller to provide a more smoothed and constant response, however this is not discussed here.

Although the rotor speed controller follows the reference well, the effect of the active power spike on the grid frequency is not seen. This is because of the presence of an ideal voltage source in the model which fixes the frequency at a constant value regardless of network conditions. Instead, the frequency drop in the simulation is the result of a step-change to the source parameters and not a true representation of a grid fault. In the coming sections this ideal voltage source will be replaced by a model that more accurately captures the grid dynamics such that the interplay between frequency and active power can be observed.

Table 4.3: Effects of frequency convergence and divergence

Δf **increases (divergence)**	Δf **decreases (convergence)**
slip s_1 decreases	slip s_1 increases
rotor speed ω_m increases	rotor speed ω_m decreases
rotor voltage v_{r1} decreases	rotor voltage v_{r1} increases

4.6.2 Frequency Divergence and Convergence

In the context of a real power system, electrical frequency is not fixed at a constant 50 Hz but instead fluctuates within prescribed tolerances depending on grid conditions. Similarly, the frequency on the LFAC-side of the PFEC is also not constant as it can be altered either by control action or due to a fault. The existence of two distinct frequencies in the PFEC make it ambiguous to refer to a drop in frequency, as one side doesn't necessarily affect the other. It makes more sense to refer to the difference between the grid frequency and the LFAC-side frequency.

Define the difference in frequency between the grid-side f_{s1} and low-frequency side f_{r1} of the PFEC by (4.45):

$$\Delta f = f_{s1} - f_{r1} \tag{4.45}$$

Depending on whether Δf is increasing or decreasing affects the conditions that are being experienced throughout the system. An increasing Δf implies that the grid frequency and the LFAC-side frequency are diverging away from one-another and a decreasing Δf implies the opposite and that the two frequencies are converging.

An example of convergence would be if the grid frequency f_{s1} drops from 50Hz to, say, 49.9Hz in the event of a fault. If the low frequency side f_{r1} is maintained at 16.7Hz then Δf will have decreased from 33.3 to 33.2. Referring to the relative difference in this way allows for a more intuitive approach as to the effects of a change in frequency on either side of the PFEC. Table 4.3 shows the effects of convergence and divergence on a number of different parameters.

These relationships can be shown mathematically by introducing the substitution for Δf into the equations for slip, rotor speed and rotor voltage to give an understanding of what to expect in the event of a grid fault or a change in operating variables. The derivations for these are shown in (4.46), (4.47), (4.48) respectively.

Slip in terms of Δf:

$$\begin{aligned} s_1 f_{s1} &= f_{r1} \\ f_{1s} - s_1 f_{s1} &= f_{s1} - f_{r1} \\ f_s(1-s) &= \Delta f \\ s_1 &= \left(1 - \frac{\Delta f}{f_{s1}}\right) \end{aligned} \tag{4.46}$$

Rotor speed in terms of Δf:

$$\begin{aligned} \omega_{r1} &= \omega_{s1}(1 - s_1) \\ \omega_{r1} &= \frac{\omega_{s1}\Delta f}{f_{s1}} \\ \omega_{r1} &= 2\pi\Delta f \\ \text{therefore:} \quad \omega_m &= \frac{2\pi\Delta f}{p1} \end{aligned} \tag{4.47}$$

Rotor voltage in terms of Δf:

$$\begin{aligned} v_{r1} &= s_1 v_{s1} \\ v_{r1} &= \left(1 - \frac{\Delta f}{f_{s1}}\right) v_{s1} \end{aligned} \tag{4.48}$$

4.7 Variable Frequency Power System Model

To investigate the response of the PFEC to a drop in grid frequency a new model must be derived which captures the dynamics of the wider network such that the grid frequency is a variable subject to disturbance. Previous models have been focused on the dynamics of the PFEC itself and have worked under the assumption that the grid

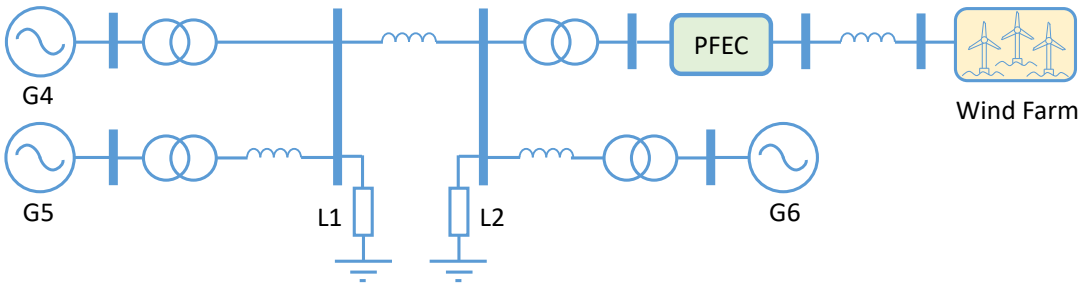

Figure 4.22: Variable frequency power system model showing the interconnection between generating units and the PFEC-enabled wind farm

frequency was a constant, never deviating from 50 Hz. The new model is designed to introduce an additional perspective such that the dynamics of the PFEC are dependent on the dynamics of the wider network and vice versa to a lesser extent. This effectively reveals the full picture because the dynamics of the grid which were previously hidden behind an ideal voltage source must now be carefully balanced to remain in synchronism and are subject to perturbations in a manner more akin to a real power system.

The network model consists of three synchronous generators of various ratings and an aggregated type-4 wind farm connected together via transmission lines represented by equivalent impedances as is shown schematically in figure 4.22. The transmission lines are arranged in such a way to separate the generating units into two distinct areas to give a two-area network model which will be important later when investigating mechanical oscillations between generating units. The three generators are sized with ratings of 900MVA, 200MVA and 200MVA while the wind farm has a rating of 100MVA to give a per unit ratio of 4.5:1:1:0.5 respectively (taking 200MVA as the base). The largest of the three generators is also equipped with a governor to regulate rotor speed and an exciter to regulate the terminal voltage. The 200MVA machines are operated with a constant torque and constant field voltage such that they cannot adjust power output or terminal voltage based on grid conditions. These functions are left entirely to the 900MVA generator to reduce the complexity of the model. The wind farm itself is represented by a 100MW VSC which provides active power to the rest of the network based on the d-current reference value id_{wind} in figure 4.23 which for compatibility

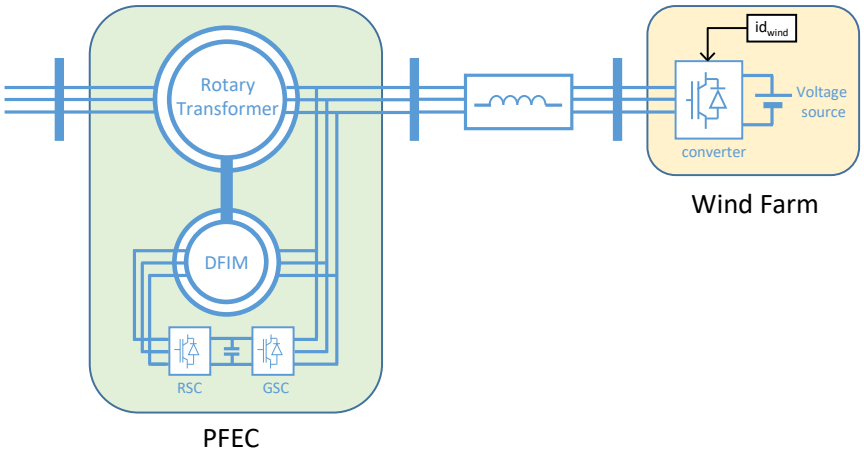

Figure 4.23: Aggregated type-4 wind farm represented by a VSC

between different simulations has been set at a constant 1 PU.

The wind farm VSC has been modified to produce power at the reduced frequency of 16.7Hz where it is then converted up to 50Hz via the PFEC for injection into the power system. All other variables have been kept the same as in scenario 1. This layout is shown in figure 4.22 and again in more detail in figure 4.23.

The governor connected to the 900MVA machine is designed to regulate the rotor speed at 1 PU. Likewise, an exciter is also fitted to the 900MVA generator to regulate the output terminal voltage. The frequency of the grid is directly proportional to the rotor speed of the synchronous machines so that a speed of 1 PU corresponds to a grid frequency of 50Hz. In the event of a loss of generation from either of the 200MVA generators, the governor will send a command to produce more active power in an attempt to correct the error in grid frequency. The generator cannot be made to produce unlimited power so at some point the governor will saturate at the maximum power output.

The power system model in this section uses a basic representation of a transmission line as an equivalent impedance. In contrast, a pi-section contains two capacitive

elements which would increase the order of the model by two for each transmission line present so these have been omitted in favour of the equivalent impedance approach to simplify the model.

4.7.1 Simulating the Loss of a Generating Unit

A generating unit is disconnected to trigger a drop in frequency. The DFIM rotor speed controller works to regulate the speed required to fix the low frequency side at 16.7Hz by making adjustments based on network conditions. When the generating unit is disconnected, the grid frequency drops and the controller adjusts the rotor speed accordingly to maintain 16.7Hz on the low frequency side. This has the effect of reducing Δf to signify the concept of converging frequencies.

Figure 4.24 shows the generator torque for the three generating units and the effects that this has on the system frequency. At t = 80s, generator 2 is disconnected as indicated by the sudden drop to zero torque and hence zero power. The reduction in active power causes the system frequency to drop from the nominal 50Hz to a lower equilibrium, at which point generator 2 is brought back online. The effects on the grid frequency, low frequency and Δf can be seen.

The expressions in (4.46) and (4.47) are demonstrated in figure 4.25 showing that as Δf decreases, slip increases and rotor speed decreases. The plot for slip shows some interesting behaviour which initially appears as a delay similar to the non-minimum phase characteristics of the DC voltage controller. A closer look at the slip in figure 4.26 shows the slip broken down into constituent parts, i.e. the grid frequency ω_{s1}, the RT rotor frequency ω_{r1}, the subtraction $\omega_{s1} - \omega_{r1}$ and the reciprocal term $1/\omega_{s1}$. The first thing to notice is the oscillation present on the grid frequency trace which occurs due to the sudden disconnection of generator 2 and percolates throughout the entire system for a short time. Secondly, the reciprocal term is seen to be the only increasing quantity which occurs due to the sharp initial fall in ω_{s1}. This positive reciprocal term produces an opposing gradient in the plot for the slip for a short time and is the reason

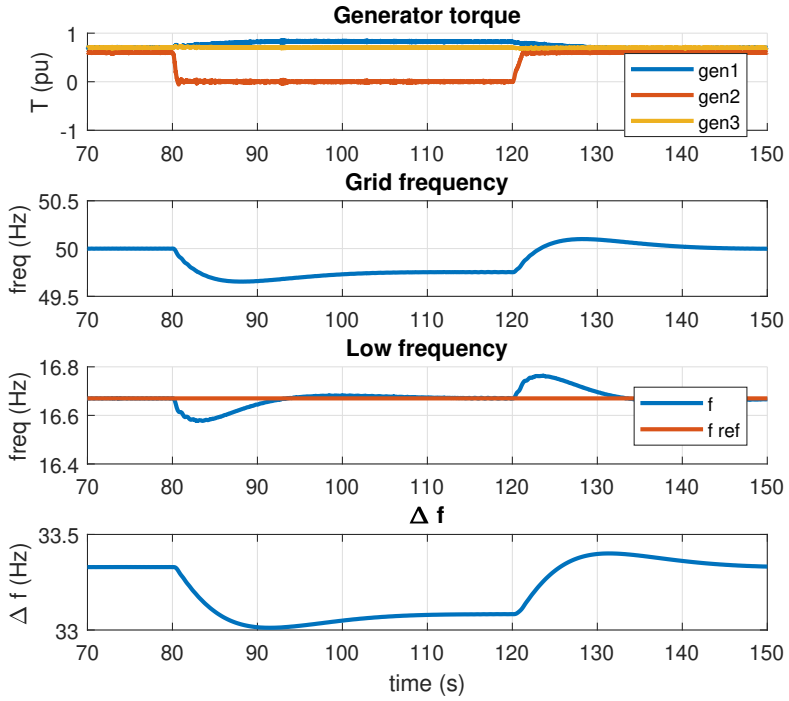

Figure 4.24: Disconnection of generator 2 and the effects on frequency throughout the system. From top to bottom: 1) Torque on generator 2 is disconnected at t = 80s then reconnected at t = 120s. 2) Grid frequency drops in response to losing a generating unit. 3) Low frequency side is held at reference levels. 4) Δf as a function of f_{grid} and f_{low}

for the short delay.

Also visible in 4.25 is the rotor speed of the PFEC showing its natural response to a drop in frequency. As the rotor speed slows, kinetic energy is released providing a natural inertial provision to the grid. When generator 2 is reconnected, the PFEC replenishes the spent kinetic energy such that the rotor speed can accelerate back to the nominal value.

A separate simulation was run to explore the effect of Δf on rotor voltage. In the previous simulation the loss of a generating unit caused the frequency to drop from 50Hz to 49.6Hz in v_r, however the effect on rotor voltage was too slight to notice graphically.

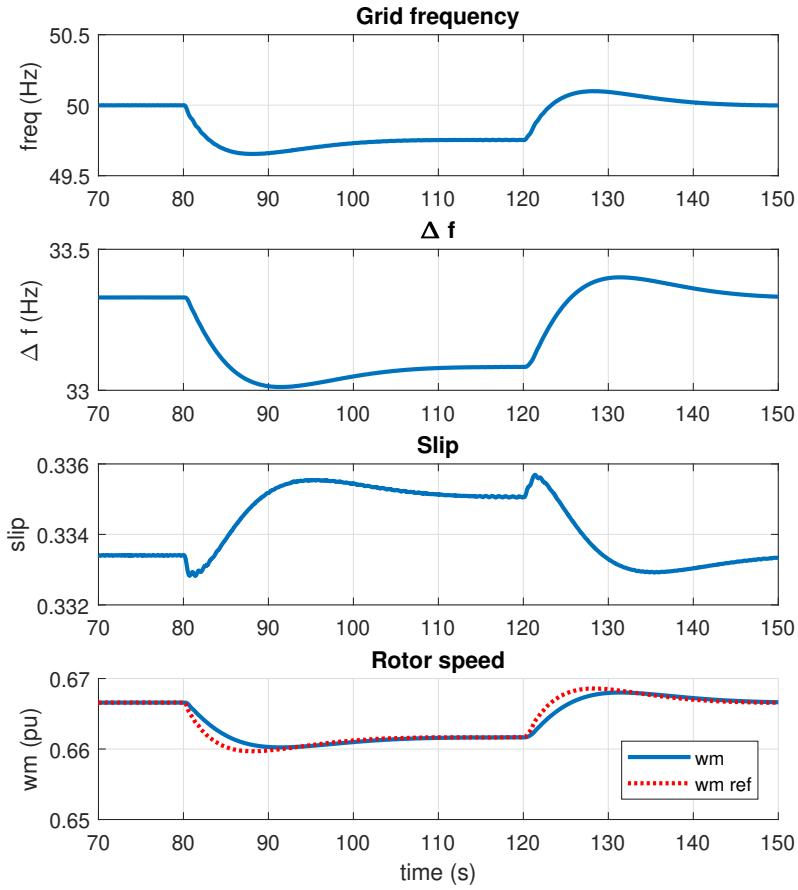

Figure 4.25: From top: 1) Grid frequency 2) Frequency difference, 3) slip showing non-linear behaviour, 4) rotor speed and setpoint

In the new simulation, the low-frequency reference point is varied in three steps from 15.5Hz to 16.7Hz and then up to 18Hz, equivalent to a drop in frequency of 1.3Hz when compared to the previous run. The effects of Δf on slip and phase voltage are shown in figure 4.27 where the inverse proportionality of voltage on Δf can be seen.

4.8 LFAC Overvoltage Limits

It has been shown that the PFEC is able to control the frequency on the LFAC-side by sacrificing the rotor voltage in order to provide real inertia to the grid. An increase

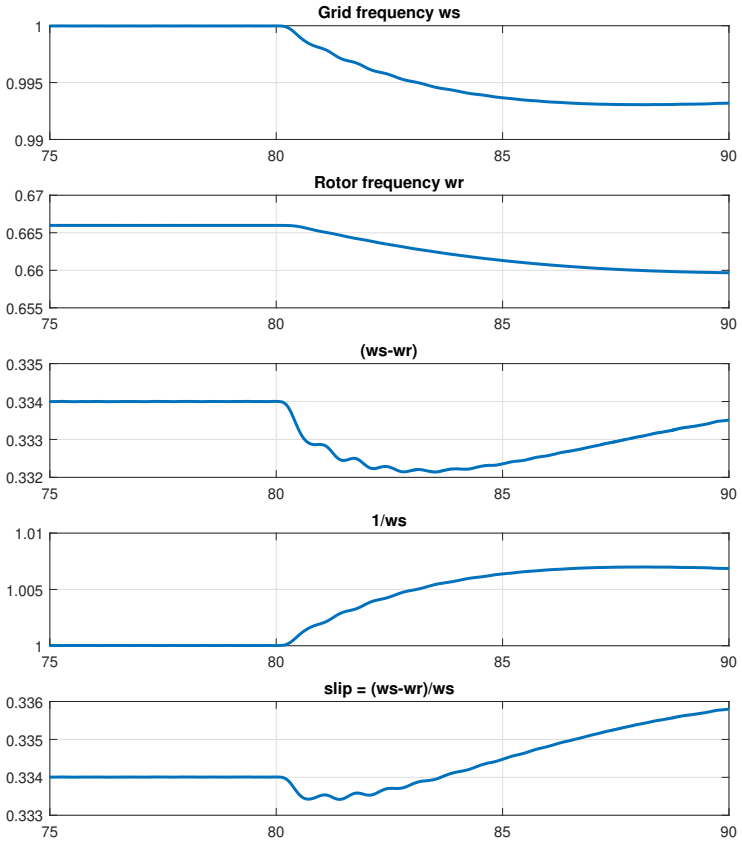

Figure 4.26: Constituent parts of slip. From top: 1) Grid frequency ω_{s1} 2) RT rotor frequency ω_{r1} 3) The (subtraction $\omega_{s1} - \omega_{r1}$) 4) The reciprocal term $1/\omega_{s1}$ 5) RT slip

in frequency characterised by a decreasing Δf causes the rotor voltage to increase proportionally to the slip. It is therefore necessary to limit the allowable frequency control region based on an overvoltage constraint imposed by the wind farm.

Low voltage ride through, or fault ride through (FRT) was initially identified because of an issue with wind generation and has since been defined by grid codes worldwide. The problem is defined in [83] which describes how wind farms had a tendency to trip if the terminal voltage dropped even below 90% of nominal for even a few milliseconds. During a transmission system fault and the subsequent voltage drop, there was

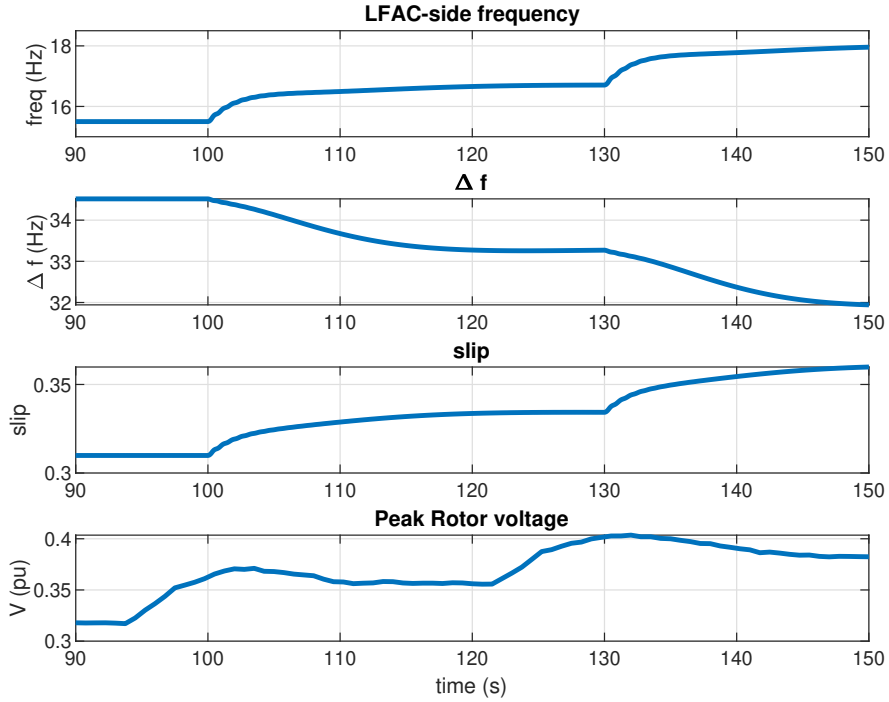

Figure 4.27: Low-frequency reference is increased from 15.5Hz to 16.7Hz and then to 18Hz at t = 100s, 130s respectively. From top: 1) Frequency on LFAC side 2) Frequency difference 3) slip 4) phase a rotor voltage

a possibility for loss of wind generation leading to frequency collapse and ultimately a blackout. FRT provides a set of rules defining when it is acceptable for a wind farm to trip or not. These criteria are shown in figure 4.15 for a range of European countries.

High-voltage ride-through (HVRT) on the other hand is not as well defined in many countries. The level of overvoltage that power converters can withstand is relatively small when compared to electrical machines so it is important to limit the overvoltage in some applications. Shown in table 4.4 is a summary of HVRT in different countries, defining the reasons for needing HVRT and the thresholds at which to trip.

The PFEC experiences an increase in rotor voltage when the frequency on the low side is increased for control purposes. Since the wind farm is connected to the rotor circuit, it is important not to increase the frequency beyond a certain threshold to prevent any unwanted tripping of wind farms. It is proposed that the HVRT limit to

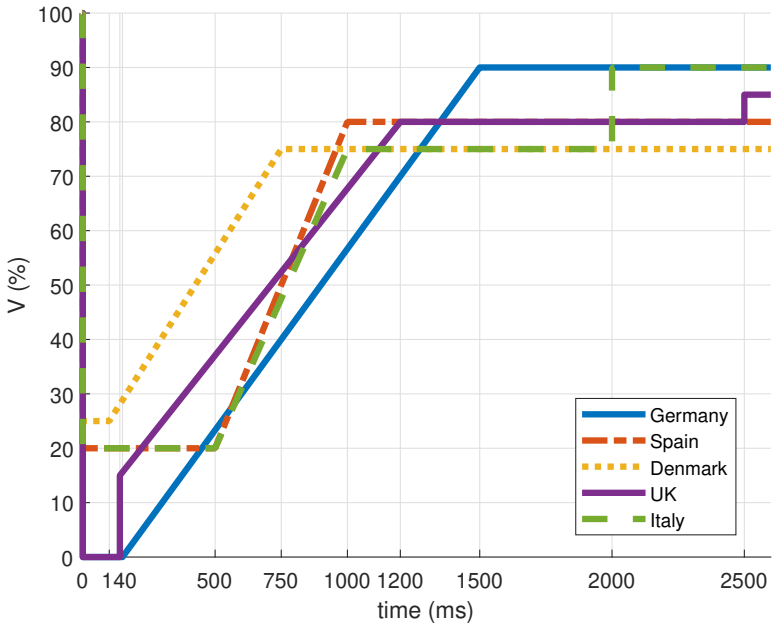

Figure 4.28: Fault ride through requirements of several grid codes in Europe

Table 4.4: HVRT summary for different countries [84]

Country	**Requirement for:**	**V profile (PU)**
Australia	Generating plant	1.3 PU, 60ms; 1.2 PU, 0.4s
Germany	Generating plant	1.2 PU, disconnect with a delay of 0.1s
Spain	Wind farm	1.2 PU, 50ms
USA	Wind farm	1.2 PU, instantaneous trip; 1.175 PU, 0.2s; 1.15 PU, 0.5s; 1.1 PU, 1s
China	Wind farm	1.2 PU, instantaneous trip; 1.15 PU, 0.2s; 1.1 PU; 2s

which the PFEC should abide is to increase rotor voltage to no more than 1.2 PU_{DFIM}, in line with the majority of values in table 4.4. The FRT curve in figure 4.28 should therefore be extended to include the HVRT condition, as shown in figure 4.29.

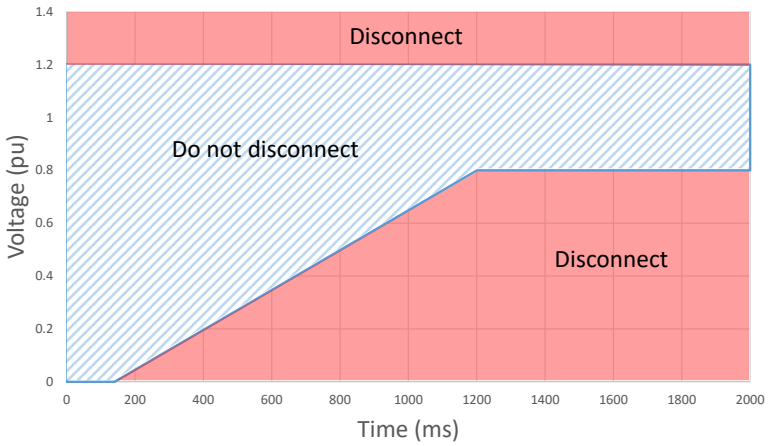

Figure 4.29: FRT conditions for PFEC connected wind farm showing overvoltage

With the overvoltage limit defined as 1.2 PU_{DFIM}, the PFEC is able to sacrifice the nominal voltage slightly to allow flexibility on the low frequency side. Frequency can therefore be manipulated until the FRT condition is exceeded. It is worth nothing that further frequency manipulation is possible using the reactive power control of the wind turbines and of the B2B converter of the DFIM to reduce the voltage amplitude in the LFAC system, as well as solutions such as tap-changing transformers, however in this thesis we will assume that those solutions are not implemented.

An approximate theoretical limit to the flexible frequency can be determined from (2.38) and (4.49).

$$v_{r1} = s_1 v_{s1} \tag{4.49}$$

Rotor voltage v_{r1} must not exceed 1.2 PU_{DFIM} in the DFIM reference frames, which corresponds to 0.4 PU_{RT} in the RT reference frame. Assuming v_{s1} is constant and equal to 1 and substituting $v_{r1} = 0.4$, we get the upper bound of slip as 0.4.

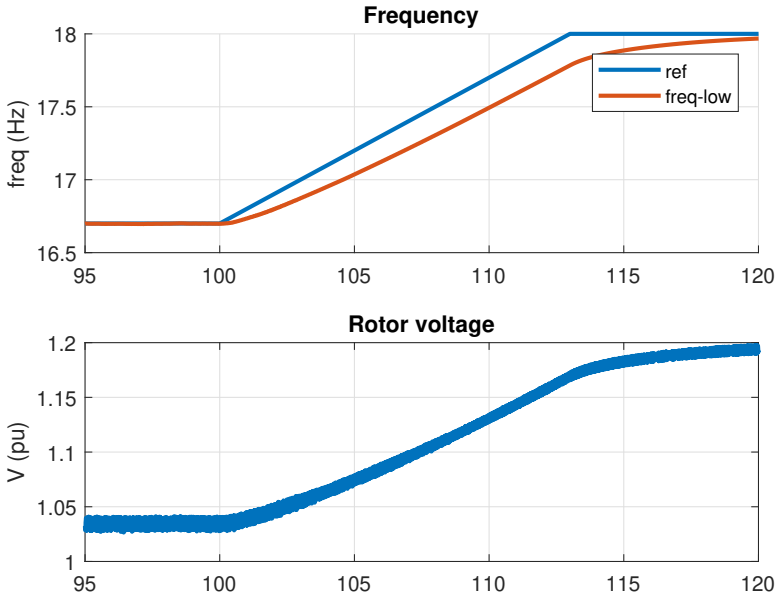

Figure 4.30: Increase in frequency set point causes increase in rotor voltage

Substituting $s_1 < 0.4$ into (2.38) gives the upper bound of rotor frequency:

$$f_{r1} < 20 \quad \text{(Hz)}$$

20Hz is therefore the theoretical limit to the flexible frequency range. Practically the limit will be smaller to provide sufficient headroom in the event of a fault. Simulation results help to demonstrate this point and show that the actual limit should be reduced.

Figure 4.30 displays the results from a simulation in which a ramp function was sent to the low frequency reference, increasing it from the nominal level of 16.7Hz up to 18Hz. The top plot shows the ramp increase and the corresponding control action, while the bottom plot shows the voltage magnitude for one phase of the rotor. At 18Hz, the 1.2 PU_{DFIM} voltage threshold is reached meaning that any further increase in slip would trigger a wind farm disconnect.

4.9 PFEC as an Energy Storage System

The same simulation demonstrating frequency thresholds has brought the prospect of battery storage into view. It is hypothesised that by reducing the rotor speed of the PFEC, enough kinetic energy may be released to charge a battery on-site at times of low demand. Power is released when the rotor experiences a decrease in speed, as shown by the derivation in (4.50):

$$\begin{aligned} E_K &= \frac{1}{2} J \omega_m^2 \\ E_K &= \int P dt \\ \text{therefore} \quad P &= \frac{1}{2} J \frac{d\omega_m^2}{dt} \end{aligned} \tag{4.50}$$

By sending a ramped decrease in rotor speed, equivalent to an increase in the low frequency reference, a constant power output is sustained for as long as the ramp occurs. By connecting a suitably sized battery to the PFEC system, this power could be captured and stored. The size of the battery depends on exactly how much power is released can be measured through simulation.

The same simulation is run again but this time with a measurement on the power output. The results are shown in figure 4.31, where it can be seen that an approximately constant level of power is produced from the deceleration from the rotor. The area under the square signal in the bottom plot indicates the rough amount of energy available for battery storage, which is calculated to be:

$$\begin{aligned} E_{store} &= \int_{101}^{113.5} P dt \\ &= 100e^6 \times \left[\frac{(0.946 - 0.9275) \times (113.5 - 101)}{3600} \right] \quad (Wh) \\ &= 6424 \quad (Wh) \\ &= 6.424 \quad (kWh) \end{aligned} \tag{4.51}$$

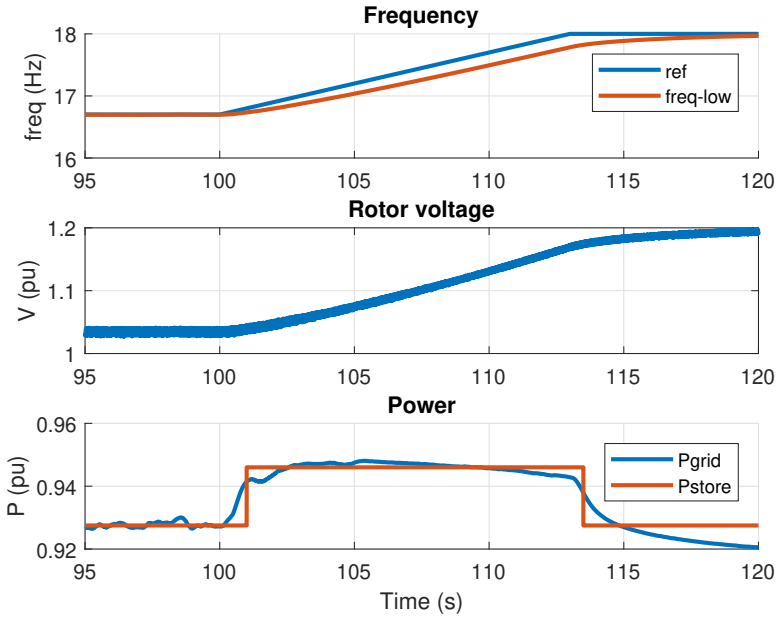

Figure 4.31: Energy stored from rotor deceleration

It is concluded that this low yield of energy does not justify the case for rotor-deceleration-based energy storage. The added complexity in design of a battery storage system combined with the increased stress on the components due to overvoltage during the charging stage does not make economic sense, especially considering that a 100MW PFEC system can only charge in incremental values of 6.5kWh.

4.9.1 Firm Frequency Response

Instead of using the deceleration of the rotor to charge a battery, it may be possible to apply for the Firm Frequency Response Service (FFR) which has the following requirements:

- Deliver a minimum of 1MW response energy
- Response provided within 10 seconds of an event, which can be sustained for a further 20 seconds

To satisfy the requirements for FFR the PFEC doesn't need to have hours of energy storage available but instead only needs to provide a response of 1MW for 20 seconds.

The question therefore becomes: 'Can the PFEC deliver an additional 1MW of power for 20 seconds, and if so, how much will the frequency change on the LFAC side?' In case the increased frequency on the LFAC side reaches dangerous values due to the associated increase in voltage magnitude, a further question would be: 'What is the minimum size of PFEC which could offer the service?'

Another simulation was conducted to answer these questions. In it, a ramped decrease in rotor speed was sent to the DFIM to produce a constant power output in much the same way as before, however this time the ramp was extended in duration to show the effects of a sustained ramp signal.

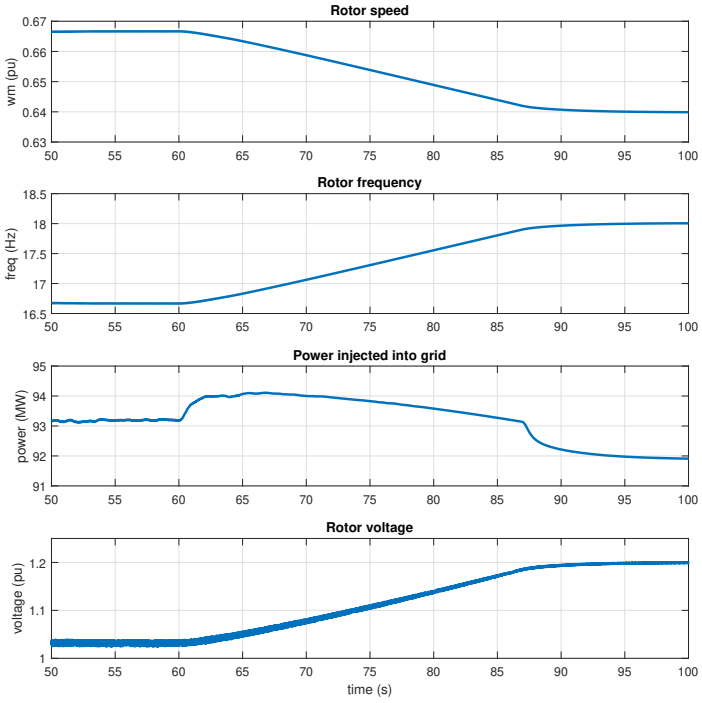

Figure 4.32: Simulation results showing PFEC potential for FFR provision

The simulation results are shown in figure 4.32. At t = 60 seconds a ramp signal is sent to the DFIM rotor speed controller to facilitate a constant deceleration corre-

sponding to an increased power output of 1MW. The ramp signal continues until the increased LFAC frequency causes the rotor voltage to reach a maximum value of 1.2 PU_{DFIM}, as this was identified as the fault ride-through limit for overvoltage. It can be seen that the 100MW PFEC is capable of providing an additional 1MW for around 10 seconds before the power begins to fall despite the ramp signal still being sent. This occurs at t = 70 seconds in figure 4.32 when the injected power begins to steadily decrease even though the rotor is still decelerating. This phenomenon reflects how the increased frequency on the LFAC side has a detrimental effect on the charging current in the cable. It can also be seen that this reduction in power output occurs before the maximum voltage of 1.2 PU_{DFIM} is reached, demonstrating that the limiting factor is more to do with the cable losses than overvoltage. Here, other mechanisms such as wind farm reactive power control or DFIM reactive power control could be used to counteract the increased reactive capacitance of the cable because of the change of frequency.

Figure 4.32 shows that the 100MW PFEC model without modification is capable of providing an additional 1MW power for 10 seconds before cable losses begin to dominate over the kinetic energy released by the rotor. Assuming that this effect scales linearly with rated power, a 200MW PFEC should therefore be able to deliver 1MW for 20 seconds (or 2MW for 10 seconds) and a 300MW PFEC, which was identified as the maximum PFEC unit size, would certainly be able to satisfy the FFR requirements. However, this analysis is based on simply slowing the down the rotor using the existing control algorithms without the development of any new control algorithms. A fully dedicated FFR power controller would certainly perform better by fixing a power output reference and having the PFEC track this increased power reference for a specified amount of time, however the effect of a reduced rotor speed and resulting increased LFAC frequency would indeed have knock-on effects on the line impedance and rotor-side voltage, each of which may impose a limit of the PFEC before the FFR criteria are met.

4.10 Theoretical Maximum 600MW Model

The machine parameters of the PFEC used throughout this chapter have been based on the parameters of the 100WM VFT by General Electric due to this being the most similar technology to the PFEC. It is reported that the theoretical maximum rating of the VFT is largely dependent on the capabilities of the collector network, in particular the brushes and slip rings which experience significant arcing at high voltage and power levels [85]. Because of this, the highest rated VFT is currently the 300MW unit located at the Linden facility. DFIMs with slightly higher ratings are found in the field of adjustable-speed pumped hydro where the current record belongs to a pair of 400MW generating units at Okawachi, Japan [86].

In light of these technological limitations, a new PFEC model has been developed to reflect the maximum size which could potentially exist to date, which has been identified as being 600MW. At first this seems to contradict the maximum criterion set by the 400MW DFIM at Okawachi, however by analysing the share of power handled by the two machines within the PFEC, the power balance can be exploited to essentially over-size the device.

A 600MW wind farm generating at the full capacity of 1 PU_{RT} produces 600MW of power which after reaching the onshore PFEC simultaneously splits into two streams. 1/3 PU_{RT} (200MW) arrives at the RT rotor terminals and the remaining 2/3 PU_{RT} (400MW) arrives at the DFIM stator terminals. These two shares of power then recombine at the RT stator terminals to inject the full 1 PU_{RT} (600MW), negating losses, into the grid. The slip rings and brushgear of the RT only handle a maximum of 200MW, and it is therefore possible to create a 600MW PFEC system using a 400MW DFIM and an RT with a collector network rated for 200MW. The remaining components of the RT such as the stator windings still need to be sized for 600MW but in this way the technological bottleneck imposed by the brushgear and slip rings is avoided. It should be noted that the concept of a brushless-PFEC is introduced in appendix A which may

alleviate this maximum power limitation by removing the slip rings altogether.

4.10.1 Reactive Power Compensation

The amount of reactive power compensation required to give a unity power factor when measured at the RT terminals is calculated by replacing the wind farm with a purely resistive load of equivalent rating, i.e. 600MW in this case. In the absence of the wind farm, the direction of power flow is reversed but the effect on the reactive power is effectively unchanged. The total reactive compensation required can then be found by measuring the reactive power consumption of each of the elements in the PFEC, namely at the terminals of the RT, DFIM, and transmission line respectively. A good approximation to the amount of reactive power compensation required can then be determined by summing each of these constituent parts together, which is found to be -0.56 PU_{RT}, or 336MVar.

A simulation was then run with the addition of 336 MVar of reactive power compensation to demonstrate the effect on the power factor of the PFEC when measured at the grid bus. The simulation results are presented in 4.33 and show the reactive power both before and after the DFIM controller is enabled at t = 5 seconds because once its q-axis controller is functioning then the reactive power will be regulated at 0 regardless of grid conditions. Showing the value of Q before the effects of control therefore demonstrates if the correct amount of compensation has been added. The benefits of proper sizing translate to less stress imposed on the q-axis controller which no longer has to work as hard to regulate Q at zero.

4.10.2 600MW PFEC Steady-State Simulation

The model described above is initialised using the 600MW PFEC parameters given in the appendix to allow the interconnection of a 16.7Hz wind farm with a 50Hz AC grid. 336 MVar reactive power compensation is added to the receiving end of a 200km

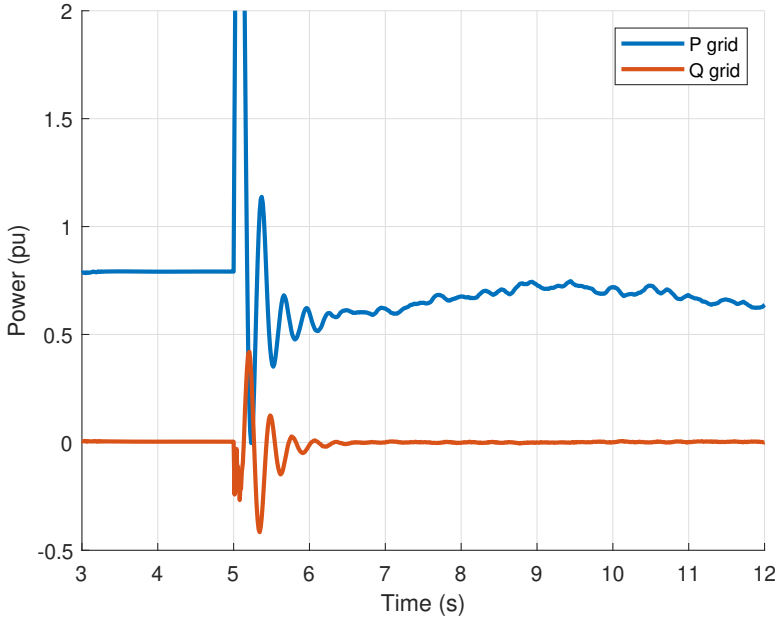

Figure 4.33: Active and reactive power (P, Q) measured at PFEC stator terminals, demonstrating unity power factor even in the absence of control

pi-section transmission line with capacitance 106nF/km to provide unit power factor when measured at RT stator terminals. The rotor speed controller is programmed to maintain a steady-state value of 2/3 PU_{RT} in the RT base. Control is switched on at t = 5 seconds to avoid large starting transients in the model. The results are simulation results are shown in figures 4.34.

Figure 4.34a shows the constantly varying wind field from the Kaimal spectrum wind model and how the resulting d-current reference value translates into power generated from the wind farm. Power is measured first at the wind bus where it is initially generated and then again at the grid bus to show the effect of the losses throughout the system which fluctuate around the 0.1 PU_{RT} mark. Figure 4.34b displays plots of the same simulation and focuses on the rotor dependent variables, i.e. the rotor current, the rotor speed and the LFAC-side frequency. Rotor current is given in *abc* values for the three phases and can be seen to follow the same patterns as both the wind and the active power delivered by the wind farm. As wind speed decreases, the amount of current in the RT rotor windings decreases thus weakening the magnetic

coupling between rotor and stator and thus allowing the rotor to accelerate slightly. The inversely proportional relationship between rotor speed and LFAC-side frequency is also seen. Likewise, the converse is true with an increasing wind speed. The rotor speed controller acts to regulate the speed at 2/3 PU_{RT} which it achieves well, only deviating by fractional amounts. The speed of response of the rotor speed could be increased or decreased by adjusting the rise time of the controller, however owing to the large mass of the PFEC, a rise time of 2 seconds seems appropriate.

4.10.3 Operating During Faulted Conditions

To investigate the effect of a grid fault on the PFEC, the model was updated to include a three-phase fault block from the Simulink library connected between the RT stator and the 50Hz AC source. At (20 + 1/50) seconds (20 plus one 50Hz AC cycle) a three-phase fault to ground is triggered which last for 4 cycles, being automatically cleared at (20 + 5/50) seconds. The fault resistance and ground resistance are set to 0.001Ω and 0.01Ω respectively.

Figure 4.35 demonstrates the effect of the three-phase fault on the PFEC which ultimately leads to instability and desynchronisation. The fault is visible by the collapse of the grid voltage after 20 seconds leading to a multitude of problems throughout the system. The stator currents become distorted, the power spikes and the system frequency is seen to oscillate wildly, both on the 50Hz side and the LFAC-side. Figure 4.35b identifies that the causes of the instability are due to the desynchronisation of the PLL used by the DFIM to synchronise with the LFAC network, which cannot operate in the absence of a voltage reference, and also the high rotor currents in the DFIM controller circuit which are seen to reach in excess of 5 PU_{RT}.

A second simulation was conducted under the same faulted conditions but with the controller and the PLL disabled. Results in figure 4.36 show the same voltage collapse but this time the PFEC recovers. Synchronism is maintained between the 50Hz and

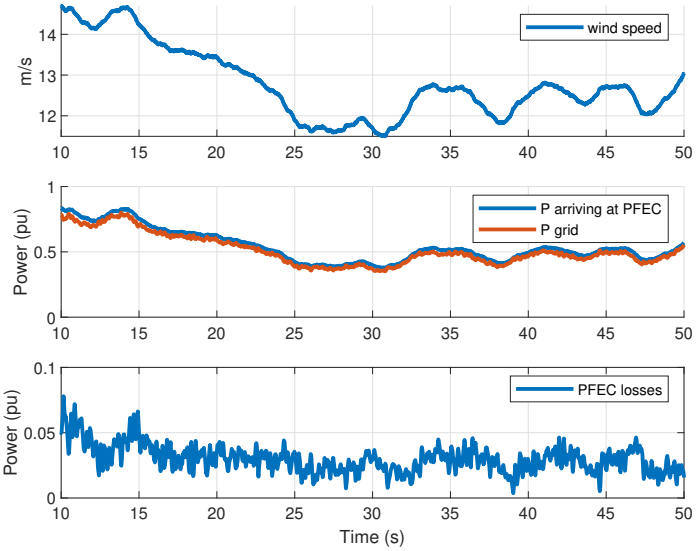

(a)

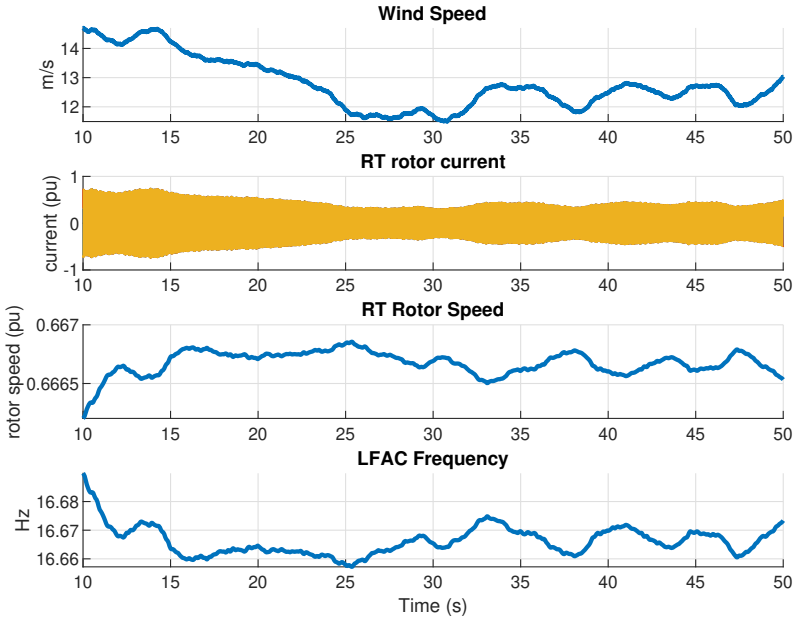

(b)

Figure 4.34: 600MW simulation results: a) Power sent from wind farm and power received at the grid bus. b) Rotor dependent variables of 600MW PFEC simulation

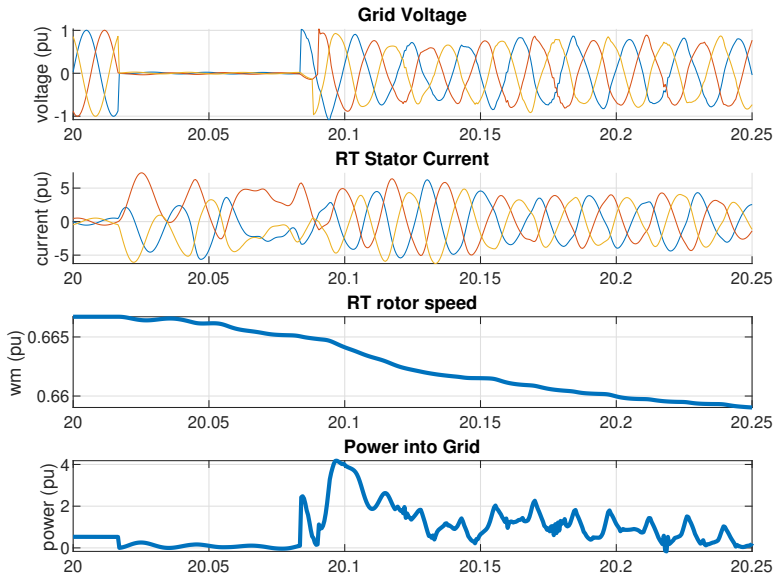

(a)

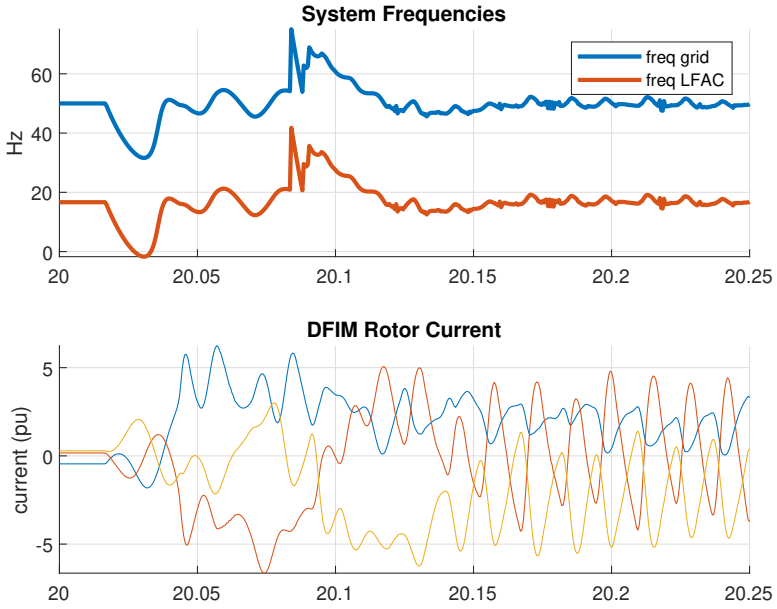

(b)

Figure 4.35: Simulation of a three phase fault: a) Voltage collapse leading to instability. b) PLL de-synchronism and high DFIM rotor currents

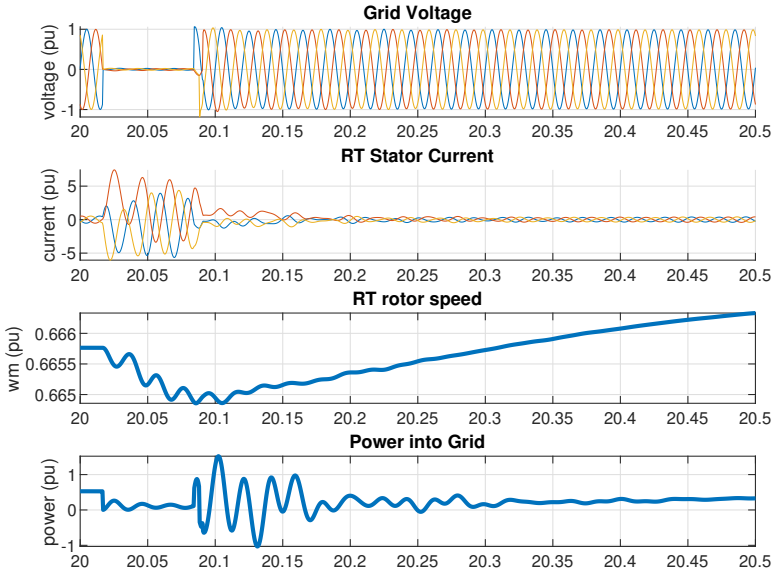

Figure 4.36: Fault in the absence of DFIM controller showing recovery

the 16.7Hz networks because of the existence of the self-sustaining property. The initial drop in rotor speed during the fault increases back to nominal values once the fault is cleared, and power flow to the grid is restored. The RT stator currents are also seen to return to sinusoidal waveforms. This shows that the core components of the PFEC are naturally stable in the event of a fault and that the dangers lie in the controller and the PLL. A possible solution to avoid these dangers could be the design of a more robust PLL or to replace the PLL with direct information of the rotor position of the RT, just like in the case of DFIG wind turbines. The addition of a current limiting device such as a crowbar to the DFIM rotor circuit could therefore be used to protect the controller from dangerous overcurrents. Once the fault has cleared, re-connection of the controller would then return the PFEC to normal operation.

4.11 Summary and Conclusions

This chapter provides simulation results and validations of the various models derived in chapter 3 with the goal of discovering some of the characteristics of the PFEC. Both the PFEC and VFT for offshore wind split the power transformation into two streams

simultaneously and are capable of allowing frequency variations between grids without losing synchronisation. However, the VFT does so at the expense of using a DC motor which is reliant on a power-electronic converter rated for the same power. The incorporation of a DFIM instead of a DC motor allows precise control over the rotor speed via the RSC without the costly requirement of fully-rated equipment. Since the electrical frequency of the LFAC network is completely dependent on the rotor speed of the PFEC, this leads to the result that frequency can be treated as a control variable and can be manipulated using a suitably designed controller.

Losses associated with the pair of induction machines within the PFEC are introduced to give an idea of the total power lost and the efficiency of this solution as a whole. The role of the power-electronic converter is also analysed to introduce the concept of a self-sustaining equilibrium: a state in which the PFEC manages to remain synchronised to the network as a natural electromechanical response even in the absence of any type of active control. The consequence is that the PFEC can be designed to be inherently stable providing that care has been taken to correctly size the pole ratios of the RT and the DFIM respectively based on the required asynchronous frequency interconnection. The results of the self-sustaining equilibrium culminate in a reference table of possible pole arrangements to enable the interconnection of a variety of different frequencies, e.g. 25Hz, 16.7Hz, 10Hz etc.

A procedure for energising and initialising the PFEC simulation is introduced and how this translates to a hypothetical real-world application. The result is that the PFEC can be energised and brought up to to the required synchronous speed by relying on the principles of induction machines without the need for an auxiliary third machine to provide the starting torque.

Finally, the theoretical maximum size of a single PFEC unit has been discussed and found to be rated at 600MW based on the limitations imposed by the slip rings and brushgear. The largest commissioned DFIM to date has a rating of 400MW and

this value has been used to impose an upper bound for the DFIM within the PFEC. By exploiting the power balance within the PFEC it is shown that 1/3 PU_{RT} of the total power arrives at the RT rotor and 2/3 PU_{RT} travels to the DFIM. Therefore, by setting the upper bound at 600MW, the shares of power that arrive at either set of slip rings are only 200MW and 400MW respectively such that the technological limitations are circumvented. Under the assumption that the RT stator windings can be rated for 600MW, the two shares of power then recombine at the RT stator to transmit the full 600MW into the network. Simulation results validate this hypothesis and provide a detailed description of the transit of power from the wind field to the grid.

Chapter 5

PFEC Synthetic Inertia Provision

This chapter investigates at how the PFEC can be retrofitted with a controller to take advantage of the stored kinetic energy in the combined rotors of the DFIM and the RT. Synthetic inertia controllers applicable to the DFIG in a wind turbine can be modified for application in the PFEC to enable the use of virtual inertia control and to help limit the rate of change of frequency (ROCOF) during a frequency disturbance. During such an event, the synthetic inertia control loop works by further reducing the rotor speed past what would normally be seen as a natural response of the machine thus releasing more kinetic energy and hence active power to the grid. Once the frequency event has cleared, the PFEC can reclaim the rotational energy that was expended and return to the optimum rotational speed.

Later in the chapter the concept of small-signal stability is introduced and how the integration of the PFEC with a conventional network affects the stability of the power system in such a manner. As was shown with the DFIG in [87], the presence of synthetic inertia control loops can have unexpected negative side effects on small-signal stability by increasing the decay time of certain mechanical oscillatory modes between generators. These low-frequency, inter-area modes can have detrimental effects on transmission capacity and stability of the power system as a whole [88]. Analysis of the results of the PFEC in various network situations will determine how the damping of these modes are affected and whether care must be taken when offering frequency

ancillary services.

5.1 Background and Motivation

Modern power systems are facing unprecedented levels of renewable energy penetration motivated by government targets and potential reductions to the cost of energy. The introduction of large scale wind power generation may lead to the decommissioning of conventional synchronous generators which will have a negative impact on the stability of the system of a whole. Without the large rotating masses and the associated inertia that these synchronous generators provide, the frequency of the system will become more sensitive to disturbances. Additionally, type-3 and type-4 variable speed wind turbines which are the most common topologies in new developments [89] are decoupled from the grid through power electronic converters, meaning that their inertia contributions cannot be 'seen' by the wider network. As the penetration of low inertia wind energy increases, the effect on power system stability becomes an important issue which needs to be addressed [90].

The concept of synthetic inertia for offshore wind is well documented in the literature [91]. Unlike a synchronous generator, the kinetic energy stored in the wind turbine blades is decoupled from the wider network and cannot be readily accessed being only be released through control action. The term synthetic comes from the fact that there is no instantaneous response to a drop in frequency in the wider network and all action is achieved through the power electronic converter. The share of wind power is now so large that system operators are revising their grid codes such that wind farms require frequency control capabilities in specific conditions [92].

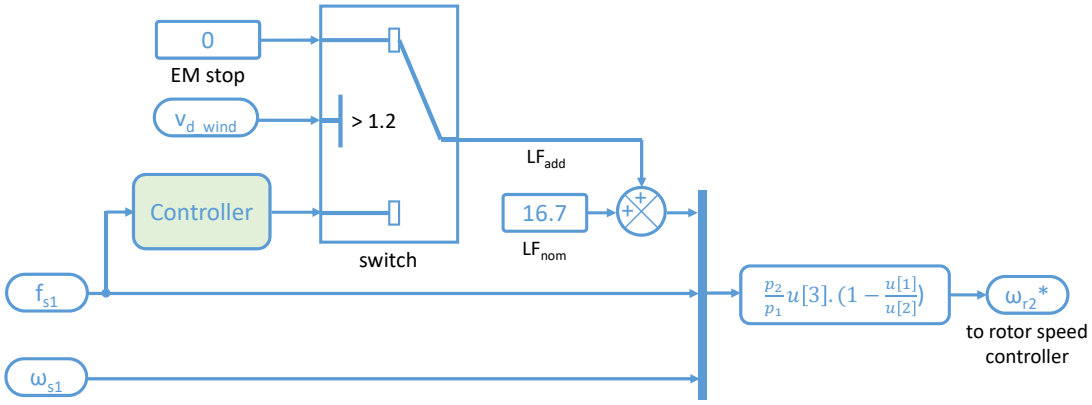

Figure 5.1: Layout of synthetic inertia controller

5.2 Synthetic Inertia Control

For the purposes of this analysis, two methods of synthetic inertia provision have been identified from their applications to the DFIG and have combined into a single hybrid controller for application to the PFEC. Each of the constituent parts of the controller work by providing an artificially manipulated set-point to the rotor speed controller. The effect of this new set-point is to exaggerate the deceleration of the rotor to release a portion of the stored kinetic energy and provide additional active power to the grid in exchange for a reduction in rotational speed. This method cannot be sustained indefinitely due to the finite quantity of kinetic energy available in the rotor, but even a small amount of additional active power will have a noticeable effect on the rate of change of frequency during a loss of generation [93], [94].

The high-level design of the proposed synthetic inertia controller is shown in figure 5.1, where it is seen to take grid frequency as an input and produces a control signal LF_{add} as an output. LF_{add} is then summed with the existing reference point in the absence of any synthetic inertia control LF_{nom} to produce a new reference termed LF_{ref}. This new setpoint is then converted into a rotor speed reference before being sent to the rotor speed controller. The derivation of the block labelled was presented in (3.145).

When there is a drop in grid frequency, the presence of LF_{add} produces a low-frequency setpoint f_{r1}^* which is larger than before, since $f_{r1}^* = LF_{nom} + LF_{add}$. The increase in LFAC-side frequency causes a drop in rotor speed reference ω_{r2}^*, and releases additional kinetic energy. This is demonstrated in (5.1).

$$\omega_{r2}^* = \frac{p_2}{p_1}\omega_{s1}\left[1 - \frac{(LF_{nom} + LF_{add})}{f_{s1}}\right] \tag{5.1}$$

The presence of the switch in figure 5.1 is to force an emergency stop if the rotor voltage becomes too large. Increasing the low frequency set point reduces the rotational speed of the rotor which in turn increases the rotor voltage. Since the wind farm is connected to the rotor circuit, this overvoltage must comply with HVRT grid codes to prevent a disconnect. The synthetic inertia controller is therefore made to trip if the magnitude of the rotor voltage reaches 1.2 PU_{DFIM}.

The hybrid PFEC synthetic inertia controller consists of a droop controller and a ROCOF controller. The former is designed to provide support if the grid frequency differs greatly from the nominal value while the second is based on the rate of change of frequency and triggers during a sharp gradient in the frequency trace.

The droop controller is based on a similar design for DFIG wind turbine applications. In a DFIG, the droop controller is based on the deviation of the system frequency from the nominal value and regulates the active power output from a wind turbine proportional to the change in [95], [96]. There is a linear relationship between active power and frequency, allowing this control scheme to adjust the power set-point according to the linear characteristic in (5.2).

$$\Delta P = -\frac{f_{meas} - f_{nom}}{R} \tag{5.2}$$

where f_{meas} is the new frequency, f_{nom} is the initial operating point and R is the droop constant.

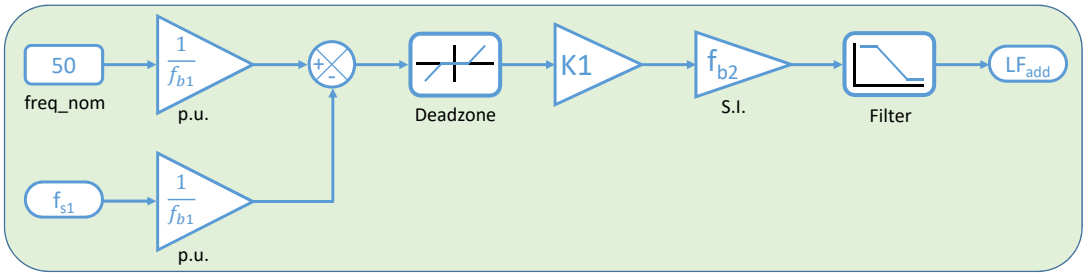

Figure 5.2: Droop synthetic inertia control block layout

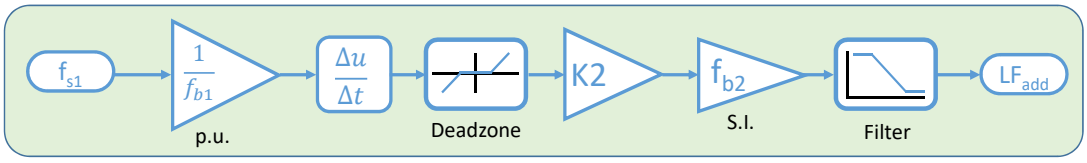

Figure 5.3: ROCOF synthetic inertia control block layout

In PFEC applications there is no active power controller since it is the rotor frequency which is being controlled. Instead, a modification is made so that this control scheme produces the LF_{add} component as required. The layout of the synthetic inertia droop controller is shown in figure 5.3. First, the frequency is converted into per unit quantities (in the RT reference frame). A deadzone is applied to the error between f_{s1} and f_{nom} to prevent the controller from participating in small frequency deviations. The error signal is then multiplied by the gain $K1$ before being converted back into SI units using the base values in the DFIM reference frame.

The second part of the controller is the ROCOF loop shown in figure 5.3 which provides a modified reference proportional to the frequency deviation and lasts until nominal frequency is restored. When f_{s1} is constant and unchanging, the output of the derivative block is zero. When f_{s1} begins to fall, the derivative signal is amplified by the gain K2 to produce LF_{add}. The deadzone and PU to SI conversions follow the same principles as in figure 5.2.

The final step is to combine these two strategies to provide frequency support both during a sharp decline in grid frequency and during a sustained deviation from the

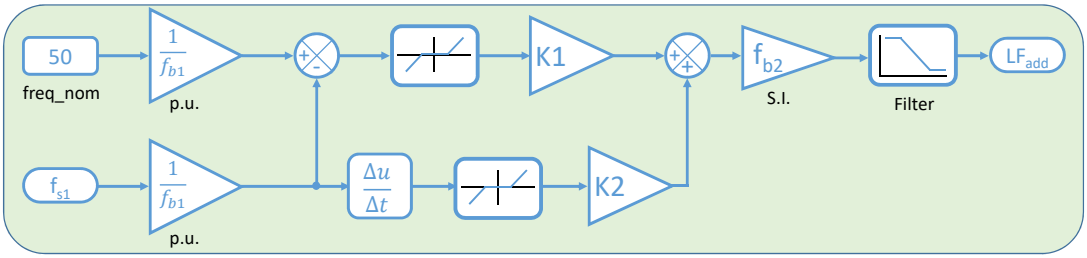

Figure 5.4: Hybrid synthetic inertia control block layout, showing the algebraic sum of the droop controller and the ROCOF controller

nominal value. This is done simply by summing the two components of the previous strategies, as shown in figure 5.4.

5.2.1 Parameter Selection

The effects of changing the parameters K1 and K2 are discussed in [96] but are also presented here due to the difference in application. Gains should be selected to provide a modest amount of support without compromising the equipment attached to the rotor circuit, i.e. the DFIM controller and the wind farm.

The criteria for choosing the parameters K1 and K2 are defined by the limit of how much the PFEC can participate to any frequency event. In synthetic inertia applications for offshore wind, only a small percentage of rated power needs to be provided for a limited time, typically below ten percent of the rated capacity [94]. For the PFEC, these parameters are chosen based on the limit imposed by the rotor voltage which increases as rotor speed decreases. If rotor voltage is allowed to exceed 1.2 PU_{DFIM} then any connected equipment may trip.

The magnitude of the rotor voltage is therefore monitored carefully to make sure it does not exceed the 1.2 PU_{DFIM} threshold as specified for HVRT, at which point the synthetic inertia controller is disconnected. For each of the synthetic inertia control strategies, the effect of a change of parameters was individually assessed against the

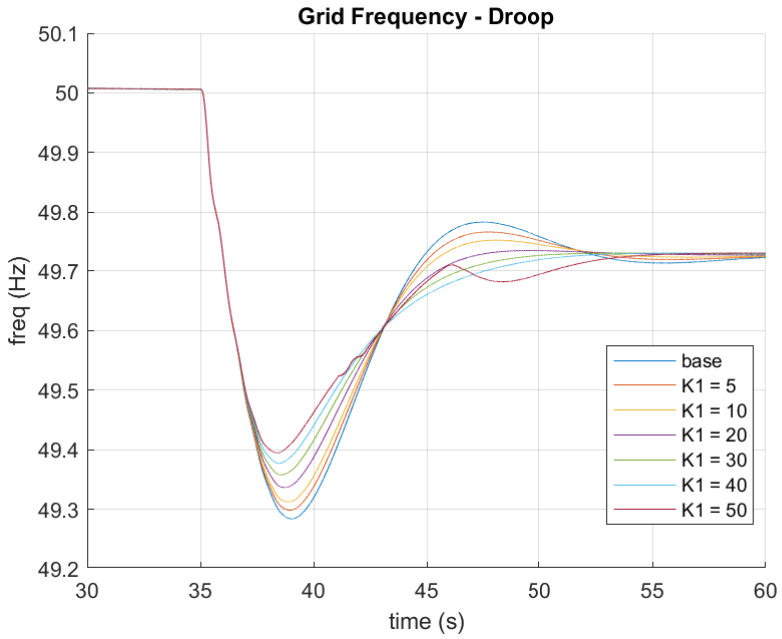

Figure 5.5: Effect changing gain K1 on frequency response. Distorted line shows voltage saturation

effect on grid frequency. In the simulations, a generating unit is taken offline at t = 35 seconds triggering a drop in frequency. The results of different gain selections are compared to a base case with no synthetic inertia controller.

For the droop controller, K1 was varied from 0 to 50 with the results plotted in figure 5.5, showing that increased gain produces a stronger frequency response. Eventually at K1 = 50, the rotor voltage saturates at 1.2PU$_{DFIM}$, triggering the EM stop and taking the synthetic inertia controller offline. It is therefore concluded that K1 must not exceed 40 for the droop controller. The saturation of rotor voltage at K1 = 50 is shown in figure 5.6. The decrease in grid frequency produces a decrease in rotor speed leading to an increased rotor voltage. With K1 set too high, this triggers the EM stop.

The same approach was taken for the ROCOF controller, in which K2 was varied from 0 to -50. Note that the negative sign is required because a drop in frequency will produce a negative gradient from the derivative block which must be converted to a

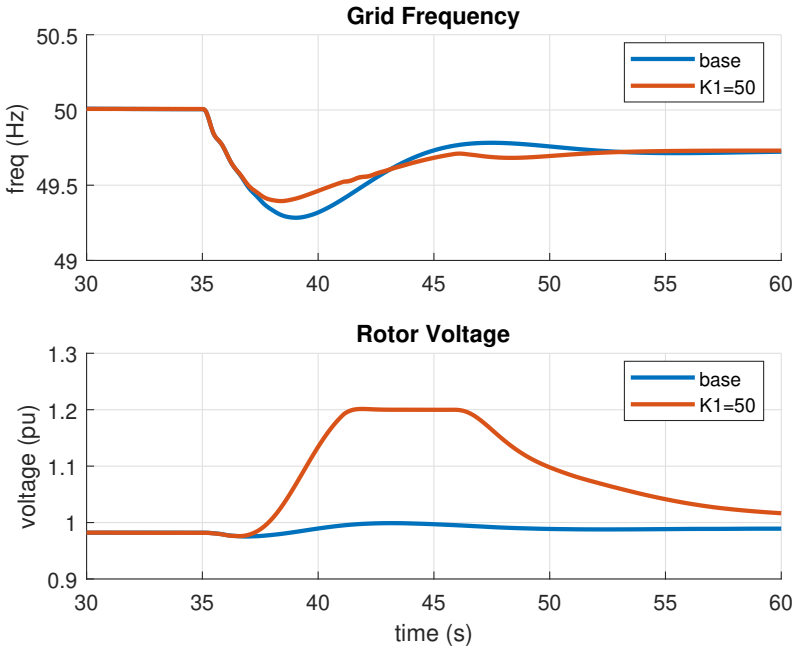

Figure 5.6: Voltage saturation due to oversized gain K1. LF_{add} from controller is too high leading to a decrease in rotor speed past that which triggers the HVRT threshold.

positive signal to provide the necessary increase to f_{r1}^{*}. The results are similar to those in the droop controller, with a more negative K2 giving rise to a stronger frequency response. The ROCOF controller begins to saturate just beyond K2 = 50, such that this is taken as the maximum value.

The combined hybrid controller is analysed in the same way to determine to correct gain proportions between K1 and K2. Each control loop participates according to different network criteria such that the saturation of each aspect of the hybrid controller must be taken into account. The results of different selections of gains K1 and K2 are shown in figure 5.8 where it is concluded that values of K1 = 30 and K2 = -40 yield acceptable results.

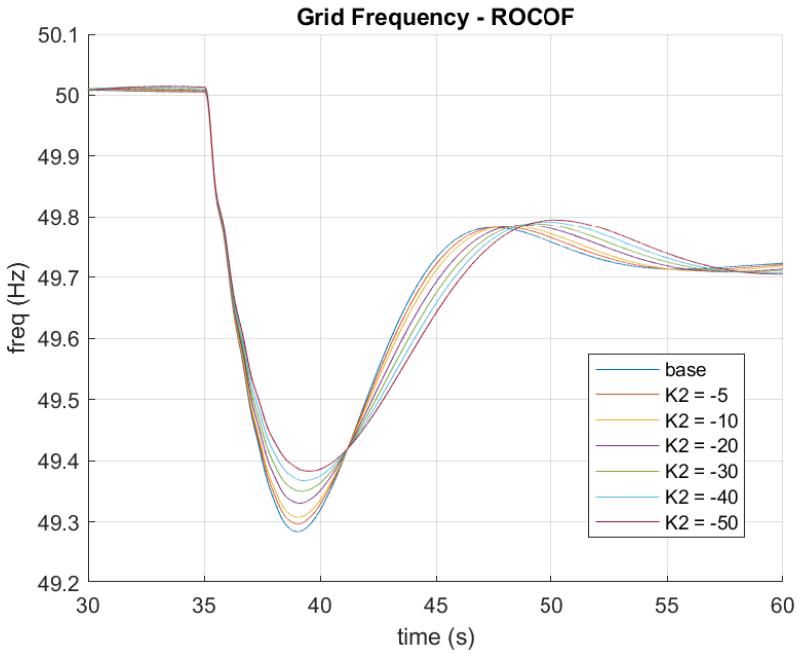

Figure 5.7: Effect of changing gain K2 on frequency response.

5.2.2 Synthetic Inertia Controller Performance

With the gains K1 and K2 now specified, the synthetic inertia controller of the PFEC can be tested in the variable frequency network model introduced in section 4.7, a schematic of which is reproduced in figure 5.9 here for reference. In the simulation, a 200MVA generating unit is taken offline at time t = 35 seconds producing a deficit in active power and triggering a frequency excursion from the nominal 50 Hz. In response to this, the governor connected to the 900MVA generating unit sends a command to ramp up the power output in an attempt to correct the error in frequency, however the deficit is too great and a new steady-state is reached that is below 50Hz.

A base case is first established by running the simulation with a PFEC without the additional synthetic controller. The drop in grid frequency is characteristic of a frequency convergence since the LFAC side is not subject to a change in frequency and Δf is therefore decreasing. The natural response of the PFEC is then to slow down, releasing kinetic energy as a result. With the introduction of the hybrid synthetic iner-

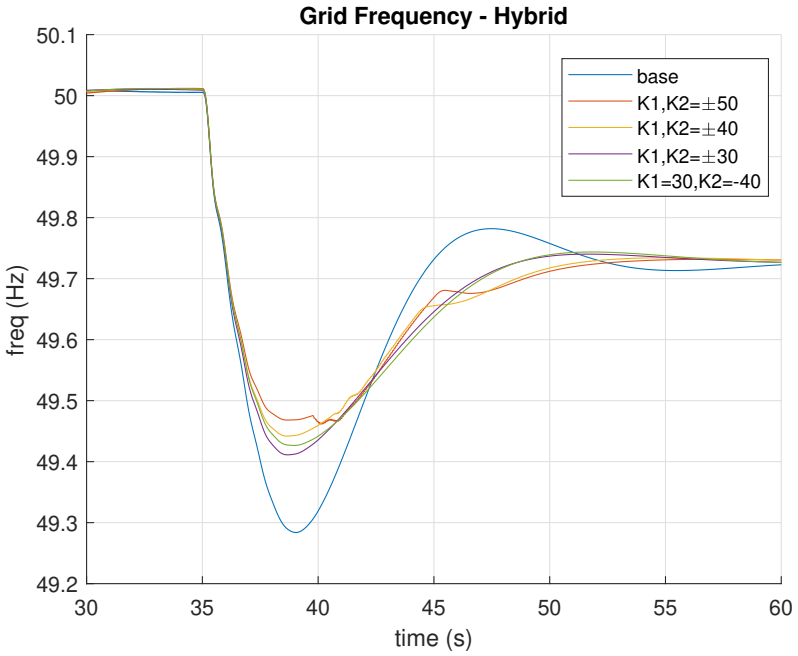

Figure 5.8: Effect of changing gains K1 and K2 on frequency response. Distorted lines show voltage saturation

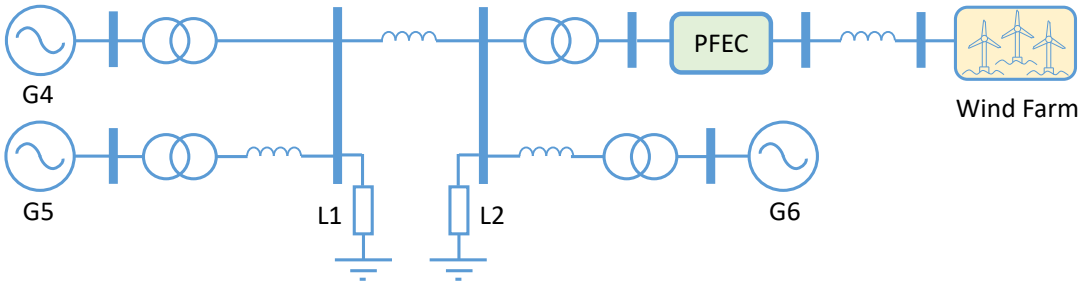

Figure 5.9: Variable frequency power system model

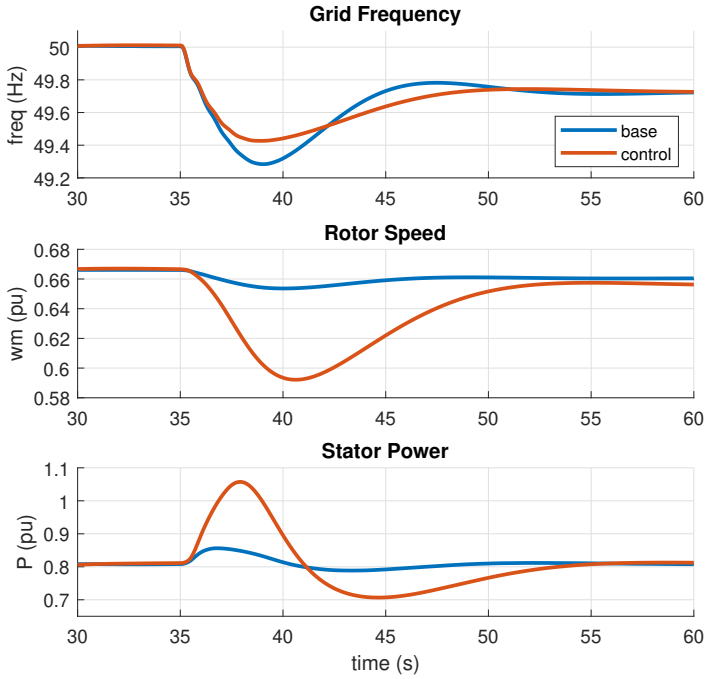

Figure 5.10: Effect of hybrid controller compared to base case. Top = grid frequency; middle = rotor speed; bottom = stator power injected into grid

tia controller the same patterns should be seen but to a much more exaggerated degree. The rotor speed will slow down more due to the additional artificial command signal; the amount of active power released by the deceleration will be greater; and the drop in grid frequency should see a noticeable reduction.

The results are shown in figure 5.10 which compares the base case of no synthetic inertia control with the control case. The grid frequency is seen to drop as a result of the loss of generation which triggers the expected natural response of the PFEC to slow down. As can be seen, the control action of the hybrid synthetic inertia controller produces a much stronger rotor speed response to the disturbance, which has the effect of releasing more active power which both arrests the frequency excursion and reduces the settling time to the new equilibrium point.

Also shown in figure 5.11 are the effects of the hybrid controller on the LFAC side

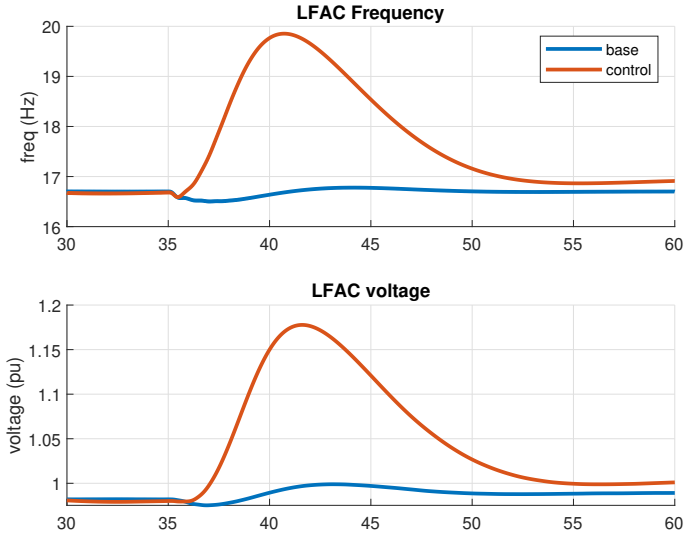

Figure 5.11: Effect of a change in f_r^* on rotor voltage. Top = low frequency; bottom = rotor voltage

network and the RT rotor voltage. In the base case without control, the LFAC side frequency is only slightly perturbed by the loss of generation and continues to be regulated at 16.7Hz. In the control case, the reduction of rotor speed has the effect of dramatically increasing the LFAC-side frequency and the LFAC-side voltage. The controller gains were selected such that 1.2PU$_{DFIM}$ voltage is never reached in fitting with the HVRT analysis but other limiting factors may also exist. The increased frequency will also have knock-on effects on the losses in the cable which may impose further restrictions on the level of participation that the PFEC can contribute to ancillary frequency services, however this is not discussed here.

5.3 Small-Signal Stability

Now that the principles of operation and kinetic energy provision have been analysed, the next step is to use these features to investigate the integration of PFEC-enabled offshore wind power to the AC network. This section will deal with this topic in detail.

The concept of small-signal stability in the context of a power system is the ability to maintain synchronism when subjected to small disturbances [72], such as those associated with a change in load or a loss of generation, where the term 'small' implies that the equations describing the dynamics may be linearised for analysis. Amendments made to the control system of the PFEC will inevitably have an effect on the power system as a whole, so making the PFEC behave more like a synchronous generator by incorporating synthetic inertia provisions may incur consequences relating to electromechanical oscillations between generating units.

This section compares the implications of the previously derived hybrid synthetic inertia controller and its effect on small-signal stability by drawing comparisons between a standard PFEC and a PFEC with synthetic inertia control. Eigenvalue analysis is conducted to study the electromechanical modes between generators and how these are affected by the PFEC both with and without synthetic inertia control.

5.3.1 Linearisation

The power system model under consideration for small-signal stability analysis is the same as the variable frequency full network model used for synthetic inertia control. It is described mathematically by a set of n linearly independent state variables of the form in (5.3), where x_i are the state variables, u_i are the inputs to the model and t is time. The complete set of differential equations is too large to display here as it contains many state-space terms which correspond to non-physical quantities, i.e. simulation settings, delays, filters etc. Additionally, since the focus of this section is on low-frequency inter-area mechanical modes between generating units, states referring

to the high frequency electrical subsystems such as those for converters and controllers have also been omitted. A condensed set of differential equations corresponding to the relevant aspects of the power system is shown in (5.4).

$$\dot{x} = f_i(x_1, ..., x_n; u_1, ..., u_m; t) \quad \text{i} = 1, \ ... \ , \text{n} \tag{5.3}$$

The state variables are a combination of physical quantities such as angle and speed, and other more abstract mathematical variables associated with the differential equations that describe the dynamics of the system [72].

The linearisation process is conducted using the Simulink control design toolbox, the procedure of which is outlined here. To begin, a set of equilibrium points must first be defined. These are the points where all of the derivative terms are simultaneously zero, implying that the system is at rest and all of the variables are constant with respect to time. Mathematically, this implies that $f(x_0) = 0$, with x_0 being an operating point. Due to the complexity of a multi-machine system, the equilibrium points of the model considered in this paper are determined from simulation. After a sufficiently long settling time, a snapshot is taken of the state variables when they are in steady-state and saved to file. This is done multiple times for different operating conditions and control strategies until a complete set of equilibrium points exist for all scenarios. The system state equations are then obtained by linearisation at an equilibrium point:

$$\begin{bmatrix} \Delta\dot{x}_{DFIM} \\ \Delta\dot{x}_{RT} \\ \Delta\dot{x}_{SG_n} \end{bmatrix} = \mathbf{A} \begin{bmatrix} \Delta x_{DFIM} \\ \Delta x_{RT} \\ \Delta x_{SG_n} \end{bmatrix} \tag{5.4}$$

where

$$x_{DFIM} = x_{RT} = \begin{bmatrix} \delta_r & \omega_r & \phi_{ds} & \phi_{qs} & \phi_{dr} & \phi_{qr} & ... \end{bmatrix}^T \tag{5.5}$$

$$x_{SG_n} = \begin{bmatrix} \delta_n & \omega_n & \phi_{d_n} & \phi_{q_n} & \phi_{kd_n} & \phi_{kq1_n} & \phi_{kq2_n} & \phi_{fd_n} & ... \end{bmatrix}^T \tag{5.6}$$

$$\text{for} \quad n = 4, 5, 6 \tag{5.7}$$

δ_r, ω_r and the ϕ's are the angle, speed and fluxes. Note that because the RT and the DFIM are both modelled as induction machines the elements within the state-space model share the same nomenclature. x_{SG} are the set of differential equations for the synchronous generators, labelled from 4 to 6 in keeping with the power system area layout shown previously in figure 4.22. These consist of δ_r, ω_r and the ϕ which are the rotor angle, rotor speed and fluxes respectively.

Small-signal stability analysis is concerned with the eigenproperties of the Jacobian matrix **A**, which is of the form in (5.8). The entries in **A** give the coupling relationships between each of the dynamic processes [97]. The eigenvalues of **A** are of the form in (5.9).

$$\mathbf{A} = \begin{bmatrix} \frac{\partial f_1}{\partial x_1} & \cdots & \frac{\partial f_1}{\partial x_n} \\ \cdots & \cdots & \cdots \\ \frac{\partial f_n}{\partial x_1} & \cdots & \frac{\partial f_n}{\partial x_n} \end{bmatrix} \tag{5.8}$$

$$\lambda_i = a_i \pm j b_i \quad \text{for} \quad i = 1...n \tag{5.9}$$

For a complex pair of eigenvalues, the real component gives the damping and the imaginary component gives the frequency of oscillation. The frequency of oscillation is given by (5.10) and the damping ratio is given by (5.11). The damping ratio is of particular importance as this determines the rate of decay of the oscillations. A high damping ratio implies that any oscillations away from the static equilibrium will decay quickly, whereas a low damping ratio implies the opposite. A high value of ζ is desirable in the context of small-signal stability. It can be seen from Equation (5.11) that the

value of ζ is largely dependent on the real component of a particular eigenvalue, such that a more-negative real component implies a higher damping ratio. This is analogous to the position of poles in control theory, where the system is stable if the poles are in the left hand plane, and a more negative real component results in a faster decay.

$$f = \frac{b}{2\pi} \qquad (Hz) \tag{5.10}$$

$$\zeta = -\frac{a}{\sqrt{a^2 + b^2}} \tag{5.11}$$

There is no one-to-one relationship between any single eigenvalue and a particular state because they each belong to the system as a whole. It is therefore necessary to define the participation matrix $\mathbf{P}$ which provides a numerical score for a each eigenvalue against a specific state. A large value (typically orders of magnitude higher than the neighbouring entries) indicates a large participation to that mode. The participation matrix is generated from the matrices of right and left eigenvalues, Λ and Ψ respectively. Note that it is standard practice to normalise these matrices such that $\Psi\Lambda = \mathbf{I}$.

$$\Lambda = \begin{bmatrix} \lambda_1 & \lambda_2 & \dots & \lambda_n \end{bmatrix} \tag{5.12}$$

$$\Psi = \begin{bmatrix} \psi_1^T & \psi_2^T & \dots & \psi_n^T \end{bmatrix}^T \tag{5.13}$$

where the right and left eigenvectors are given by Equations (5.14) and (5.15) respectively.

$$\mathbf{A}\lambda_i = \lambda\lambda_i = 0 \tag{5.14}$$

$$\psi_i\mathbf{A} = \lambda\psi_i = 0 \tag{5.15}$$

$$\lambda_i = \begin{bmatrix} \lambda_{1i} \\ \\ \lambda_{2i} \\ \\ \dots \\ \\ \lambda_{ni} \end{bmatrix} \quad ; \quad \psi_i = \begin{bmatrix} \psi_{1i} & \psi_{2i} & \dots & \psi_{ni} \end{bmatrix} \tag{5.16}$$

The modal matrices Λ and Ψ are then used to form the participation matrix $\mathbf{P}$, the entries of which will be used to determine the dominant eigenvalues for each state.

$$\mathbf{P} = \begin{bmatrix} p_1 & p_2 & \dots & p_n \end{bmatrix}$$
$$\text{where} \quad p_i = \begin{bmatrix} \lambda_{1i}\psi_{i1} \\ \\ \lambda_{2i}\psi_{i2} \\ \\ \dots \\ \\ \lambda_{ni}\psi_{in} \end{bmatrix} \tag{5.17}$$

$\lambda_{ki} = k$th row, ith column of modal matrix Λ.
$\psi_{ik} = i$th row, kth column of modal matrix Ψ.

5.4 Network Scenarios

The effects on small-signal stability of the different synthetic inertia controllers are now analysed in a variety of network scenarios.

5.4.1 Scenario 1

The first scenario to be considered compares the results between a low frequency PFEC-connected wind farm and a PFEC with synthetic inertia control. In this scenario there are no additional network constraints, i.e. a power system under heavy load or a weak grid as these are covered in subsequent runs in scenarios 2 and 3 respectively.

In scenario 1 the system appears as in figure 4.22. The simulation is initialised and linearised at a snapshot in time once the system reaches steady-state resulting in a state-space representation of the model which contains all of the necessary information for small-signal stability analysis. Applying the procedure to generate the participation matrix in (5.17) we get a table which gives a numerical score against each eigenvalue against with every mode. This information can then be used to identify which eigenvalues contribute the most towards a specific mode, i.e. the inter-area mechanical mode between generators, which will have a numerical score that is orders of magnitude larger than any neighbouring entries.

The pair of eigenvalues that participate the most towards the inter-area mechanical mode are given in table 5.1 which shows the inter-area eigenvalues λ_{IA1} and λ_{IA2}, the real and imaginary parts, the frequency and the damping for both simulations with and without synthetic inertia control.

It is also possible to plot the mode shape of the inter-area oscillatory mode which is presented in figure 5.12 and shows the swinging of generators 4, 5 and 6 against each other. G5 and G6 can be seen to swing more readily off of G4 since G4 is the largest generating unit and has the largest inertia so serves as a kind of anchor point for the system.

Figure 5.13 is a pole plot displaying the trajectories of the eigenvalues between the simulations. As the control strategies are introduced, the eigenvalues can be seen to shift further to the right-hand-side representing a decreased stability characterised by a reduction in damping. This can be seen in table 5.1 which shows how damping is reduced with the introduction of the PFEC with synthetic inertia control. The damping

Table 5.1: Frequency and damping of inter-area modes for scenario 1

Scenario	**Eigenvalues**	**Real**	**Imag**	**freq.**	ξ
PFEC	λ_{IA1}, λ_{IA2}	-2.266	$\pm$10.471	1.667	0.212
PFEC w/ control	λ_{IA1}, λ_{IA2}	-2.028	$\pm$10.469	1.666	0.190

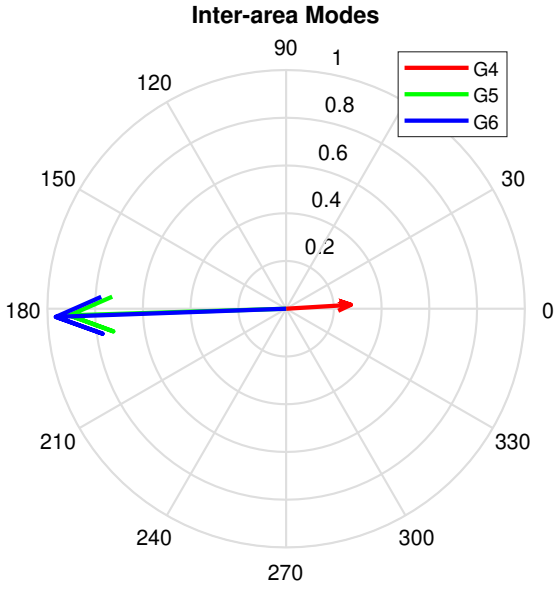

Figure 5.12: Inter-area mechanical mode shapes of generator 4, 5 and 6 respectively

Table 5.2: Frequency and damping of inter-area modes for scenario 2

Scenario	**Eigenvalues**	**Real**	**Imag**	**freq.**	ξ
PFEC	λ_{IA1}, λ_{IA2}	-2.123	$\pm$10.228	1.623	0.203
PFEC w/ control	λ_{IA1}, λ_{IA2}	-1.311	$\pm$9.571	1.523	0.136

ratio is reduced from 0.212 to 0.190 in the PFEC and synthetic inertia control runs respectively. Similarly, the real component of the eigenvalue increases from -2.266 then -2.028.

5.4.2 Scenario 2 - Heavy Load

Scenario 2 investigates the effects on small-signal stability of the PFEC on a heavily loaded network. In this simulation, the balancing mechanism is removed from generator 4 such that the governor can no longer command the release of extra power in the event of a disturbance. When one of the other generators is taken offline, the frequency can not recover fully and instead settles at a new equilibrium.

The effects of the PFEC and synthetic inertia control on the electromechanical oscillations of the system are very similar to those in the base case of scenario 1. The

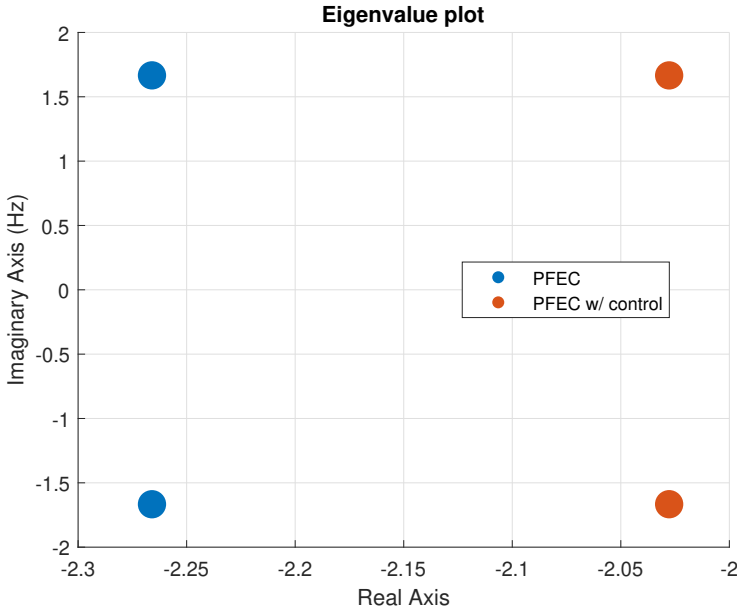

Figure 5.13: Inter-area mode eigenvalues under normal network conditions

same pattern of reduced damping of the inter-area mode can be seen in table 5.2. When the PFEC is augmented with synthetic inertia control the system becomes less stable from a small-signal stability point of view. The pole plot in figure 5.14 visualises the trend in table 5.2 and shows a shift of the eigenvalues to the right.

5.4.3 Scenario 3 - Weak Grid

The final scenario investigates the effect of a weak grid on the system eigenvalues. Governor action is restored to generator 4 but the tie-line connecting the two areas is reduced in strength by increasing the value of the impedance to simulate a longer transmission line. Such lines are common when a distant generating station must be connected to a load centre over a considerable distance. The impedance is increased from the initial per unit value of $Z_{G1_{old}} = 0.002 + j0.2$ to $Z_{G1_{new}} = 0.008 + j0.8$, representing a four-fold increase.

The effect on the system eigenvalues can be seen in figure 5.15. The system is less damped overall than the base case of scenario 1 however this effect is small enough to be negligible. The results are given in table 5.3.

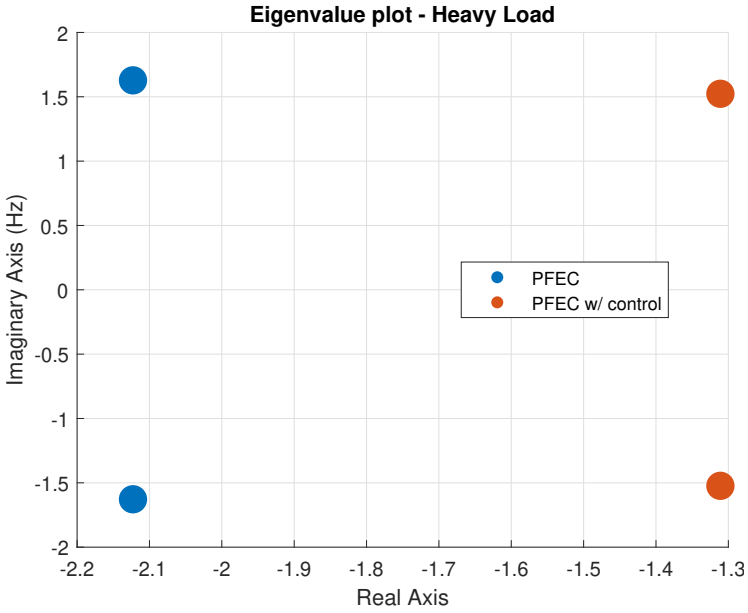

Figure 5.14: Inter-area mode eigenvalues under heavy load conditions

Table 5.3: Frequency and damping of inter-area modes for scenario 3

Scenario	**Eigenvalues**	**Real**	**Imag**	**freq.**	ξ
PFEC	λ_{IA1}, λ_{IA2}	-1.996	$\pm$10.515	1.674	0.187
PFEC w/ control	λ_{IA1}, λ_{IA2}	-1.953	$\pm$10.563	1.681	0.182

5.5 Summary and Conclusions

Results have shown that the PFEC is capable of being augmented with a synthetic inertia control to provide additional support to the grid in the event of a loss of generation and subsequent frequency drop. The PFEC naturally improves frequency stability as an inherent property of its inertia and large rotating mass, the kinetic energy of which can be extracted to provide active power to the network in such a situation. By incorporating additional control loops the participation to frequency support can be exaggerated significantly at the expense of the conditions on the LFAC-side network. The hybrid synthetic inertia controller can be tuned to drastically increase the amount of kinetic energy that is extracted from the rotor which has been shown to arrest the ROCOF and to decrease the settling time after a disturbance. The cost of the increased participation comes in the form of overvoltage on the LFAC-side which

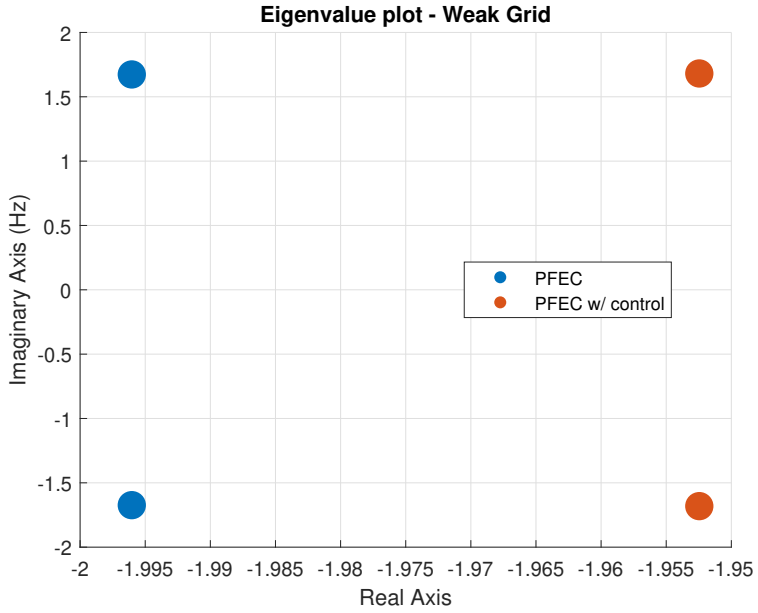

Figure 5.15: Inter-area mode eigenvalues in weak grid network conditions

increases in inverse proportion with the slip, and an increase in LFAC-side frequency, the consequences of which will be felt as increased losses along the transmission line. The overvoltage constraint has been incorporated into the controller design which automatically disconnects if the voltage exceeds 1.2PU_{DFIM} on the LFAC-side, however further investigation into cable losses arising from the increased LFAC-side frequency is required to identify the maximum amount of frequency provision before unacceptable charging currents are encountered in the line. This last task is left outside the remit of this thesis.

Despite the fact that the PFEC shows good improvements to frequency stability with the introduction of synthetic inertia control, the small-signal stability tells a different story. The effect of augmenting the PFEC with inertia control decreases the small-signal stability of the power system by reducing the damping coefficients of certain electromechanical modes. Results have shown that the time taken for the linearised system to recover from small perturbations increases with the introduction of the inertia controller as evidenced by the increased decay times of the inter-area oscillations between generating units. These findings agree with the results found in [87] which de-

termined that the introduction of a synthetic inertia controller to a DFIG also reduces small-signal stability overall. The inertia control strategy makes the DFIG, and hence the PFEC by extension, behave more like a synchronous machine and therefore plays a more active role in the inter-area modes between generating units. The amount of participation to frequency support that a single PFEC unit may engage in should therefore be treated with caution due to the inherent trade-off between frequency stability and small-signal stability.

Chapter 6

Development of a Cost Model

This chapter explores the potential economic implications of any future PFEC transmission system and how this compares to the commercially available options of HVAC and HVDC. Costs for offshore wind vary greatly depending on the method of power transmission used and the number of factors which need to be taken into account are numerous, including not only the capital costs, but also the costs of installation, commissioning, O&M, and losses. Costs for HVAC are more easily estimated as there exists a large amount of data from installed wind farms. HVDC poses a greater problem due to the limited number of installations and the bespoke nature of each system. Lastly there is the PFEC, of which there exists no information at all. The lack of commercial projects either in LFAC transmission or in the PFEC method of frequency conversion means any estimate must contain a number of assumptions derived from the most similar equipment available.

The low frequency transmission facet of the PFEC can be treated in almost the same approach as HVAC due to the similarities in equipment. For example, platform costs may be derived in the same way as for HVAC, which provisions made due to the increased variable costs associated with the larger electrical equipment required for low frequency. The main piece of bespoke apparatus appears onshore and is that of the electromechanical frequency converter. This is similar in design to the VFT by General Electric of which cost data does exist, albeit in very limited supply.

Pieces of equipment that are common to all three options can be omitted from the analysis when it is practical to do so. For example, costs relating to the wind turbines themselves are not included, neither are the overhead lines used to connect the entire system to the rest of the grid. Other simplifications can be made by omitting installation costs because these are impossible to determine accurately for the PFEC as no such data exists.

The approach taken in developing a cost model is based on the work presented in [98],[99] and [100] where capital costs are split into the following categories:

- Offshore platform and plant costs (OPPC)
- Onshore platform and plant costs (OPC)
- Cable costs (CBC)
- Compensation costs (QC)
- Loss costs (LC)

The following sections introduce numerical methods of estimating the costs for each of these categories and combines to provide a cost function for each of the three transmission systems, namely HVAC; HVDC; and the PFEC.

6.1 Acronyms

Variable	Description
OPPC	Offshore platform and plant costs (M£)
OPC	Onshore plant costs (M£)
CBC	Cable costs (M£)
QC	Compensation costs (M£)
LC	Loss costs (M£)
TLC_{on}	Offshore terminal losses cost (M£)
RLC	Route losses cost (M£)
TLC_{off}	Onshore terminal losses cost (M£)
S_t	Rated power (MW)
$C_{p_{dc}}$	Offshore DC platform cost (M£)
$C_{p_{ac}}^{50}$	Offshore 50Hz AC platform cost (M£)
$C_{p_{ac}}^{16.7}$	Offshore 16.7Hz AC platform cost (M£)
C_{vsc}	VSC cost (M£)
C_{tr}^{50}	50Hz transformer cost (M£)
$C_{tr}^{16.7}$	16.7Hz transformer cost (M£)
C_{VFT}	VFT cost (M£)
C_{DFIM}	DFIM cost (M£)
t_c	Cable cost (M£/km)
l_c	Cable length (km)
n_c	Number of cable sets
V	Voltage (kV)
R	Resistance (Ω/km)
C	Capacitance (nF/km)
f	Frequency (Hz)
Q_c	Compensation cost per MVar (£M/Mvar)
pf	Power factor
η_{off}	Efficiency of offshore VSC
η_{on}	Efficiency of onshore VSC
η_t	Efficiency of transformers
η_g	Efficiency of hydro-generator
T_{op}	Operating hours (hr)
δ	Load loss factor
E_{op}	Energy price (£M/MW)
f_r	Frequency ratio

6.2 HVAC Cost Model

6.2.1 Cost of AC Offshore Platform

The offshore platform and plant costs are some of the largest of the entire transmission system since it involves a complex steel structure which must be able to support upwards of 2000 tonnes. For high power scenarios it is also common to use multiple platforms however this approach is not included here. Table 6.1 shows some typical figures of tonnage against power capacity.

The offshore platform and plant costs (OPPC) can be grouped into fixed costs and variable costs. Fixed costs include the structure of the offshore platform and any facilities required. Variable costs include the electrical subsystems which will scale depending on power capacity such as the collection network, the transformers and the switchgear. The collection network and AC switchgear will be common to all three transmission topologies and so can be omitted from the model. This results in the offshore plant costs for an AC system being described by the transformer costs and the platform costs as in (6.1) with the terms described in (6.3) and (6.2) [99].

$$OPPC_{ac} = C_{p_{ac}}^{50} + C_{tr}^{50} \tag{6.1}$$

$$C_{p_{ac}}^{50} = 2.2806 + 0.07983St \qquad \text{(M£)} \tag{6.2}$$

$$C_{tr}^{50} = 0.03843S_t^{0.751} \qquad \text{(M£)} \tag{6.3}$$

where S_t is the rated power of the system (MW), C_{tr}^{50} is the capital cost of a 50Hz transformer and $C_{p_{ac}}^{50}$ is the capital cost of an 50Hz offshore platform. All prices are given in M£.

6.2.2 Cost of AC Onshore Platform

Onshore AC platform costs are similar to those for offshore plant costs but with the omission of the offshore structure. Many of the components will be of the same spec-

ification but without the strict constraints on weight and space [101] and so can be omitted by the same logic as for the offshore plant, i.e. that costs associated with the switchgear and the substation enclosure are omitted. Onshore plant costs are therefore approximated by the size of the transformer [99]:

$$OPC_{ac} = C_{tr}^{50} = 0.03843 S_t^{0.751} \qquad \text{(M£)} \tag{6.4}$$

6.2.3 Cost of AC Cables

HVAC cables have an effective range beyond which it is either not economical or not possible to transfer active power due to the presence of reactive power. Longer cables generate more reactive power and have a reduced maximum power carrying capability. Beyond a certain length it becomes necessary to either upgrade to a larger diameter cable, increase the number of sets or increase the amount of reactive power compensation. The parameters of some common AC cables are given in table C.7 and the maximum power carrying capabilities of these cables are shown with and without compensation in figure 2.12 and figure 2.11 respectively.

The cost of the AC cables is given by (6.5) [98]:

$$CBC = t_c l_c n_c \tag{6.5}$$

where t_c = cable cost per km, l_c = length (km), n_c = number of sets.

6.2.4 Cost of AC Compensation

One of the main parameters which limits active power transmission in a subsea cable is the requirement of reactive power compensation. The close proximity of cables arranged in a tight bundle generates a large amount of reactive power across its length. This effect is orders of magnitude higher in subsea cables than in overhead lines and beyond a certain length the cable generates too much reactive power for this to be an economical

solution. The amount of reactive power generated from this capacitive charging current can be expressed as (6.6).

$$Q_c = V^2 2\pi f C l_c \tag{6.6}$$

where Q_C = reactive power (Var), V = voltage (V), f = frequency (Hz), C = capacitance (F), l_c = cable length (km).

Reactive power compensation can either be installed at either end of the cable or by installing additional support structures along the cable length. While the latter has started to become a viable option there is to date only one system that uses this approach [102] and the difficulty in pricing this option is difficult. Instead the focus here is an even distribution at either end of the cable.

Some costs of reactive power compensation are given in [103] which give an average cost of Q_{comp} = 0.0537 (M£/MVar). Applying this to (6.6) gives the total cost of compensation as (6.7).

$$QC_{ac} = 0.0537 \cdot V^2 2\pi f C l_c \tag{6.7}$$

6.2.5 Cost of AC Losses

The power loss cost in a transmission system can be split into route losses and terminal losses with a separate loss calculation for the onshore and offshore terminals respectively as shown in (6.8). Using assumptions given in [104], the HVAC losses are presented in (6.9) - (6.11).

$$LC = TLC_{off} + TLC_{on} + RLC \tag{6.8}$$

with:

$$TLC_{off_{ac}} = S_t \cdot pf(1-\eta_t)T_{op}\delta E_{op} \tag{6.9}$$

$$TLC_{on_{ac}} = \left[S_t \cdot pf\eta_t - 3\left(\frac{S_t \cdot p_f\eta_t}{n_c \cdot \sqrt{3}V}\right)^2 R_c l_c n_c\right](1-\eta_t)T_{op}\delta E_{op} \tag{6.10}$$

$$RLC_{ac} = 3\left(\frac{S_t \cdot pf\eta_t}{n_c \cdot \sqrt{3}V}\right)^2 R_c l_c n_c T_{op}\delta E_{op} \tag{6.11}$$

where S = rated power, pf = power factor, η_t is the efficiency of the onshore and offshore transformers, T_{op} = total operation hours, δ = loss load factor, E_{op} = energy price, n_c = number of cable sets, V = voltage, R_c = cable resistance, l_c = cable length. The values of these assumptions are given in the appendix.

6.3 HVDC Cost Model

6.3.1 Cost of DC Offshore Platform

A major source of investment cost for HVDC transmission is in the design and installation of the offshore platform and plant which are considerably more expensive than their HVAC counterparts. The difference in cost can be attributed to the VSC and the increased material requried to support the extra mass, which can be more than 10,000 tonnes 6.1.

Platform Type	Water Depth (m)	Size (m) W x H x L	Total Weight (tonnes)
300MW AC	20 - 40	20, 18, 25	1800
500MW AC	30 - 50	31, 18, 39	2100
400MW DC	30 - 40	35, 21, 52	3200
1000MW DC	40+	50, 21, 50	10000 - 14000
Accommodation	40+	35, 21, 35	3000 - 5000

Table 6.1: Example offshore platform weights and dimensions [103]

It is stated in the literature that the cost of a DC substation platform is on average 250% higher than an equivalent AC option [25], however this is if anything an understatement as it does not reflect the experiences faced by recent offshore HVDC developers. Losses due to delays have been reported by Siemens to have totalled 800 million euros across four installations, including BorWin2 [105] and similarly, ABB have reportedly made a loss on a number of offshore wind projects relating to the offshore converter platforms and as such will no longer take on the risk involved in the installation of future projects [106][107]. Due to the nature of the cost overruns it is not possible to simply apply a numerical correction to the cost function stated in the literature and instead an alternative approach to determining a cost function based on empirical data is sought.

There is inherent difficulty in determining an accurate cost function for the offshore DC platform and plant due to the limited amount of installations worldwide, however

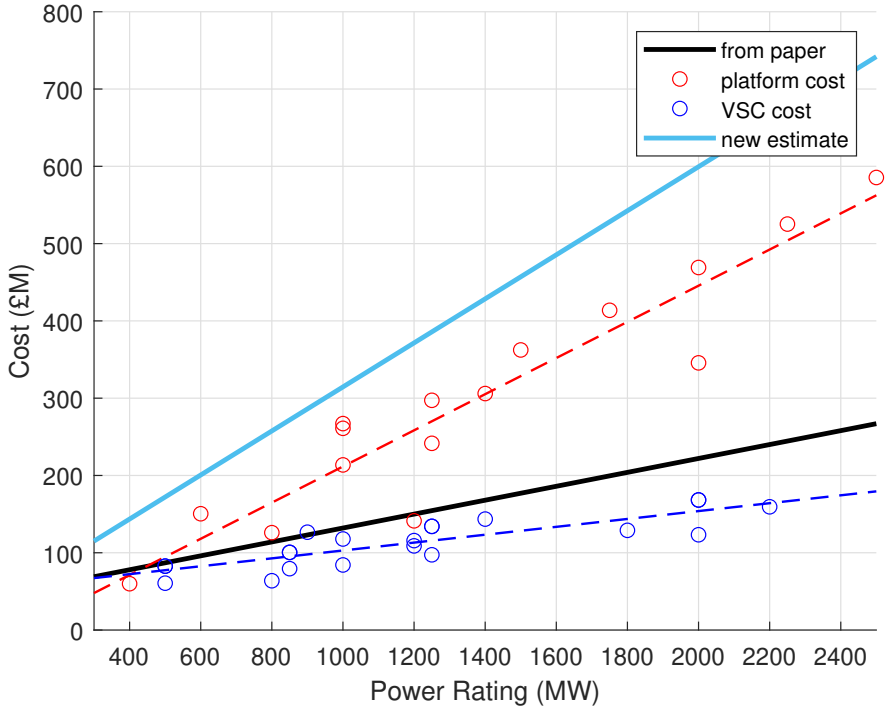

Figure 6.1: Published data on DC offshore platform and VSC costs is used to provide a new cost estimate over the original provided by the literature

cost parameter sets for the limited amount of data that do exist has been widely used and published in the literature.

The data shown in figure 6.1 is a combination of VSC costs and platform costs based on the information provided in [108]. The equations of the respective lines of best fit can then be used to produce a new cost estimate per MW for the DC offshore platform and plant which differs from that which is used in the literature [25]. The new cost estimate is described by (6.14) and the comparison between the previously accepted literature value and the new estimate is also visible in figure 6.1.

$$OPPC_{dc} = C_{pdc} + C_{vsc} \tag{6.12}$$

$$= (-22.274 + 0.2339S_t) + (51.937 + 0.051S_t) \tag{6.13}$$

$$= 29.663 + 0.285S_t \tag{6.14}$$

where C_{pdc} and C_{vsc} are the cost functions for the DC platform and VSC respectively. Note that one of the consequences of using this simple approach is visible in the expression for C_{pdc}, which has a negative y-intercept implying that the fixed costs for the offshore platform are negative. However, this is not necessarily a problem over the range of interest in this study (300MW - 900MW) because the deviation between the literature cost function and the new model is small.

6.3.2 Cost of DC Onshore Plant

The DC onshore converter station is defined in (6.15) [109].

$$OPC_{dc} = 16.2 + 0.081 S_t \qquad \text{(M£)} \tag{6.15}$$

6.3.3 Cost of DC Cables

HVDC cables do not experience the same reactive power-based drawbacks as HVAC cables and can boast an almost unlimited range. Another advantage of DC cables are the reduced number of conductors required to carry the power leading to a better cable utilisation ratio. The cost per km for an HVDC cable is the same as in (6.5) with the parameters updated to those presented in table C.8 which gives the parameters for some common configurations.

6.3.4 Cost of DC Losses

The same equations that were presented for AC losses in (6.9) - (6.11) also apply to DC but with a substitution for the efficiencies of the onshore and offshore converters and an adjustment to the route cost due to the reduced number of conductors:

$$TLC_{off_{dc}} = S_t \cdot pf(1 - \eta_{off}) T_{op} \delta E_{op} \tag{6.16}$$

$$TLC_{on_{dc}} = \left[S_t \cdot pf \eta_{off} - 3 \left(\frac{S_t \cdot p_f \eta_{off}}{n_c \cdot \sqrt{3} V} \right)^2 R_c l_c n_c \right] (1 - \eta_{on}) T_{op} \delta E_{op} \tag{6.17}$$

$$RLC_{dc} = 2 \left(\frac{S_t \cdot pf \eta_{off}}{n_c \cdot V} \right)^2 R_c l_c n_c T_{op} \delta E_{op} \tag{6.18}$$

6.4 PFEC Cost Model

Capital costs for the PFEC are difficult to approximate accurately and will require a number of assumptions to be made. Many of the components within the PFEC-based transmission system can be directly taken from an equivalent LFAC system (minus the power converter), however there are also issues with this approach since there are no existing or proposed LFAC systems for offshore wind. Cost models for hypothetical LFAC components are present in the literature and tend to be based on similar technology used in nominal frequency AC but with a correction applied to account for the reduced frequency which often implies an increase in material.

The cost of the motor-generator set within the PFEC is more difficult to provide an estimated for but one can look towards the most similar technology for an idea of where to start. The rotary transformer is very similar in design to a VFT which consists of a large induction machine with stator and rotor windings rated for full power. The DFIM present in the PFEC is no different to any other DFIM apart from its large power rating which renders many scaling algorithms for generator size and cost for offshore wind relatively useless. However, similar technology exists within the relatively new area of adjustable speed pumped hydro which boasts asynchronous machines together with PRCs of up to 400MW. This not only provides an ideal place to start in developing a costing estimate but also provides confidence that the large power ratings are not a deterrent to the realisation of PFEC technology. Note that although a 600MW PFEC was introduced in section 4.10, the VFT remains the most similar technology to the PFEC, and costing data of VFTs is limited to 300MW. For this reason, the costing analysis to follow is based on a 300MW PFEC.

The modularity of the PFEC can also be exploited when developing a cost estimate such that individual PFEC units can be connected in parallel to reach the required power rating. This allows the existing cost data for a 300MW VFT to be applied in multiples to reach various power scenarios. Of course this implies that all costs can

be treated as modular and does not discriminate between fixed and variable costs, however this assumption is made for the duration of this work such that a certain degree of uncertainty is unavoidable.

6.4.1 Cost of PFEC Offshore Platform

PFEC offshore costs can be treated in roughly the same way as for HVAC but with provisions for the reduced frequency. The main contributions to the increased cost over conventional HVAC are the transformers and the offshore structure which will have to increase in size to accommodate the reduced frequency. With a transmission frequency of 16.7Hz, the transformers will need to have three times the core volume to establish the required magnetic flux. This three-fold increase in core area may not necessarily result in triple the total cost of a standard transformer as there are components that will not scale linearly with frequency, such as coolant and windings [36]. A report in [99] gives a good analysis of how transformer cost scales with frequency and is presented in (6.20).

$$C_{tr}^{16.7} = \left[\frac{0.325 f_r + 0.22 f_r + \sqrt[3]{f_r^2}}{0.325 + 0.22 + 0.164}\right] C_{tr}^{50} \tag{6.19}$$

$$\text{with} \quad f_r = \frac{50}{16.7} \approx 3 \tag{6.20}$$

where f_r is the frequency ratio between the high frequency system and the low frequency system, which in this case is equal to 3.

With roughly three times the transformer volume than in the HVAC system, the offshore platform will need to accommodate the extra weight which will also incur an increased cost. Many of the fixed costs will remain the same but some of the variable costs will need to increase. Based on work done in [99], the cost of an HVAC platform can be scaled to a non-standard frequency using the law in (6.21).

$$C_p^{16.7} = 0.88\left[2.534 + 0.0887 S_t\left(\frac{1}{3} + \frac{f_r}{3}\right)\right]; \tag{6.21}$$

where $C_p^{16.7}$ is the capital cost in £M of the offshore platform. This gives the total offshore platform and plant cost for the PFEC as in (6.22).

$$OPPC_{pfec} = C_p^{16.7} + C_{tr}^{16.7} \tag{6.22}$$

6.4.2 Cost of PFEC Onshore Platform

As was stated in the introduction to PFEC cost modelling, the PFEC and the VFT by GE share some key components which can be used as a initial starting point in developing a cost model for onshore plant costs. Figure 6.2 is a sketch which compares the core components of a 300MW VFT and an equivalently sized hypothetical PFEC installation and pairs-up the most similar technology between the two systems, with further descriptions itemised in table 6.2. It can be seen that on a component-by-component level, the two systems are remarkably similar and can therefore be treated as approximately isomorphic. Note that passive line elements such as harmonic filters, reactors and capacitor banks have not been included for simplicity but these are nonetheless present in both systems.

Item #	VFT	PFEC
1	Transformer (50Hz)	Transformer (50Hz)
2	VFT (300MW)	RT (300MW)
3	DC drive motor (12MW)	DFIM (200MW)
4	Thyristor speed drive (12MW)	B2B-VSC (20MW)
5	Transformer (50Hz)	Transformer (16.7Hz)
6	Enclosure	Enclosure
7	Switchgear / protection	Switchgear / protection

Table 6.2: Comparison between VFT and PFEC components based on figure 6.2

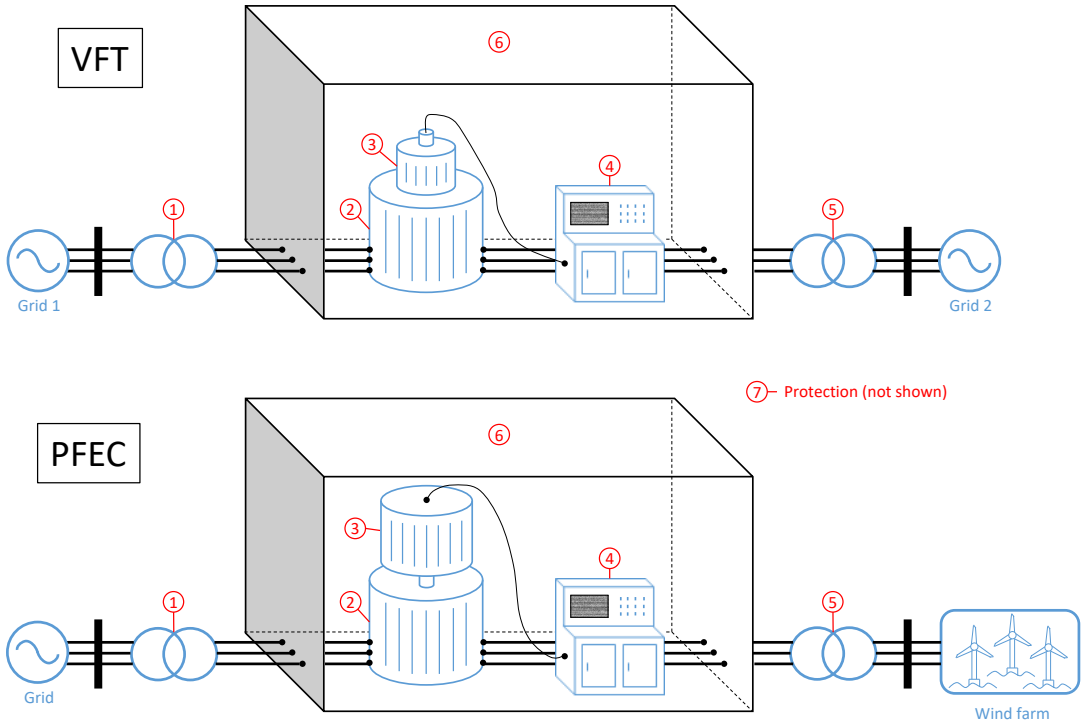

Figure 6.2: Comparison of required components for a) VFT and b) PFEC

Every difference between the VFT and the PFEC incurs an extra cost on the PFEC side implying that the PFEC is a more costly system, as expected. As seen in table 6.2, low frequency transformers require more iron to establish the magnetic flux which incurs extra materials cost. The 12MW DC drive motor and associated thyristor-based controller present in the VFT has its PFEC equivalent as a 200MW DFIM with a 20MW B2B-VSC thus bringing about the most considerable difference between the

two systems. The implications of the 200MW DFIM will also have consequences in the size of the facility, the protection system, filters, ventilation etc.

At the time of writing there are only three VFT installations worldwide, based in Laredo, Texas; Linden, New Jersey and Langlois, Quebec respectively. Of these three, only Laredo and Linden have publicly available cost information which is given as a raw figure and does not detail the individual component breakdown. Laredo is a 100MW VFT facility which provides an interconnection between Texas and Mexico and was stated as costing $74M for the VFT unit and related facilities [110]. Linden is a 300MW VFT facility which links the electrical networks of New Jersey and Quebec. It is stated in [111] that the regional transmission organisation PJM allocated $132M to the Linden VFT, which includes direct connection facilities estimated at $18 million and network upgrades estimated at $14.5 million [112]. Connection costs and upgrades are also likely to apply to any future HVAC or HVDC system and can therefore be subtracted from the total to give the cost of a 300MW VFT facility of approximately £79.6M (adjusted to GBP). Under the modularity assumptions stated earlier, a 600MW VFT facility would comprise of 2x 300MW VFTs and cost approximately £160M. Likewise a 900MW VFT facility would contain 3x 300MW VFT units and cost approximately £240M.

Costs for the VFT at Langlois were never published, but GE have stated that the two 100 MW VFTs developed for Québec have a cost similar to a 200MW DC back-to-back transmission system of the same capacity [85].

The cost of the 200MW DFIM can be obtained from information published on adjustable speed pumped hydro. Globally, there are 270 pumped hydroelectric storage stations of which 36 units consist of variable-speed machines. 17 of these are currently in operation and the remaining 19 are under construction, totalling 3,569MW and 4,558MW respectively. In all of these hydro stations, a DFIM motor-generator is the standard design for the variable speed machine. [113]. As with the VFT, cost

information on these large DFIMs is limited and only available in small quantities. In fact, the only publicly available cost figure which details both the generator costs and the associated electrical equipment is provided for the Linthal-Limmern adjustable speed pumped hydro station in Switzerland, in which Alstom were awarded a contract of £160M to develop 4x 250MW DFIMs and ABB were awarded a £96M contract to provide the electrical equipment (note that values have been converted to GBP). Under similar modularity assumptions used for the VFT unit cost in which there is no difference between variable and fixed costs, the total cost of a single 250MW DFIM and controller equates to approximately £64M. Note that a 250MW DFIM would be considered to be oversized when applied to a 300MW PFEC, as would the DFIM controller which is typically sized to provide a ±30% deviation from the synchronous speed when the PFEC only requires ±10%.

Using these costing estimates, an approximate upper and lower bound can be produced for a 300MW PFEC onshore plant. The lower bound is obtained by adding the cost of an additional 250MW DFIM to the full VFT facility. This method inevitably results in some costs being counted twice (i.e. the DC drive motor and thyristor drive) while leaving some out completely (i.e. increased footprint of facility) but it is assumed that these can be negated as the VFT and DFIM unit costs will dominate overall. An approximate upper bound for a 300MW PFEC can be found by multiplying the entire costs of a 300MW VFT facility by 2. In this way the requirement of a 200MW DFIM would be more than covered by the extra 300MW rotary transformer. The cost of the 20MW VSC would be partially covered by the 2x 4MW DC drive motors and thyristor drives now present with any remaining costs being covered by the overhead from the now oversized additional 300MW rotary transformer. Finally, the difference in cost between a 50Hz and 16.7Hz transformer is described in (6.20) and is less than a factor of two, ensuring that this upper bound does not underestimate any component in table 6.2.

The upper and lower bounds for a 300MW PFEC onshore plant are given by (6.23) and (6.24) which can then be used to provide an estimate for any integer multiple of

300MW under the modularity assumption.

$$OPC_{pfec}^{UB} = 2C_{VFT} = £159.2\text{M} \tag{6.23}$$

$$OPC_{pfec}^{LB} = C_{VFT} + C_{DFIM} = £79.6\text{M} + £64\text{M} = £143.6\text{M} \tag{6.24}$$

6.4.3 Cost of PFEC Cables

Cables for low frequency AC transmission are of exactly the same design as those in HVAC. A lower frequency benefits the transmission of power due to the linear relationship of charging current on frequency, meaning that the range of an HVAC cable in a one-third frequency environment is able to roughly increase the transmission distance three-fold. The lower frequency also helps reduce the sheath and dielectric losses, as well as reducing the resistance of the cable due to the reduced skin effect [114]. The same cables derived from [104] for HVAC transmission are therefore presented here as LFAC cables, with the only difference being the reduced resistance, which at 16.7Hz is around two-thirds of its 50Hz counterpart.

6.4.4 Cost of PFEC Compensation

Compensation costs for the PFEC are calculated in the same way as for HVAC but with a reduced frequency term in (6.7).

6.4.5 Cost of PFEC Losses

The losses of the PFEC follow the same form as in (6.8) in that they consist of the terminal losses and the route losses. Offshore terminal losses might be assumed to increase due to the larger transformers, but despite the larger volume the core losses would be reduced because of the one-third frequency. Based on the analysis in [115], the efficiency of a low frequency transformer would be close to a standard transformer. Thus the power losses of the offshore platform of the PFEC can be treated in the same way as for HVAC. The same is true for the route costs, except with a reduced frequency term inserted into (6.11).

The main difficulty in calculating the cost of onshore losses for the PFEC comes in trying to determine the total efficiency of the onshore plant. The most closely related relative of the PFEC is the VFT which is cited as being up to 99% efficient, however the rotational speeds of the VFT are considerably lower to those in the PFEC and this assumption is therefore not valid. Instead, one can look again to the hydro-power industry for an equivalently sized variable speed DFIM which are stated as having efficiencies of up to 98% and 98.5% [79],[80].

Assuming the more conservative estimate of 98% for both machines, the total efficiency of the PFEC for a 16.7Hz system can be calculated based on (6.25) which was previously derived from (3.2) and (3.3) respectively.

$$\eta_{pfec} = \left(\frac{2\eta_g^2 + \eta_g}{3} \right) \tag{6.25}$$

where η_g = efficiency of a typical variable speed hydro-generator.

6.4.6 O&M Costs

Another source of potential benefits of the PFEC comes from the reduced O&M costs of this network solution. Compared to HVDC the number of components in the PFEC is significantly lower which reduces the overall failure rate of the system. The sheer number of IGBTs in HVDC, for example, combined with their susceptibility to fault currents is a source of much of the total downtime experienced by an HVDC transmission system, especially when the faults occur on the offshore converter platform. A case study reported in [116] places the total O&M costs of the HVDC transmission system as 3% of total capital expenditure.

O&M costs for the PFEC are understandably difficult to estimate with any certainty, but it is again possible to compare with the most similar available equipment. VFT O&M figures are not in the public domain so instead one can look towards hydropower. A report in [117] gives a good breakdown of what is included in their O&M

expenditure and it is found that the vast majority of costs are related to the refurbishment of electrical and mechanical equipment with an average value of O&M costs given as between 2% and 2.5% of capital expenditure. Applying this figure to the PFEC and comparing with an HVDC system with roughly the same terminal costs as in figure 6.3, it can be expected that the PFEC system will benefit from decreased O&M which may be compounded by the ease of access of the onshore converter plant.

6.4.7 Alternative Revenue Streams

What is not included in the total costs is the potential income that would arise from participating in ancillary services to the grid and the various revenue streams that exist for these service. National grid offer financial incentives to asset holders if they can contribute to things such as frequency response [118] with some of the revenue streams detailed in table 6.3.

The inertia of the PFEC is beneficial to the stability of the grid frequency and should be considered as a key advantage over the other methods of power transmission, but the energy contained within the machine can also be released at will to provide even more support. This latter type of active participation to frequency response can be very lucrative with National Grid offering a set tariff based on the amount of power delivered over a desired period of time.

Table 6.3: Revenue steams and indicative values offered by National Grid

Revenue Stream	**Indicative Value**
Enhanced frequency response (EFR)	60 - 105 k£ (MW/year)
Firm frequency response (FFR)	50 - 145 k£ (MW/year)
Fast reserve (FR)	50 - 70 k£ (MW/year)
Short term operative reserve (STOR)	20 - 35 k£ (MW/year)
Capacity market (CM)	22.5 k£ (MW/year)
Triad avoidance (TA)	30 k£ (MW/year)
Capturing split energy (CSE)	Site dependent
Managing imbalance risk (MIR)	7 - 30.6 k£ (MW/year)
Wholesale price arbitrage (WPA)	20 k£ (MW/year)
Black start (BS)	Undisclosed

By decreasing the rotor speed of the PFEC, the kinetic energy of the combined machines can be released at will. Decreasing the rotor speed will have the effect of increasing the frequency on the 16.7Hz side, causing voltages to increase. Care must therefore be taken not to damage equipment from overvoltage in this way, but even a small decrease in rotor speed as a response to a frequency event will result in a huge release of active power and a large source of additional income.

6.5 Discussion of Results

Three different power level scenarios have been considered for the cost analysis of the three systems. These consist of a low power 300MW system, a medium power 600MW system and a high power 900MW system, chosen such that the modular approach derived from VFT and DFIM costings are applicable. As will be seen in the plots it is often necessary to change to a larger diameter cable and/or increase the number of conductors to account for the charging current in the cable, resulting in a cost function with step-wise increments as transmission distance increases. Also since the costs for the PFEC include an upper and a lower bound, the plots will contain a shaded band of potential costs rather than a solid line.

6.5.1 Low Power Scenario

Results for the low power scenario are presented in figure 6.3. Terminal costs of the three systems can be assessed at the point where the lines cross the y-axis. HVAC therefore have the lowest terminal costs followed by HVDC and then the PFEC as the most expensive. This is in agreement with the predictions stated in [52] which notes that the VFT cost per MW is close to that of back-to-back HVDC technology, therefore a PFEC which incorporates a VFT and a DFIM is certainly likely to exceed the terminal costs of HVDC.

Unsurprisingly, at these low power levels the HVAC transmission option remains

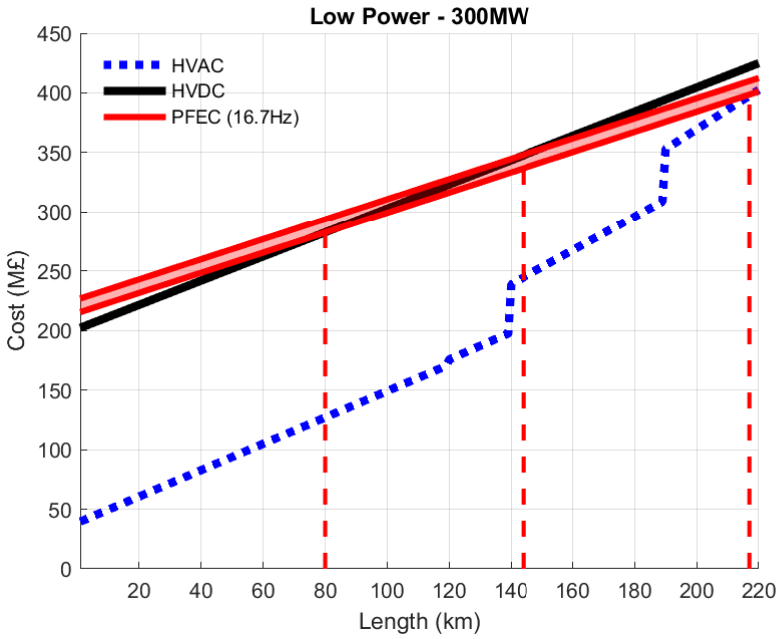

Figure 6.3: Capital costs per km for a 300MW HVAC; HVDC; and PFEC transmission system respectively. Dashed lines represent crossover points in cost.

the most economical in terms of capital cost over the entire range specified. It is not until beyond the 200km point that the HVAC system begins to look less attractive and allowing the lower bound of the PFEC to edge in. Of interest are the crossover points between HVDC costs and the PFEC, with the lower bound occurring at 80km and the upper bound at 145km. Providing that the previous assumptions hold, the true value is likely to reside somewhere within this range and implies that the PFEC may offer a cost effective alternative to HVDC transmission for medium range wind farms.

6.5.2 Medium Power Scenario

Results for the 600MW systems are shown in figure 6.4 and show a similar trend between HVAC and HVDC to those in the 300MW scenario, where HVAC remains the most economical option for a large range of distances. Unlike in the low power scenario the PFEC is found to be consistently the most expensive option for almost the whole range considered in the study. The terminal costs of the PFEC are just too high to compete with HVDC which begins to excel at high levels of power transmission, and although

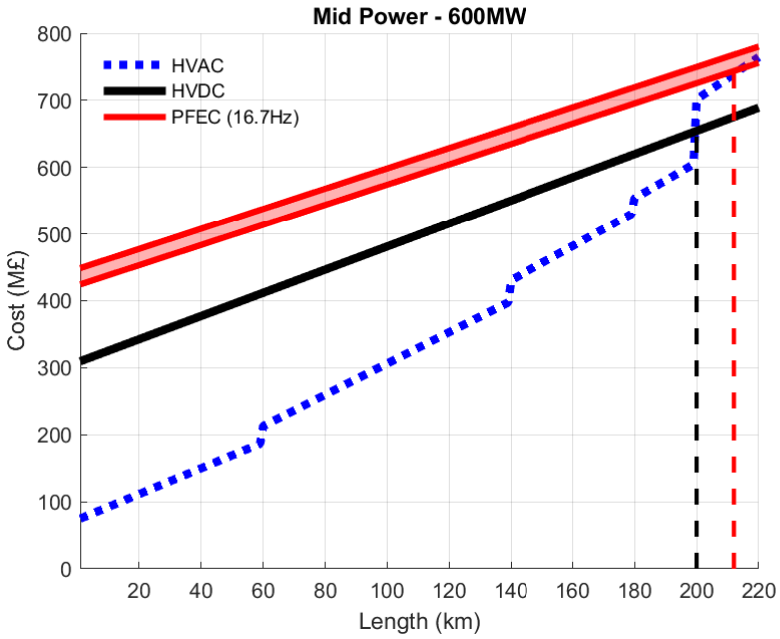

Figure 6.4: Capital costs per km for a 600MW HVAC; HVDC; and PFEC transmission system respectively

the gradient of the PFEC cost function is slightly less than HVDC, the crossover never occurs within the range.

6.5.3 High Power Scenario

At the highest power level considered in this analysis the costs of the PFEC continue to climb while those of HVDC continue to decrease. As power rating increases HVDC becomes more and more attractive due to it's essentially unlimited range and immunity from the effects of cable charging currents which have detrimental effects on both of the AC options. Terminal costs of the PFEC are considerable higher than the other two options at this point, caused largely by the requirement of parallel 300MW machines rather than one single motor-generator set rated for the full 900MW. The current state of DFIM technology maxes out at around 400MW such that the parallel machine requirement is unlikely to be alleviated in the near future. It is concluded based on these studies that the PFEC is not a viable choice for wind farms of this magnitude.

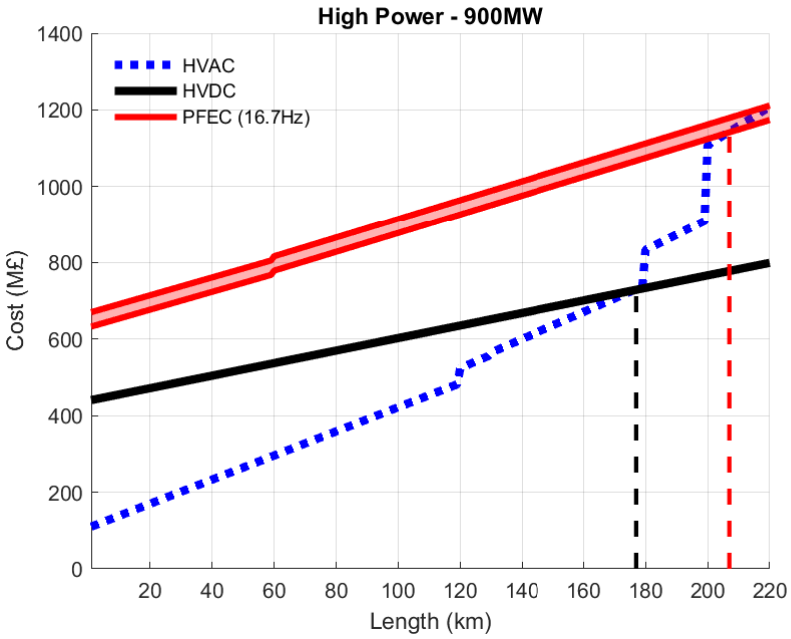

Figure 6.5: Capital costs per km for a 900MW HVAC; HVDC; and PFEC transmission system respectively

6.6 Summary and Conclusion

In this chapter a cost assessment of the PFEC has been conducted for the purposes of assessing it against equivalent HVAC and HVDC transmission systems. Existing cost data and scaling laws derived from the literature have been combined to give an upper and lower bound of the CAPEX of a PFEC system. Care has been taken when making assumptions by comparing the technology of the PFEC to the most similar technology currently in existence and overestimating costs when necessary in an attempt to avoid positive-bias. Three power transmission scenarios were assessed, ranging from a low power wind farm of 300MW to a medium power of 600MW and then a high power of 900MW.

The costing functions introduced in this chapter have been derived from a range of sources, both algorithmic and empirical with data taken from many real-world installations found globally. Projected costs for HVAC installations are the most reliable of the those presented here because of the maturity of the technology and the large

number of HVAC installations worldwide. The commonly used costing functions for HVDC that are present in the literature have been modified to more accurately reflect the recent experiences of HVDC for offshore wind in industry, where extensive delays and adverse weather conditions have led to massively inflated costs. The difficulty in quantifying the value of this risk has led to an alternative approach in measuring cost based on empirical data, which when compared to the literature approach provides a similar costing curve that is not beyond the realms of possibility.

Costs of the PFEC as a method of power transmission have been estimated based on theoretical cost models of LFAC transmission but without the inclusion of the power-electronic frequency converter. Instead, published cost figures from the most similar technology have been used, i.e. the VFT and high power DFIMs found in adjustable-speed pumped hydro to provide an upper and a lower bound for total onshore costs. The limited number of VFT facilities and adjustable speed pumped-hydro stations are a source of uncertainty when trying to determining the PFEC onshore plant costs such that a number of sweeping assumptions have had to be made. However, care has been taken not to underestimate the potential costs of the PFEC and to err on the side of caution by preferring to double-count components rather than to omit when such instances are unavoidable.

Results have shown that LFAC-based PFEC transmission may be competitive with HVDC in the application to medium range, low power offshore wind farms (where the term low is relative to the other power ratings considered in this study and considered to be around 300MW). At distances between 80km and 145km the cost function of the PFEC crosses over with that of HVDC, however both options remain significantly more expensive than HVAC when only capital costs are taken into account. Despite this, the number of offshore wind farms that are opting for HVDC transmission over HVAC are increasing in number, so the high terminal costs are not as much as a deterrent as would appear at a glance. It therefore seems logical to state that: if HVDC transmission systems appear attractive to an offshore wind farm developer then perhaps there is

room for PFEC-based LFAC in the future given the advantages it provides in terms of offshore multi-terminal deployment, maintenance, robustness and compatibility with AC networks. Furthermore the CAPEX of the PFEC does not present the full picture of the levelised cost of energy of using the LFAC-PFEC solution for offshore wind power, which has proven to favour long lasting solutions even when the initial investment is high.

Chapter 7

Conclusions and Future Work

7.1 Conclusions

This work has presented the PFEC as a novel device to enable the low frequency connection of offshore wind. Throughout the literature it is often assumed that any future LFAC transmission system for offshore wind will be power electronic based with the method of frequency conversion being that of a VSC or a cycloconverter, however this work has demonstrated that an alternative novel approach does exist. This work contains the theory and operating principles of the PFEC which are used to develop models and to explore some of the many characteristics of how this machine operates.

A model of the PFEC was developed in chapter 3 and verified through simulation in chapter 4 where it was shown that the PFEC can indeed provide an interconnection between the low frequency wind farm and the utility grid. The PFEC model was shown to be fully controllable but also stable in the absence of the power electronic converter thanks to the specific arrangement of poles which provide a natural equilibrium between the DFIM and the RT. The method of correct pole sizing to achieve this natural equilibrium was generalised such that the PFEC is versatile over a range of frequencies and not just a 16.7Hz asynchronous connection. The stability of the PFEC in the absence of power electronics was tested which verified the existence of the equilibrium point. While in this state all controllability over the device is lost but the device does

not lose synchronism.

In chapter 5 the control system of the PFEC was equipped with additional control loops designed to exploit the large inertia of the PFEC for ancillary services. The DFIG synthetic inertia control strategies which are common in modern wind turbines were modified for application to the PFEC to extract kinetic energy from the rotor during a frequency excursion. Results show that a PFEC equipped with such a controller can provide enough active power to the grid and make a noticeable improvement to the frequency nadir. Also in this chapter are the consequences of the synthetic inertia controller which comes at the expense of the small-signal stability of the power system and result in a reduced damping. The synthetic inertia controller makes the PFEC behave more like a synchronous machine and therefore participates to the oscillatory modes between generators and reduces stability.

Chapter 6 developed a CAPEX model designed to compare the capital costs of the PFEC to that of HVAC and HVDC. Using cost data from the most similar technology available it was found that the PFEC is not cost effective at high power ratings (600MW - 900MW) as this would involve multiple PFEC units connected in parallel. However when considering a 300MW system the PFEC was shown to be similar in cost to that of HVDC which is consistent with the literature, becoming slightly cheaper over a transmission distance of around 80km. The fact that 300MW HVDC installations do currently exist for offshore wind despite their significantly increased CAPEX over HVAC suggests that there may be a case for using a PFEC for low power wind farms in the future.

Appendix A provides a possible solution to the maximum theoretical sizing of a PFEC unit by considering a brushless approach. It is reported in the literature that the slip rings determine the maximum possible rating of the VFT and hence the PFEC by extension. A model for a brushless-PFEC that uses a pair of double-stator induction machines is developed and new controllers for this hypothetical machine are derived

and tested in appendix A.

Finally, appendix B details the current progress in developing a PFEC prototype which so far has been limited to just the controller which acts as the interface between computer and the DFIM. The custom converter board was tested and shown to be suitable for applying control to the DFIM. This work was interrupted by the Covid-19 pandemic and remains unfinished, but will be built upon in future projects with the ultimate goal of developing a working PFEC prototype.

7.2 Future Work

There are still plenty of aspects about the PFEC that were not covered in this work which demand future attention, the most important of which is the continued development of a working prototype. Some characteristics of the PFEC have been verified through simulation and the next step is to verify these through experimentation, however issues relating to Covid-19 and the effect this has had on lab access have severely hindered efforts in completing the PFEC on time. A more thorough look into the losses and efficiencies of a PFEC system is also needed, as is a detailed analysis on reactive power flows throughout the network.

In the development of a cost model in chapter 6 it was assumed that multiple PFEC units could be connected in parallel to achieve greater power ratings, however the consequences of this were not discussed. Studies therefore need to be run on the stability of using parallel PFECs and whether there are any adverse effects on the power system.

This work has been focused on relatively large PFEC units specifically for offshore wind ranging in size up to 600MW, however there may be benefits in exploring smaller units on the order of kilowatts for use in electric vehicles. Future work could look into the advantages of these small-scale rotary converters to provide low-frequency power supplies in the rapidly growing EV market.

Appendix A

Brushless-PFEC

The parameters of the rotary transformer and DFIM within the PFEC have been based on existing VFT technology. The reason for this is that an induction machine cannot be scaled to be arbitrarily large due to limiting factors surrounding the rated capacity and rated voltages. At present, the VFT manufactured by GE has a capacity of 105MVA with a theorised upper limit of 200 - 300MW based on the opinions of relevant experts [85]. The main limiting factors that influence this number are:

1. Slip rings: The VFT is restricted by the maximum allowable current rating of the collector system, namely by the graphite brushes. The capacity and maintenance of the carbon brushes are a key issue in the operation and cost of the VFT.

2. Insulation requirements: The current carried by the carbon brushes can be reduced by having a larger rated voltage, however this leads to higher requirements for the design of the insulation around the rotating parts of the machine. The rated voltages of existing hydro-generators can be used as the limit of technology due to their size, with reported voltages exceeding 18kV and up to 21kV being quite common. [119], [79].

The brushless-doubly-fed induction machine (BDFM) negates the need for slip rings by means of a twin stator and a nested-loop rotor. All connections are made through either one of the stators meaning that there is no direct electrical connection to the rotor circuit. The resulting device is therefore free from one of the main limiting factors

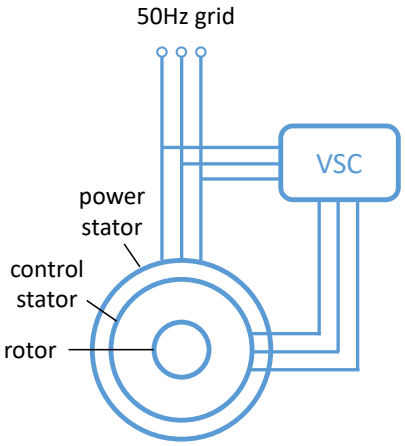

Figure A.1: BDFM concept showing the two stators and the non-electrically connected rotor.

to up-scaling the rated capacity, as well as benefiting from the reduced maintenance associated with brush wear.

A.1 BDFM Theory

The stator of the BDFM is equipped with two pairs of stator windings which differ in pole number to avoid direct coupling with each other. The windings of stator 1 are connected to the power grid directly so this stator is therefore known as the power-stator, or p-stator for short. The windings of stator 2 are supplied with a converter to handle only a fraction of this power. The converter allows control over this part of the circuit, so stator 2 is referred to as the control stator, or c-stator. This configuration, shown in figure A.1, has the advantage of reducing the rating of the power electronics in much the same way as with a standard DFIG [120]. The rotor is specially designed with a nested-loop configuration to couple the two stators.

With the presence of two stators, the BDFM is essentially two machines housed in the same unit and can therefore operate at more than one speed. If one stator supply is left unconnected, then the BDFM can operate as a simple induction machine. De-

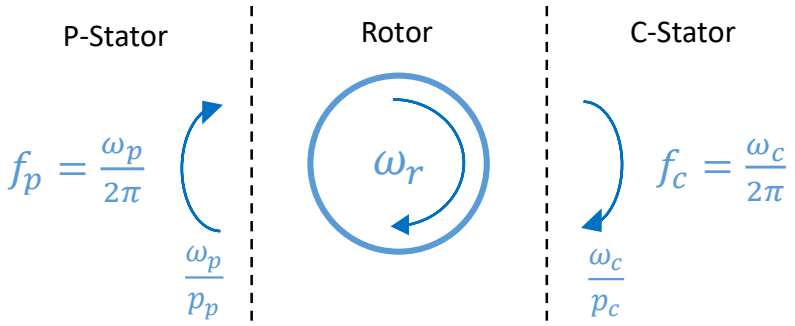

Figure A.2: Rotation of fundamental fields [121]

pending on which stator is connected the BDFM operates with either p_p pole pairs or p_c pole pairs.

On the other hand, if the second stator is short-circuited, then the BDFM behaves as a cascaded induction machine with the characteristics of a (p_p+p_c) pole pair machine.

The final mode of operation is the doubly-fed mode which will be the focus of this chapter. In this design, the p-stator is coupled to the c-stator through the rotor which rotates in a way to synchronise the two frames. It is a requirement of the BDFM that the direct coupling between the p- and c- stators is to be avoided, which can be achieved by setting $p_p \neq p_c$. If the p-stator has p_p poles and is connected to a three-phase supply with angular frequency ω_p, then the airgap flux will rotate at ω_p/p_p (rad/s). Similarly for the c-stator, the flux will rotate at ω_c/p_c (rad/s). This effect is shown in figure A.2.

These conditions give a fundamental magnetic flux density equal to that in (A.1).

$$\begin{aligned} b_p(\theta,t) &= \hat{B}_p \cos\left(\omega_p t - p_p\theta\right) \\ b_c(\theta,t) &= \hat{B}_c \cos\left(\omega_c t - p_c\theta\right) \end{aligned} \tag{A.1}$$

Or in the rotor reference frame:

$$\begin{aligned} b_p^{'}(\theta^{'},t) &= \hat{B}_p \cos\left((\omega_p - \omega_r p_p)t - p_p\theta^{'}\right) \\ b_c^{'}(\theta^{'},t) &= \hat{B}_c \cos\left((\omega_c - \omega_r p_c)t - p_c\theta^{'}\right) \\ \text{where} \quad \theta^{'} &= \theta + \omega_r t \end{aligned} \tag{A.2}$$

In order for the currents induced by $b_p^{'}$ to couple with those produced by $b_c^{'}$, the condition in (A.3) for the travelling waves must be satisfied.

$$(\omega_p - \omega_r p_p) = \pm(\omega_c - \omega_r p_c) \tag{A.3}$$

The two possible solutions to this equality are presented in (A.4), which give the possible synchronous speeds of the BDFM in doubly-fed operation.

$$\omega_r = \frac{\omega_p + \omega_c}{p_p + p_c} \qquad\qquad \omega_r = \frac{\omega_p - \omega_c}{p_p - p_c} \tag{A.4}$$

The cross-coupling of the two stator fields relies on the modulation behaviour of the specially designed rotor which is connected in a nested-loop design as shown in figure A.3. The nested cage rotor has a similar construction to a squirrel cage, however instead of all bars being connected together at the two end rings, the bars are subdivided into $(p_p + p_c)$ groups called nests. In figure A.3a there are 4 nests, selected for a BDFM with $p_p = 3$ and $p_c = 1$. Since the p-stator and c-stator are both confined to the same core, special care must be taken to avoid any direct coupling between the two by means of a suitably chosen pole pair combination [122].

The number of loops is selected to reduce the harmonic content in the rotor MMF. As loop number increases, harmonic content decreases but so does the space between loops, meaning that there is less space for the flux to pass. Typically 3 to 6 loops are selected [123], such that the 2 loops in figure A.3a are there to merely illustrate the concept.

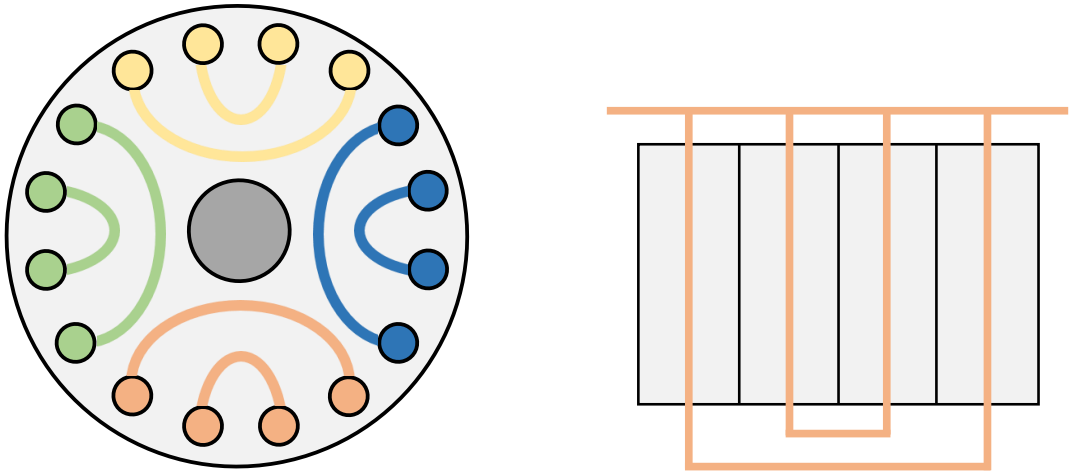

(a) Radial view showing 4 distinct nests, each with 2 loops

(b) Axial view of nested-loop rotor with common end ring

Figure A.3: BDFM rotor construction

A number of rotor winding structures have been proposed, such as the nested-loop winding shown in figure A.3b, as well as isolated nested-loop windings; nested-loop windings with two common rings [124]; series loop windings [125] and multi-phase double-layer windings [126]. All of these produce the same cross-coupling mode of operation but with differences in rotor resistance, leakage inductance and control properties, however these are not discussed here.

A.2 Modelling

The modelling process of the BDFM is based on the same approach as for the 5th order dq-model of an induction machine, with the main difference being the presence of an additional stator circuit in the state equations.

The presence of multiple electrical circuits with different excitation frequencies produce multiple reference frames which make it complicated to apply the well known theory of induction machine control. A unified reference frame is therefore derived in [127] which allows a single reference frame to be used rather than a different frame for each of the three circuits, namely the p-stator, c-stator and rotor. The equations describing the dynamics of the brushless doubly-fed induction machine in the unified dq-reference frame are shown in (A.5) - (A.10).

$$v_{pd} = R_p i_{pd} + \frac{d\psi_{pd}}{dt} - \omega_p \psi_{pq} \tag{A.5}$$

$$v_{pq} = R_p i_{pq} + \frac{d\psi_{pq}}{dt} + \omega_p \psi_{pd} \tag{A.6}$$

$$v_{cd} = R_c i_{cd} + \frac{d\psi_{cd}}{dt} - [\omega_p - (p_p + p_c)\omega_r]\psi_{cq} \tag{A.7}$$

$$v_{cq} = R_c i_{cq} + \frac{d\psi_{cq}}{dt} + [\omega_p - (p_p + p_c)\omega_r]\psi_{cd} \tag{A.8}$$

$$v_{rd} = R_r i_{rd} + \frac{d\psi_{rd}}{dt} - [\omega_p - p_p\omega_r]\psi_{rq} \tag{A.9}$$

$$v_{rq} = R_r i_{rq} + \frac{d\psi_{rq}}{dt} + [\omega_p - p_p\omega_r]\psi_{rd} \tag{A.10}$$

where v is the terminal voltage, R is the winding resistance, i is the winding current, ψ is the flux linkage, ω_p is the angular speed of the power stator, ω_r is the angular mechanical speed of the rotor, and p is the number of poles. The subscripts d and q refer to the d- and q- axes, while the subscripts p, c, r refer to the p-stator, c-stator and the rotor respectively.

The main advantage of transforming to a d,q reference frame is that the coefficients in the inductance matrix no longer vary with time. The inductance matrix with

constant coefficients is presented in vector form in (A.11), where $\vec{\psi_p} = \psi_{pd} + j\psi_{pq}$ for example. Here, L_{lp}, L_{lc}, L_{lr} are the leakage inductances of the p-stator, c-stator and rotor respectively. M_p is the mutual inductance between the p-stator and rotor and M_c is the mutual inductance between the c-stator and rotor.

$$\begin{bmatrix} \vec{\psi_p} \\ \vec{\psi_c} \\ \vec{\psi_r} \end{bmatrix} = \begin{bmatrix} (L_{lp} + M_p) & 0 & M_p \\ 0 & (L_{lc} + M_c) & M_c \\ M_p & M_c & (L_{lr} + M_p + M_c) \end{bmatrix} \begin{bmatrix} \vec{i_p} \\ \vec{i_c} \\ \vec{i_r} \end{bmatrix} \tag{A.11}$$

Rearranging (A.11) for current as the dependent variable gives:

$$\vec{i_p} = \frac{\vec{\psi_p} - M_p(\vec{i_p} + \vec{i_r})}{L_{lp}} \tag{A.12}$$

$$\vec{i_c} = \frac{\vec{\psi_c} - M_c(\vec{i_c} + \vec{i_r})}{L_{lc}} \tag{A.13}$$

$$\vec{i_r} = \frac{\vec{\psi_c} - M_p(\vec{i_p} + \vec{i_r}) - M_c(\vec{i_c} + \vec{i_r})}{L_{lr}} \tag{A.14}$$

If the state equations are modelled directly in the form in (A.5) - (A.10), then the interplay between the currents and flux linkages in (A.12) - (A.14) results in algebraic loops being formed in the simulation. To counter this, the crossover between current and flux linkage can be avoided such that flux linkage is the dependent variable. Introducing the change of variables in (A.15) - (A.16):

$$\vec{\psi_{mp}} = M_p(\vec{i_p} + \vec{i_r}) \tag{A.15}$$

$$\vec{\psi_{mc}} = M_c(\vec{i_c} + \vec{i_r}) \tag{A.16}$$

and combining with (A.12) - (A.14) gives current in terms of the new variables.

$$\vec{i_p} = \frac{\vec{\psi_p} - \vec{\psi_{mp}}}{L_{lp}} \tag{A.17}$$

$$\vec{i_c} = \frac{\vec{\psi_c} - \vec{\psi_{mc}}}{L_{lc}} \tag{A.18}$$

$$\vec{i_r} = \frac{\vec{\psi_r} - \vec{\psi_{mp}} - \vec{\psi_{mc}}}{L_{lr}} \tag{A.19}$$

Substituting the new values for current in (A.17) - (A.19) into (A.15) and (A.16) gives:

$$\vec{\psi_{mp}} = L_X\left(\frac{\vec{\psi_p}}{L_{lp}} - \frac{\vec{\psi_r}}{L_{lr}} - \frac{\vec{\psi_{mc}}}{L_{lr}}\right) \tag{A.20}$$

$$\vec{\psi_{mc}} = L_Y\left(\frac{\vec{\psi_c}}{L_{lc}} - \frac{\vec{\psi_r}}{L_{lr}} - \frac{\vec{\psi_{mp}}}{L_{lr}}\right) \tag{A.21}$$

where

$$\frac{1}{L_X} = \left(\frac{1}{L_{lr}} + \frac{1}{L_{lp}} + \frac{1}{M_p}\right) \tag{A.22}$$

$$\frac{1}{L_Y} = \left(\frac{1}{L_{lr}} + \frac{1}{L_{lc}} + \frac{1}{M_c}\right) \tag{A.23}$$

Solving (A.20) and (A.21) simultaneously gives $\vec{\psi_{mp}}$ and $\vec{\psi_{mc}}$ entirely in terms of fluxes as in (A.24) and (A.25), thus avoiding the algebraic loop in the simulation process.

$$\vec{\psi_{mp}} = \frac{L_X[(\vec{\psi_r}(L_Y - L_{lr})L_{lp} - L_{lr}^2\vec{\psi_p})L_{lc} + L_Y L_{lp} L_{lr}\vec{\psi_c}]}{L_{lc}L_{lp}(L_X L_Y - L_{lr}^2)} \tag{A.24}$$

$$\vec{\psi_{mc}} = \frac{L_Y[(\vec{\psi_r}(L_X - L_{lr})L_{lp} + L_X L_{lr}\vec{\psi_p})L_{lc} - L_{lp} L_{lr}^2\vec{\psi_c}]}{L_{lc}L_{lp}(L_X L_Y - L_{lr}^2)} \tag{A.25}$$

The state-space model described by (A.5) - (A.10) can now be rearranged to integral form for simulation, and by using the substitutions (A.17) - (A.19) can be presented in

a form without algebraic loops as in (A.26) - (A.31).

$$\psi_{pd} = \int v_{pd} - \frac{R_p}{L_{lp}}(\psi_{pd} - \psi_{mpd}) + \omega_p \psi_{pq} \quad dt \tag{A.26}$$

$$\psi_{pq} = \int v_{pq} - \frac{R_p}{L_{lp}}(\psi_{pq} - \psi_{mpq}) - \omega_p \psi_{pd} \quad dt \tag{A.27}$$

$$\psi_{cd} = \int v_{cd} - \frac{R_c}{L_{lc}}(\psi_{cd} - \psi_{mcd}) + [\omega_p - (p_p + p_c)\omega_r]\psi_{cq} \quad dt \tag{A.28}$$

$$\psi_{cq} = \int v_{cq} - \frac{R_c}{L_{lc}}(\psi_{cq} - \psi_{mcq}) - [\omega_p - (p_p + p_c)\omega_r]\psi_{cd} \quad dt \tag{A.29}$$

$$\psi_{rd} = \int v_{rd} - \frac{R_r}{L_{lr}}(\psi_{rd} - \psi_{mpd} - \psi_{mcd}) + s_p \omega_p \psi_{rq} \quad dt \tag{A.30}$$

$$\psi_{rq} = \int v_{rq} - \frac{R_r}{L_{lr}}(\psi_{rq} - \psi_{mpq} - \psi_{mcq}) - s_p \omega_p \psi_{rd} \quad dt \tag{A.31}$$

where s_p is the slip of the p-stator, given by $s_p = \dfrac{\omega_p - p_p \omega_r}{\omega_p}$.

A.2.1 Torque Derivation

The equations presented in (A.26) - (A.31) describe the electrical dynamics of the BDFM, which can be combined with the the rotor dynamics in (A.32) to give the full 7th-order model of the BDFM.

$$\omega_r = \frac{1}{J} \int \left(T_e - T_m - T_{damp}\right) \quad dt \tag{A.32}$$

where J is the inertia of the rotor, T_e is the electromagnetic torque, T_m is the mechanical load torque and T_{damp} is the damping torque.

This section focuses on the derivation of the electromagnetic torque term, T_e in (A.32). First, introduce a change of variables to define the self-inductance of the p-stator, c-stator and rotor respectively.

$$\begin{aligned} L_{pp} &= L_{lp} + M_p \\ L_{cc} &= L_{lc} + M_c \\ L_{rr} &= L_{lr} + M_p + M_c \end{aligned} \tag{A.33}$$

such that the inductance matrix from (A.11) becomes:

$$\begin{bmatrix} \vec{\psi_p} \\ \vec{\psi_c} \\ \vec{\psi_r} \end{bmatrix} = \begin{bmatrix} L_{pp} & 0 & M_p \\ 0 & L_{cc} & M_c \\ M_p & M_c & L_{rr} \end{bmatrix} \begin{bmatrix} \vec{i_p} \\ \vec{i_c} \\ \vec{i_r} \end{bmatrix} \tag{A.34}$$

Rearranging (A.34) gives an expression for rotor current

$$\vec{i_r} = \frac{\vec{\psi_p}}{M_p} - \frac{L_{pp}\vec{i_p}}{M_p} \tag{A.35}$$

$$\vec{i_r} = \frac{\vec{\psi_c}}{M_c} - \frac{L_{cc}\vec{i_c}}{M_c} \tag{A.36}$$

The active power of the BDFM is given by the sum of the real contributions of power from each of the p-stator, c-stator and rotor as shown in (A.37).

$$P_e = \frac{3}{2}\big(\Re e[\vec{v_p}\vec{i_p}^*] + \Re e[\vec{v_c}\vec{i_c}^*] + \Re e[\vec{v_r}\vec{i_r}^*]\big) \tag{A.37}$$

Written in full, the individual contributions to active power from each circuit are presented in (A.38) - (A.40).

$$\Re e[\vec{v_p}\vec{i_p}^*] = R_p|i_p|^2 + \Re e\big[\frac{d\vec{\psi_p}}{dt}.\vec{i_p}^*\big] + \Re e\big[j\omega_p\vec{\psi_p}\vec{i_p}^*\big] \tag{A.38}$$

$$\Re e[\vec{v_c}\vec{i_c}^*] = R_c|i_c|^2 + \Re e\big[\frac{d\vec{\psi_c}}{dt}.\vec{i_c}^*\big] + \Re e\big[j(\omega_p - (p_p + p_c)\omega_r)\vec{\psi_c}\vec{i_c}^*\big] \tag{A.39}$$

$$\Re e[\vec{v_r}\vec{i_r}^*] = \underbrace{R_r|i_r|^2}_{\text{losses}} + \underbrace{\Re e\big[\frac{d\vec{\psi_r}}{dt}.\vec{i_r}^*\big]}_{\text{inductor}} + \underbrace{\Re e\big[js_p\omega_p\vec{\psi_r}\vec{i_r}^*\big]}_{\text{electromagnetic}} \tag{A.40}$$

The three bracketed terms in (A.40) correspond to the copper losses in the windings, the transient power of the inductor and the electromagnetic power respectively. The latter of these terms is associated with the production of electromagnetic torque and is defined by (A.41).

$$T_e = \frac{P_e}{\omega_r} \tag{A.41}$$

Substituting (A.38) - (A.40) into (A.37) gives P_e as:

$$P_e = \frac{3}{2}\left(\Re e\big[j\omega_p\vec{\psi_p}\vec{i_p}^*\big] + \Re e\big[j(\omega_p - (p_p + p_c)\omega_r)\vec{\psi_c}\vec{i_c}^*\big] + \Re e\big[js_p\omega_p\vec{\psi_r}\vec{i_r}^*\big]\right) \quad \text{(A.42)}$$

To eliminate the presence of the j-transformations from (A.42), the identity in (A.43) can be used.

$$\Re e\big[j\vec{X_1}\vec{X_2}^*\big] = \Im m\big[\vec{X_2}\vec{X_1}^*\big] = -\Im m\big[\vec{X_1}\vec{X_2}^*\big] \quad \text{(A.43)}$$

Rearranging (A.42) based on this identity gives P_e as:

$$P_e = \frac{3}{2}\left(\Im m\big[\vec{\psi_p}\vec{i_p}^*\big]\omega_r + \Im m\big[\vec{i_c}\vec{\psi_c}^*\big](\omega_r - (p_p + p_c)\omega_r) + \Im m\big[\vec{i_r}\vec{\psi_r}^*\big]s_p\omega_p\right) \quad \text{(A.44)}$$

The contribution to electromagnetic power from the rotor can be isolated from (A.44) to give (A.45).

$$P_{e_r} = \frac{3s_p\omega_p}{2}.\Im m\big[\vec{i_r}\vec{\psi_r}^*\big] \quad \text{(A.45)}$$

The conjugate term $\vec{\psi_r}^*$ is equal to that in (A.46):

$$\vec{\psi_r}^* = L_{rr}\vec{i_r}^* + M_p\vec{i_p}^* + M_c\vec{i_c}^* \quad \text{(A.46)}$$

which can be substituted into (A.45) and simplified to give the rotor electromagnetic power contribution as:

$$P_{e_r} = \frac{3s_p\omega_p}{2}.\Im m\big[M_p\vec{i_r}\vec{i_p}^* + M_c\vec{i_r}\vec{i_c}^*\big] \quad \text{(A.47)}$$

substituting the values of $\vec{i_r}$ from (A.35) - (A.36) into (A.47) and simplifying gives the rotor power as (A.48)

$$P_{e_r} = \frac{3s_p\omega_p}{2}.\Im m\big[\vec{\psi_p}\vec{i_p}^* + \vec{\psi_c}\vec{i_c}^*\big] \quad \text{(A.48)}$$

Substituting (A.48) back into the full equation for electromagnetic power gives

electromagnetic power as (A.49).

$$P_e = \frac{3\omega_r p_p}{2}.\Im m\left[\vec{\psi_p}^{\,*}\vec{i_p}\right] + \frac{3\omega_r p_c}{2}.\Im m\left[\vec{\psi_c}\vec{i_c}^{\,*}\right] \tag{A.49}$$

Finally, from (A.41), the electromagnetic torque is presented as

$$T_e = \frac{3p_p}{2}.\Im m\left[\vec{\psi_p}^{\,*}\vec{i_p}\right] + \frac{3p_c}{2}.\Im m\left[\vec{\psi_c}\vec{i_c}^{\,*}\right] \tag{A.50}$$

It can be seen that the total electromagnetic torque T_e of the BDFM is defined as the algebraic sum of the individual torque contributions of the p-stator and the c-stator respectively:

$$T_e = T_{ep} + T_{ec} \tag{A.51}$$

$$\text{where} \quad T_{ep} = \frac{3p_p}{2}.\Im m\left[\vec{\psi_p}^{\,*}\vec{i_p}\right] \tag{A.52}$$

$$\text{and} \quad T_{ec} = \frac{3p_c}{2}.\Im m\left[\vec{\psi_c}\vec{i_c}^{\,*}\right] \tag{A.53}$$

The full 7th-order dq model is therefore described by the state equations presented in (A.26) - (A.31) and (A.50).

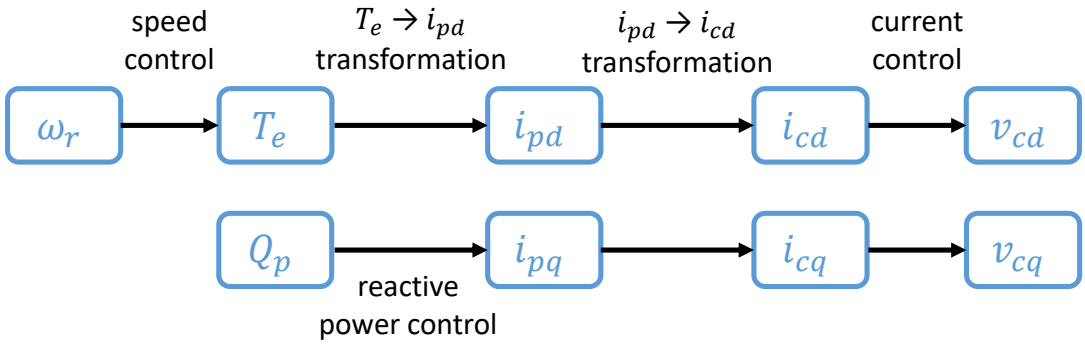

Figure A.4: Block diagram showing cascaded control strategy of BDFM

A.3 Control Design

As the name suggests, control of the BDFM can be accomplished by manipulating the currents in the control-stator circuit by means of a voltage sourced converter. This is analogous to control of the DFIM in which the rotor circuit is similarly controlled by a VSC.

By means of a suitably designed controller, the d-axis can be used to control the speed or torque of the rotor (depending on the application) and the q-axis can be used to control the reactive power at the p-stator terminals. This control scheme is shown as a flow chart in A.4 which shows the steps that must be taken to access the c-stator circuit for the d and q axes respectively.

Unlike in the standard DFIM which possesses only a single stator, A.4 shows that there is an additional transformation in the BDFM that is required to find a relationship between the currents in the p-stator and those in the c-stator.

A.3.1 ip to ic current transformation

Setting the $\frac{d}{dt}$ terms in (A.5) - (A.10) to zero gives the steady state model of the BDFM:

$$\vec{v_p} = R_p\vec{i_p} + j\omega_p\vec{\psi_p} \tag{A.54}$$

$$\vec{v_c} = R_c\vec{i_c} + j[\omega_p - (p_p + p_c)\omega_r]\vec{\psi_c} \tag{A.55}$$

$$0 = R_r i_r + js_p\omega_p\vec{\psi_r} \tag{A.56}$$

substituting for $\vec{\psi_p}$, $\vec{\psi_c}$ and $\vec{\psi_r}$ from (A.34) gives:

$$\vec{v_p} = R_p\vec{i_p} + j\omega_p L_{pp}\vec{i_p} + j\omega_p M_p\vec{i_r} \tag{A.57}$$

$$\vec{v_c} = R_c\vec{i_c} + j[\omega_p - (p_p + p_c)\omega_r]L_{cc}\vec{i_c} + j[\omega_p - (p_p + p_c)\omega_r]M_c\vec{i_r} \tag{A.58}$$

$$0 = R_r\vec{i_r} + js_p\omega_p L_{rr}\vec{i_r} + js_p\omega_p M_p\vec{i_p} + js_p\omega_p M_c\vec{i_c} \tag{A.59}$$

Since there is no electrical connection to the rotor, the rotor circuit is short-circuited and the voltage is therefore zero. Rearranging (A.59) gives an expression for rotor current which can be used in further derivations.

$$\vec{i_r} = \frac{-js_p\omega_p}{(R_r + js_p\omega_p L_{rr})}\left[M_p\vec{i_p} + M_c\vec{i_c}\right] \tag{A.60}$$

To allow the independent control of active and reactive currents, a dq-reference frame is required to generate the orthogonal components. The dq-axis is aligned such that:

$$v_{pd} = \hat{v_p} = -\omega_p\psi_{pq} \qquad\qquad v_{pq} = 0 \tag{A.61}$$

where $\hat{v_p}$ is the p-stator peak phase voltage. Since the current lags the voltage by 90° and flux is proportional to current, the flux of the p-stator can be written as in (A.62).

$$\psi_{pd} = 0 \qquad\qquad \psi_{pq} = -\hat{\psi_p} \tag{A.62}$$

A common approach to determining the relationship between $\vec{i_p}$ and $\vec{i_c}$ is by using (A.57) with the p-stator voltage equal to that in (A.61) while neglecting the p-stator resistance R_p [120], [128]. Substituting $\vec{i_r}$ from (A.60) into (A.57) and rearranging for $\vec{i_c}$ gives:

$$i_{cd} = \left[\frac{L_{pp}L_{rr} - M_p^2}{M_p M_c}\right] i_{pd} + \left[\frac{L_{pp}R_r}{s_p\omega_p M_p M_c}\right] i_{pq} + \left[\frac{\psi_p R_r}{s_p\omega_p M_p M_c}\right] \tag{A.63}$$

$$i_{cq} = \left[\frac{L_{pp}L_{rr} - M_p^2}{M_p M_c}\right] i_{pq} - \left[\frac{L_{pp}R_r}{s_p\omega_p M_p M_c}\right] i_{pd} + \left[\frac{\psi_p L_{rr}}{M_p M_c}\right] \tag{A.64}$$

similarly

$$i_{pd} = \left[\frac{M_p M_c}{(L_{pp}L_{rr} - M_p^2)}\right] i_{cd} - \left[\frac{L_{pp}R_r}{s_p\omega_p(L_{pp}L_{rr} - M_p^2)}\right] i_{pq} - \left[\frac{\psi_p R_r}{s_p\omega_p(L_{pp}L_{rr} - M_p^2)}\right] \tag{A.65}$$

$$i_{pq} = \left[\frac{M_p M_c}{(L_{pp}L_{rr} - M_p^2)}\right] i_{cq} + \left[\frac{L_{pp}R_r}{s_p\omega_p(L_{pp}L_{rr} - M_p^2)}\right] i_{pd} - \left[\frac{\psi_p L_{rr}}{(L_{pp}L_{rr} - M_p^2)}\right] \tag{A.66}$$

Equations (A.63) - (A.66) define the $\vec{i_p}$ to $\vec{i_c}$ transformation in figure A.4 and demonstrate the relationship between $\vec{i_c}$ and $\vec{i_p}$ (and vice versa). This is shown in block layout in figure A.5 where it can be seen that the d and q components are not fully orthogonal as there exists a cross-coupling between the two axes.

Note that the cross-coupling coefficient terms are dependent on slip and may be neglected as compared to the direct coupling term if the speed of the rotor is within $\pm 50\%$ of the synchronous speed. This gives the result of $\vec{i_p}$ being linear with $\vec{i_c}$.

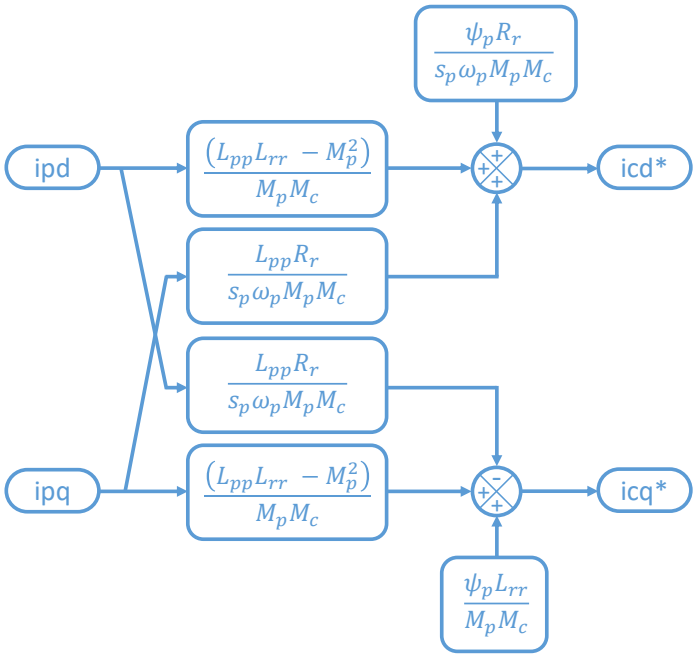

Figure A.5: Relationship between $\vec{i_p}$ and $\vec{i_c}$ showing the cross-coupling terms.

A.3.2 C-Stator Current Control

The currents in the c-stator can be controlled by adjusting the terminal voltage such that any desired flow of current is achieved. A relationship between $\vec{i_c}$ and $\vec{v_c}$ is therefore required. From (A.7) and (A.8), the terminal voltage of the c-stator is presented as:

$$v_{cd} = R_c i_{cd} + \frac{d\psi_{cd}}{dt} - \left[\omega_p - (p_p + p_c)\omega_r\right]\psi_{cq} \tag{A.67}$$

$$v_{cq} = R_c i_{cq} + \frac{d\psi_{cq}}{dt} + \left[\omega_p - (p_p + p_c)\omega_r\right]\psi_{cd} \tag{A.68}$$

The expressions for $\vec{\psi_c}$ are given from (A.11):

$$\psi_{cd} = L_{cc} i_{cd} + M_c i_{rd} \tag{A.69}$$

$$\psi_{cq} = L_{cc} i_{cq} + M_c i_{rq} \tag{A.70}$$

By using the same dq axis alignment defined in (A.61) and (A.62), the rotor current

terms in (A.69) and (A.70) can be written in terms of $\vec{i_p}$ by rearranging (A.11):

$$\psi_{pd} = L_{pp} i_{pd} + M_p i_{rd} \tag{A.71}$$

$$\psi_{pq} = L_{pp} i_{pq} + M_p i_{rq} \tag{A.72}$$

$$\implies i_{rd} = \frac{-L_{pp} i_{pd}}{M_p} \qquad (\text{since } \psi_{pd} = 0) \tag{A.73}$$

$$\implies i_{rq} = \frac{-\psi_p - L_{pp} i_{pq}}{M_p} \qquad (\text{since } \psi_{pq} = -\psi_p) \tag{A.74}$$

Using the previously derived relationship between $\vec{i_c}$ and $\vec{i_p}$ in (A.65) and (A.66), $\vec{i_r}$ can now be expressed in the form in (A.75) and (A.76).

$$\begin{aligned} i_{rd} =& \left(\frac{-L_{pp} M_c}{L_{pp} L_{rr} - M_p^2} \right) i_{cd} + \frac{L_{pp} \psi_p R_r}{s_p \omega_p M_p (L_{pp} L_{rr} - M_p^2)} \\ &+ \left(\frac{L_{pp}^2 R_r}{s_p \omega_p M_p (L_{pp} L_{rr} - M_p^2)} \right) i_{pq} \end{aligned} \tag{A.75}$$

$$\begin{aligned} i_{rq} =& \left(\frac{-L_{pp} M_c}{L_{pp} L_{rr} - M_p^2} \right) i_{cq} + \frac{L_{pp} \psi_p L_{rr}}{M_p (L_{pp} L_{rr} - M_p^2)} \\ &- \left(\frac{L_{pp}^2 R_r}{s_p \omega_p M_p (L_{pp} L_{rr} - M_p^2)} \right) i_{pd} - \frac{\psi_p}{M_p} \end{aligned} \tag{A.76}$$

Substituting (A.75) and (A.76) into (A.69) and (A.70) gives:

$$\begin{aligned} \psi_{cd} =& \left(\frac{L_{cc} L_{pp} L_{rr} - L_{cc} M_p^2 - M_c^2 L_{pp}}{L_{pp} L_{rr} - M_p^2} \right) i_{cd} + \frac{M_c L_{pp} \psi_p R_r}{s_p \omega_p M_p (L_{pp} L_{rr} - M_p^2)} \\ &+ \left(\frac{M_c L_{pp}^2 R_r}{s_p \omega_p M_p (L_{pp} L_{rr} - M_p^2)} \right) i_{pq} \end{aligned} \tag{A.77}$$

$$\begin{aligned} \psi_{cq} =& \left(\frac{L_{cc} L_{pp} L_{rr} - L_{cc} M_p^2 - M_c^2 L_{pp}}{L_{pp} L_{rr} - M_p^2} \right) i_{cq} + \frac{M_c L_{pp} \psi_p L_{rr}}{M_p (L_{pp} L_{rr} - M_p^2)} \\ &- \left(\frac{M_c L_{pp}^2 R_r}{s_p \omega_p M_p (L_{pp} L_{rr} - M_p^2)} \right) i_{pd} - \frac{M_c \psi_p}{M_p} \end{aligned} \tag{A.78}$$

Finally, substituting (A.77) and (A.78) into (A.67) and (A.68) and ignoring the cross-coupling terms gives a relationship between the terminal voltage and the current

of the c-stator as required.

$$v_{cd} = R_c i_{cd} + \frac{d}{dt}\left[\left(\frac{L_{cc}L_{pp}L_{rr} - L_{cc}M_p^2 - M_c^2 L_{pp}}{L_{pp}L_{rr} - M_p^2}\right) i_{cd}\right] \tag{A.79}$$

$$v_{cq} = R_c i_{cq} + \frac{d}{dt}\left[\left(\frac{L_{cc}L_{pp}L_{rr} - L_{cc}M_p^2 - M_c^2 L_{pp}}{L_{pp}L_{rr} - M_p^2}\right) i_{cq}\right] \tag{A.80}$$

The cross-coupling terms are treated as a disturbance and are therefore not present in the control design. Because of this, we see that the constant terms multiplying i_{cd} and i_{cq} in (A.79) and (A.80) respectively are identical, meaning that the controller will be exactly the same for both the d and q axis.

It should also be mentioned that the choice of alignment performed in (A.61) and (A.62) does not affect the design of the controller. For example, if instead v_d is taken to be zero, then the change is only experienced by the constant terms in (A.75) and (A.76). Since these constant terms eventually appear in the differential operator in (A.67) and (A.68), these cancel out resulting in a design of the controller which is invariant under the choice of dq alignment.

Proceeding with just the d-axis, (since the d and q axis are identical), the transfer function from $i_{cd}(s)$ to $v_{cd}(s)$ in the s-plane is obtained from rearranging (A.79):

$$\frac{i_{cd}(s)}{v_{cd}(s)} = \left[\frac{L_{pp}L_{rr} - M_p^2}{R_c(L_{pp}L_{rr} - M_p^2) + s(L_{pp}L_{cc}L_{rr} - L_{cc}M_p^2 - M_c^2 L_{pp})}\right] \tag{A.81}$$

It can be seen that exists one stable pole located at:

$$s = \frac{-R_c(L_{pp}L_{rr} - M_p^2)}{(L_{pp}L_{cc}L_{rr} - L_{cc}M_p^2 - M_c^2 L_{pp})} \tag{A.82}$$

This pole can be cancelled with a PI controller, which when applied to (A.81) gives the open loop gain of the system as:

$$\ell_i(s) = \frac{K_p}{s}\left(s + \frac{K_i}{K_p}\right)\left[\frac{L_{pp}L_{rr} - M_p^2}{R_c(L_{pp}L_{rr} - M_p^2) + s(L_{pp}L_{cc}L_{rr} - L_{cc}M_p^2 - M_c^2 L_{pp})}\right] \tag{A.83}$$

Introducing the substitution:

$$\frac{K_i}{K_p} = \frac{R_c(L_{pp}L_{rr} - M_p^2)}{(L_{pp}L_{cc}L_{rr} - L_{cc}M_p^2 - M_c^2L_{pp})} \tag{A.84}$$

the open loop gain becomes:

$$\ell_i(s) = \frac{K_p}{s}\left[\frac{L_{pp}L_{rr} - M_p^2}{(L_{pp}L_{cc}L_{rr} - L_{cc}M_p^2 - M_c^2L_{pp})}\right] \tag{A.85}$$

finally, introducing the substitution for K_p we get:

$$K_p = \left[\frac{(L_{pp}L_{cc}L_{rr} - L_{cc}M_p^2 - M_c^2L_{pp})}{L_{pp}L_{rr} - M_p^2}\right]\alpha_{ic} \tag{A.86}$$

where α_{ic} defines the bandwidth of the system. Substituting (A.86) into (A.84) gives the integral gain of the controller:

$$K_i = R_c\alpha_{ic} \tag{A.87}$$

such that the open loop and closed loop gains of the system are presented in (A.88) and (A.89), as required.

$$\ell_i(s) = \frac{\alpha_{ic}}{s} \tag{A.88}$$

$$L_i(s) = \frac{\alpha_{ic}}{s + \alpha_{ic}} \tag{A.89}$$

The PI controller could now be built based on the parameters above, but due to the presence of the disturbances from the cross-coupling terms, it is advisable to introduce an additional internal feedback term to improve disturbance rejection. The specific derivation is omitted here since it follows the exact process as was done for the PFEC in a previous chapter. The parameters with the inclusion of the internal feedback term

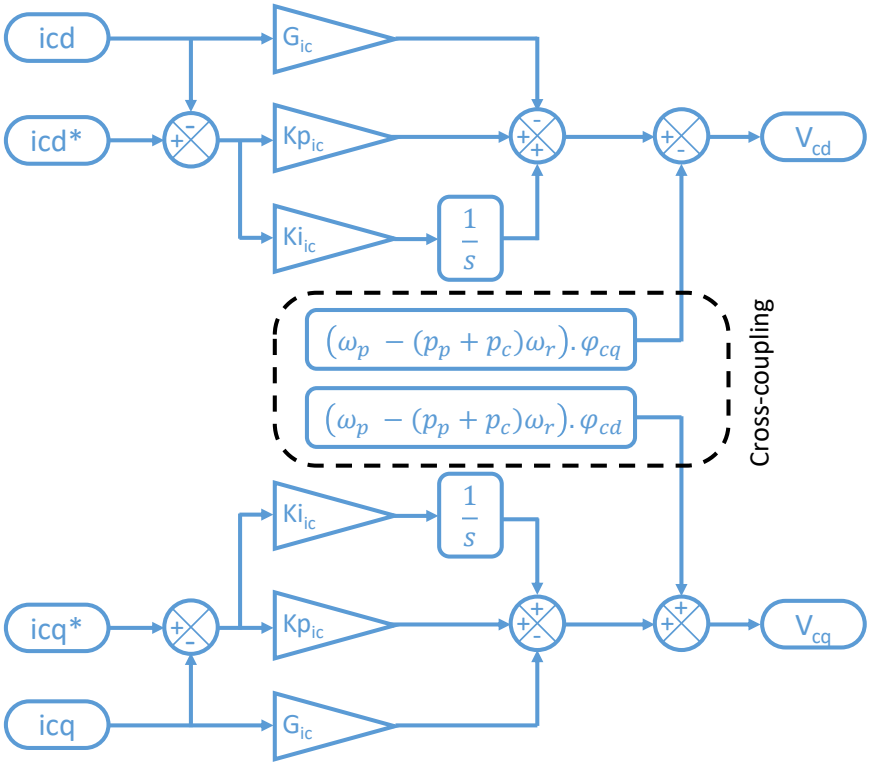

Figure A.6: Control of ic current

are given in (A.90) - (A.92).

$$K_p = \left[\frac{(L_{pp}L_{cc}L_{rr} - L_{cc}M_p^2 - M_c^2 L_{pp})}{L_{pp}L_{rr} - M_p^2}\right]\alpha_{ic} \tag{A.90}$$

$$K_i = (G_{ic} + R_c)\alpha_{ic} \tag{A.91}$$

$$G_{ic} = \left(\frac{-R_c(L_{pp}L_{rr} - M_p^2) + (L_{pp}L_{cc}L_{rr} - L_{cc}M_p^2 - M_c^2 L_{pp})}{L_{pp}L_{rr} - M_p^2}\right)\alpha_{ic} \tag{A.92}$$

The control system block layout is presented in figure A.6 showing the cross-coupling terms between the d and q axes, as well as the internal feedback term to improve disturbance rejection.

A.3.3 Rotor Torque Control

Although torque is not a control variable in application of the brushless-PFEC, its derivation is included here for completeness as it contains vital information needed for the ultimate goal of controlling rotor speed.

From (A.50), the electromagnetic torque is given by (A.93).

$$T_e = \frac{3}{2}p_p\big(i_{pq}\psi_{pd} - i_{pd}\psi_{pq}\big) + \frac{3}{2}p_c\big(i_{cd}\psi_{cq} - i_{cq}\psi_{cd}\big) \tag{A.93}$$

We know that $\psi_{pd} = 0$ and $\psi_{pq} = -|\psi_p|$ from (A.62), so these terms can be evaluated immediately. We also have expressions for $\vec{\psi_c}$ in terms of $\vec{i_c}$ from (A.77) and (A.78), and $\vec{i_c}$ in terms of $\vec{i_p}$ from (A.63) and (A.64). Using these substitutions, it is possible to express electromagnetic torque entirely in p-stator variables, as in (A.94).

$$\begin{aligned} T_e =& \left(\frac{3\psi_p(p_p + p_c)}{2}\right)i_{pd} - \left(\frac{3p_c\psi_p R_r L_{pp}}{2s_p\omega_p M_p^2}\right)i_{pq} - \frac{3p_c\psi_p^2 R_r}{2s_p\omega_p M_p^2} \\ & - \left(\frac{3p_c L_{pp}^2 R_r}{2s_p\omega_p M_p^2}\right)(i_{pd}^2 + i_{pq}^2) \end{aligned} \tag{A.94}$$

(A.94) defines the transformation between T_e and i_{pd} referred to in figure A.4, however for simplicity of design, the quadratic terms are neglected. This transformation is shown in block form in figure A.7.

Looking at (A.94), it can be seen that torque can be controlled with i_{pd} directly since this is the only term not dependent on the slip. The other terms in (A.94) can be treated as disturbances and thus do not appear in the design of the torque controller.

Neglecting the cross-coupling and constant terms in (A.94) gives the torque as:

$$T_e = \left(\frac{3\psi_p(p_p + p_c)}{2}\right)i_{pd} \tag{A.95}$$

Transforming (A.95) to the s-plane and rearranging gives the transfer function from

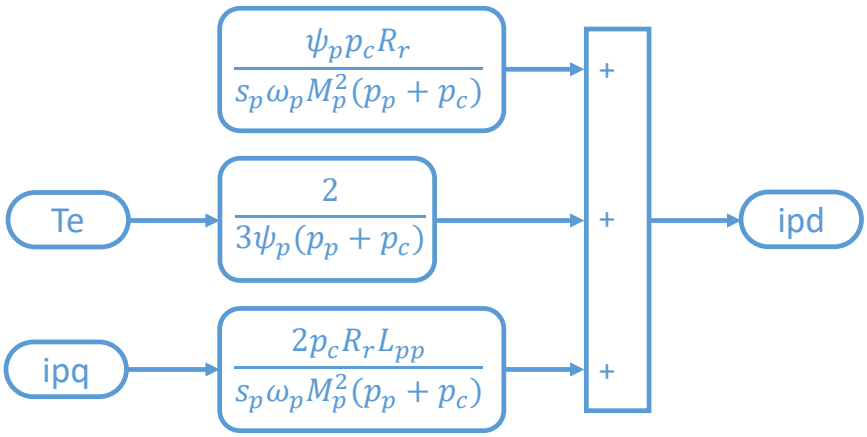

Figure A.7: Transformation from Te to ipd

$T_e(s)$ to $i_{pd}(s)$ as:

$$\frac{T_e(s)}{i_{pd}(s)} = \frac{3(p_p + p_c)\psi_p}{2} \tag{A.96}$$

By introducing an integral term to eliminate stead-state errors, the open loop gain of the plant with the controller is given by (A.97).

$$\ell_T(s) = \left(\frac{K_{iT}}{s}\right)\left(\frac{3\psi_p(p_p + p_c)}{2}\right) \tag{A.97}$$

The integral gain of the system is therefore:

$$K_{iT} = \frac{2\alpha_T}{3\psi_p(p_p + p_c)} \tag{A.98}$$

The control layout of the torque controller is presented in figure A.8.

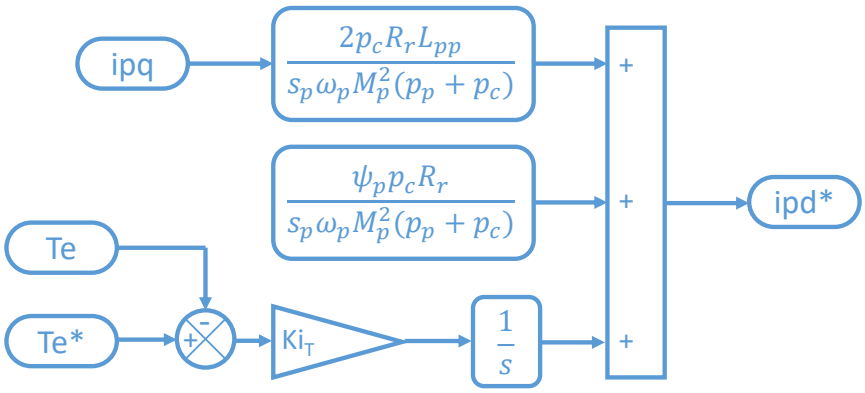

Figure A.8: Control of T_e used to produce a reference current signal i_{pd} for use in the current transformation

A.3.4 Rotor speed controller

The rotor speed controller derivation follows the same process as for the normal DFIM, since the dynamics are described by the same equation, (A.99).

$$\frac{d\omega_r}{dt} = \frac{1}{J}(T_e - T_m - T_{damp}) \tag{A.99}$$

A PI controller tuned with the parameters in (A.100) - (A.102) is therefore sufficient. Note that the additional internal feedback gain has been introduced following the same process as for the DFIM to improve disturbance rejection.

$$K_{p\omega} = J\alpha_\omega \tag{A.100}$$

$$K_{i\omega} = \alpha(B + G_\omega) \tag{A.101}$$

$$G_\omega = J\alpha_\omega - B \tag{A.102}$$

The block layout of the rotor controller is presented in figure A.9, showing the generation of the reference torque signal which is then used in the transformation from T_e to i_{pd}.

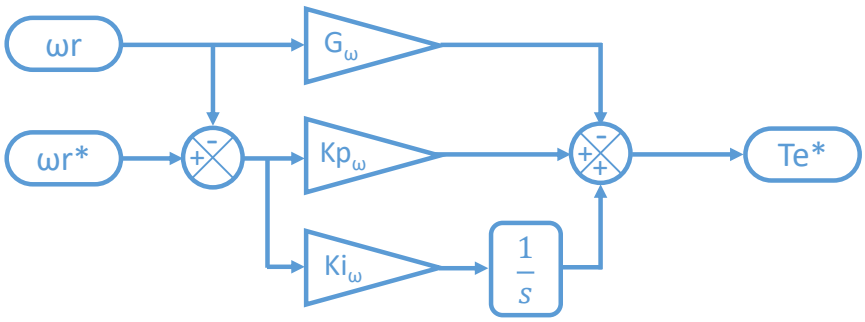

Figure A.9: Rotor speed controller with internal feedback term G_ω

A.3.5 Reactive Power Controller

The reactive power controller derivation also follows the same process as for the DFIM, since the dynamics are described by the same equation, (A.103).

$$Q_p = \frac{3}{2}\left(v_{pq}i_{pd} - v_{pd}i_{pq}\right) \tag{A.103}$$

Using (A.61), this reduces to:

$$Q_p = -\frac{3}{2}v_{pd}i_{pq} \tag{A.104}$$

Transforming to the s-plane and rearranging gives the transfer function from Q_p to i_{pq} as:

$$\frac{i_{pq}(s)}{Q_p(s)} = -\frac{2}{3\omega_p\psi_p} \tag{A.105}$$

By introducing an integral term to eliminate stead-state errors, the open loop gain of the plant with the controller is given by (A.106).

$$\ell_Q(s) = \left(\frac{K_{iQ}}{s}\right)\left(\frac{-2}{3\omega_p\psi_p}\right) \tag{A.106}$$

The integral gain of the system is therefore:

$$K_{iQ} = \frac{-3\omega_p\psi_p}{2}.\alpha_Q \tag{A.107}$$

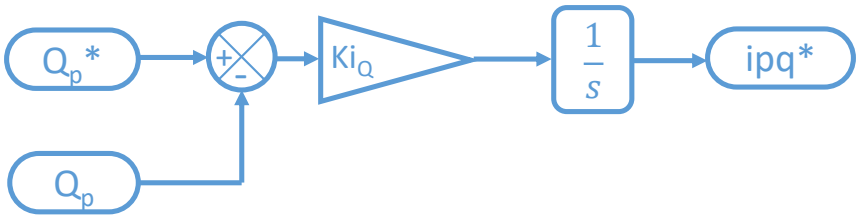

Figure A.10: Reactive power controller

The block layout of the reactive power controller is presented in figure A.10, showing the generation of the reference current which is then used in the transformation from i_{pq} to i_{cq}.

A.4 Performance

The performance of the model and the controllers is tested to validate the equations presented.

In the first simulation, the p-stator of the BDFM is connected to a three phase 50Hz voltage source and the c-stator is short circuited. Upon energising the p-stator circuit, the machine will accelerate up to the synchronous speed which is determined by the combination of poles between the p-stator and c-stator circuits. Once at the synchronous speed, the electromagnetic torque will remain at zero, resulting in neither an acceleration or deceleration of the rotor.

Figure A.11 shows the startup of the BDFM. As described, the rotor reaches the synchronous speed of 1PU and the electromagnetic torque becomes zero. There is some non-linear behaviour associated with the cross-coupling terms in the torque plots which manifests itself as a ripple in the rotor speed.

The second simulation shows the reaction of the current controller to a step change in reference signal. At t = 2s, a command of 0.2PU is sent to the controller, which quickly acts to eliminate the error between i_{cd} and i^*_{cd}. The result is shown in figure

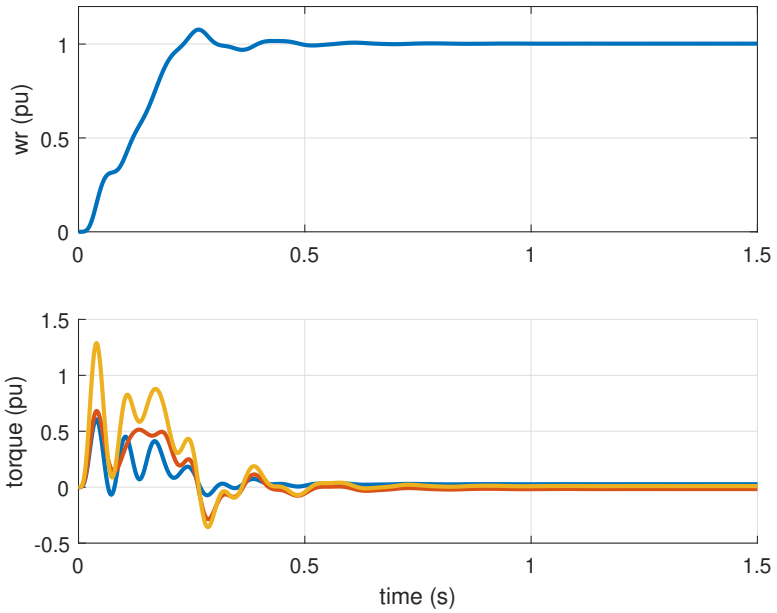

Figure A.11: Startup plots of BDFM. Top: rotor speed. Bottom: Electromagnetic torque

A.12a, where the effect of the cross-coupling terms is visible by the ripple present on i_{cq}.

Figure A.12a shows good disturbance rejection helped largely by the addition of the internal feedback term. The improvement is visible in figure A.12b where the response to the same step change is shown before and after the addition of the internal feedback term. With G_{ic} present, the time taken to reach steady state is significantly improved.

The performance of the rotor speed controller is plotted in figure A.13. Also shown in this plot are the electromagnetic torque contributions from the p- and c-stators respectively, as well the p-stator dq current. The machine is started at zero speed until at t = 1s a command of 1PU rotor speed is sent. The electromagnetic torque spikes to cause a rapid acceleration to the new reference speed, which can be seen as an increase in i_{pd} current in the bottom plot. The effect of the cross-coupling terms is also visible on the i_{pq} current.

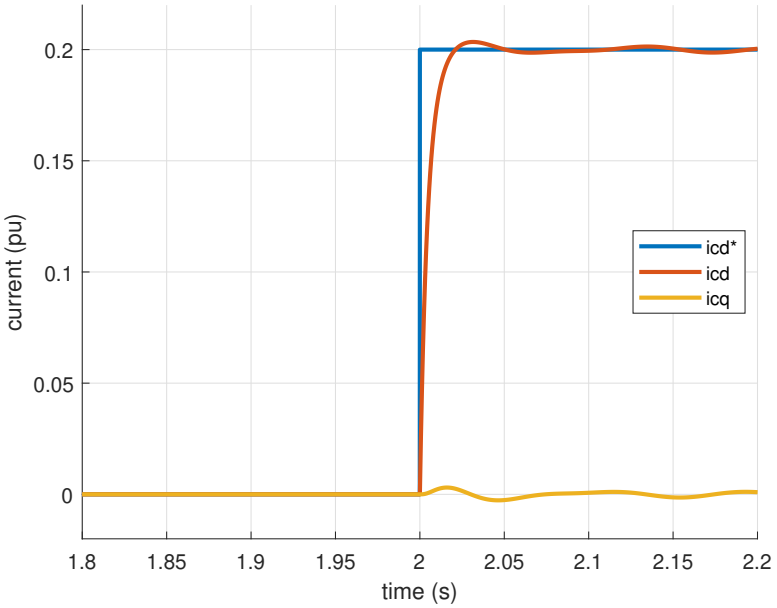

(a) Response of controller to a step change in reference signal. Also visible is the effect of cross-coupling on i_{cq}.

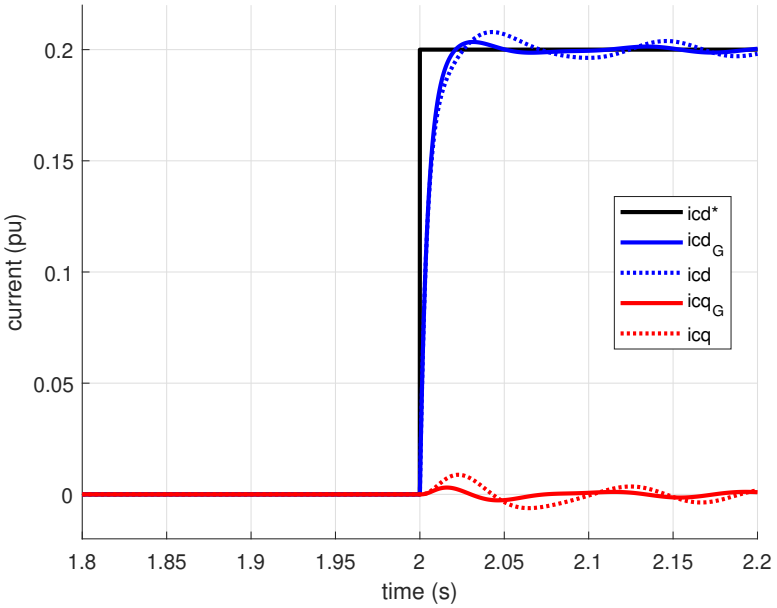

(b) Improved disturbance rejection due to internal feedback term. The subscript G denotes the presence of the internal feedback loop

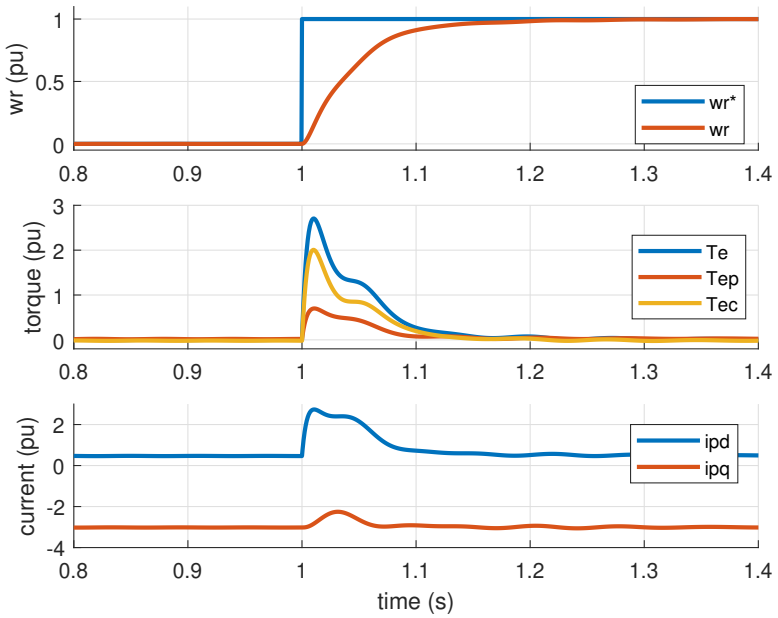

Figure A.13: Rotor speed controller performance. Top: rotor speed. Middle: torque. Bottom: $\vec{i_p}$ current.

A.5 Application to the VFT and PFEC

The variable frequency transformer is currently being used as an alternative to HVDC in a number of locations in the Americas. The construction of the VFT is essentially just a large DFIM with a fully-rated rotor circuit such that it can provide an interconnection between two asynchronous networks. The transferral of power between the stator and rotor circuit relies on the use of brushgear to enable an electrical connection to the rotating shaft of the rotor. As discussed earlier these components are prone to wear, meaning that the VFT could benefit from the advantages of brushless operation [129].

The concept of the brushless-PFEC follows automatically from the B-VFT. By introducing a second BDFM designed to maintain the rotor at a specific speed, an interconnection between two asynchronous frequencies is possible. From (A.4), the rotor spins at a speed proportional to the difference between the two frequencies. This can be rearranged to provide a relationship between the electrical frequency at either

stator (A.108), and the rotor speed required to maintain this synchronism.

$$f_c = \frac{(p_p + p_c)\omega_r}{2\pi} - f_p \tag{A.108}$$

where ω_p and ω_c are the excitation angular frequencies supplied to the two stator windings.

Application of the BDFM to the brushless-PFEC follows the same process as with the standard DFIM. Before connecting the machines together, a few key adjustments must be made, such as getting the correct balance of poles between the two machines such that the steady-state rotor speed is equal to the difference in frequency on the stator and rotor side of the rotary transformer. For an interconnection of 50:16.7 (Hz), this ratio is 2:1 wrt to the rotary transformer. That is, the rotary transformer must have twice as many poles as the BDFM.

Secondly, the coupled-shaft of the two machines must be modelled such that they behave as a single rotor. This is achieved by setting the electromagnetic torque output of the rotary transformer to be equal to the mechanical torque input of the BDFM. Likewise, the rotor speed output of the BDFM is set as the rotor speed input of the rotary transformer. The latter step causes the mechanical dynamics of the RT to be bypassed, since the rotor speed is no longer defined by the swing equation in (A.32). As a result, the inertia of the rotary transformer is neglected and must instead be incorporated into the BDFM, which now possesses the total inertia of the machine.

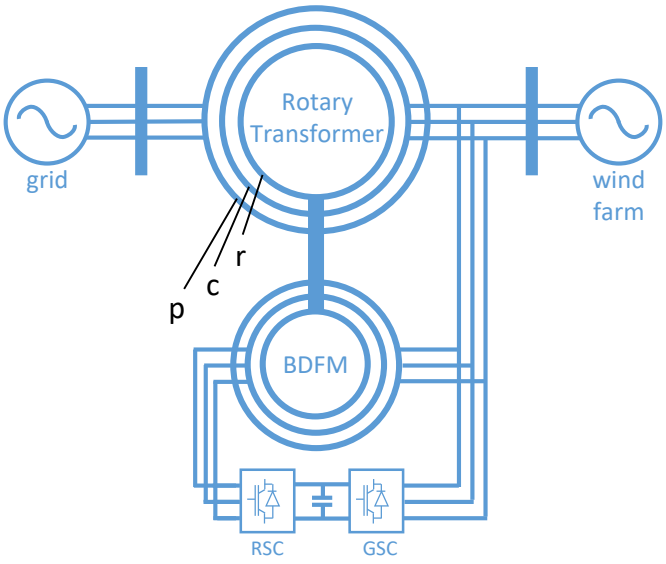

Figure A.14: Schematic of brushless PFEC layout, showing the dual stator configuration. p, c and r denote the power stator, control stator and rotor respectively.

Figure A.14 shows the schematic of the brushless-PFEC. The p-stator of the rotary transformer is connected to the 50Hz network and the c-stator is connected to the low frequency wind farm. The machine labelled BDFM acts to motor the rotary transformer and keep the speed constant at the synchronising frequency. The BDFM is connected to the c-stator circuit of the rotary transformer and must therefore be designed to operate at a low frequency and voltage. Also shown is the B2B-VSC allowing vector oriented control over the c-stator variables. For consistency with previous chapters these have retained the acronyms RSC and GSC, despite there being no electrical connection to the rotor circuit.

The B-PFEC is simulated as being connected to a 50Hz grid and a 16.7Hz wind farm. At steady-state, the rotor speed is naturally maintained at 1 PU_{BDFM} in the BDFM base, which allows minimal use of the controllers. This translates as 0.67 PU_{RT} in the rotary transformer base, thus allowing the interconnection of the prescribed wind farm. These results are shown in figure A.15. The top plot shows the steady-state rotor speeds in two respective bases while the bottom plot shows the electrical frequency on either side of the rotary transformer, demonstrating that the B-PFEC does indeed

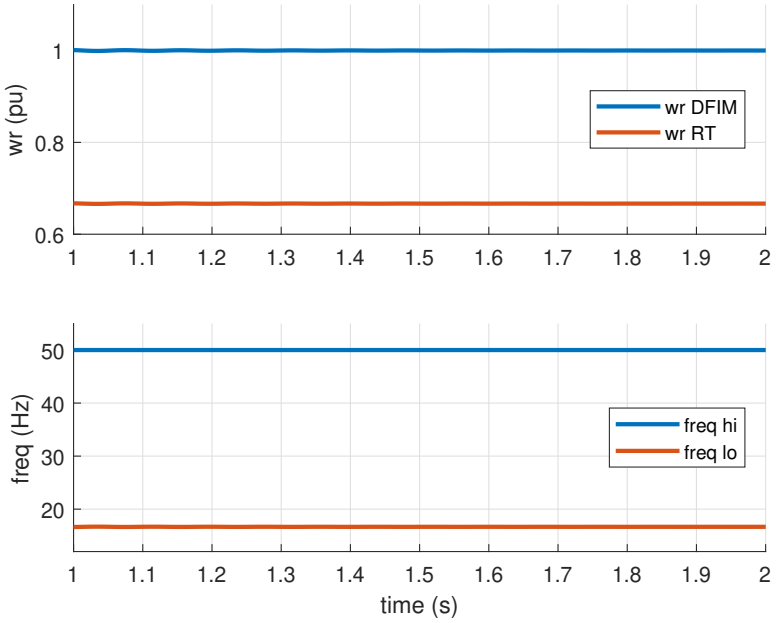

Figure A.15: Steady-state plots of BPFEC. Top: rotor speed with respect to the BDFM base and the RT base. Bottom: electrical frequency in Hz on the high and low sides of the rotary transformer

enable the low-frequency connection of offshore wind without the need for brushgear.

Appendix B

Hardware Development

Note: Because of the restrictions imposed by Covid-19 and the resulting lack of laboratory access, this sections is incomplete, however it serves as a good starting point for any future development of the PFEC.

The move from simulation to experimental validation requires the development of specific hardware to provide the control. In simulation the DFIM is controlled by a B2B-VSC which manipulates the rotor voltage to produce any value of current that is desired based on the operation of the controller. In the hardware, this control will be accomplished through the use of a custom converter board which can take as its inputs the various electronic signals from the machine i.e. rotor speed, current, active and reactive power, and use these to output a controlled rotor voltage based on a sinusoidal PWM scheme.

The custom converter board consists of two main components; a digital signal processor (DSP) and a three-phase converter. The former is responsible for interfacing the hardware to a computer to enable the use of Matlab for designing and implementing the controllers. Automatic Matlab generated C code can be directly applied to the DSP which allows the use of the familiar Simulink block-layout approach to control design which has been widely used through this thesis. The amount of time saved as a result of this approach is huge as there is no requirement of learning to program in C,

and although the quality of the automatic C code is not as efficient or elegant as that of a skilled programmer, the trade-off between quality of code and time taken makes it a very attractive option.

The latter can be any kind of commercial three-phase motor drive board which takes as an input the PWM signals from the DSP and outputs a controlled current into the rotor circuit of the DFIM. There are many commercial converter boards on the market but the objective here is to make the experimental equipment affordable and modular for future applications. For these reasons the STEVAL-IPM15B has been selected because of its compact size and modest price tag.

A flow chart of the signal cascade between computer and motor is presented in figure B.1. The Matlab C code is generated within the Simulink control design software and then sent directly to the DSP where it undergoes some signal conditioning, which will be covered in the following sections. The DSP acts as the interface between software and hardware to receive digital signals from the computer and to send electronic signals to the converter board. The interface between the DSP and the converter board is not a standard piece of equipment and will therefore need to be custom made. Finally, the converter board relays the electronic signals from the DSP to the DFIM to provide control over the PFEC. Measurements of the phase voltage, current and DC bus voltage of the machine can be sent back to the analogue-to-digital converters (ADC) within the DSP via the converter board where they can be visualised in real time.

B.1 DSP

The primary responsibility of the DSP is to convert between the real-world analogue signals of the motor and the digital signals of the computer (and vice versa). The DSP chosen for the application to the PFEC will be the Texas Instruments TMS320F28335, which provides high-performance for a relatively small cost and allows the direct use of Matlab generated C code. The F28335 is shown in figure B.2 and is based on the technology of the 32-bit C2000 microcontrollers which have been optimised for closed-

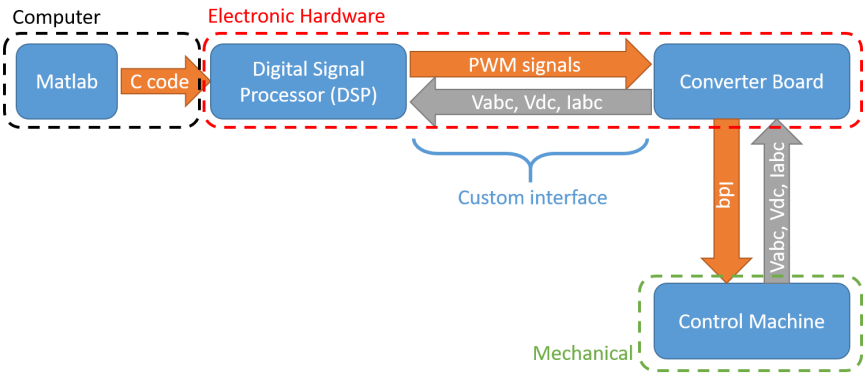

Figure B.1: Signal cascade of desired controller

Figure B.2: Texas Instruments TMS320F28335

loop performance in real-time control applications such as industrial motor drives [130].

The F28335 has 16 ADC ports for converting between analogue and digital signals; 6 dedicated ePWM ports; and several other on-board functions, most of which will not be utilised in the development of the PFEC control board. A pin-out table of the F28335 is provided in figure B.3.

B.2 STEVAL-IPM Board

The converter board has been selected as the STEVAL-IPM15B which is rated for a power of 1.5kW. This is an IGBT-based motor drive power board designed for driving

V33D-ISO	1	51	V33D-ISO
ISO-RX-RS232	2	52	ISO-TX-RS232
	3	53	
	4	54	
	5	55	
GND_ISO	6	56	GND_ISO
ADCIN-B0	7	57	ADCIN-A0
GND	8	58	GND
ADCIN-B1	9	59	ADCIN-A1
GND	10	60	GND
ADCIN-B2	11	61	ADCIN-A2
GND	12	62	GND
ADCIN-B3	13	63	ADCIN-A3
GND	14	64	GND
ADCIN-B4	15	65	ADCIN-A4
	16	66	
ADCIN-B5	17	67	ADCIN-A5
GPIO-58 / MCLKR-A / XD21 (EMIF)	18	68	GPIO-59 / MFSR-A / XD20 (EMIF)
ADCIN-B6	19	69	ADCIN-A6
GPIO-60 / MCLKR-B / XD19 (EMIF)	20	70	GPIO-61 / MFSR-B / XD18 (EMIF)
ADCIN-B7	21	71	ADCIN-A7
GPIO-62 / SCIRX-C / XD17 (EMIF)	22	72	GPIO-63 / SCITX-C / XD16 (EMIF)
GPIO-00 / EPWM-1A	23	73	GPIO-01 / EPWM-1B / MFSR-B
GPIO-02 / EPWM-2A	24	74	GPIO-03 / EPWM-2B / MCLKR-B
GPIO-04 / EPWM-3A	25	75	GPIO-05 / EPWM-3B / MFSR-A / ECAP-1
GPIO-06 / EPWM-4A / SYNCI / SYNCO	26	76	GPIO-07 / EPWM-4B / MCLKR-A / ECAP-2
GND	27	77	+5V in
GPIO-08 / EPWM-5A / CANTX-B / ADCSOC-A	28	78	GPIO-09 / EPWM-5B / SCITX-B / ECAP-3
GPIO-10 / EPWM-6A / CANRX-B / ADCSOC-B	29	79	GPIO-11 / EPWM-6B / SCIRX-B / ECAP-4
GPIO-48 / ECAP5 / XD31 (EMIF)	30	80	GPIO-49 / ECAP6 / XD30 (EMIF)
GPIO-84	31	81	GPIO-85
GPIO-86	32	82	+5V in
GPIO-12 / TZ-1 / CANTX-B / MDX-B	33	83	GPIO-13 / TZ-2 / CANRX-B / MDR-B
GPIO-15 / TZ-4 / SCIRX-B / MFSX-B	34	84	GPIO-14 / TZ-3 / SCITX-B / MCLKX-B
GPIO-24 / ECAP-1 / EQEPA-2 / MDX-B	35	85	GPIO-25 / ECAP-2 / EQEPB-2 / MDR-B
GPIO-26 / ECAP-3 / EQEPI-2 / MCLKX-B	36	86	GPIO-27 / ECAP-4 / EQEPS-2 / MFSX-B
GND	37	87	+5V in
GPIO-16 / SPISIMO-A / CANTX-B / TZ-5	38	88	GPIO-17 / SPISOMI-A / CANRX-B / TZ-6
GPIO-18 / SPICLK-A / SCITX-B	39	89	GPIO-19 / SPISTE-A / SCIRX-B
GPIO-20 / EQEPA-1 / MDX-A / CANTX-B	40	90	GPIO-21 / EQEPB-1 / MDR-A / CANRX-B
GPIO-22 / EQEPS-1 / MCLKX-A / SCITX-B	41	91	GPIO-23 / EQEPI-1 / MFSX-A / SCIRX-B
GPIO-87	42	92	+5V in
GPIO-28 / SCIRX-A / Resv / TZ5	43	93	GPIO-29 / SCITX-A / Resv / TZ6
GPIO-30 / CANRX-A	44	94	GPIO-31 / CANTX-A
GPIO-32 / I2CSDA / SYNCI / ADCSOCA	45	95	GPIO-33 / I2CSCL / SYNCO / ADCSOCB
GPIO-34 / ECAP1 / XREADY (EMIF)	46	96	+5V in
GND	47	97	TDI
TCK	48	98	TDO
TMS	49	99	TRSTn
EMU1	50	100	EMU0

Figure B.3: Pin-out table for F28335

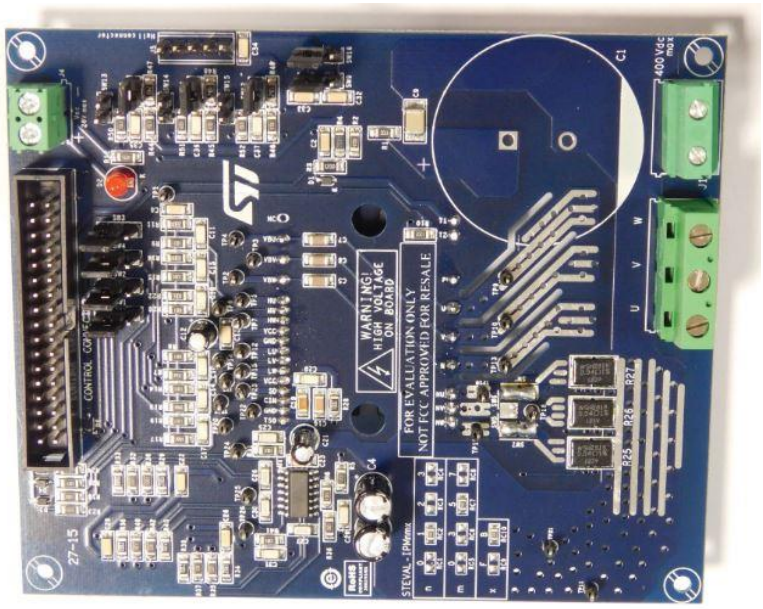

Figure B.4: STEVAL-IPM 1500W converter board

high power motors and 3-phase inverters and has been specifically designed for field-oriented control (FOC) of an induction motor, making it consistent with the work done previously in simulation. The STEVAL-IPM board is shown in figure B.4 and consists of an interface circuit, bootstrap capacitors, snubber capacitor, hardware short-circuit protection, fault event signal and temperature monitoring [131].

B.3 Power Supply

The custom DSP-STEVAL board requires a power supply which will ultimately be fed from the mains in its final iteration. From the original mains-supply, a set of constant DC voltages of different levels will be derived to power the various aspects of both the DSP and the STEVAL board, as well as providing offset voltages for the op-amp network. During testing the power will be supplied by a constant DC voltage source limited to a touch-safe 50V in keeping with health and safety regulations, but the full design of the mains-operated device is presented here for completeness.

In total there are seven difference voltage levels which are required to provide power the various board elements:

- 400V DC connection for STEVAL board
- 20V auxiliary power supply for STEVAL board
- +5V voltage source for DSP and op-amp positive rail
- -5V voltage for op-amp negative rail
- 3.3V voltage source for DSP
- 3V reference for schottkey protection
- 1.5V reference for op-amp offset

With the exception of the 400V DC circuit of the STEVAL board which must be supplied by an external source, the remaining voltages can be derived from a 230VAC supply. The mains supply is fed into a transformer which steps down the voltage from 230VAC to 20V then with the aid of a bridge rectifier and a smoothing capacitor, a constant DC 20V source is produced. It is from this 20V DC reference that all other voltages are derived. For the auxiliary STEVAL power supply, the 20V reference is sent through a linear voltage regulator to produce a constant 20V. The ±5V voltages are formed using an isolated DC/DC converter with a dual output. 3.3V is produced from the +5V output through another linear regulator. The 3V and 1.5V references are both produced from the +5V voltage source using voltage dividers and op-amp voltage followers.

B.4 Signal Conditioning

Some signal conditioning is required to enable a link between the DSP and the converter board. This is for the purpose of protecting the delicate electronics of the DSP from the relatively high voltages sent from the converter. The ADC inputs of the DSP are rated for 3 volts whereas the voltage levels of the converter board can be significantly

higher. Regardless of the voltage levels of the STEVAL board, the voltage range must be transformed into the range of 0 - 3V using a combination of voltage dividers and op-amps before they can be fed to the ADC inputs of the DSP. The signals of interest from the converter and their associated voltage levels are given below:

- Phase voltages v_{abc}: 125V RMS
- Phase currents I_{abc}: displayed as an equivalent voltage in the range of 0 - 3.3V
- DC voltage v_{dc}: 400V

Take the phase voltage V_a, for example. The STEVAL board is rated up to an RMS value of 125V which corresponds to a peak of 176.8V which must be brought down to the range of 0 - 3V before it can be connected to the DSP. It is also beneficial to capture data in the event of a fault so there should be extra headroom to accommodate for overvoltage. It is therefore proposed that a range of ±250V should correspond to the DSP requirement of 0 - 3V.

B.4.1 Phase Voltages

The voltage levels coming from the three phases of the DFIM need to be transformed into the range of 0 - 3V for the sake of the DSP. This can be done with a voltage divider followed by a pair of op-amps.

The voltage divider steps-down the voltage by a specified amount based on the value of the resistors. In the phase voltage example, the voltage range of ±250V is brought down to the range of ±1.5V. The sinusoidal 1.5V signal will then be offset by 1.5V by an op-amp to achieve the 0 - 3V range as required.

The equation for the voltage divider is given by:

$$V_{out} = V_{in}\left[\frac{R_2}{R_1 + R_2}\right] \tag{B.1}$$

Where in this example $V_{in} = 250$, $V_{out} = 1.5V$ and R_1, R_2 are the resistances to

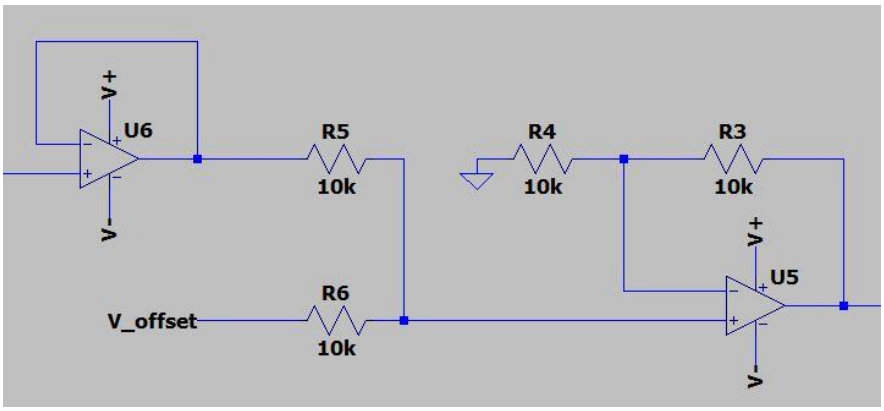

Figure B.5: Op amp cascade

be determined. By introducing the substitution $\frac{V_{out}}{V_{in}} = x$ and rearranging for R_1 this becomes:

$$R_1 = R_2\left[\frac{1-x}{x}\right] \tag{B.2}$$

where x is the ratio of V_{out} to V_{in} which in this example is equal to $1.5/250 = 0.006$. By choosing $R_2 = 3\text{k}\Omega$, the value of R_1 is found to be $500\text{k}\Omega$. This is not a standard resistor size and so a $300\text{k}\Omega$ and a $200\text{k}\Omega$ are placed in series.

A sinusoidal voltage of $1.5V_{peak}$ now leaves the voltage divider and is sent through a pair of op-amps. The first op-amp acts as voltage follower and produces a provides a high impedance input - low impedance output. The high impedance on the input side means that measurements can be taken without affecting the source, that is, the impedance is too high to sink any meaningful amounts of current, and the low impedance output can be used to drive a load, which in this case will be a measurement device.

The second op-amp acts as a non-inverting summing amplifier and applies an offset of 1.5V to bring the -1.5-1.5V range up to 0 - 3V as required since the DSP cannot take negative voltages. The op-amp cascade is shown in figure B.5 where the left op-amp is the voltage follower and the right op-amp is the summing amplifier.

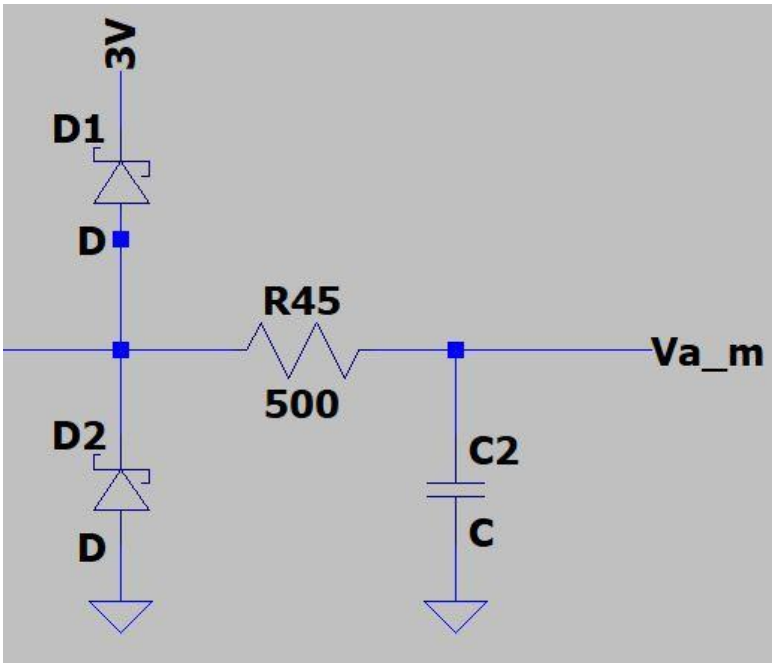

Figure B.6: Schottky diode protection

An additional protection step is added to the output to further shield the DSP from damage in the event of overvoltage. Two Schottky diodes are positioned as in figure B.6, one to deal with positive overvoltages, and one to deal with negative overvoltages (undervoltages). The positive-phase diode has a 3V reference on the cathode causing it to be reverse-biased under normal operation. Should the voltage exceed 3V on the anode in the event of fault i.e. if there is a larger potential difference on the anode than the cathode wrt. ground, then the diode becomes forward biased and begins to conduct current away from the sensitive circuit of the DSP. A similar thing occurs with the Schottky diode connected to ground, where if a potential difference smaller than 0V is detected, the diode conducts and provides a safe passage to ground. Also shown in the figure is a small current-limiting resistor of 500Ω and a small capacitor to filter the output. The voltage and current waveforms of the Schottky protection stage are shown in figure B.7.

The complete signal conditioning stage for the three phase voltages is shown in figure B.8 which combines the voltage divider; voltage follower; non-inverting summing

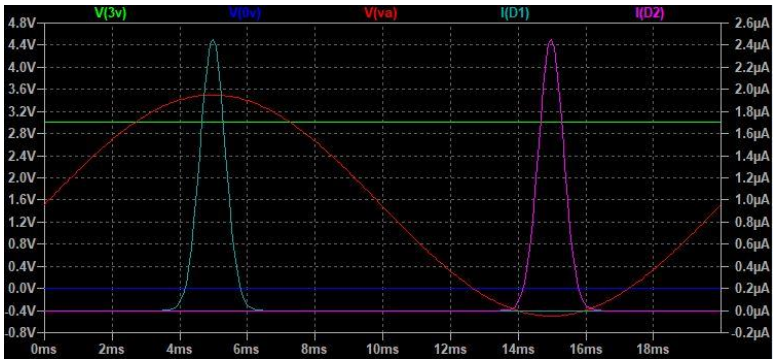

Figure B.7: Schottky voltage and current waveforms

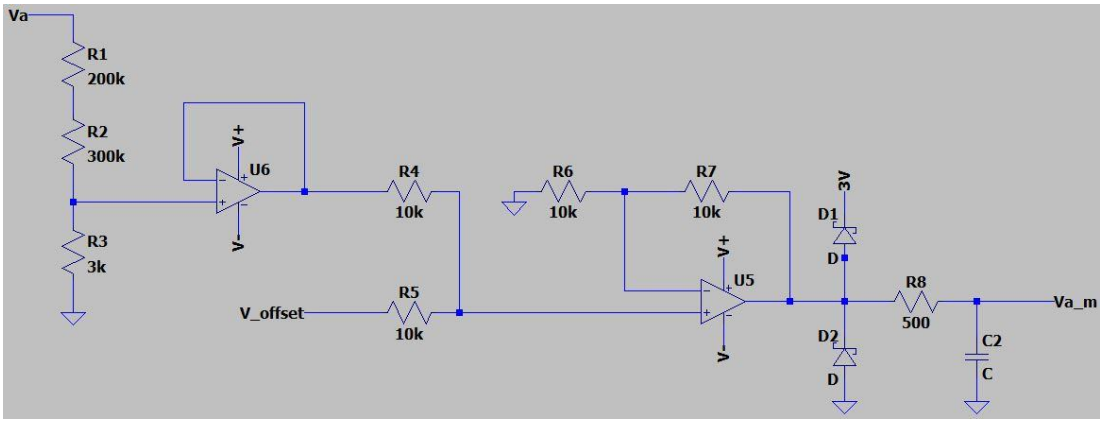

Figure B.8: Signal conditioning circuit for motor phase voltages

amplifier; and Schottky diode protection. Shown in figure B.9 are the voltage waveforms after each stage.

B.4.2 DC Voltage

As with the phase voltages, the DC voltage measurements must also be brought into the DSP operating range of 0-3V. The IPM converter board operates at a nominal DC voltage of 400V but to capture overvoltage behaviour, additional headroom must be included such that a range of 0-500V is transformed into 0-3V. This is achieved with a voltage divider with R1 = 500kΩ and R2 = 3kΩ. Note that for ease of procurement the 500kΩ resistor is split into a series connection of a 200kΩ and a 300kΩ resistor. As with the phase voltages, this conditioned signal is then passed through an op amp configured as a voltage follower such that measurements can be taken without affecting

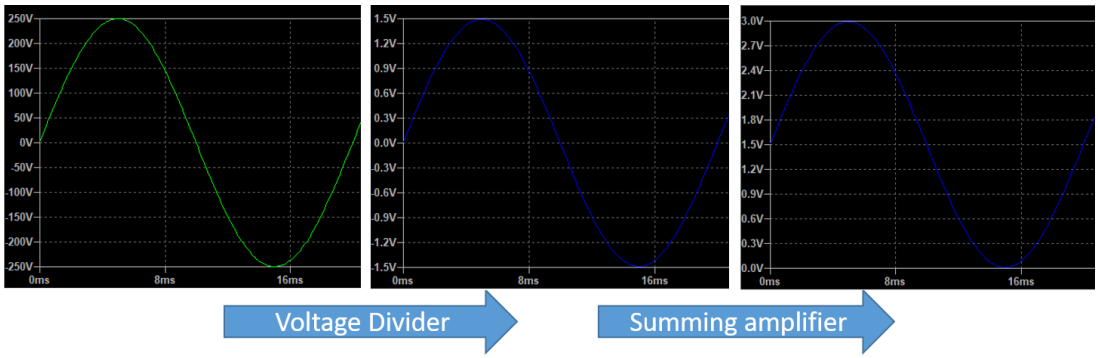

Figure B.9: Voltage waveforms throughout the circuit

the original signal. Finally, a Schottky diode protection system is again fitted to protect the ADC inputs of the DSP.

B.4.3 Phase Currents

The IPM converter board is equipped with a current sensing amplifying network which uses an on-board op-amp with a single positive supply of 3.3V. Bidirectional current sensing is required so an output offset of 1.65V represents zero current. 3.3V is too high to connect directly to the DSP, and it would be beneficial to include headroom to detect overcurrents, so for these reasons an output range of 0 - 4V will be made to correspond to the DSP's operating range of 0 - 3V.

To scale 4V down to 3V, a voltage divider is used with R1 = 1kΩ and R2 = 3kΩ. This signal is then sent through a voltage follower in the same way as for the phase voltages such that measurements can be taken without affecting the source.

B.4.4 Temperature Sensing

The STEVAL board has a dedicated pin to record the internal temperature of the chip which can be utilised to give a real-time visual representation of the temperature of the device and to check if it is operating within safe margins. The layout in figure B.10 shows how an op-amp network can function as a comparator circuit to light

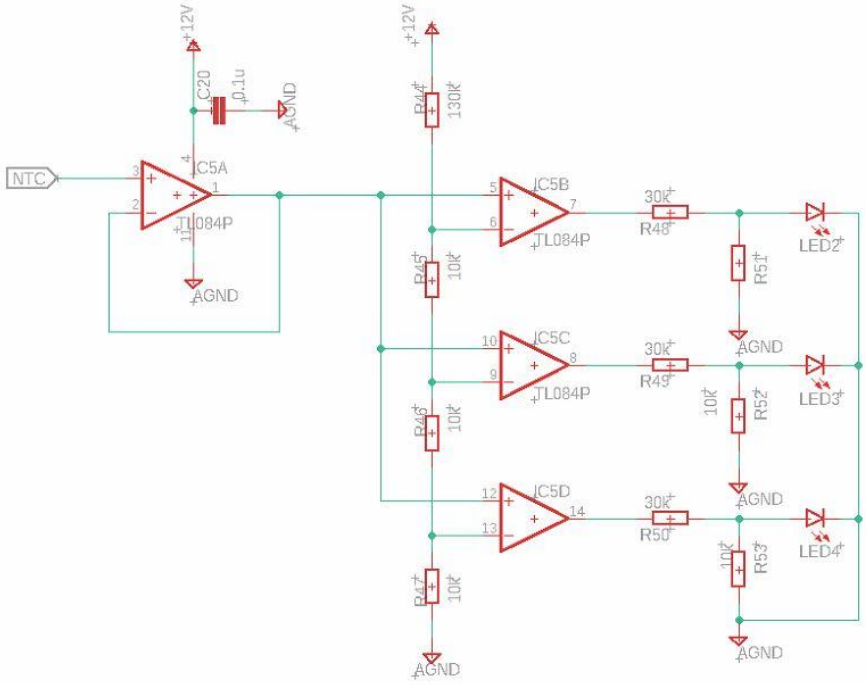

Figure B.10: Op-amp comparator circuit to visually display internal chip temperature specific LEDs corresponding to different operating temperatures when certain voltage thresholds are reached.

The NTC pin connects to a thermistor circuit within the STEVAL board which provides an equivalence between the operating temperature and a voltage signal. The relationship between chip temperature and NTC voltage is linear and is shown in figure B.11. In the LED temperature sensing circuit, the threshold voltages are divided into the three groups corresponding to three different LED colours.

1. Green - cool, voltage range = 0 - 1.5V
2. Amber - mid-range temperature, voltage range = 1.5 - 2.25V
3. Red - hot, voltage range = 2.25 - 3V

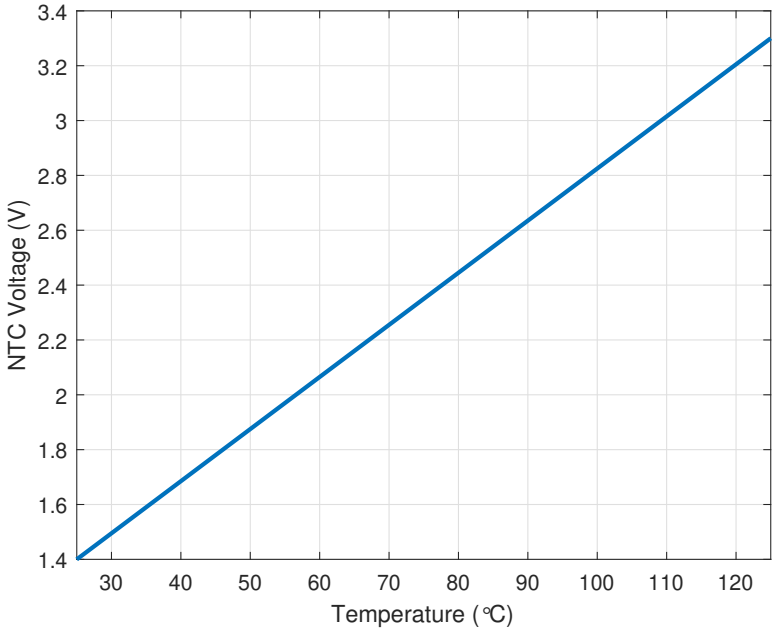

Figure B.11: Thermistor circuit relating operating temperature to a voltage level

B.5 Schematic Design

The various elements described in the previous sections are brought together in Eagle PCB design software to produce a schematic for manufacture. The completed schematic is presented in figure B.12. A two-level PCB board was used to minimise the number of wire links required between connections, with blue representing the front side and red the reverse side.

The completed circuit board with all components in place is shown in figures B.14 and B.15 respectively. The green circuit board is the custom DSP interface complete with power supply and signal conditioning, and the blue STEVAL motor control board is positioned below. A ribbon connector is used to relay the relevant signals between the two.

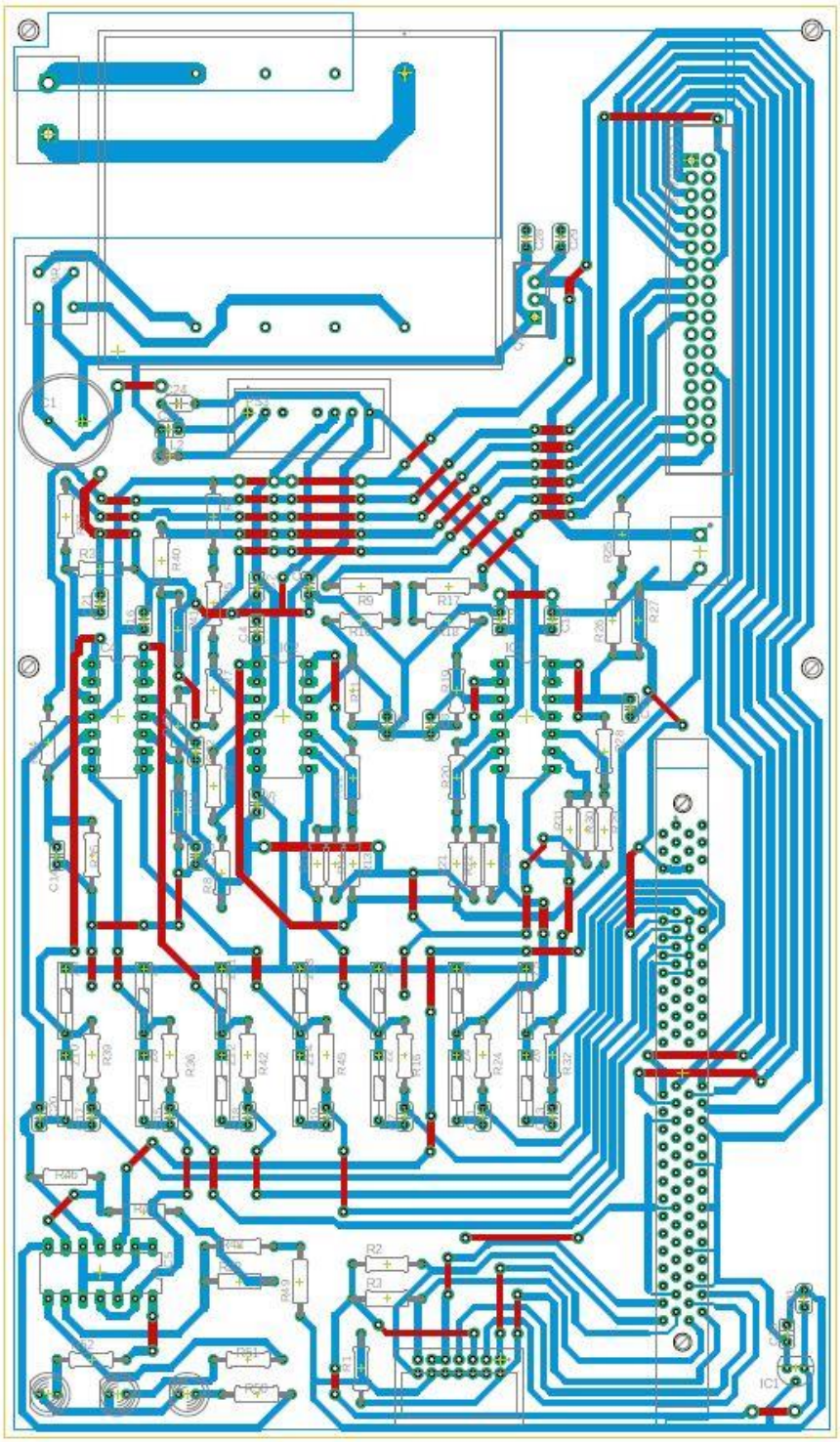

Figure B.12: Schematic design within Eagle

B.6 Validation and Testing

Other than a couple of minor connection issues, the board functioned correctly and provided the DSP with the 0 - 3V range required for safe operation. In total, two mistakes were found: one was a poorly soldered op-amp which accidentally bridged two legs together. The other was a missing 5V source in the ribbon cable connecting to the STEVAL board which was easily fixed by soldering a additional length of wire to the 5V bus.

During testing, the touch-safe health and safety requirements limited the maximum voltage to 50V DC such that the operation of the transformer part of the board could not be verified experimentally, however due to the simplicity of this section of the circuit this is of no primary concern. Instead of a direct mains AC connection, a 20V constant DC source was instead applied to the output terminals of the bridge rectifier to replicate the output under normal operation. The various voltage references were all found to be reliably produced, and each signal conditioning stage worked as intended, providing the DSP with an acceptable range of voltages.

To test the PWM circuit required for field-oriented control of the PFEC, the board was energised as described above using a 20VDC constant source to provide power to the various elements. A separate 50V DC source was then applied to the DC circuit of the STEVAL board. Note that this would optimally be a 400V DC source in real-world applications as specified above, however due to health and safety regulations the maximum allowable voltage was 50V at this time.

Due to only having access to a single signal generator, the high and low pulses could not be sent simultaneously for the high- and low-IGBTs respectively. Instead, the experiment was adapted such that only a single generator was needed by grounding the high-IGBT and driving just the low-IGBT with a 3V square wave pulse. This set-up is shown in schematic form in figure B.13 and experimentally in figures B.14 and B.15 in

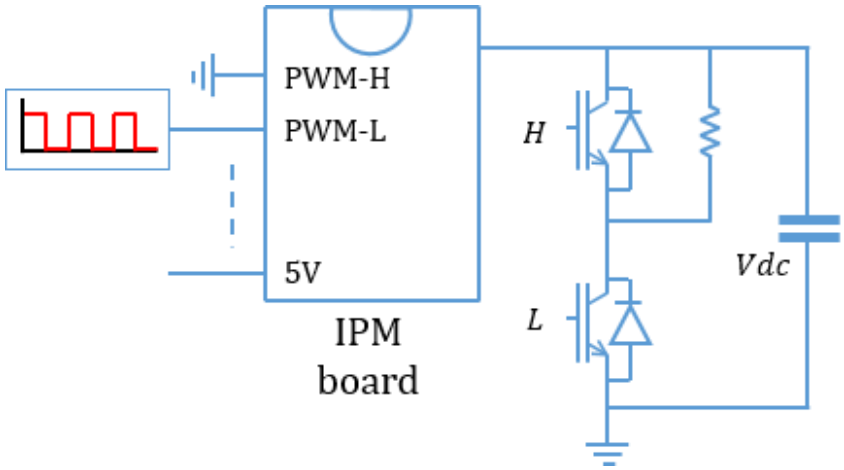

Figure B.13: Schematic representation of PWM test

which the square wave and ground connections are applied directly to the appropriate pins where the F28335 control card of the DSP would normally sit. When a pulse is sent, the low-IGBT should open to provide a snapshot of the DC voltage reflected in phase-A of the motor connection and thus an indication that the connection from DSP-to-STEVAL-to-motor is continuous. If this is the case then the board functions as intended and the F28335 control card can be equipped to provide the PWM signal directly from Matlab.

Results are shown in figure B.16 and B.17 which demonstrate that the circuit works as expected. The square wave output measured in phase-A of the motor circuit perfectly reflects the applied DC voltage and has good sharpness up to around 20kHz. As the frequency of the applied square wave signal increases, the effects of the built-in filters become more visible and exhibit themselves by a prominent smoothing effect which is demonstrated in B.18. This effect is necessary to eliminate voltage spikes and is caused by the snubber circuits within the STEVAL board. This effect is not shown at the switching frequencies of interest to the PFEC which are typically around 2kHz for a delay time of 1ms thus demonstrating that good control with this layout is indeed possible.

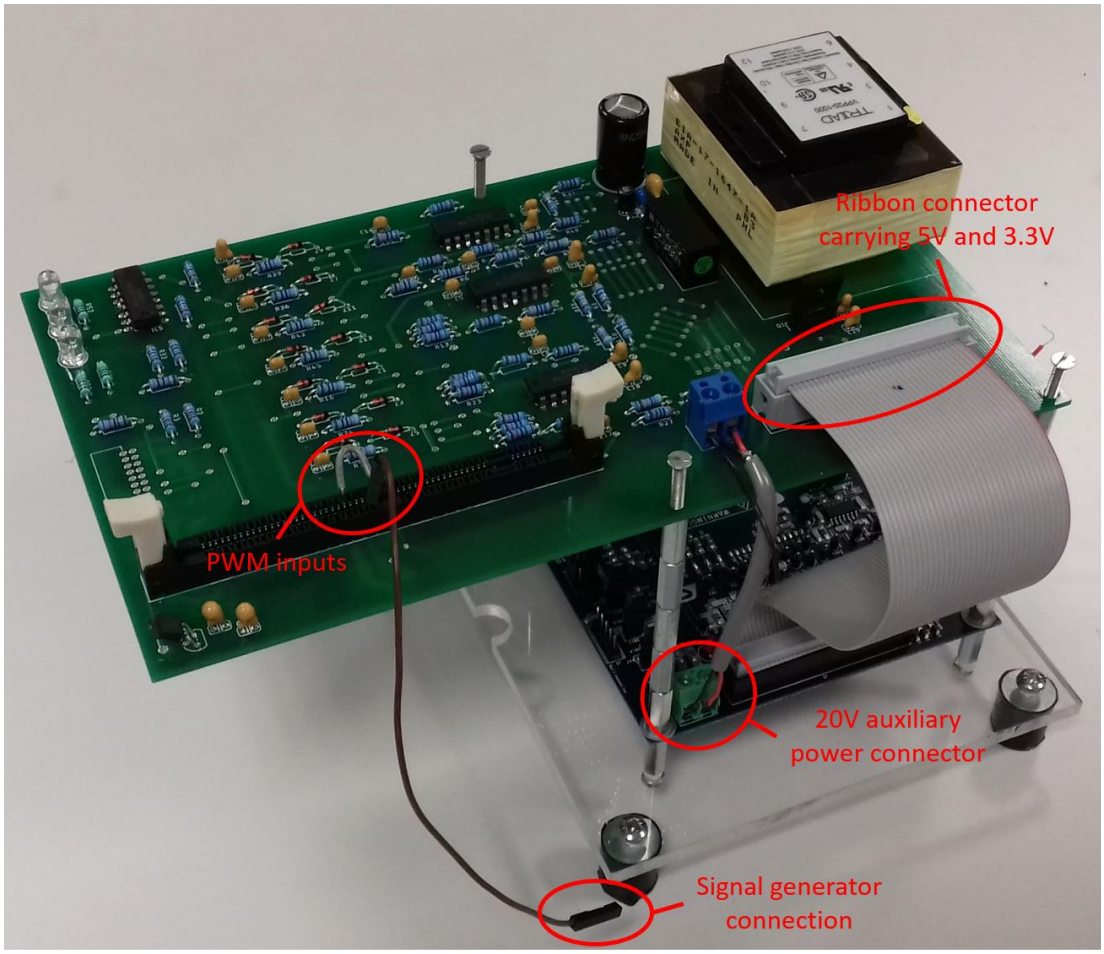

Figure B.14: Experimental set-up for DSP ePWM output

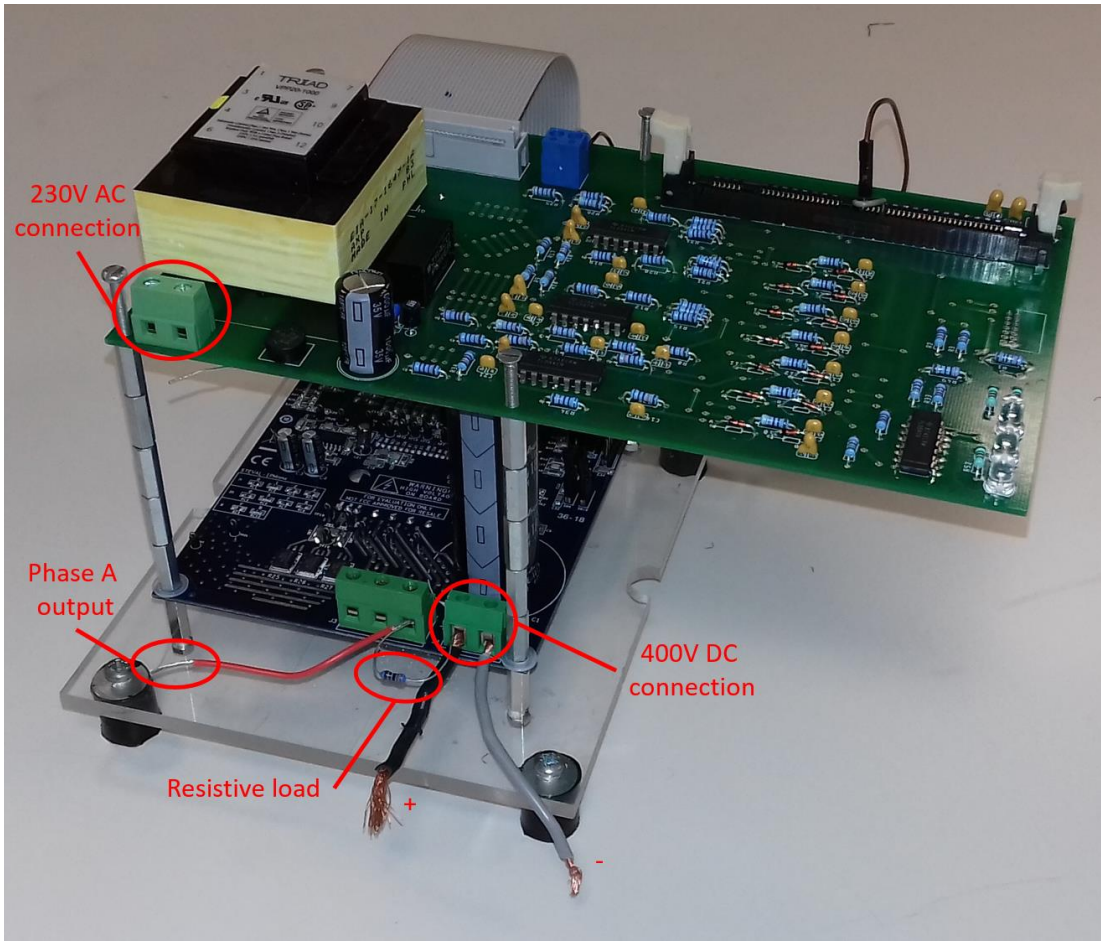

Figure B.15: Experimental set-up for DSP ePWM output

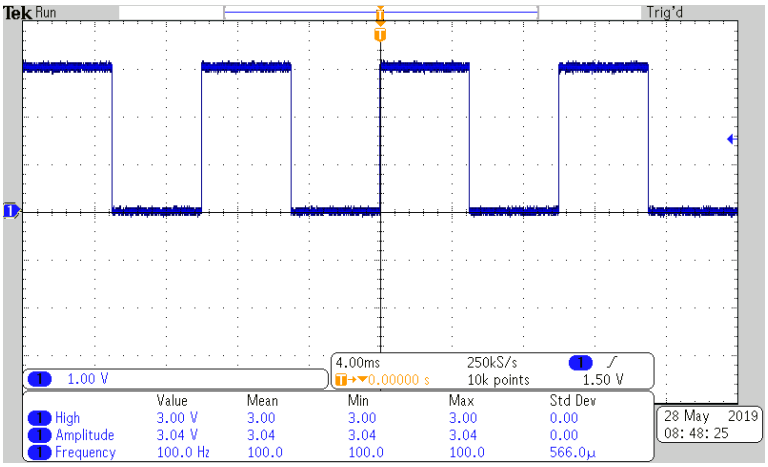

Figure B.16: 3V PWM signal applied to ePWM pin. Resolution = 1V, frequency = 100Hz

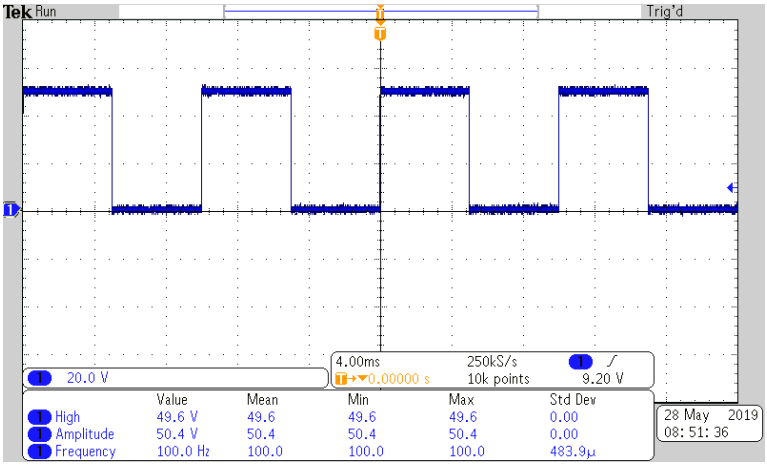

Figure B.17: Snapshot of DC voltage measured in phase-A motor connection. Resolution = 20V

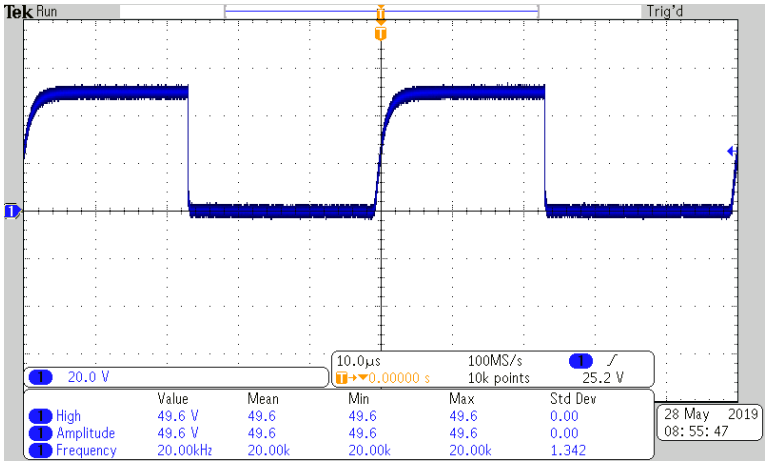

Figure B.18: Smoothing effect of in-built snubber circuits at high frequencies

Appendix C

Simulation Parameters

C.1 Configuration Parameters

The Simulink configuration parameters used in all simulations are the same and are given in table C.1.

C.2 PFEC Model Parameters

The machine parameters for the RT and DFIM used in the 100MW and 600MW PFEC simulation in chapters 4 and 5 are presented in C.2. The tuning parameters of the DFIM controllers are given in C.3. The simulation parameters for the synchronous generators together with the governor and exciter parameters in chapter 5 are presented in tables C.4 and C.5 respectively.

C.3 Base System

The PFEC possesses two base systems, one for each of the RT and the DFIM. The defining equations are given in table C.6 where the subscripts 1 and 2 refer to the RT

Table C.1: Configuration Parameters

Parameter	**Symbol**	**Value**
Sample Time	T_s	$20e^{-6}$ (s)
Solver	ode23t	Stiff trapezoidal

Table C.2: RT and DFIM Simulation Parameters

Parameter	**Symbol**	**RT**	**DFIM**
Rated power	P_n (MVA)	100	66.7
Terminal voltage	V_n (kV)	23	7.67
Stator frequency	f_s (Hz)	50	16.7
Stator resistance	R_s (PU)	0.005	0.005
Rotor resistance	R_r (PU)	0.005	0.005
Stator leakage inductance	L_{ls} (PU)	0.09	0.09
Rotor leakage inductance	L_{lr} (PU)	0.09	0.09
Magnetising inductance	L_m (PU)	10	10
Inertia constant	H (s)	0	4+4
Friction factor	D	0.01	0.01
Pole pairs	p	2	1

Table C.3: DFIM Controller Parameters

Parameter	**Symbol**	**Value**
DC link voltage	v_{dc} (kV)	18.78
Capacitance	C (F)	$10000e^{-6}$
GSC resistance	R_{gsc} (PU)	0.0015
GSC inductance	L_{gsc} (PU)	0.15
GSC current rise time	T_{igsc} (s)	0.002
GSC DC voltage rise time	T_{dc} (s)	0.015
GSC reactive power rise time	T_{Qgsc} (s)	0.5
RSC current rise time	T_{irsc} (s)	0.05
RSC rotor speed rise time	T_{wr} (s)	2
RSC reactive power rise time	T_{Qs} (s)	1

Table C.4: Synchronous generator machine parameters

Parameter	**Symbol**	**Gen4**	**Gen5**	**Gen6**
Rated power	P_n (MVA)	900	200	200
Terminal voltage	V_n (kV)	20.0	13.8	13.8
Frequency	f (Hz)	50	50	50
Stator resistance	R_s (PU)	0.0025	0.00285	0.00285
d-axis synchronous reactance	X_d (PU)	1.8	1.305	1.305
d-axis transient reactance	X'_d (PU)	0.3	0.296	0.296
d-axis subtransient reactance	X''_d (PU)	0.25	0.252	0.252
q-axis synchronous reactance	X_q (PU)	1.7	0.474	0.474
q-axis subtransient reactance	X''_q (PU)	0.25	0.243	0.243
Leakage reactance	X_l (PU)	0.2	0.18	0.18
d- transient s-c time const.	T'_d (s)	8.0	1.01	1.01
d- subtransient s-c time const.	T''_d (s)	0.03	0.053	0.053
q- subtransient s-c time const.	T''_q (s)	0.05	0.1	0.1
Inertia coefficient	H (PU)	9.75	3.2	3.2
Friction factor	D (PU)	0	0	0
Pole pairs	p	2	2	2

Table C.5: Governor and exciter simulation parameters

Governor	**Symbol**	**Value**
Low-pass filter time constant	Kp	1
Regulator gain	Rp (PU)	0.04
Speed relay time constant	Trm (s)	0.001
Servo-motor time constant	Tsm (s)	0.15
Nominal speed	Ns (rpm)	3000
Steam turbine time constants	[T2, T3, T4, T5] (s)	[0, 10, 3.3, 0.5]
Steam turbine torque fractions	[F2, F3, F4, F5] (PU)	[0, 0.36, 0.36, 0.28]
Exciter		
Regulator gain	Ka	200
Time constant	Ta (s)	0.001

Table C.6: Base system for RT and DFIM respectively

Parameter	**Symbol**	**RT**	**DFIM**	**Description**
Base power	S_b	$P_{n_{RT}}$	$P_{n_{RT}}$	RT rated power as base
Base frequency	$f_{b_{(1,2)}}$	f_{s1}	f_{s2}	stator elec. freq.
Base voltage	$V_{b_{(1,2)}}$	$\sqrt{\frac{2}{3}}v_{s1}$	$\sqrt{\frac{2}{3}}v_{s2}$	peak phase voltage
Base current	$I_{b_{(1,2)}}$	$\frac{2}{3}\frac{S_b}{V_{b1}}$	$\frac{2}{3}\frac{S_b}{V_{b2}}$	peak phase current
Base impedance	$Z_{b_{(1,2)}}$	$\frac{V_{b1}}{I_{b1}}$	$\frac{V_{b2}}{I_{b2}}$	-
Base inductance	$L_{b_{(1,2)}}$	$\frac{Z_{b1}}{2\pi f_{b1}}$	$\frac{Z_{b2}}{2\pi f_{b2}}$	-
Base capacitance	$C_{b_{(1,2)}}$	$\frac{1}{L_{b1}}$	$\frac{1}{L_{b2}}$	-
Base elec. radians	$\omega_{b_{(1,2)}}$	$2\pi f_{b1}$	$2\pi f_{b2}$	-
Base mech. radians	$\omega_{bm_{(1,2)}}$	$\frac{2\pi f_{b1}}{p_1}$	$\frac{2\pi f_{b2}}{p_2}$	-
Base torque	$T_{b_{(1,2)}}$	$\frac{S_b}{\omega_{bm1}}$	$\frac{S_b}{\omega_{bm2}}$	-
Base damping coeff.	$D_{b_{(1,2)}}$	$\frac{T_{b1}}{\omega_{bm1}}$	$\frac{T_{b2}}{\omega_{bm2}}$	-

and the DFIM respectively.

C.4 Cable Parameters

Tables C.7, C.8 and C.9 give the parameters for some common HVAC, HVDC and LFAC cables respectively.

Table C.7: Some common HVAC cables [104]

#	Voltage V (kV)	Size (mm^2)	Resistance R (mΩ/km)	Capacitance C (nF/km)	Steady-state current (A)	Cost t_c (M£/km)
1	132	630	39.5	209	818	0.685
2	132	800	32.4	217	888	0.796
3	132	1000	27.5	238	949	0.86
4	220	500	48.9	136	732	0.815
5	220	630	39.1	151	808	0.85
6	220	800	31.9	163	879	0.975
7	220	1000	27	177	942	1.0
8	400	800	31.4	130	870	1.4
9	400	1000	26.5	140	932	1.55
10	400	1200	22.1	170	964	1.7
11	400	1400	18.9	180	1015	1.85
12	400	1600	16.6	190	1036	2.0
13	400	2000	13.2	200	1078	0.215

Table C.8: Some common HVDC cables [104]

#	Voltage V (kV)	Size (mm^2)	Resistance R (mΩ/km)	Steady-state current (A)	Cost t_c (M£/km)
1	150	1000	22.4	1644	0.67
2	150	1200	19.2	1791	0.73
3	150	1400	16.5	1962	0.785
4	150	1600	14.4	2123	0.84
5	150	2000	11.5	2407	0.9
6	300	1000	22.4	1644	0.855
7	300	1200	19.2	1791	0.94
8	300	1400	16.5	1962	1.015
9	300	1600	14.4	2123	1.090
10	300	2000	11.5	2407	1.175

Table C.9: LFAC cable data

#	Voltage V (kV)	Size (mm^2)	Resistance R (mΩ/km)	Capacitance C (nF/km)	Steady-state current (A)	Cost t_c (M£/km)
1	132	630	26.2	209	818	0.685
2	132	800	21.5	217	888	0.796
3	132	1000	18.2	238	949	0.86
4	220	500	32.4	136	732	0.815
5	220	630	25.9	151	808	0.85
6	220	800	21.1	163	879	0.975
7	220	1000	17.9	177	942	1.0
8	400	800	20.8	130	870	1.4
9	400	1000	17.5	140	932	1.55
10	400	1200	14.6	170	964	1.7
11	400	1400	12.5	180	1015	1.85
12	400	1600	11.0	190	1036	2.0
13	400	2000	8.7	200	1078	0.215

C.5 PFEC Matlab Code

```
1  %% Simulation Parameters
2  Ts = 20e-6;
3
4  %% PFEC Parameters
5  Sb = 100e6;                          % Base power (VA)
6  % Generator Parameters (pu)
7  for gen = 1
8  Pn(gen) = 100e6;                     % machine rated
       power
9  Vn(gen) = 23e3;                      % phase-to-phase
       RMS voltage
10 freq(gen) = 50;                      % grid Frequency
11 Rs(gen) = 0.005;                     % stator winding
       resistance (pu)
12 Rr(gen) = 0.005;                     % rotor winding
       resistance (pu)
```

```
13 Lls(gen) = 0.09;                          % stator leakage
       inductance (pu)
14 Llr(gen) = 0.09;                          % rotor leakage
       inductance (pu)
15 Lm(gen) = 10;                             % mutual
       inductance (pu)
16 H(gen) = 4+4;                             % inertia constant
       (includes RT and DFIM) (sec)
17 D(gen) = 0.01;                            % damping constant
18 P(gen) = 4;                               % poles
19 p(gen) = P(gen)/2;                        % pole pairs
20 end
21 % Motor Parameters (pu)
22 for gen = 2
23 Pn(gen) = Pn(1)*2/3;
24 Vn(gen) = Vn(1)*1/3;
25 freq(gen) = freq(1)*1/3;
26 Rs(gen) = 0.005;
27 Rr(gen) = 0.005;
28 Lls(gen) = 0.09;
29 Llr(gen) = 0.09;
30 Lm(gen) = 10;
31 H(gen) = H(1);
32 D(gen) = 0.01;
33 P(gen) = 2;
34 p(gen) = P(gen)/2;
35 end
36 %% Base System
37 % PFEC Generator and Motor
38 for area = 1:2
```

```
39 Vb(area) = sqrt(2/3)*Vn(area);                % peak phase
       voltage
40 fb(area) = freq(area);                        % AC system
       freuency
41 Ib(area) = Sb/(3/2*Vb(area));                 % peak phase
       current
42 Zb(area) = Vb(area)/Ib(area);                 % base impedance
43 Lb(area) = Zb(area)/(2*pi*fb(area));          % base inductance
44 wbm(area) = (2*pi*fb(area))/p(area);          % base mechanical
       speed (rad/s)
45 Tb(area) = Sb/wbm(area);                      % base damping
       torque (Nm)
46 Db(area) = Tb(area)/wbm(area);                % base damping
       coefficient Nm/(rad/s)
47 end
48 % Wind farm
49 for area = 3
50 Vn(area) = Vn(2);
51 freq(area) = freq(2);
52 Vb(area) = sqrt(2/3)*Vn(2);
53 Ib(area) = 2/3*Sb/Vb(area);
54 Zb(area) = Vb(area)/Ib(area);
55 wb(area) = 2*pi*freq(2);
56 Lb(area) = Zb(area)/wb(area);
57 end
58
59 % PFEC Generator Parameters (SI)
60 for gen = 1
61 RsSI(gen) = Rs(gen)*Zb(gen);                                  %
       stator resistance (ohm)
```

```
62 LlsSI(gen) = Lls(gen)*Lb(gen);                                    %
       stator leakage inductance (H)
63 RrSI(gen) = Rr(gen)*Zb(gen);                                      % rotor
       resistance (seen from stator side) (ohm)
64 LlrSI(gen) = Llr(gen)*Lb(gen);                                    % rotor
       leakage inductance (seen from stator side) (H)
65 LmSI(gen) = Lm(gen)*Lb(gen);                                      %
       machine mutual inductance (H)
66 Lss(gen) = LlsSI(gen)+LmSI(gen);                                      %
       stator self-inductance  (H)
67 Lrr(gen) = LlrSI(gen)+LmSI(gen);                                      %
       rotor self-inductance  (H)
68 J(gen) = (2*H(gen)*Pn(gen))/(wbm(gen)^2);                              %
       inertia (Kg.m^2)
69 DSI(gen) = D(gen)*Db(gen);                                        %
       damping coefficient/Friction Factor(matlab) (N.m)
70 end
71 % PFEC Motor Parameters (SI)
72 for gen = 2
73 RsSI(gen) = Rs(gen)*Zb(gen);                                          %
       stator resistance (ohm)
74 LlsSI(gen) = Lls(gen)*Lb(gen);                                       %
       stator leakage inductance (H)
75 RrSI(gen) = Rr(gen)*Zb(gen);                                         %
       rotor resistance (seen from stator side) (ohm)
76 LlrSI(gen) = Llr(gen)*Lb(gen);                                      %
       rotor leakage inductance (seen from stator side) (H)
77 LmSI(gen) = Lm(gen)*Lb(gen);                                        %
       machine mutual inductance (H)
```

```
78 Lss(gen) = LlsSI(gen)+LmSI(gen);                    %
       stator self-inductance (H)
79 Lrr(gen) = LlrSI(gen)+LmSI(gen);                    %
       rotor self-inductance (H)
80 J(gen) = (2*H(gen)*Sb)/(wbm(gen)^2);                % inertia
       (Kg.m^2)
81 DSI(gen) = D(gen)*Db(gen);                          %
       damping coefficient/Friction Factor(matlab) (N.m)
82 end
83
84 %% PLL Parameters (Timbus)
85 Tr_PLL = 0.1;                                      % settling
       time (s)
86 zeta = sqrt(2)/2;                                  % damping
       ratio (5% overshoot)
87 T_i = Tr_PLL*(zeta^2)/2.3;
88 Kp_PLL = 9.2/Tr_PLL;
89 Ki_PLL = Kp_PLL/T_i;
90
91 % B2B-VSC Parameters
92 S_B2B = 2*Pn(1);                                   % power
       rating of the B2B converter (W)
93 Vdc_nom = Vn(2)*2;                                 % nominal dc
       link voltage (V)
94 C = 100000e-6;                                    % DC bus
       capacitance (F)
95 RgscPU = 0.0015;                                  %
       resistance between GSC and AC grid (pu)
96 LgscPU = 0.15;                                    %
       inductance between GSC and AC grid (pu)
```

```
97  Rgsc = RgscPU*Zb(2);                                % resistance
        between GSC and AC grid (ohm)
98  Lgsc = LgscPU*Lb(2);                                % Inductance
        between GSC and AC grid (H)
99
100 %% Controllers
101 % GSC controllers
102 Tr_igsc = 2e-3;                                      % rise
       time of current control loop (s)
103 Tr_dc = 30e-3;                                       % rise
       time voltage control loop (s)
104 Tr_Qgsc = 0.1;                                       % Rise
       time of GSC reactive power control (s)
105 % RSC controllers
106 Tr_irsc = 20e-3;                                     % Rise
       time of rotor current control loop (s)
107 Tr_wr = 5;                                           % Rise
       time rotor speed (s)
108 Tr_Qs = 0.1;                                         % Rise
       time of stator reactive power control (s)
109 % GSC current controller
110 alpha_igsc = 2.2/Tr_igsc;                            %
       controller bandwith (rad)
111 G_igsc = (alpha_igsc*Lgsc)-Rgsc;                     % active
       damping gainn
112 Kp_igsc = alpha_igsc*Lgsc;                           %
       proportional gain
113 Ki_igsc = alpha_igsc*(Rgsc+G_igsc);                  % integral
        gain
114 % DC voltage controller
```

```
115 alpha_vdc = 2.2/Tr_dc;                                    %
    controller bandwith (rad)
116 G_vdc = (alpha_vdc*C)/(3*Vb(2));                          % active
    damping gain
117 Kp_vdc = (alpha_vdc*C)/(3*Vb(2));                         %
    proportional gain
118 Ki_vdc = alpha_vdc*G_vdc;                                 % integral
     gain
119 % Reactive power control loop
120 alpha_Qgsc = 2.2/Tr_Qgsc;                                 %
    controller bandwith (rad)
121 Ki_Qgsc = 2/3*alpha_Qgsc/Vb(2);                          % integral
    gain calculation
122 % RSC current controller
123 alpha_i_rsc = 2.2/Tr_irsc;                                %
    controller bandwith (rad)
124 G_irsc = (-Rr(2)*Lss(2)+alpha_i_rsc*(Lrr(2)*Lss(2)-LmSI(2)^2))
    /Lss(2);
125 Kp_irsc = alpha_i_rsc*(Lrr(2)*Lss(2)-LmSI(2)^2)/Lss(2);
126 Ki_irsc = alpha_i_rsc*(RrSI(2)+G_irsc);
127 % rotor speed controller
128 alpha_wr = 2.2/Tr_wr;
129 G_wr = (alpha_wr*J(2))-DSI(2);
130 Kp_wr = alpha_wr*J(2);
131 Ki_wr = alpha_wr*(G_wr+DSI(2));
132 % Stator reactive power controller equations
133 alpha_Qs = 2.2/Tr_Qs;
134 Ki_Qs = -2*alpha_Qs*(L1sSI(2)+LmSI(2))/(3*LmSI(2));
135
136 %% Transmission Line
```

```
137 % 220kV underground PIPE line parameters
138 dist = 100;
139 Vline = 220e3;
140 R_line = 0.018*dist;                          % cable
    resistance (ohm/km)
141 L_line = 3.2e-3*dist;                         %
    inductance (H/km)
142 C_line = 0.21e-6*dist;                        %
    capacitance (F/km)
143 % Converter Parameters
144 Vdc_wind = Vn(3)*5;
145 R_wind = 0.0015*Zb(3);
146 L_wind = 0.15*Lb(3);
147 % Controller
148 Tr_iwind = 10e-3;
149 alpha_iwind = 2.2/Tr_iwind;                   %
    controller bandwidth (rad)
150 G_iwind = (alpha_iwind*L_wind)-R_wind;        % active
    damping gain
151 Kp_iwind = alpha_iwind*L_wind;                %
    proportional gain
152 Ki_iwind = alpha_iwind*(R_wind+G_iwind);      % integral
     gain
```

Bibliography

[1] UK Government. *Offshore Wind Sector Deal*. Tech. rep. 2020, pp. 1–26.

[2] Wind Europe. *Offshore Wind in Europe - Key trends and statistics 2017*. Tech. rep. 2018.

[3] Espen Olsen, Urban Axelsson, and Andre Canelhas. "Low Frequency AC Transmission on large scale Offshore Wind Power Plants, Achieivng the best from two worlds?" In: *13th Wind Integration Workshop* October 2017 (2014).

[4] Kristian Weiland. "New technological challenges operating the 110 KV, 16.7 HZ grid for railway power supply in Germany". In: *IET Conference Publications*. 550 CP. 2009, pp. 7–9.

[5] Tsuyoahi Funaki and Kenji Matsuura. "Feasibility of the Low Frequency AC transmission". In: *IEEE Power Engineering Society Winter Meeting*. 2000.

[6] Qi Wang, Xiaohu Chen, and Yanchao Ji. "Control for maximal wind energy tracing in matrix converter AC excited brushless doubly-fed wind power generation system". In: *IECON Proceedings (Industrial Electronics Conference)* (2006), pp. 718–723.

[7] M. S. Carmeli et al. "MVDC connection of offshore wind farms to the transmission system". In: *SPEEDAM 2010 - International Symposium on Power Electronics, Electrical Drives, Automation and Motion* 22.1 (2010), pp. 1201–1206.

[8] Hao Chen, Michael H. Johnson, and Dionysios C. Aliprantis. "Low-frequency ac transmission for offshore wind power". In: *IEEE Transactions on Power Delivery* 28.4 (2013), pp. 2236–2244.

[9] Nikolas Flourentzou, Vassilios G. Agelidis, and Georgios D. Demetriades. "VSC-based HVDC power transmission systems: An overview". In: *IEEE Transactions on Power Electronics* 24.3 (2009), pp. 592–602.

[10] Serhiy Bozhko et al. "Control of offshore DFIG-based wind farm grid with line-commutated HVDC connection". In: *EPE-PEMC 2006: 12th International Power Electronics and Motion Control Conference, Proceedings* 22.1 (2007), pp. 1563–1568.

[11] Sakis Meliopoulos et al. *Low Frequency Transmission Final Project Report*. Tech. rep. PSERC, 2012.

[12] The Crown Estate and DNV GL. *Sharing Lessons Learned and Good Practice in Offshore Transmission*. Tech. rep. 2014, p. 80.

[13] Nan Qin et al. "Offshore wind farm connection with low frequency AC transmission technology". In: *2009 IEEE Power and Energy Society General Meeting, PES '09* (2009), pp. 1–8.

[14] Dongbo Zhao et al. "Reliability evaluation with cost analysis of alternate wind energy farms and interconnections". In: *2012 North American Power Symposium, NAPS 2012*. IEEE, 2012, pp. 1–6.

[15] W. Fischer, R. Braun, and I. Erlich. "Low frequency high voltage offshore grid for transmission of renewable power". In: *IEEE PES Innovative Smart Grid Technologies Conference Europe* (2012), pp. 1–6.

[16] ABB and Cien/Endesa Group. *Brazil-Argentina HVDC Interconnection*. 2020.

[17] ABB, E.ON, and DB Energie. *World's most powerful rail frequency converter*. Tech. rep.

[18] T Takada. "New Direct Observation Technique for Electric Charge Behavior in Insulating Materials and Its Application to Power Cables". In: *CIGRE session*. 1998, pp. 15–303.

[19] Henrik Waje-andreassen. "Low Frequency AC Transmission". PhD thesis. Norwegian University of Science and Technology, 2016.

[20] TELE-FONIKA Kable S.A. *High and Extra High Voltage Cables.*

[21] Sidney Gierschner, Hans Gunter Eckel, and Mark Matthias Bakran. "A competitive medium frequency AC distribution grid for offshore wind farms using HVDC". In: *2013 15th European Conference on Power Electronics and Applications, EPE 2013* February 2018 (2013).

[22] José Luis Domínguez-García et al. "Effect of non-standard operating frequencies on the economic cost of offshore AC networks". In: *Renewable Energy* (2012).

[23] P B Wyllie et al. "Low Frequency AC Transmission - Elements of a Design for Wind Farm Connection". In: *11th IET International Conference on AC and DC Power Transmission* 1 (2015), pp. 1–5.

[24] ABB. *ABB powers rail traffic in Germany.* Tech. rep. 2009.

[25] Jovana Dakic et al. "Optimal Design of an HVAC Transmission System for Offshore Wind Power Plants Including Mid-cable Reactive Power Compensation". In: *IEEE Transactions on Power Delivery* (2020).

[26] E. H. Camm et al. "Characteristics of wind turbine generators for wind power plants". In: *2009 IEEE Power and Energy Society General Meeting, PES '09* (2009), pp. 4–8.

[27] Seetha Chaithanya, V. Naga Bhaskar Reddy, and R. Kiranmayi. "A State of Art Review on Offshore Wind Power Transmission Using Low Frequency AC System". In: *International Journal of Renewable Energy Research* 8.1 (2018), pp. 52–58.

[28] Shenquan Liu et al. "Integrating Offshore Wind Power Via Fractional Frequency Transmission System". In: *IEEE Transactions on Power Delivery* 32.3 (2017), pp. 1253–1261.

[29] Zhuoyan Song et al. "PMSG-based fractional frequency wind power system". In: *2014 IEEE Innovative Smart Grid Technologies - Asia, ISGT ASIA 2014* (2014), pp. 302–306.

[30] E Khalafalla and S Dun. "A high-performance, controlled cycloconverter for traction power application". In: *IEEE/ASME Joint Railroad Conference*. 1991.

[31] B. R. Pelly. *Thyristor Phase-Controlled Converters and Cycloconverters: Operation, Control and Performance*. Wiley-Blackwell, 1971.

[32] Yongnam Cho, George J. Cokkinides, and A. P. Meliopoulos. "Advanced time domain method for remote wind farms with LFAC transmission systems: Power transfer and harmonics". In: *2012 North American Power Symposium, NAPS 2012* (2012), pp. 1–6.

[33] Nathalie Holtsmark and Marta Molinas. "Matrix converter efficiency in a high frequency link offshore WECS". In: *IECON Proceedings (Industrial Electronics Conference)* (2011), pp. 1420–1425.

[34] Patrick W. Wheeler et al. "Matrix converters: A technology review". In: *IEEE Transactions on Industrial Electronics* 49.2 (2002), pp. 276–288.

[35] Jonathan Ruddy. "Low Frequency AC Transmission for Offshore Wind". PhD thesis. University College Dublin, 2017.

[36] Jonathan Ruddy, Ronan Meere, and Terence O'Donnell. "Low Frequency AC transmission for offshore wind power: A review". In: *Renewable and Sustainable Energy Reviews* 56 (2016), pp. 75–86.

[37] Xifan Wang and Xiuli Wang. "Feasibility study of fractional frequency transmission system". In: *IEEE Transactions on Power Systems* 11.2 (1996), pp. 962–967.

[38] P. P. Biringer and J. D. Lavers. "Recent advances in the design of large magnetic frequency changers". In: *IEEE Transactions on Magnetics* 12.6 (1976), pp. 823–828.

[39] Takuma Sudani and Kazuo Bessho. "An Analytical Investigation on the Efficiency of a Magnetic Frequency Tripler with Series-Connected Reactors". In: *IEEE Transactions on Magnetics* 23.4 (1987), pp. 1956–1963.

[40] Nikola Tesla. *Dynamo Electric Machine*. 1888.

[41] Hermann Sundhaussen. *Ward-Leonard Control System.* 1935.

[42] John Laury. "Stability of Low-Frequency AC Railways". PhD thesis. Lulea University of Technology, 2019.

[43] P Tavner. "Condition Monitoring of Rotating Electrical Machines". In: *IET Electric Power Applications* 1.5 (2007), pp. 215–247.

[44] Yong Min You, Thomas A. Lipo, and Byung Il Kwon. "Design and analysis of a novel grid-connected to rotor type doubly fed induction machine". In: *IEEE Transactions on Magnetics* 48.2 (2012), pp. 919–922.

[45] N. L. Zietsman and N. Gule. "Design and evaluation of a 1.2 kVA single phase rotary transformer". In: *Proceedings - 2016 22nd International Conference on Electrical Machines, ICEM 2016* (2016), pp. 1466–1472.

[46] Marek Adamowicz, Ryszard Strzelecki, and Piotr Mysiak. "Cascaded doubly fed induction generator using PFC rectifiers". In: *2009 Compatability and Power Electronics* (2009), pp. 186–190.

[47] Kostyantyn Protsenko and Xu Dewei. "Modeling and control of brushless doubly-fed induction generators in wind energy applications". In: *Conference Proceedings - IEEE Applied Power Electronics Conference and Exposition - APEC* 23.3 (2007), pp. 529–535.

[48] Siming Wei et al. "Motor-generator pair: a novel solution to provide inertia and damping for power system with high penetration of renewable energy". In: *IET Generation, Transmission & Distribution* 11.7 (2017), pp. 1839–1847.

[49] S Wei et al. "A possible configuration with motor-generator pair for renewable energy integration". In: *CSEE Journal of Power and Energy Systems* 3.1 (2017), pp. 93–100.

[50] Yingkun Zhou et al. "Experiment Study on the Control Method of Motor-Generator Pair System". In: *IEEE Access* 6 (2017), pp. 925–936.

[51] S. Williamson and A.C. Ferreira. "Generalised theory of the brushless doubly-fed machine. Part 2: Model verification and performance". In: *IEE Proceedings - Electric Power Applications* 144.2 (1997), p. 123.

[52] Paul E. Marken et al. "VFT - A smart transmission technology that is compatible with the existing and future grid". In: *2009 IEEE/PES Power Systems Conference and Exposition, PSCE 2009* (2009), pp. 1–7.

[53] Elizabeth R. Pratico et al. "VFT operational overview -the Laredo project". In: *2007 IEEE Power Engineering Society General Meeting, PES*. 2007.

[54] R J Piwko et al. "Variable Frequency Transformer – A New Alternative For Asynchronous Power Transfer". In: *Inaugural IEEE PES 2005 Conference and Exposition in Africa*. 2005.

[55] R J Piwko et al. "Variable Frequency Transformer – FACTS Technology For Asynchronous Power Transfer". In: *IEEE/PES Transmission and Distribution Conference and Exhibition*. 2006.

[56] Arezki Merkhouf, Pierre Doyon, and Sanjoy Upadhyay. "Variable frequency transformer - Concept and electromagnetic design evaluation". In: *IEEE Transactions on Energy Conversion* 23.4 (2008), pp. 989–996.

[57] Rongxiang Yuan et al. "Simulation model and characteristics of variable frequency transformers used for grid interconnection". In: *2009 IEEE Power and Energy Society General Meeting, PES '09*. 2009, pp. 1–5.

[58] Gesong Chen and Xiaoxin Zhou. "Digital simulation of variable frequency transformers for asynchronous interconnection in power system". In: *Proceedings of the IEEE Power Engineering Society Transmission and Distribution Conference*. 2005.

[59] General Electric. *Linden VFT Information Memorandum - Transmission Scheduling Rights Auction*. Tech. rep. 2015.

[60] Xiaoqian Li et al. “Capacitor voltage balancing control based on CPS-PWM of modular multilevel converter”. In: *IEEE Energy Conversion Congress and Exposition: Energy Conversion Innovation for a Clean Energy Future, ECCE 2011, Proceedings* (2011), pp. 4029–4034.

[61] Joachim Holtz. “Pulsewidth Modulation - A Survey”. In: *IEEE Transactions on Industrial Electronics* 39.5 (1992).

[62] Amirnaser Yazdani and Reza Iravani. *Voltage-Sourced Converters in Power Systems: Modeling, Control, and Applications*. 2010, p. 541.

[63] Jeffrey Umland and Mohammed Safiuddin. “Magnitude and Symmetric Optimum Criterion for the Design of Linear Control Systems: What is it and how does it compare with the others?” In: *IEEE Transactions on Industry Applications* 26.3 (1990), pp. 489–497.

[64] Ronald B Standler. *Protection of Electronic Circuits from Overvoltages*. 2012, p. 464.

[65] Rolf Ottersten. “On Control of Back-to-Back Converters and Sensorless Induction Machine Drives”. PhD thesis. Chalmers University of Technology, 2003.

[66] David Campos-gaona, Rafael Peña-alzola, and Martin Ordonez. “Nonminimum Phase Compensation in VSC-HVDC Systems for Fast Direct Voltage Control”. In: *IEEE transactions on power delivery* 30.6 (2015), pp. 2535–2543.

[67] David Campos-Gaona et al. *Offshore Wind Energy Generation*. 2014.

[68] Chee-Mun Ong. *Dynamic Simulation of Electric Machinery Using Matlab*. 1998.

[69] Evgenije Adzic et al. “PLL Synchronization in Grid- Connected Converters”. In: *6th PSU-UNS International Conference on Engineering and Technology*. May. 2013.

[70] Adrian Timbus et al. “Synchronization Methods for Three Phase Distributed Power Generation Systems. An Overview and Evaluation”. In: *IEEE 36th Conference on Power Electronics Specialists, 2005.* 2005 (2005), pp. 2474–2481.

[71] Ion Boldea. *The Electric Generators Handbook*. CRC Press, 2015, p. 1100.

[72] P Kundur. *Power system stability and control.*

[73] Alexandra von Meier. *Electric Power Systems - A Conceptual Introduction.* 9. Wiley, 2007, pp. 1143–1147.

[74] John Grainger and William Stevenson. *Power Aystem Analysis.* 2nd ed. McGraw Hill, 2016.

[75] Christian Wessels, Fabian Gebhardt, and Friedrich Wilhelm Fuchs. "Fault ride-through of a DFIG wind turbine using a dynamic voltage restorer during symmetrical and asymmetrical grid faults". In: *IEEE Transactions on Power Electronics* 26.3 (2011), pp. 807–815.

[76] Stephen Chapman. *Electric Machinery Fundamentals.* 5th ed. Vol. 53. 9. McGraw Hill, 2012, p. 680.

[77] Nektarios Karakasis et al. "Efficiency increase in a wind system with Doubly Fed Induction Generator". In: *IECON Proceedings (Industrial Electronics Conference)* (2016), pp. 4091–4096.

[78] General Electric Company. *Variable Frequency Transformer - Fact Sheet.* Tech. rep. 2004.

[79] General Electric Company. *Connecting Water to Wire.* 2016.

[80] Chao Yang, Xiaobo Yang, and Yao Chen. "Integration of variable speed hydropower generation and VSC HVDC". In: *2015 17th European Conference on Power Electronics and Applications, EPE-ECCE Europe 2015* (2015).

[81] Vladimir Lazarov, Zahari Zarkov, and Ludmil Stoyanov. "Experimental Study of Losses in Doubly-Fed Induction Generator". In: *Ecological Engineering and Environment Protection* 3 (2012), pp. 34–40.

[82] Jan Machowski, Janusz Bialek, and James Bumby. *Power system stability and control.* May. 2017, p. 450.

[83] National Grid. *GC0062 – Fault Ride Through.* Tech. rep., pp. 1–78.

[84] C. Rong, A. Mats, and X. Hailian. "Methods for transient AC overvoltage reduction at wind farm terminal". In: *China International Conference on Electricity Distribution, CICED* 2016-Septe.Ciced (2016), pp. 10–13.

[85] Gesong Chen, Xiaoxin Zhou, and Rui Chen. *Variable Frequency Transformers for Large Scale Power Systems*. 2018.

[86] Tokyo Electric Power Company, Tokyo Electric Power Services, and Japan International Cooperation Agency. *Final Report on Feasibility Study on Adjustable Speed Pumped Storage Generation Technology*. Tech. rep. January. 2012.

[87] Edgar Lucas, David Campos-Gaona, and Olimpo Anaya-Lara. "Assessing the impact of DFIG synthetic inertia provision on power system small-signal stability". In: *Energies* 12.18 (2019).

[88] Yuxiao Xia et al. "Damping inter-area modes of oscillation and improving transmission capacity using global PSS". In: *2009 International Conference on Energy and Environment Technology, ICEET 2009* 2.50677046 (2009), pp. 107–110.

[89] J. B. Ekanayake, L. Holdsworth, and N. Jenkins. "Comparison of 5th order and 3rd order machine models for doubly fed induction generator (DFIG) wind turbines". In: *Electric Power Systems Research* 67.3 (2003), pp. 207–215.

[90] Mohamed Edrah, Kwok L. Lo, and Olimpo Anaya-Lara. "Impacts of high penetration of DFIG wind turbines on rotor angle stability of power systems". In: *IEEE Transactions on Sustainable Energy* 6.3 (2015), pp. 759–766.

[91] Yuan Zhang Sun et al. "Review on frequency control of power systems with wind power penetration". In: *2010 International Conference on Power System Technology* (2010), pp. 1–8.

[92] Ciaran Roberts. *Review of International Grid Codes*. Tech. rep. February. Lawrence Berkeley National Laboratory, 2018, p. 64.

[93] Hydro-Quebec TransEnergie. *Technical requirements for the connection of generation facilities to the hydro-québec transmission system*. Tech. rep. May. 2003, pp. 1–110.

[94] Stewart Whyte and National Grid. *Grid Code Frequency Response Working Group - National Grid*. Tech. rep. 2012.

[95] Mohammad Dreidy, H. Mokhlis, and Saad Mekhilef. "Inertia response and frequency control techniques for renewable energy sources: A review". In: *Renewable and Sustainable Energy Reviews* 69.November 2015 (2017), pp. 144–155.

[96] Zhiheng Zhang et al. "Comparison of inertia control methods for DFIG-based wind turbines". In: *2013 IEEE ECCE Asia Downunder - 5th IEEE Annual International Energy Conversion Congress and Exhibition, IEEE ECCE Asia 2013* (2013), pp. 960–964.

[97] Jing Ma et al. "Research on the impact of DFIG virtual inertia control on power system small-signal stability considering the phase-locked loop". In: *IEEE Transactions on Power Systems* 32.3 (2017), pp. 2094–2105.

[98] X. Xiang, M. M. C. Merlin, and T. C. Green. "Cost Analysis and Comparison of HVAC , LFAC and HVDC for Offshore Wind Power Connection". In: *IET 12th International Conference on AC andDC Transmission* (2016), pp. 14–19.

[99] José Luis Domínguez-García et al. "Effect of non-standard operating frequencies on the economic cost of offshore AC networks". In: *Renewable Energy* 44 (2012), pp. 267–280.

[100] M. Dicorato et al. "Guidelines for assessment of investment cost for offshore wind generation". In: *Renewable Energy* 36.8 (2011), pp. 2043–2051.

[101] The Crown Estate, ORE Catapult, and BVG Associates. *Guide to an Offshore Wind Farm*. Tech. rep. 2019.

[102] Orsted. *Hornsea Project One*.

[103] National Grid ESO. *Electricity Ten Year Statement - Appendix E*. Tech. rep. 2015.

[104] Predrag Djapic, Goran Strbac, and Centre for Sustainable Electricity and Distributed Generation. *Cost benefit methodology for optimal design of offshore transmission systems*. Tech. rep. 2008.

[105] Patrick Smith. *Siemens commissions 800MW BorWin2*. 2015.

[106] Patrick Smith. *Costs force ABB to abandon offshore converter work*. 2014.

[107] David Weston. *Offshore wind costs dampen ABB earnings*. 2014.

[108] Philipp Härtel et al. "Review of investment model cost parameters for VSC HVDC transmission infrastructure". In: *Electric Power Systems Research* 151 (2017), pp. 419–431.

[109] Hakan Ergun, D. Van Hertem, and R. Belmans. "Transmission system topology optimization for large-scale offshore wind integration". In: *IEEE Transactions on Sustainable Energy* 3.4 (2012), pp. 908–917.

[110] T&D World. *Texas Variable Frequency Transformer Installation*. 2007.

[111] LLC Monitoring Analytics. *State of the Market Report for PJM*. Tech. rep. New Jersey, 2017, p. 391.

[112] PJM Interconnection. *PJM Transmission Interconnection #G22 Linden 230 kV VFT Impact Study Report*. Tech. rep. 2004.

[113] Energy Storage Association. *Variable Speed Pumped Hydroelectric Storage*.

[114] W. Fischer, R. Braun, and I. Erlich. "Low frequency high voltage offshore grid for transmission of renewable power". In: *IEEE PES Innovative Smart Grid Technologies Conference Europe* (2012), pp. 1–6.

[115] Thomas Luth et al. "High-frequency operation of a DC/AC/DC system for HVDC applications". In: *IEEE Transactions on Power Electronics* 29.8 (2014), pp. 4107–4115.

[116] Callum Maciver, Keith R.W. Bell, and Dusko P. Nedic. "A reliability evaluation of offshore HVDC grid configuration options". In: *IEEE Transactions on Power Delivery* 31.2 (2016), pp. 810–819.

[117] IRENA. *Renewable Energy Technologies: Cost Analysis Series - Hydropower*. Tech. rep. 3. 2012.

[118] National Grid ESO. *Frequency Response Services*.

[119] Takao Kuwabara et al. “Design and Dynamic Response Characteristics of 400MW Adjustable Speed Pumped Storage Unit for Ohkawachu Power Station”. In: *IEEE Transactions on Energy Conversion* 11.2 (1996), pp. 376–384.

[120] Shiyi Shao, Ehsan Abdi, and Richard McMahon. “Vector control of the brushless doubly-fed machine for wind power generation”. In: *2008 IEEE International Conference on Sustainable Energy Technologies, ICSET 2008* (2008), pp. 322–327.

[121] Paul C Roberts. “A Study of Brushless Doubly-Fed (Induction) Machines”. In: September 2004 (2005), p. 311.

[122] Peng Han et al. “Brushless Doubly-Fed Machines : Opportunities and Challenges”. In: 4.2 (2018).

[123] Michael S. Boger, Alan K. Wallace, and René Spec. “Investigation of appropriate pole number combinations for brushless doubly fed machines applied to pump drives”. In: *IEEE Transactions on Industry Applications* 32.1 (1996), pp. 189–194.

[124] S. Williamson. “Generalised theory of the brushless doubly-fed machine. Part 1: Analysis”. In: *IEE Proceedings: Electric Power Applications* 144.2 (1997), pp. 111–121.

[125] Hamed Gorginpour, Behzad Jandaghi, and Hashem Oraee. “A novel rotor configuration for brushless doubly-fed induction generators”. In: *IET Electric Power Applications* 7.2 (2013), pp. 106–115.

[126] Fei Xiong and Xuefan Wang. “Design of a low-harmonic-content wound rotor for the brushless doubly fed generator”. In: *IEEE Transactions on Energy Conversion* 29.1 (2014), pp. 158–168.

[127] Javier Poza et al. “Unified Reference Frame dq Model of the Brushless Doubly Fed Machine”. In: 153.5 (2006).

[128] Werner Leonhard. *Control of Electrical Drives*. Vol. 22. 1986, pp. 612–613.

[129] A.S Abdel-Khalik et al. “Brushless Doubly Fed Induction Machine as a Variable Frequency Transformer”. In: *IET International Conference on Power Electronics, Machines and Drives*. 2012.

[130] Texas Instruments Incorporated. *TMS320F2833x, TMS320F2823x Digital Signal Controllers (DSCs)*. 2016.

[131] STMicroelectronics and ST. *STEVAL-IPM User Manual*. 2018.